

AD-A276 324



MATERIALS

AND

MANUFACTURING

PROCESSES

DTIC  
ELECTE  
MAR 01 1994  
S E

94-06682



190pgs



94 2 28 089

Volume 9

Number 1

1994

**Best  
Available  
Copy**

**MATERIALS AND MANUFACTURING PROCESSES**

**January 1994**

**Aims and Scope.** *Materials and Manufacturing Processes* is a journal in the English language providing an international forum for current developments and future direction in the area of materials and manufacturing processes. Manuscripts may fall into several categories including full articles, solicited reviews, or commentary, unsolicited reviews or commentary, and patent and book reviews.

**Identification Statement.** *Materials and Manufacturing Processes* (ISSN: 1042-6914) is published six times a year in the months of January, March, May, July, September, and November for the institutional rate of \$545.00 and the individual rate of \$35.00 by Marcel Dekker, Inc., P.O. Box 5005, Monticello, NY 12701-5185.

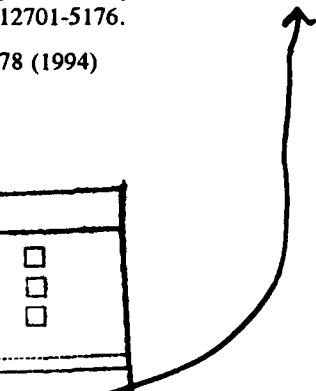
Volume	Issues	Institutional Rate	Individual Professionals and Student Rate	Foreign Postage		
				Surface	Airmail To Europe	Airmail To Asia
9	6	\$545.00	\$35.00	\$22.50	\$33.00	\$39.00

Your order must be prepaid by personal check or may be charged to MasterCard, VISA, or American Express. Please mail payment with your order to: Marcel Dekker Journals, P.O. Box 5017, Monticello, New York 12701-5176.

CODEN: MMAPET 9(1) i-ii, 1-178 (1994)  
ISSN: 1042-6914

Printed in the U.S.A.

Accession For	
NTIS CRA&I	<input type="checkbox"/>
DTIC TAB	<input type="checkbox"/>
Unannounced	<input type="checkbox"/>
Justification	
By	<b>\$35.00</b>
Distribution	
Availability Codes	
Dist	Availability Codes
<b>A-1</b>	<b>21</b>



①

# MATERIALS AND MANUFACTURING PROCESSES

## Editors

T.S. SUDARSHAN  
*Materials Modification, Inc.*  
2929-P1 Eskridge Center  
Fairfax, Virginia 22031  
phone # (703) 560-1371  
fax # (703) 560-1372

T.S. SRIVATSAN  
*Department of Mechanical  
Engineering*  
*The University of Akron*  
Akron, Ohio 44325  
phone # (216) 972-6196  
fax # (216) 972-6027



## Review Board

- O. AUCIELLO, *MCNC, P.O. Box 12889, Research Triangle Park, NC 27709-2889*  
D.G. BHAT, *Valenite, 1711 Thunderbird Drive, Troy, MI 48084*  
R.L. BROWN, *The Gillette Company, Gillette Park, Boston, MA 02106*  
S.T. BULJAN, *Norton Company, 1 New Bond Street, Worcester, MA 01615*  
R. DOWDING, *U.S. Army Materials Technology Laboratories, Watertown, MA 02172*  
K. ISHIZAKI, *Nagaoka University of Technology, Nagaoka, Niigata 940-21, Japan*  
M. JEANDIN, *Ecole Nationale Supérieure des Mines de Paris, B.P. 87, 91003, Evry, Cedex, France*  
H. KATZMAN, *The Aerospace Corporation, MS M2-248, P.O. Box 92957, Los Angeles, CA 90009*  
R.J. LEDERICH, *McDonnell Douglas Aerospace, P.O. Box 516, St. Louis, MO 63166-0516*  
K.L. LIN, *Materials Engineering, National Cheng Kung University, Tainan, Taiwan 70101, ROC*  
J.J. MOORE, *Metallurgical Engineering, Colorado School of Mines, Golden, CO 80401*  
S. NOURBAKHS, *Polytechnic Institute, 333 Jay Street, Brooklyn, NY 11201*  
S. RAGHAVAN, *Materials Science, University of Arizona, Tucson, AZ 85721*  
W.O. SOBOYEJO, *Materials Engineering, Ohio State University, Columbus, OH 43210*  
G. SMOLIK, *P.O. Box 1625, Idaho National Engineering Laboratory, Idaho Falls, ID 83415*  
J.B. TERRELL, *Reynolds Metals Company, P.O. Box 27003, Richmond, VA 23261*  
W. WALLACE, *National Aeronautical Establishment, Ottawa, KIAOR6, Canada*  
J.D. WHITTENBERGER, *NASA Lewis Research Center, MS 49-1, Cleveland, OH 44135*

DTIC QUALITY INSPECTED 1

## **MATERIALS AND MANUFACTURING PROCESSES**

---

**Indexing and Abstracting Services.** Articles published in *Materials and Manufacturing Processes* are selectively indexed or abstracted in:

■ Abstracts Journal of the Institute of Scientific Information of the USSR Academy of the Sciences ■ Academy of Sciences of the USSR ■ Advanced Ceramics Bulletin ■ Advanced Composites Bulletin ■ Applied Mechanics Reviews ■ ASM International—Materials Information ■ Cambridge Scientific Abstracts ■ Ceramics Bulletin ■ Chemical Abstracts ■ Corrosion Abstracts ■ Engineering Index ■ INSPEC ■ ISI—Materials Science Citation Index ■ Japan Abstracts ■ Japan Institute of Metals ■ Rapra Abstracts ■ UNIDO-Tech Monitor

**Manuscript Preparation and Submission.** See end of issue.

Copyright ©1994 by Marcel Dekker, Inc. All rights reserved. Neither this work nor any part may be reproduced or transmitted in any form or by any means, electronic or mechanical, microfilming and recording, or by any information storage and retrieval systems without permission in writing from the publisher.

The Journals of Marcel Dekker, Inc. are available in microform from: RESEARCH PUBLICATIONS, 12 Lunar Drive, Drawer AB, Woodbridge, Connecticut, 06525, (203) 397-2600 or Toll Free 1-800-REACH-RP (732-2477). Outside North and South America: P.O. Box 45, Reading, RG1 8HF, England, 0734-583247.

Authorization to photocopy items for internal or personal use, or the internal or personal use of specific clients, is granted by Marcel Dekker, Inc., for users registered with the Copyright Clearance Center (CCC) Transactional Reporting Service, provided that the base fee is paid directly to CCC, 222 Rosewood Drive, Danvers, MA 01923. For those organizations that have been granted to photocopy license by CCC, a separate system of payment has been arranged.

Contributions to this journal are published free of charge.

This journal is printed on acid-free paper.

## **Diamond Materials for Electromagnetic Railguns**

**Narendra B. Dahotre, Mary Helen McCay, and  
T. Dwayne McCay**

Center for Laser Applications  
The University of Tennessee Space Institute  
Tullahoma, Tennessee 37388

### **Abstract**

The use of diamond film insulator in electromagnetic railguns is currently being seriously considered since the state of the art in synthetic diamond exceeds the requirements of electromagnetic railguns. The reasons for not using diamond, however, include the major difficulty in producing diamond insulators in the required shape and size that can survive the harsh railgun environment. This paper reviews railgun operation dynamics and potential materials including diamond for high performance of railguns. It further reviews the present status of scientific, technological and commercial developments of diamond coatings. Alternate coatings and the properties that make them amenable for railgun applications are also discussed.

### **1.0 Introduction**

Electromagnetic railguns have been the subject of active research and development for the past decade and a half (1-8). During this period substantial enthusiasm existed for the development of plasma armature accelerators operating at velocities of 20 to 50 km/sec. The basis for this optimism was a common notion that plasma armatures could couple magnetic force to projectiles at almost any velocity up to the speed of light and that the principal velocity limitation was

projectile-bore interactions. To date however, considerable research efforts in this direction have so far failed to achieve the high velocities predicted in the beginning. In fact, only a few experiments (2,3) have been successful in reaching the apparent barrier of 6 to 7 km/sec. As a result, a consensus is building among the research community that the plasma armature itself has strong interactions with the railgun structure and these interactions are the dominant factor limiting the performance of plasma armature railguns.

The kinetic processes which act upon the plasma armature in a conventional electromagnetic railgun (in sequential order following the armature as shown in Figure 1) are: main plasma, plasma tail, neutral region and restrike plasma. These events occur in a quasi-equilibrium state of the armature which is generally achieved after having moved a typical distance of 20 to 40 diameters. The main plasma is highly ionized at temperatures from 20,000 to 30,000 K and dissipates power at a level of several MW/cm<sup>2</sup>. Most of the primary plasma is strongly magnetized and the boundary layers are thin due to magneto-hydrodynamic effects. This results in a high drag coefficient ( $C_f = 0.003 - 0.005$ ). The intense heat and radiation flux at the walls ablate material which in turn is ionized and added to the armature plasma. The electromagnetic force accelerates the ablated material almost to the velocity of the main plasma. Viscous boundary forces slowly drag most of this ablated material backward into the plasma tail region. The ablated material continues to radiate and conduct energy to the walls. In the tail region the power flux is lower and less of the wall material is ionized. The neutral gas from the walls begins to mix into the plasma, quenching the conductivity. A cool boundary layer develops which grows into the plasma until finally the conductivity becomes too low for current to flow. This makes the end of the plasma tail.

The gas entering the neutral region is still very hot. Although it is moving at a velocity substantially below that of the plasma, it is in turbulent flow and both heat and momentum are rapidly coupled to the wall. This causes further vaporization

of material from the walls. (Metal rails may not be vaporized if the rate of conduction cooling into the rail exceeds the rate of heat input from the gas.) The gas velocity in the heated region will continue to decrease due to viscous drag against the wall and due to the admixture of material vaporized from the insulator.

This region is called the neutral region because the gas is neutral in the sense that the high gas density and weak ionization result in a very low electrical conductivity. No current flow is observed by conventional diagnostics. However, if a sufficiently high electric field is applied to this gas, the resultant small current flow will lead to run-away ionization and reestablishment of a hot, low density, highly ionized plasma, called the restrike arc. The electric field required to cause such a breakdown depends primarily upon neutral gas density and level of residual ionization and also secondary factors such as gas temperature, gas composition and electrode surface conditions. As the plasma armature velocity increases, the electric field increases until the breakdown field is reached. Since the gas velocity is lowest near the breach and rail damage is often greatest near the breach, it is quite common for breakdown to occur in the breach region.

When these events occur, the parameter which has a strong experimental correlation with railgun velocity is breakdown field for restrike ( $\epsilon_B$ ), which is predicted by equation (1), where  $I$  is the armature current,  $V_A$  is the armature voltage,  $\alpha_R$  is the rail mass addition coefficient for ablation,  $\alpha_I$  is the insulator mass addition coefficient for vaporization,

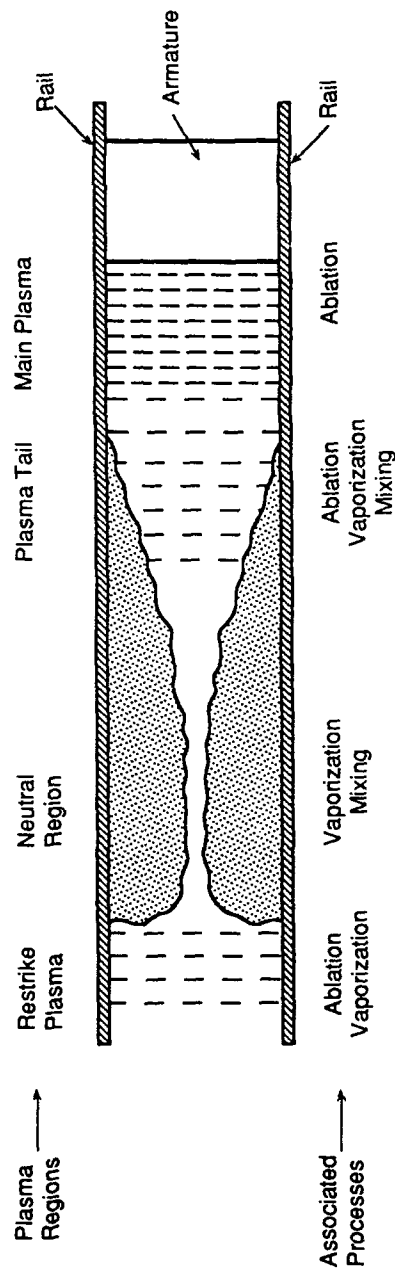


Figure 1: Schematic of the Plasma Armature in a Railgun (9).

$$V_a = V_g + \frac{0.7 (\epsilon/N) V_A (\alpha_R + \alpha_I)}{A \pi R V_p L} - \frac{V_A}{L I} \quad (1)$$

Equation (2) shows the expression for R is the bore radius,  $V_p$  is the plasma velocity, L is the inductance gradient,  $V_g$  is the gas velocity,  $V_a$  is the armature velocity, A is the average atomic weight of the gas (9).

breakdown field (9).  $\epsilon$  is an electric field, N is the particle density,  $\delta_N$  is the neutral gas density and the term  $(\epsilon/N)$  is the threshold value for electrical breakdown.

$$\epsilon_B = (\epsilon/N) \frac{\delta_N}{A} \quad (2)$$

This equation predicts an armature velocity for restrike which is a weak function of current but scales linearly with the armature voltage  $V_A$ .

Based on the earlier explanation, it is evident that the arc restrike is the principle armature velocity limiting process. Both experiment and theory (2-4, 10,11) predict that velocities in excess of 6 to 8 km/sec will not be achieved unless restrike is controlled. Such techniques for restrike control include a) increasing the breakdown voltage of the gas in the bore, b) introducing external circuit changes by adapting a multi-stage, segmented railgun, c) lowering the electric field acting in the restrike region by increasing the velocity of the neutral gas using a high velocity injector, d) eliminating vaporized material from the bore by applying the magnetic force against the viscous drag force, e)

reducing the armature power dissipation by lowering the armature voltage or the armature current, and f) using improved rail and armature materials.

### 1.1 Materials for High Performance Railguns

All of the above techniques have been attempted for increasing railgun performance and have achieved only limited success, largely due to limitations in the design. In view of these limitations, new techniques for the synthesis of advanced materials have opened the possibility of tailoring suitable materials for specific rail and insulator applications in electromagnetic railgun barrels. The proper selection of such materials for the successful performance of bore components will depend on several practical as well as technological factors. In particular, the materials must survive multiple shots under rapid-fire bursts without suffering significant deterioration in performance.

In order to meet these requirements, the materials used to form the bore must operate without significant degradation in a dynamic environment which combines extreme thermal, mechanical and electrical loading conditions. This behavior can be understood from the restrike velocity relationship given by equation 1. If restrike limits velocity, then the best results will be obtained when  $(\alpha_I + \alpha_R)/A$

is large and the bore has a high particle density to insulate against breakdown. This quantity is maximized by using materials with low atomic weight (small  $A$ ) and low heat of vaporization (large  $\alpha_v$ ). Materials which potentially might satisfy these requirements are organic insulators, organic composites, conventional ceramics, advanced ceramics and reinforced ceramic composites. A partial list of candidate materials for the rail, insulator and armature applications, together with their thermophysical properties, are listed in Table 1.

A review of the open technical literature uncovers very little about the evaluation of alternate materials for railgun insulators. The study by Bedford (12) was not comprehensive and did not provide specific recommendations on the possible usefulness of materials for railgun applications. Recent unpublished (13) studies confirmed the effectiveness of diamond film insulators in an ablation free environment to achieve 4 km/s velocity with 1.4 g Lexan projectiles. In another unpublished study (14) host of materials including pure metals, alloys, coated surfaces, insulators and graphite have been subjected to an incident flux of 33 GW/m<sup>2</sup> over 100  $\mu$ s to develop a heat flux erosion data base. In contrast, a study conducted by Rosenwasser and Stevenson (15) adopted a systematic approach to first identify railgun bore design environments followed by selection and evaluation of various advanced insulator materials with the potential to meet these requirements. They established a figure-of-merit based on thermophysical and mechanical

properties to quantify the ability of insulator materials to resist brief, intense heat pulses in railgun environments. Such quantification of the performance of insulator materials was done by calculating figure-of-merit for arc melting/erosion resistance (AMR), transient thermal shock resistance (TSR) and relative fracture resistance (FR) which are expressed approximately as shown in equations (3), (4) and (5).  $\rho$  is the density,  $C_v$  is the specific heat at constant volume,  $K$  is the thermal conductivity,  $T_v$  is the wall melting or dissociation temperature,  $T_i$  is the initial wall surface temperature, MOR is the modulus of rupture or flexural bending strength,  $\nu$  is the Poisson's ratio,  $E$  is the Young's modulus,  $\alpha$  is the thermal expansion coefficient,  $\sigma_f$  is the fracture strength and  $H$  is the hardness.

$$AMR \approx 0.5 (\pi \rho C_v K)^{1/2} (T_v - T_i) \quad (3)$$

$$TSR \approx \frac{MOR (1 - \nu) (\rho C_v K)^{1/2}}{E \alpha} \quad (4)$$

$$FR \approx \sigma_f (H/E)^{-1/6} \quad (5)$$

Based on these equations, the results of their evaluations along with a comparison of hardness for some candidate materials are shown in Table 2. The authors did not include diamond in this study, as synthetic diamond technology was in its infancy at the time of the study.

Table 1. Thermophysical and Mechanical Properties of Ceramics, Metals and Alloys

Properties	Materials												
	Diamond	Al <sub>2</sub> O <sub>3</sub>	SiC	Si <sub>3</sub> N <sub>4</sub>	SiO <sub>2</sub>	TiC	TiB <sub>2</sub>	LiN	ZrO <sub>2</sub> Y <sub>2</sub> O <sub>3</sub>	W	Mo	Graphite	NiAl
Crystalline Structure	Cubic	Hcp	Cubic	Hcp	Amorphous	Cubic	Hcp	Cubic	Tetragonal	Cubic	Cubic bcc	Hcp	Cubic
Density, Kg.m <sup>-3</sup>	3515	3980	3210	3180	2200	4920	4520	5440	6100	19310	10220	2250	5900
Hardness, Kg.mm <sup>-2</sup>	8000-10400	2100	2500	2000	550-750	2800	3000	1700	1300	4000	2350	30-100*	330
Young's Modulus, GPa	900-1050	390	440	310	73	450	410	600	290	350	325	8-15	----
Poisson's Ratio	0.20	0.23	0.17	0.22	0.17	0.19	----	----	0.24	----	----	----	----
Tensile Strength, MPa	----	300	175	350-425	30-70	250-475	----	----	45	1520	655	6-70	83-290
Compressive Strength, MPa	----	3400	1400-3400	700-2750	700-1400	1375-2950	1350	1300	2000	----	----	16-186	----
Flexural Strength, MPa	1000-1050	500-600	675	800-900	50-120	860	250	----	500-700	----	----	----	----
Fracture Toughness, MPa.m <sup>1/2</sup>	----	4.9	4.6	3.5-4.0	----	4.0	----	----	8.5-9.5	----	----	----	----

\* measured by the Shore scleroscope

Hcp indicates hexagonal crystalline structure

Table 1. Thermophysical and Mechanical Properties of Ceramics, Metals and Alloys (continued)

Properties	Materials												
	Diamond	Al <sub>2</sub> O <sub>3</sub>	SiC	Si <sub>3</sub> N <sub>4</sub>	SiO <sub>2</sub>	TiC	TiB <sub>2</sub>	TiN	ZrO <sub>2</sub> Y <sub>2</sub> O <sub>3</sub>	W	Mo	Graphite	NiAl
Thermal Conductivity, W.m <sup>-1</sup> .K <sup>-1</sup>	900-2100	35	85-120	31	1.2	27	65	22	1.8	130	146	25-470	----
Specific Heat, J.Kg <sup>-1</sup> .K <sup>-1</sup>	530	920	710	720	670	520	960	595	630	132	276	700-850	----
Coeff. of Thermal Expn. x 10 <sup>-6</sup> C <sup>-1</sup>	1.0	7.1	4.3	3.0	0.9	7.2	4.6	8.1	11	4.5	5.4	1.2-8.2	----
Electrical Resistivity μΩ.cm	10 <sup>11</sup> -10 <sup>26</sup>	10 <sup>20</sup>	10 <sup>5</sup>	10 <sup>18</sup>	10 <sup>15</sup> , 10 <sup>18</sup>	60	10-60	20-30	10 <sup>16</sup>	5.3	5.2	500- 3000	22
Melting or Decomposition Temp./(Operating Temp.), °C/(°C)	3800/ (1000)	2050/ (1800)	2830/ (1700)	1900/ (1500)	1650/ (575)	3065/ (700)	2790/ (1400)	2950/ (500)	2760/ (1700)	3410/ (190)	2610/ (400)	3677	1640
Boiling Temp., °C	----	----	----	----	----	----	----	----	----	5700	5560	----	----

(continued)

Table 1. Thermophysical and Mechanical Properties of Ceramics, Metals and Alloys (continued)

Prop-rties	Materials												
	Ni	α-Ti	Ti-6Al-4V	Cu	Cu/2 Al <sub>2</sub> O <sub>3</sub>	Cu/4 Al <sub>2</sub> O <sub>3</sub>	Cu/7 Al <sub>2</sub> O <sub>3</sub>	Al	2014 Al	2024 Al	6061 Al	5056 Al	356 Al
Crystalline Structure	Cubic fcc	Hcp	Hcp	Cubic fcc	Cubic fcc/Hcp	Cubic fcc/Hcp	Cubic fcc/Hcp	Cubic fcc					
Density, Kg.m <sup>-3</sup>	8902	4575	4430	8940	8820	8810	8800	2699	2800	2770	2700	2640	2685
Hardness, Kg.mm <sup>-2</sup>	80-115	220	300	35-60*	65*	68-80*	75-83*	23-44*	45-135*	47-130*	30-95*	65-100*	60-80*
Young's Modulus, GPa	207	105	115	112-130	105	112	142	62	72.4	72.4	68.3	71.7	72.4
Poisson's Ratio	0.31	0.33	0.33	0.308	---	---	---	---	0.33	0.33	---	0.33	0.33
Tensile Strength, MPa	317	350	900	220-400	325-725	460-600	485-585	40-150	186-483	185-500	124-310	290-415	172-260
Compressive Strength, MPa	---	---	---	---	---	---	---	---	---	---	---	---	---
Flexural Strength, MPa	---	---	---	---	---	---	---	---	---	---	---	---	---

\* HRB scale, using 500 kg load, 10 mm diameter ball, 30 sec. loading duration.

Table 1. Thermophysical and Mechanical Properties of Ceramics, Metals and Alloys (continued)

Properties	Ni	$\alpha$ -Ti	Ti-6Al-4V	Cu	Cu/2 Al <sub>2</sub> O <sub>3</sub>	Cu/4 Al <sub>2</sub> O <sub>3</sub>	Cu/7 Al <sub>2</sub> O <sub>3</sub>	Al	2014 Al	2024 Al	6061 Al	5056 Al	356 Al
Fracture Toughness, MPa.m <sup>1/2</sup>	---	---	---	---	---	---	---	---	---	---	---	---	---
Thermal Conductivity, W.m <sup>-1</sup> .K <sup>-1</sup>	82.9	17.3	7.3	398	360	353	339	247	192	190	180	120	155
Specific Heat, J.Kg <sup>-1</sup> .K <sup>-1</sup>	471	512	610	386	380	380	422	900	---	875	896	904	963
Coeff. of Thermal Expn. x 10 <sup>-6</sup> .C <sup>-1</sup>	13.3	9.5	9.5	16.5	19.5	19.6	20	23.6	22.5	23.8	23.6	24.1	22.5
Electrical Resistivity $\mu\Omega$ .cm	6.85	42	0.171	1.673	1.92	1.94	2.03	2.66	3.4	3.4	3.7	5.9	4.42
Melting or Decomposition Temp./ (Operating Temp.), °C/(°C)	1453	1675/ (370)	1650/ (370)	1083	1083	1083	1083	660	638	638	652	638	615
Boiling Temp. °C	2730	3260	---	2595	2595	2595	2595	2494	---	---	---	---	---

Table 2. Calculated Insulator Figure-of-Merit

Material	AMR* MW/m <sup>2</sup> x 10 <sup>2</sup>	TSR** MW/m <sup>2</sup>	FR*** MPa <sup>1.33</sup> .m <sup>0.66</sup>	Hardness Kg.mm <sup>-2</sup>
Lexan	0.227	0.202	-----	< 15
Al <sub>2</sub> O <sub>3</sub>	12.113	0.953	3.39	2100
Mullite	4.094	0.468	2.86	620
SiC	27.629	3.03	7.66	2500
Si <sub>3</sub> N <sub>4</sub>	12.873	5.03	8.55	2000
PSZ	5.231	5.92	21.50	1300
AlN	13.967	1.91	6.35	1400
Al <sub>2</sub> O <sub>3</sub> /SiC <sub>w</sub>	12.701	1.47	16.00	2100

- \* Arc Melting/Erosion Resistance  
 \*\* Transient Thermal Shock Resistance  
 \*\*\* Relative Fracture Resistance  $K_{IC}^{4/3}$

Parker (9) later extended the concept of figure-of-merit to evaluate the suitability of various materials for use with plasma armatures. This figure-of-merit establishes an upper limit on the quantity  $Ft^{1/2}$  for ablation free operation with a given material (F is the heat flux and t is the exposure time). This quantity in turn defines a new figure-of-merit for a number of insulator and rail materials. Table 3 presents the calculated figure-of-merit for a number of insulator and rail materials. Both of these studies indicated that the materials investigated

have reasonable values of figure-of-merit for railgun operation. However, Lexan polycarbonate, although a high strength insulator, suffered considerable ablation and severe thermal cracks. Conventional ceramics (Al<sub>2</sub>O<sub>3</sub>, Mullite, SiC) on the other hand, underwent surface melting followed by surface fracture from the pressure stresses. The weight losses in the advanced ceramics (e.g. Si<sub>3</sub>N<sub>4</sub>, PSZ (partially stabilized zirconia), AlN) were insignificant, but they showed a phase instability at high temperature with the formation of a new surface layer infested

**Table 3. Figure-of-Merit for Candidate Railgun Materials**

Material	Figure-of-Merit, MWs <sup>1/2</sup> /m <sup>2</sup>
SiO <sub>2</sub> (vitreous)	2.4
Sialon	8.5
Si <sub>3</sub> N <sub>4</sub>	15.5
Al <sub>2</sub> O <sub>3</sub>	20.6
SiC	35.8
BN (pyrolytic)	42.0
C (diamond)	210.0
Cu	35.0
Mo	46.0
W	58.0
C (graphite)	73.0

with microcracks. In view of these experimental observations and theoretical considerations, diamond film presently appears to be the best candidate insulator for railgun applications. Accordingly, the following discussion describes the status of diamond film technology and its possible application for both insulator and rail coatings.

### 1.2 Properties of Diamond

The unique properties of diamond are being utilized for a large number of advanced materials applications. The development of new low pressure

techniques for creating crystalline diamond films and coatings has opened a new era in diamond technology. These developments offer the potential for exploiting the unique properties of diamond in applications such as coatings for bearings and cutting tools, free standing windows, lens coatings for visible and infrared (IR) transmission, and thin films for high temperature, high power semiconductor devices.

Carbon occurs widely in its elemental form as crystalline and amorphous solids. Diamond, graphite, lonsdaleite (sometimes called hexagonal diamond

Table 4. Crystal Structure Data for Diamond

Symmetry	Cubic
Space group	Fd3m
Atoms per unit cell	8
Lattice parameter (298 K), Å	3.56683
Theoretical density (298 K), g/cm <sup>3</sup>	3.51525
Carbon-carbon bond distance, Å	1.54450
Positions of atoms	(000), (½½0), (0½½), (½0½), (¼¼¼), (¾¾¼), (¼¾¾), (¾¼¾)

because its structure and properties are similar to those of diamond) and carbynes (cross-linked linear carbon polytypes) are the crystalline allotropes of carbon. Each of these phases of carbon is formed from carbon hybridized in an  $sp^3$ ,  $sp^2$  and/or  $sp$  state. The diamond crystalline structure is the modified face centered cubic with interatomic distances of 0.154 nm. Each carbon atom is covalently bonded to its four carbon neighbors using (tetrahedrally directed)  $sp^3$  atomic orbitals. The crystallographic data for diamond is shown in Table 4 (16). The {001} planes of graphite form parallel to the {111} planes of diamond (15).

The tetrahedral,  $sp^3$ , carbon-carbon bonds in diamond account for such properties as extreme hardness, chemical inertness, high electrical resistivity, high dielectric strength, high thermal conductivity, high density and optical transparency to visible and IR radiation. Based on these properties, diamond is

used for various advanced applications some of which are listed in Table 5 (17).

Diamonds are resistant to all acids, even at high temperatures. They can, however, be etched by fluxes of caustic alkalis, various oxysalts and metals. Etch figures were formed with  $NaClO_4$  and  $KOCl_4$ , both very strong oxidants, on {111} faces at 380°C.  $O_2$ ,  $CO$ ,  $CO_2$ ,  $H_2$ ,  $H_2O$  and  $Cl_2$  at high temperature have also been used to etch diamonds. In oxygen, appreciable oxidation begins at about 600°C with burning occurring in an oxygen jet at 720°C and in air at 850°C. If diamond is heated in a clean, inert environment, the onset of graphitization begins at about 1500°C. The rate increases rapidly until about 2100°C where a 0.1 carat octahedron is totally converted to graphite in less than 3 minutes (16) with {001} planes of graphite parallel to the {111} planes of diamond (18).

**Table 5. Properties and Applications of Diamond Coatings**

<b>Properties</b>	<b>Applications</b>
Hardest known material	Coatings for cutting tools
Low coefficient of friction	Abrasive coatings
High thermal conductivity (highest known at room temperature)	Coatings for bearings
Low thermal expansion	Heat sinks for electronic devices
Heat resistive	High-power microwave devices
Acid resistive	Radio-frequency electronic devices
Radiation resistive (to X-ray, ultraviolet, $\gamma$ -ray)	High-speed electronic devices
Electrical insulator	Sensors for severe environments
High band gap semiconductor (either p or n-doped)	Window and lens materials
Low dielectric constant	Electro-optic devices
High hole mobility	
Visible and infrared transparent	
Large refractive index	

Table 6 lists a number of the thermal properties of diamond including thermodynamic properties of diamond and the graphite to diamond transition (16). The maximum thermal conductivity occurs at about 80 K. At room temperature, the conductivity of diamond is about four times greater than that of beta-silicon carbide, fifteen times greater than that of silicon, and five times greater than that of copper. Small amounts of boron impurity, as used for semiconductor doping, have little effect on the thermal conductivity of diamond. Nitrogen impurities, however, markedly affect its conductivity (19). (The tendency of nitrogen to cluster in diamond may cause this effect). The

natural type IIa diamond contains very little nitrogen impurity, whereas type Ia contains up to about 0.1 at.% nitrogen. This is reflected in the thermal conductivity of type IIa being about three times that of type Ia (18).

Near room temperature, diamond is the hardest known material and has a low coefficient of friction. Diamond is perfect for many abrasives and wear-resistant applications, except for its chemical interactions at high temperature with ferrous alloys (16). Cleavage fracture occurs primarily along the {111} planes although the energy differences for several planes are quite small (16). At room temperature

Table 6. Thermal Properties of Diamond

Properties	Values
Thermal conductivity, W/cm.K at 293 K	
Type Ia	6-10
Type IIa	20-21
Thermal diffusivity, cm <sup>2</sup> /s for Type IIa	
at 77 K	4800
at 298 K	10
Coefficient of thermal expansion, 10 <sup>-6</sup> /K	
at 193 K	0.4
at 293 K	0.8
at 400-1200 K	1.5-4.8
Debye temperature $\Theta$ , K at T > 600 K	1880
Heat of sublimation, kJ/mol	669
Thermal shock resistance parameter, W/m	3.8 x 10 <sup>6</sup>
Specific heat, J/mol.K	
at 293 K	4.2 x 10 <sup>4</sup> T
at 1800 K	24.7
at 3000 K	26.3
Oxidation rate, g/cm <sup>2</sup> .s	
on (111) plane	2.38
on (100) plane	0.167
Activation energy of oxidation, KJ/mol.K at 823-1023 K	172-184
Transition reaction: Graphite $\leftrightarrow$ Diamond	
$\Delta H_{298}$ , J/mol	1872 $\pm$ 75
$\Delta S_{298}$ , J/mol.K	-3.22
Equilibrium pressure at 2000 K, Pa	64 x 10 <sup>8</sup>
Volume change at 2000 K transition, cm <sup>3</sup> /mol	1.4

diamond behaves as an elastic brittle solid. However, above 1800°C dislocations become relatively mobile, and it is possible to produce appreciable plastic deformation. The coefficient of friction ( $\mu$ ) of diamond on diamond is about 0.1 in air and about 1.0 under

vacuum. If the surfaces are cleaned under vacuum by heating or bombardment, the high value of unity is approached. The actual friction depends on the crystallographic surface of the diamond. The {111} surface shows an isotropic  $\mu$  of 0.005 in air, whereas the

**Table 7. Mechanical Properties of Diamond**

Properties	Values
Density, g/cm <sup>3</sup>	3.52
Elastic constants, GPa	C <sub>11</sub> = 950-1079 C <sub>12</sub> = 120-330 C <sub>44</sub> = 430-578
Young's modulus, GPa	700-1200
Bulk modulus, GPa	440-590
Poisson's ratio	0.10-0.29
Tensile strength, GPa	16.4-32.4
Flexure strength, MPa	1050
Compressive strength, GPa	8.68-16.53
Fracture toughness, MPa.m <sup>1/2</sup>	3.4
Cleavage energy, J/m <sup>2</sup>	10-20
Hardness, GPa on (001) face on (110) and (111) faces	56-102 58-88
Sliding Coefficient of friction in air in vacuum	0.05-0.10 0.9
Sound velocity, m/s (100) face (110) face	17500 18200

{100} cube face gives values of 0.05 along the <011> direction and 0.1 to 0.15 along the <010> direction (20). The mechanical properties of diamond are summarized in Table 7 (21).

Table 8 lists electronic and optical properties of diamond (20, 21). For virtually every electronic property, diamond is unmatched. It possesses the highest electrical resistivity of all

Table 8. Electrical and Optical Properties of Diamond

Properties	Values
Electrical resistivity (at 298 K), $\Omega\cdot\text{cm}$ Type Ia Type Ib Type IIa Type IIb	$10^3\text{-}10^{16}$ $10^3\text{-}10^{16}$ $10^3\text{-}10^{16}$ $10\text{-}10^7$
Dielectric constant (at 298 K, 1 Mhz)	5.5-5.7
Breakdown strength, V/cm	$>10^7$
Activation energy, eV Type IIb (90-290 K) B-doped (270-710 K) Al-doped (270-710 K) Be-doped (270-710 K)	0.29-0.37 0.0029-0.087 0.32 0.20-0.35
Band gap energy (at 298 K), Ev	5.2-5.6
Effective mass Holes ( $m_h/m_0$ ) Type Iib Electrons ( $m_e/m_0$ ) Type Iib	$<1.0$ 0.2
Carrier mobility, $\text{cm}^2/\text{V}\cdot\text{s}$ Hole Electrons	1200-1600 1800-2200
Dissipation factor Carrier lifetime, s	0.0002 $10^{-10}$
Saturated electron velocity, cm/s Absorption edge, $\mu\text{m}$ Refractive index	$2.7 \times 10^7$ 0.2 2.42

materials; the resistivity decreases with increasing temperature. The electrical properties of diamond are primarily dependent upon impurity type and concentration. In the case of

polycrystalline diamond, additions of transition metal solvents may render them as electrically conductive as some alkali, Group IIIa, and even some of the transition metals (22). As semi-

conductors, diamonds exhibit the highest saturated electron velocity, the lowest dielectric constant, the highest dielectric strength and the largest band gap of any semi-conducting material (23).

The most prevalent acceptor impurity in both natural and synthetic Type IIb diamonds is boron. Both boron concentration and the temperature range selected determine the activation energy. Generally, crystals with lower concentrations of uncompensated boron have higher activation energies, while those with higher concentration tend to have lower activation energies due to the onset of impurity band conduction (24).

Exhibiting high transparency throughout the visible, near infrared, and thermal infrared, pure diamond has the widest spectral transmission range of all known solids (0.225 to 25  $\mu\text{m}$ ) (25-27). Theoretically, ideal diamond crystals should be absolutely transparent to visible light, but impurities and other defects in the crystal structure affect absorption in the visible region. The dispersion of diamond is high (0.062) and as a result, its refractive index,  $n$ , is highly wavelength dependent (18). Furthermore, the refractive index decreases when subjected to hydrostatic pressure and increases upon heating (16, 18).

### **1.3 Rail Environments and Projected Diamond Performance**

The extreme thermal, mechanical and electrical dynamic loading conditions

during typical railgun operation promote surface wear and erosion for most of the known insulating and rail materials. The life time of these components are significantly reduced by the ablation, melting and erosion of both the bore insulator and conducting rails. This material loss is primarily the result of thermal energy transfer during arcing between the armature and the rail and, to a lesser extent, the mechanical interaction of the projectile with the bore.

Ideally, the entire current pulse in a railgun would be carried from rail to rail by a solid armature with no arcing or transition to a hybrid armature. If such performance is possible to a velocity of 3 km/s, then the rail environment is less extreme, and the rail heating will arise from frictional heating and ohmic dissipation. If arcing does occur, then the thermal loading will increase significantly. Transition from solid to arcing contact is a complex phenomenon influenced by a concentration of current near the rear of the armature which results from the velocity skin effect and frictional heating of the microstructure of the sliding interface. Diamond coatings have the potential to reduce both these effects. Diamond has a very low coefficient of friction under certain conditions and can be doped to conduct current. However, it is not known how the railgun environment will affect the surface of the diamond. Electrodynamics simulations have shown that a thin layer of material with a low electrical conductivity placed on the inner surface of a highly conducting rail can signifi-

Table 9. Calculated Resistance Values for Diamond

Material	Arc Melting/Erosion Resistance (AMR), $Mws^{1/2}.m^2$	Thermal Shock Resistance (TSR), $Mws^{1/2}.m^2$	Fracture Resistance (FR), $MPa^{1.33}.m^{0.66}$
Diamond	210	49.6	5.09

cantly reduce the current concentration caused by the velocity skin effect.

In view of these observations, resistance values of diamond were calculated using earlier equations 3, 4, and 5 along with its thermal and mechanical properties in Tables 6 and 7. These values are listed in Table 9. The resistance values for diamond listed in Table 9 are much higher than those listed in Tables 2 and 3 for various other insulator and rail materials. The high values for melting/erosion, thermal shock and fracture resistance project extended life performance for diamond under the extreme conditions of railgun operation.

## 2.0 Status of Diamond Coatings

Natural diamonds are produced deep within the earth's crust at extremely high temperatures and pressures. The carbon phase diagram is shown in Figure 2 (28-30). The three stable phase fields are graphite at lower pressures, diamond at high pressures and liquid at extremely

high temperatures. Also depicted in the figure are the regions where diamonds have been synthesized by man. In the central portion of the diagram two regions are shown where diamonds are produced commercially by the simultaneous application of static high pressure and temperature to graphite with or without catalysts, such as Ni, Fe, Mn, Cr, or Co. The catalysis method produces most of the synthesized commercial industrial diamond used throughout the world in micron to millimeter size range. A variation of this method utilizing the above catalysts as solvent is used to synthesize polycrystalline diamond, usually in the form of disks 5 to 10 mm in diameter.

The top region in the diagram is where dynamic explosive shock provides direct conversion of graphite to diamond, yielding diamonds in the nanometer to micron size range. The lattice planes of the diamonds do not all have sufficient time to stack in normal cubic sequence and, therefore, consist of both cubic and non-cubic diamond polytypes. At the

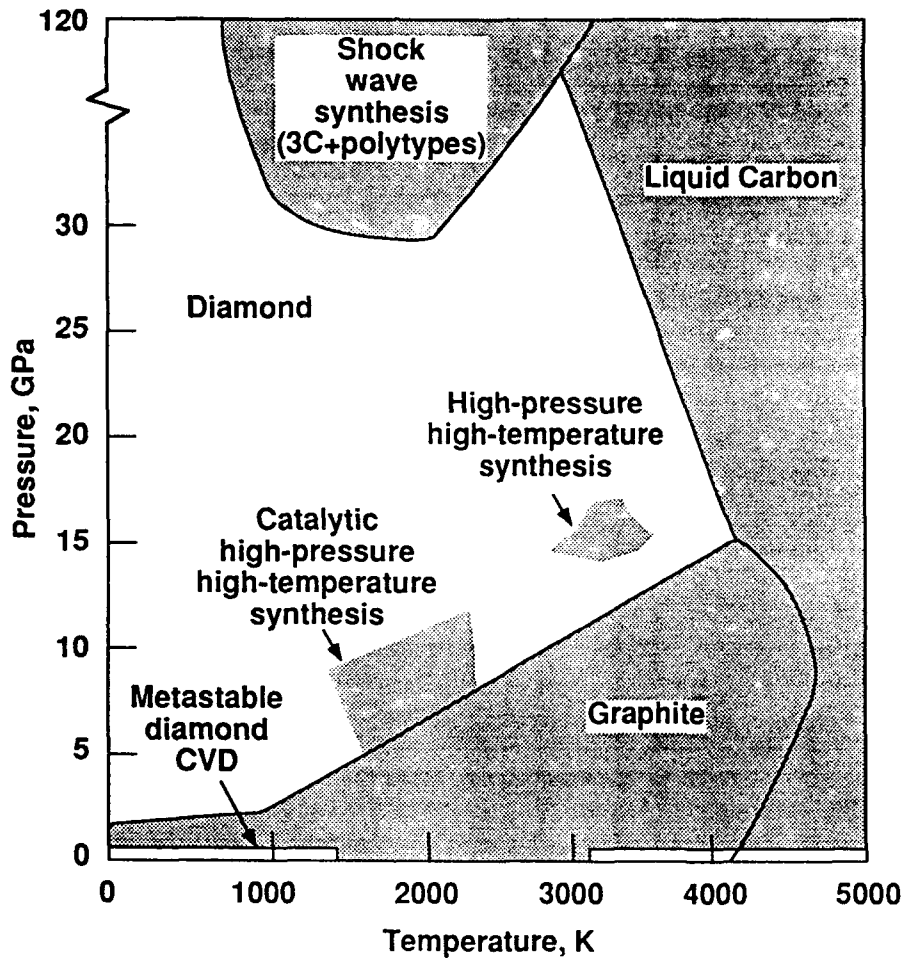


Figure 2: The carbon phase diagram sputtering (37), microwave plasma assistance (37, 39), laser beam (40), and electron beam (41).

bottom of the diagram, at pressures of one atmosphere or less, lies the region where diamond films can be synthesized metastably by chemical vapor deposition (CVD). This thin film CVD process has been greatly advanced over the past decade via hot filament (31, 32), ion

beam (33, 34), rf sputtering (35, 36), dc Various hydrocarbon CVD precursors have been used successfully including methane, ethanol, ethylene, benzene and monosubstituted benzenes. The typical process consists of a reactant gas at less than atmospheric pressure and containing

> 95% hydrogen which is activated by passing it through a plasma or past an  $\approx 2000^\circ\text{C}$  filament before contacting an  $800^\circ\text{C}$  to  $1000^\circ\text{C}$  substrate on which the diamond is deposited.

Many scientific and technological difficulties must be overcome before this deceptively simple-looking "metastable" coating technology can be utilized to produce practical diamond coatings on railgun components. The understanding of process factors such as the role of atomic hydrogen (which controls the extent of graphite, i.e.  $\text{sp}^2$  bond formation and growth rate), the role of the hydrocarbon precursor, (controls C/H ratio in the input gas), the effect of oxygen (controls formation of diamond and rate of deposition), the method of deposition (which controls rate of deposition and deposit morphology), the type and size of the substrate (controls bonding between diamond film and substrate) and the doping elements. The following description touches briefly upon these factors in terms of their influence on diamond coating science and technology.

### **2.1 Role of Atomic Hydrogen**

Hydrogen enhances the rate of diamond growth and reduces or eliminates codeposition of graphite (42). Activating the hydrocarbon precursor gas prior to deposition increases the diamond growth rates from  $\text{\AA}/\text{hr}$  to  $\mu\text{m}/\text{hr}$ . The precursor gas can be activated by flowing in an electric discharge or flowing over a hot tungsten filament before encountering

the lower temperature deposition region. The precursor gas is saturated with atomic hydrogen to superequilibrium concentration ( $> 90$  at.%) at the growth surface which reduces graphite codeposition by behaving like a "solvent" for graphite. The rate of removal of graphite by activated hydrogen is generally orders of magnitude faster than that for diamond (20).

### **2.2 Role of Hydrocarbon Precursor**

The nature of the precursor hydrocarbon gas has little effect on the deposition behavior. Both saturated and unsaturated hydrocarbons as input gas, although they have different C/H ratios, produce diamond film with similar growth features. The density of nucleation and the growth rates are essentially the same (43). This relative independence of diamond growth on the nature of the input hydrocarbon species is due to the fact that most hydrocarbon sources tend to chemically transform to common product species such as acetylene.

### **2.3 Effect of Oxygen**

The addition of oxygen ( $\sim 0.4$  mol.%) to the input precursor gas reduces the concentration of acetylene ( $\text{C}_2\text{H}_2$ ) relative to methane ( $\text{CH}_4$ ) in the exhaust gas (44). The reduction in  $\text{C}_2\text{H}_2$  is produced by the pyrolysis of methane or hydrogenation of non-diamond carbon. Furthermore, the deposition of graphite or amorphous carbon is suppressed by a reduction of the acetylene concentration

or the oxidation of non-diamond carbon, so that the quality of the deposited diamond is improved. With the addition of oxygen, the growth rate of diamond increases, and the total pressure for diamond synthesis can be extended. Oxygen can be added to precursor gas either as a molecular gas or in the form of water vapor.

#### **2.4 Method of Deposition**

The morphology of vapor-deposited diamond crystallites is dominated by cubic {100} and octahedral {111} surfaces and {111} twin planes. Cubo-octahedral exhibiting both {100} and {111} surfaces are also common. The creation of a particular surface morphology appears to depend on the method of deposition. Matsumoto and Matsui (31) found the domination of {100} and {111} surface crystallites in diamond grown in a hot-filament assisted CVD system. On the contrary, in the diamond grown using microwave plasma-assisted CVD (45) at temperatures of 900°C and lower {111} faces dominate the crystallite morphology, and at 1000°C and higher, {100} faces are predominant. At low CH<sub>4</sub> (precursor gas) concentrations, {111} faces are predominant and, at high concentrations, {100} faces are predominant.

#### **2.5 Substrates for Deposition**

Diamond films are attractive for both electronic and mechanical applications because of their excellent electrical,

mechanical and thermal properties (Tables 6-8). However, before such applications can be realized, more research is necessary to develop reasonably large non-native substrates for the growth of diamond films

Diamond has been vapor deposited on a wide variety of substrate materials, but the dominant substrate has been single-crystal silicon. Examples of substrate materials used are Si, Ta, Mo, W, SiC, WC, diamond, Si<sub>3</sub>N<sub>4</sub>, Al<sub>2</sub>O<sub>3</sub>, BN, Ni, Cu, Au, graphite and SiO<sub>2</sub> (11, 46-50). The durability and eventual successful use of diamond film grown on any substrate is largely dependent on the adhesion strength between the film and the desired substrate. Adhesion is related to the nature and the strength of the binding forces at the interface of the film and the substrate where they are in physical contact with each other. This, in turn, strongly depends on several factors such as the chemical nature and cleanliness of the substrate, the film growth temperature (500-1000°C), lattice constant, thermal expansion coefficient, surface energy of the film and the substrate, nucleation density of the film on the substrate, substrate morphology, etc. In some cases, the diamond nucleation rates and adhesion also vary with the tendency to form intermediate reaction layers (e.g. carbides).

In earlier attempts by Lee et al. (48) the growth of diamond on W and Ni substrate resulted in the reproducible deposition of larger diamond crystals than with the other substrates. This is

believed to be related to the higher surface-free energy (3111 and 2072 ergs/cm<sup>2</sup> respectively) and closer lattice (3.165 and 3.524 Å respectively) match of tungsten and nickel to diamond (3387 ergs/cm<sup>2</sup> and 3.567 Å). It may also be due to the lower nucleation density of diamond films on these substrates. The surface energy differences also appear to affect the particle profile as one expects, that is, higher surface energy substrates (i.e. closer to diamond) yield particles having surfaces with lower indices (48). High quality diamond films (high value of sp<sup>3</sup>/sp<sup>2</sup> bonded ratio) can be grown on silicon and tungsten due to their structural match with diamond and the high surface free energy. However, nickel, due to its catalytic nature, converts various hydrocarbons into crystalline graphite, thereby degrading the quality of diamond film. The materials molybdenum and tantalum appear to be unsuitable candidates as substrates for growing diamond film. They produce the poorest quality films by forming a substantial amount of sp<sup>2</sup> bond graphite component. This is believed to be caused by the larger mismatch in surface energy and atomic spacing between these substrates and diamond. Such mismatches are also believed to contribute to small highly defective diamond grains.

Diamond films grown on hard substrates such as Al<sub>2</sub>O<sub>3</sub>, SiC, Si<sub>3</sub>N<sub>4</sub>, WC develop thermal strain during cooling after growth. This occurs primarily due to differences in thermal expansion coefficient and secondarily due to factors

such as lattice mismatch between the substrate and/or interfacial reaction layer and diamond. However, for substrates such as nickel which have a lower yield point, the thermal expansion mismatch may be accommodated in the substrate by plastic deformation. An additional problem is created during diamond growth by CVD since the substrate must be maintained at relatively high temperatures (500-900°C). This requires that these substrates should not incur any phase transition in bulk.

It is also important to physically prepare the substrate surface prior to diamond deposition in order to obtain successful nucleation rates and high quality diamond films. Such preparation of the substrate surface is essential to create nucleation sites for diamond crystallites which may reduce or enhance nucleation rate. By increasing nucleation rate, the high temperature exposure time before a contiguous film of particles appear, can be decreased (51). In addition, surface preparation is required in certain specific situations where a selective deposition of diamond film is required. Surface preparation techniques include, scratching with diamond paste, sand blasting, etc.

For successful performance of diamond for variety of applications, it is very important to evaluate the coating for its adherence to the substrate. However, only limited reports (46, 52-55) have been published on the adhesion of the diamond films to the substrate. Most of these reports have evaluated the

adherence performance qualitatively and they lack in quantitative data. This lack of quantitative information may be due to absence of the standard testing method. Although, few researchers (49, 54, 55) have reported the adhesion performance of diamond films quantitatively, they have adopted different methods of testing in doing so. Cheng et al. (54) used the indentation adhesion tests to evaluate adhesion strength of diamond films. A Rockwell hardness tester with a Brale diamond cone indenter was employed to apply discrete loads. Only the minimum load at which the film cracks and the next lower available loads were recorded as the range of crack initiation load,  $P_{cr}$ . The slope,  $dP/dX$  of the indentation load versus the lateral crack diameter curve is used as a measure to differentiate the quality of adherence between the coating and the substrate. The result of such adhesion tests are tabulated in Table 10.

In another attempt (45), the z-axis (perpendicular to the substrate) pull test was employed to determine the adhesion strength of the as-grown diamond thin film on various substrates. The non-diamond side of the substrates was bonded to a backing plate of alumina using epoxy to obtain a rigid test set-up.

A test stud was bonded to the diamond surface which was inserted into the platen support of the test equipment until the diamond material fails. Table 11 lists adhesion strength results of these tests.

Furthermore, Peebles and Pobe used acoustic emission scratch adhesion testing to measure the critical load for failure of the diamond thin films grown on silicon substrate (55). For these tests, a Rockwell C diamond tip with  $120^\circ$  cone angle and  $200 \mu\text{m}$  tip radius was used with a loading rate of  $100 \text{ N}\cdot\text{min}^{-1}$  and a table speed of  $10 \text{ mm}\cdot\text{min}^{-1}$ . A number of samples from various zones were tested, including the outer zone, the intermediate zone, the center zone and a number of edge pieces. On each sample, at least four separate parallel scratches were made in order to assure a statistically representative critical load determination for each sample failure.

Table 12 shows the critical load values for local and total film adhesion failure for each sample tested as determined from the acoustic emission curves. As these tests are conducted under various loading conditions for different film thicknesses, they will necessarily not predict the bonding performance under required conditions. It will be appropriate to test films in given set of thermal and mechanical loading conditions. There is no published data available about the evaluation of diamond films for railgun application.

## **2.6 Doping**

Arcing with solid armatures occurs near the back of the armature where the velocity skin effect causes a high current concentration. Electromagnetic simulations have shown that the current concentration can be reduced substan-

Table 10. Indentation Adhesion Test Results

Substrate	Deposition Temp. °C	Deposition Time, min.	Dp/Dx, Kgf/mm	P <sub>cr</sub> , Kgf
Pure W	880	120	Flaking	-----
Pure W	980	180	133	< 10
94.3% WC, 5.7% Co	880	120	100	10-20
94.3% WC, 5.7% Co	980	120	162	10-20
SiAlON	880	120	60	20-30
SiAlON	980	120	60	20-30

Table 11. Z-axis Pull Adhesion Strength Test Results

Substrate	Film Thickness, μm	Adhesion Strength, X 10 <sup>2</sup> Kg.m <sup>-2</sup>
Cu/Al as a standard (no diamond coating)	-----	62639
Si	19.0	26067
Si	10.5	21564
Al <sub>2</sub> O <sub>3</sub>	9.0	31583
Si <sub>3</sub> N <sub>4</sub> /Si	10.0	33108
SiO <sub>2</sub> /Si	9.0	27020
Mo	10.5	poor adhesion

tially through the use of a lower conductivity coating on a highly conducting (copper) rail. This layer should have a conductivity approximately one hundredth that of copper to

achieve a uniform current density at a velocity of 3 km/s. Diamond film with its exceptional thermal and frictional characteristics would make a highly effective rail coating if its conductivity

**Table 12. Critical Loads for Diamond Films Adhesion Failure Obtained Using Acoustic Emission Scratch Adhesion Test**

Zone	Local Failure Load Newtons	Total Failure Loads Newtons
Edge	$2.6 \pm 0.3$	$9.3 \pm 0.6$
Edge	$2.9 \pm 0.1$	$8.5 \pm 2.1$
Outer	$2.9 \pm 0.1$	$11.5 \pm 2.0$
Outer	$2.6 \pm 0.3$	$13.3 \pm 2.7$
Intermediate	2.4	$10.4 \pm 1.6$
Intermediate	$2.5 \pm 0.2$	$10.0 \pm 1.6$
Center	$2.8 \pm 0.2$	$9.9 \pm 0.2$

can be controlled by doping to provide the desired characteristics. Due to the small lattice spacing and high energy of the crystal lattice, the number of impurities capable of entering into diamond in the atomic dispersed form is limited. There are only a few elements (boron, phosphorus, lithium) which may give a large concentration of carriers and provide substantial conductivity at 300 K upon their introduction into the diamond lattice. Boron is known to be the impurity which converts diamond into a p-type semiconductor. It is to be noted that boron may be introduced artificially into all of the main types of diamond. But although diamond can be easily doped p-type with boron, n-type doping is very difficult. Nitrogen is a well-known deep donor. The only confirmed shallow n-type dopant is

lithium, which is believed to occupy an interstitial position and to diffuse rapidly at elevated temperatures. Doping diamond either p- or n-type lowers the activation energy for self-diffusion by about 3 eV (52), thereby increasing atomic transport and improving the annealing of lattice defects. This suggests that the doping during growth leads to better quality films.

In general, an impurity can be incorporated into a diamond film in three ways: (i) during growth, which is determined by solubility and kinetic effects, (ii) by in-diffusion, which is solely determined by solubility and, (iii) by ion-implantation, which is solubility-independent. The solubility of the donor impurities such as Li, P and Na in diamond is very low. Therefore,

Table 13. Classification of Synthetic Semiconducting Diamond

Crystal Type		Symbol	Impurity Content $\times 10^{18}$ atoms/cm <sup>3</sup>		Resistivity $\Omega$ .cm
Doping	Compensation		Boron	Nitrogen	
low	middle	$p^-n^+$	0.1-1	1-100	$10^5$ - $10^6$
low	low	$p^-n^-$	0.1-1	< 0.1	$10^3$ - $10^4$
high	middle	$p^+n^+$	1-100	1-100	$10^3$ - $10^4$
high	low	$p^+n^-$	1-100	< 0.1	$10^1$ - $10^2$

they cannot be introduced into diamond by an equilibrium process such as in-diffusion. The kinetic trapping methods such as during-growth or ion-implantation are the alternative methods. Such implantation of diamond can reduce the resistivity of diamond substantially ( $1$  to  $10^{-3}$   $\Omega$ -cm for boron concentration on the order of  $10^{20}$  atoms/cm<sup>3</sup>) (39).

Several workers (57-59) have used ions of lithium, boron, carbon, nitrogen, aluminum, phosphorus, arsenic, antimony and bismuth with energies usually 40 keV for doping diamond. The dose has generally been kept below  $10^{24}$  atoms/cm<sup>3</sup> to inhibit graphitization. In all cases, a semiconducting layer with different resistivity levels were formed on the diamond surface which exhibited p or n- type behavior. This conducting layer, however, vanished on annealing for 2 hr at 1670 K. The only significant results appeared to have been achieved

with boron. In a recent attempt on boron doping of diamond synthesized under low (< 1 bar) and ultra-high (45 kbar) pressures, Spitsyn et al. (59) have studied some electrical properties. The electrical resistance depended on the method of introducing boron into the crystallization medium and also on the concentration of boron and the degree of its compensation in diamond by the donor nitrogen impurity. The resistance of diamond decreases regularly with increasing content of boron in the crystallization medium up to 0.5 at.%. Further increase in the content of boron has little effect on conductivity. This is due to the increased intensity of the formation of electrically neutral B-N complexes in such crystals. Thus taking the arbitrary boundary between the weakly and strongly doped crystals as regards the concentration of boron to be in the range of  $10^{17}$ - $10^{18}$  atoms/cm<sup>3</sup>, the authors (59) have classified the boron doped samples according to the degree

of compensation which is shown in Table 13. These low values of resistivity suggest that diamond could be used as an electrical conducting coating for a copper rail. The resistivity is similar to that of plasma, and would provide for a nearly uniform current distribution at the required velocity of 3 km/s. However, in the railgun application large coulomb transfers occur ( $\approx 10^4$  C/m<sup>2</sup>), and it is not clear how the diamond coatings would respond to large pulsed current transfers.

### **2.7 Cost and Availability of Diamond Coatings**

A major increase in activity around the world on both the science and the technology of vapor deposited diamond is quite apparent today. This activity is a result of a combination of demands from product designers for new super materials, decades of unheralded research on low pressure diamond growth and the breakthroughs of the 1970's which increased diamond growth rates ( $\mu\text{m/hr}$ ) while decreasing the codeposition of graphite. Unfortunately, the major research and development problems which still restrict the full commercialization of products incorporating diamond films are not trivial.

These generic problem areas are:

- i) lowering substrate temperatures (< 200°C)
- ii) controlling nucleation rates

- iii) better adhesion to a variety of substrate materials (materials with large coefficient of expansion)
- iv) eliminating graphite codeposition
- v) controlling defect densities
- vi) uniform thickness on irregular shapes
- vii) depositing thick layers (> 1 mm)
- viii) increasing growth rates (> 10  $\mu\text{m/min}$ )
- ix) depositing over large surface areas (> 8 x 10<sup>3</sup> mm<sup>2</sup>)

These problems are also responsible for the extremely high cost of the diamond films. Unless these problems are solved completely, the diamond film technology will not make the transition to full commercialization. At present, the production of diamond films is conducted as part of research activities primarily devoted to efforts to understand the fundamental science. These research activities are being conducted at industrial and government research laboratories and also at universities. Industries in the United States with activities in low-pressure diamond growth include large companies such as Air Products, Alcoa, Amp, Armstrong, DuPont, Exxon, Ford, General Electric, General Motors, GTE, Hercules, IBM, AT&T, Kennametal, Martin Marietta, Phillips, PPG, Raytheon, Sandvik, Texas Instruments

and Westinghouse. Some of these companies do produce diamond commercially for their own specific uses such as optical coating, cutting tool coating and heat sinks in electronic packaging. The partners in these efforts from academia are located in places such as, Pennsylvania State University, University of North Carolina-Raleigh, Auburn University, Ohio State University and University of Florida. One cannot simply buy diamond from these academic sources. However, diamond can be obtained by joining hands with them in research activities. In contrast, recently established companies such as Diamonex (a spinoff of Air Products), Crystallume Inc. and Norton Diamond Film do routinely sell diamond for applications including optical coatings, cutting tool inserts and electronic packaging. However, their capabilities are limited to thin film ( $< 1$  mm) over small areas ( $< 80$  cm<sup>2</sup>) and relatively simple surface profiles (flat). They often are willing to work on complex applications requiring diamond film but the cost of such efforts is substantial and varies according to the application. In addition, the success of such efforts will be uncertain.

The cost of thin-film diamond depends largely on deposition rate, bath size and yield. It also partly depends on the method of deposition. The recent attempts by some researchers (60, 61) have used ordinary oxygen-acetylene flames at atmospheric pressure to grow crystalline diamond. These types of efforts will definitely cost less than the

conventional methods used to grow diamond. At present, diamond films at a rate of 10-15  $\mu\text{m/hr}$  can be made using CVD with a plasma torch. The cost of diamond grown using this technique is about \$50/carat (one carat = 6.25 cm<sup>2</sup> x 100  $\mu\text{m}$ ) (13). According to another estimate (62) a carbide insert coated with 5  $\mu\text{m}$  thick diamond layer costs \$40/piece. This was achieved using five 10 cm<sup>2</sup> reactors depositing diamond film at a rate of 0.5  $\mu\text{m/hr}$ . The same source predicts that the identical insert with a 5  $\mu\text{m}$  thick diamond coating will be produced in the future at a cost of \$8.70/piece using two 30 cm<sup>2</sup> reactors depositing diamond film at a rate of 2  $\mu\text{m/hr}$ . This means that larger reactors and higher deposition rates can lower per piece cost as shown in Figure 3.

### **3.0 Alternate Coating Technologies**

In view of the difficulties associated with growing large areas of good quality diamond film on various substrates at relatively low cost for railgun applications, one could consider alternate coating materials and coating methods for films with comparable properties, such as the well tested and proven technology of hard coatings of carbides, nitrides, and oxides.

These hard coatings provide low wear and are generally capable of sustaining heavy loads, high speeds, and high temperatures for extended periods without deterioration. Thermophysical and mechanical properties of selected

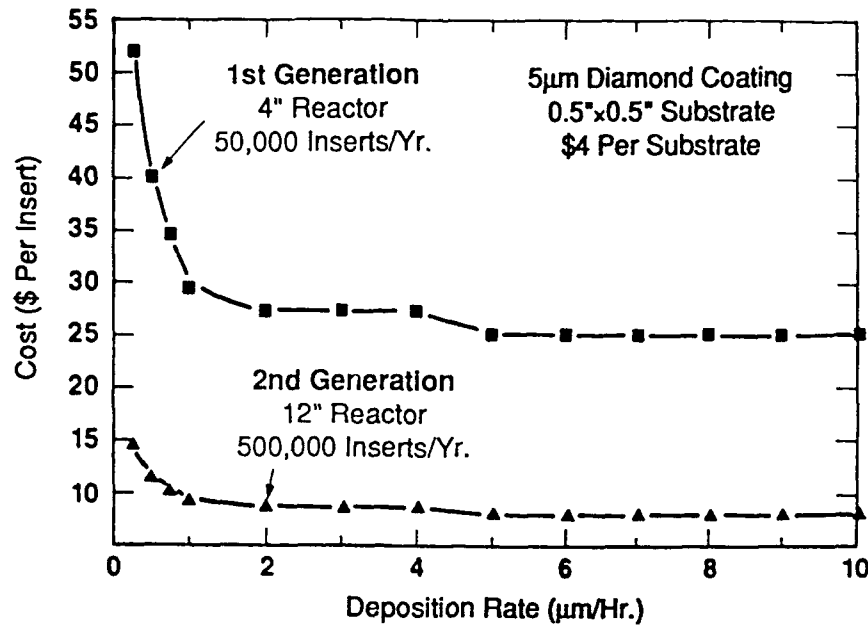


Figure 3: Manufacturing cost as a function of deposition rate for diamond.

materials used for hard coatings are listed in Table 1. Diamond-like-Carbon coatings or bonding free-standing polycrystalline diamond with a substrate may also provide usable but less expensive materials.

### 3.1 Oxide Coatings

Sputtered and spin coated SiO<sub>2</sub> coatings are semiconducting. Sputtered SiO<sub>2</sub> coatings are deposited by magnetron sputtering from an SiO<sub>2</sub> target. Spin-coated SiO<sub>2</sub> coatings are produced by the sol-gel method. Plasma enhanced CVD (PECVD) coatings of SiO<sub>2</sub> are deposited by plasma enhanced reaction of SiH<sub>4</sub> with N<sub>2</sub>O or CO<sub>2</sub> gases (63, 64).

### 3.2 Carbide Coatings

SiC is another promising coating because of some outstanding properties such as high hardness, good oxidation resistance at high temperatures, inertness to corrosive media, and high electrical resistivity. SiC coatings up to 12-15 µm in thickness are applied by rf reactive ion plating in which Si is evaporated in a C<sub>2</sub>H<sub>2</sub> gas atmosphere (65). Coatings up to a thickness of 100 µm are applied by CVD at 800 to 1200°C (66).

### 3.3 Nitride Coatings

Si<sub>3</sub>N<sub>4</sub> has high hardness and good chemical resistance. Due to its good

dielectric properties it has applications as an electrical insulator. It also has good oxidation resistance principally due to formation of a protective silica layer.  $\text{Si}_3\text{N}_4$  coatings have been applied by sputtering, CVD and PECVD (63, 67). Coating by CVD and PECVD processes can be produced by reaction with  $\text{NH}_3$  at substrate temperatures as low as 300-400°C.

### **3.4 Diamond-Like-Carbon (DLC) Coatings**

The term DLC is often used to indicate a variety of noncrystalline carbon materials, ranging from amorphous to microcrystalline and typically containing a few to about 50 at.% hydrogen. The structure of DLC coatings is predominantly amorphous. However, small areas within the coatings show polycrystalline or even single-crystalline graphitic or diamond structure. Usually being a mixture of amorphous and microcrystalline structure, the DLC coatings are very smooth and featureless.

DLC can be grown using dc, rf and magnetron sputtering, ion beams, and plasmas. DLC may comprise 30 to 60 at.% hydrogen with perhaps 50 to 70% of the carbon sites having an  $\text{sp}^3$  bond configuration. Sometimes hydrogen is deliberately incorporated in the sputtered or ion plated DLC coatings to increase the optical band gap, i.e. to reduce optical absorption. The band gap is controlled by the fraction of tetrahedral ( $\text{sp}^3$ ) versus trigonal or graphite ( $\text{sp}^2$ ) bonding. Therefore this technique

produces a larger optical band gap and consequently has a high electrical resistivity. Hydrogenated DLC are generally more resistant to galvanic corrosion due to their high electrical resistivity (37). High-energy surface bombardment with argon ions results in DLC coatings with higher light transmittance, resistivity and hardness, suggesting an increase of  $\text{sp}^3$  bond and decrease of  $\text{sp}^2$  bonds.

The structure ( $\text{sp}^3/\text{sp}^2$  ratio) and properties of the coatings depend critically on the deposition technique and the process parameters since, for example, the hydrogen concentration changes by changing the process parameters. The DLC coatings produced by ion beam sputtering have high hardness and high density compared to those produced by PECVD. However, ion beam deposition is a low-rate growth process compared to rf or dc PECVD methods. Thus, DLC coatings have properties comparable to diamond coatings but may be produced with better control at relatively low substrate temperatures (< 600°C).

### **3.5 Bonding Free Standing Diamond**

As mentioned earlier, growing diamond on most of the substrates poses problems such as mismatch in thermal expansion coefficients and lattice parameters. Also, the existing methods of growing diamond requires the substrates to be heated to about 900-1000°C which, in turn, eliminates low melting temperature materials and materials which experience

phase transition at these temperatures. In this context, an approach that involves growing a diamond film on a sacrificial substrate and then attaching this film to the required substrate using a bonding material appears promising.

For cutting tool applications, a monolayer of diamond particles is routinely galvanically bonded to a steel core (67). Some times, instead of galvanic bond, an Ag-Mn-Zr alloy with a high percentage of silver is also used to braze diamond grits to a metal support (69). In a separate attempt (70), an abrasive tool was manufactured by brazing a monolayer of diamond grits to a steel substrate using a Ni-Cr based alloy. The concept was modified recently by Chattopadhyay et al. (63) to bond diamond particles to a steel substrate. A commercially available Ni-Cr hardfacing alloy was first flame sprayed on a steel substrate with an oxyacetylene gun followed by induction brazing (at 1080°C) of sprinkled diamond particles (~ 250 µm) in an argon atmosphere for 30 seconds. Chromium was segregated preferentially to the interface with diamond to form a chromium-rich reaction product which promoted the weldability of the alloy.

For the low strength and low temperature applications, diamond can be joined to metals, ceramics and diamonds using a Direct Chemical Bonding (DCB) technique (71). The process is called Intragene™ and it is a proprietary process from Advanced Technology Inc. Adding a few wt% of

transition metal powders to tin and heating them in a non-oxidizing atmosphere produces a direct strong chemical bond to diamond. This metallized diamond can then be brazed to a variety of other materials. In order to obtain a high temperature bond between ceramic-ceramic or ceramic-metal such as diamond-diamond or diamond-copper, Dahotre and McCay (72) have recently proposed a laser induced reaction joining (LIRJ) technique to create a high temperature joint by synthesizing compounds from mixture of reactive elemental metal powders.

#### **4.0 Summary**

Diamond films have the potential to significantly extend the useful life of both insulator and rail components of a railgun barrel. Their hardness, strength, transparency and high thermal conductivity will resist surface erosion in the presence of arcing contacts. Perhaps the most exciting possibility for the application of diamond coatings in railguns is to use them as conducting coatings on the rail surfaces. This application has the potential to extend the velocity at which arcing transition from solid to hybrid armatures occurs and may significantly reduce the harsh environment expected on the bore surfaces.

However, given the current state of commercialization of CVD deposition processes, it is not clear that diamond

films can be grown in sufficient sizes on substrates suitable for railgun components. Diamond cannot substitute directly for the monolithic insulator components found in conventional railguns, and new innovative barrel designs will be needed to take advantage of their unique properties. These designs might employ lamination concepts where relatively small individual components would be assembled into the larger component structures required for the barrel. Additional research must be conducted to determine the suitability of diamond coatings for railgun applications. In particular, semiconducting diamond films must be evaluated for pulsed high current applications, and the mechanical behavior of the coatings under the influence of large mechanical and thermal dynamic loading must be evaluated for substrate materials which are suitable for railgun components.

### **5.0 Acknowledgments**

The authors gratefully acknowledge Professor Dennis Keefer and Professor Roger Crawford for introducing them to this subject and for their comments on the manuscript.

### **6.0 References**

1. Rashleigh, S.C., and R.A. Marshall, *Journal of Applied Physics*, Vol.49, p.2540, (1978).
2. Hawk, R.S., A.L. Brooks, F.J. Deadrick, J.K. Scudder, C.M. Fowler, R.S. Caird, and D.R. Peterson, *The Institute of Electrical and Electronics Engineers Transactions on Magnetics*, Vol.MAG-18, No.1, p.82, (1982).
3. Tower, M.M., and C.H. Haight, *The Institute of Electrical and Electronics Engineers Transactions on Magnetics*, Vol.MAG-20, No.2, p.298, (1984).
4. Thio, Y.C., *Final Report, DOE/ER/13048-3*, Westinghouse Research and Development Laboratory, Pittsburgh, PA, (June, 1986).
5. Sedghinasab, A., D. Keefer, and H. Crowder, *The Institute of Electrical and Electronics Engineers Transactions on Plasma Science*, Vol.17, No.3, p.360, (1989).
6. Keefer, D., *The Institute of Electrical and Electronics Engineers Transactions on Plasma Science*, Vol.17, No.3, p.455, (1989).
7. Smith, L.M., and D. Keefer, *The Institute of Electrical and Electronics Engineers Transactions on Plasma Science*, Vol.17, No.3, p.501, (1989).
8. Keefer, D., *The Institute of Electrical and Electronics Engineers Transactions on Plasma Science*, Vol.17, No.3, p.446, (1989).

9. Parker, J.V., the Institute of Electrical and Electronics Engineers Transactions on Magnetics, Vol.MAG-25, No.1, p.418, (1989).
10. Hawk, R.S., W.J. Nellis, G.H. Newman, J. Rego, and A.R. Suseoff, The Institute of Electrical and Electronics Engineers Transactions on Magnetics, Vol.MAG-22, No.6, p.1510, (1986).
11. Schnurr, N.M., J.F. Kerrik, and J.V. Parker, The Institute of Electrical and Electronics Engineers Transactions on Magnetics, Vol.MAG-22, No.6, p.1733, (1986).
12. Bedford, A.J., The Institute of Electrical and Electronics Engineers Transactions on Magnetics, Vol.MAG-20, p.352, (1984).
13. Stefani, F., and K.C. Radford, 10th Electromagnetic Launcher Association Meeting, Dayton, OH, (Sept. 15-17, 1992).
14. Bourham, M., J. Gilligan, and O. Hankins, 10th Electromagnetic Launcher Association Meeting, Dayton, OH, (Sept. 15-17, 1992).
15. Rosenwasser, S.N., and R.D. Stevenson, The Institute of Electrical and Electronics Engineers Transactions on Magnetics, Vol.MAG-22, No.6, p.1722, (1986).
16. Field, J.E., Properties of Diamond, Academic Press, London, (1979).
17. Nishimura, K., K. Kobashi, Y. Kawate, and T. Horiuchi, KOBELCO Technology Review, No.2, p.49, (1987).
18. Orlov, Y.L., The Mineralogy of the Diamond, John Wiley & Sons, New York, (1977).
19. Yoder, M.N., Novel Refractory Semiconductors, eds. D. Emin, T.L. Aselage, and C. Wood, Materials Research Society, Pittsburgh, PA, p.315, (1987).
20. Spear, K.E., Journal of the American Ceramic Society, Vol.72, No.12, p.171, (1989).
21. Ownby, P.D., and R.W. Stewart, Ceramics and Glasses: Engineered Materials Handbook, Vol.4, American Society for Metals International, p.823, (1990).
22. Bowden, F.P., and D.Tabor Physical Properties of Diamond, ed. R. Berman, Clarendon Press, Oxford, p.184, (1965).
23. Yoder, M.N., SPIE Proceedings, ed. A. Feldman and S. Holly, Vol.969, The International Society for Optical Engineering, San Diego, CA, p.106, (August 16-17, 1988).
24. Williams, A.W.S., E.C. Lightowers, and A.T. Collins, Journal of Physics C: Solid State Physics, Vol.2, No.8, p.1727, (1970).

25. Clark, C.D., Physical Properties of Diamond, ed. R. Berman, Clarendon Press, Oxford, p.295, (1965).
26. Kemmey, P.J., and P.T. Wedepohl, Physical Properties of Diamond, ed. R. Berman, Clarendon Press, Oxford, p.325, (1965).
27. Hench, L.L., and J.K. West, Principles of Electronic Ceramics, John Wiley & Sons, New York, (1990).
28. Buchmann, P.K., and R. Messier, Chemical Engineering News, Vol.67, No.20, p.24, (1989).
29. Bundy, F.P., Journal of Geophysics Research, Vol.85, No.B12, p.6930, (1980).
30. DeVries, R.C., Annual Review in Materials Science, Vol.17, p.161, (1987).
31. Matsumoto S., and Y. Matsui, Journal of Materials Science, Vol.18, p.1785, (1983).
32. Kobashi, K., K. Nishimura, Y. Kawate, and T. Horiuchi, Physical Review B, Vol.38, No.6, p.4067, (1988).
33. Weissmantel, C., K. Breuer, D. Dietrich, V. Ebersbach, H. J. Erler, B. Rau, and G. Reisse, Thin Solid Films, Vol.96, p.31, (1982).
34. Weissmantel, C., K. Breuer, and B. Winde, Thin Solid Films, Vol.100, p.383, (1983).
35. Bewilogua, K., B. Rau, B. Rother, and C. Weissmantel, Proceedings of International Conference on Diamond Crystallization Under Reduced Pressure, Warsaw, Poland, (1985).
36. Cho, N.H., K.M. Krishnan, D.K. Veirs, M.D. Rubin, C.B. Hopper, B. Bhushan, and D.B. Bogy, Materials Research Society Symposium Proceedings, Vol.164, p.309, (1990).
37. Bhushan, B., Tribology and Mechanics of Magnetic Storage Devices, Springer Verlag, New York, (1990).
38. Kamo, M., Y. Sato, S. Matsumoto, and N. Setaka, Journal of Crystal Growth, Vol.62, p.642, (1983).
39. Fujimori, M., T. Imai, and A. Doi, Vacuum, Vol.36, p.99, (1986).
40. Fink J., T. Muller-Heinzerling, J. Pfluger, A. Bubenzer, P. Koidl, and G. Crecelius, Solid State Communications, Vol.47, p.687, (1983).
41. Sawabe, A., T. Inuzuka, Thin Solid Films, Vol.137, p.89, (1986).
42. Chauhan, S.P., J.C. Angus, and N.C. Gardner, Journal of Applied Physics, Vol.47, No.11, p.4746, (1976).

43. Sato, Y., M. Kamo, and N. Setaka, Proceedings of 8th International Symposium Plasma Chemistry, ed. K. Akashi, and A. Kinbara, Vol.1, International Union of Pure and Applied Chemistry, Oxford, England, p.2446, (1987).
44. Kawato K., and K. Kondo, Japanese Journal of Applied Physics, Vol.26, No.9, p.1429, (1987).
45. Badzian, A.R., Advances in X-ray Analysis, Vol.31, eds. C.S. Barrett, J.V. Gilfrich, R. Jenkins, J.C. Russ, J.W. Richardson, and P.K. Predecki, Plenum, New York, p.113, (1988).
46. Badzian, A.R., T. Badzian, R. Roy, R. Messier, and K.E. Spear, Materials Research Bulletin, Vol.23, p.531, (1988).
47. Spitsyn, B.V., L.L. Bouilov, and B.V. Deryagin, Journal of Crystal Growth, Vol.52, p.219, (1981).
48. Lee, Y.H., K.J. Bachmann, J.T. Glass, Y.M. LeGrice, and R.J. Nemanich, Applied Physics Letters, Vol.57, No.18, p.1916, (1990).
49. Ramesham, R., T. Roppel, R.W. Johnson, and J.M. Chang, Thin Solid Films, Vol.212, p.96, (1992).
50. Ramesham, R., and T. Roppel, Journal of Materials Research, Vol.7, No.5, p.1144, (1992).
51. Dennig, P.A., and D.A. Stevenson, New Diamond Science and Technology, ed. R. Messier, J.T. Glass, J.E. Butler, and R. Roy, Materials Research Society, Pittsburgh, PA, p.403, (1991).
52. Murakawa, M., S. Tsuchi, H. Miyazawa, and Y. Hirose, Surface and Coatings Technology, Vol.36, p.303, (1988).
53. Suzuki, H., H. Matsubavo, and N. Horie, Journal of the Japanese Society for Powder Metallurgy, Vol.33, p.262, (1986).
54. Kuo, C.T., T.Y. Yen, and T.H. Huang, Journal of Materials Research, Vol.5, No.11, p.2515, (1990).
55. Peebles, L.M., and L.E. Pope, Journal of Materials Research, Vol.5, No.11, p.2589, (1990).
56. Berndolc, J., A. Antonelli, T.M. DelSole, Y. Bar-Yam, and S.T. Pantelides, Physical Review Letters, Vol.61, p.2689, (1988).
57. Okano, K., H. Kiyota, T. Terasaki, T. Kurosu, M. Iida, and T. Nakamura, New Diamond Science and Technology, eds: R. Messier, J.T. Glass, J.E. Butler, and R. Roy, Materials Research Society, Pittsburgh, PA, p.917, (1991).
58. Bernholc, J., S.A. Kajihara, and A. Antonelli, New Diamond Science

- and Technology, eds: R. Messier, J.T. Glass, J.E. Butler, and R. Roy, Materials Research Society, Pittsburgh, PA, p.917, (1991).
59. Spitsyn, B.V., A.E. Alexenko, G.A. Sokolina, and V.A. Laptev, New Diamond Science and Technology, eds: R. Messier, J.T. Glass, J.E. Butler, and R. Roy, Materials Research Society, Pittsburgh, PA, p.917, (1991).
60. Hirose, Y., and M. Mitsuizumi, New Diamond, Vol.4, No.3, p.34, (1988).
61. Yazu, S., S. Sato, and N. Fujimory, Proceedings of the Society of Photo-optical Instrumentation Engineers, Vol.969, Diamond Optics, eds. A. Feldman, and S. Holly, The Society of Photo-Optical Instrumentation Engineers, Bellingham, WA, (1988).
62. Craig, P., Cutting Tool Engineering, Vol.44, No.1, (1992).
63. Hess, D.W., Journal of Vacuum Science and Technology, Vol.A2, p.244, (1984).
64. Reinberg, A.R., Journal Electronic Materials, Vol.8, p.345, (1979).
65. Fukutomi, M., M. Fujitsuka, H. Shinno, M. Kitajima, T. Shikama, and M. Okada, in Proceedings of 7th International Conference on Vacuum Metallurgy, Vol.1, The Iron & Steel Institute of Japan, Tokyo, p.99, (1982).
66. Brusch, R., Thin Solid Films, Vol.126, p.313, (1985).
67. Stiglich, J.J., and D.K. Bhat, Thin Solid Films, Vol.72, p.503, (1980).
68. Chattopadhyay, A.K., L. Chillet, and H.E. Hintermann, Journal of Materials Science, Vol.26, p.5093, (1991).
69. Slack, G.A., and W.S. Knapp, US Patent 4239502, (1980).
70. Lowder, J.T., and E.M. Tausch, US Patent 4018576, (1977).
71. Intrater, J., Machine Design, Nov. 23, (1989).
72. Dahotre, N.B., and M. H. McCay, unpublished work, (1993).

## **Synthesis of Diamond Thin Films on TC4 by Using a Scanning Linear Flame**

**G.F. Zhang and X. Zheng**

Department of Materials Science and Engineering  
Northwestern Polytechnical University  
Xi'an, 710072, Shaanxi, P.R.China

### **Abstract**

A scanning linear flame is used to deposit diamond films over a large area, and with high quality and good continuity by employing appropriate cooling means for the substrate. It is found that the structure and morphology of the deposited films mainly depend on the substrate temperature, the ratio of O<sub>2</sub> to C<sub>2</sub>H<sub>2</sub> flow rate and the relative position of the substrate with respect to the flame. These factors affecting the structure and morphology of diamond films are interrelated. Moreover, the influences of surface pretreatments on nucleation and growth of diamond films are also studied. The experimental results show that the nucleation density of diamond films is enhanced by scratching the surface of the substrate with diamond grit and initially coating a mechanical pump oil layer. For the substrate surface etched with metallographic etching acid, the nucleation and growth of diamond films are very uniform. In addition, the adhesion between the film and substrate is enhanced. Nucleation is favored on the prominent features of the substrate, i.e. scratch and crystal boundary.

### **1.0 Introduction**

Being the hardest crystal in nature and with many other superior properties, diamond films have become one of the most significant functional materials in modern technological applications (1). Up to now, various CVD methods, such as thermal CVD, RF or DC plasma

CVD, microwave plasma CVD and combustion flame etc. (2,3), have been used to synthesize diamond films. The combustion flame deposition technology is one of the most attractive methods as it has many advantages such as higher film forming rate, larger film deposition area, lower cost and ease of operation.

If a fixed flame is blowing perpendicularly against the substrate, the deposited diamond film is non-uniform across the substrate surface and the variation of the quality of the film with position radially outward from the center of the flame axis is noticeable. In order to deposit a continuous diamond film, the factors affecting the uniformity need to be eliminated. A practical method for the elimination is moving flame deposition. In addition, it is very important to study the effects of the substrate surface character and state on the nucleation of diamond films and to strengthen the deposition process of diamond films by changing them through adequate pretreatment measures as well.

## 2.0 Experimental Details

The experimental equipment consists of an oxyacetylene torch and a water-cooled copper mount for the substrates. The flow rates of  $O_2$  and  $C_2H_2$  gases are controlled by float-type flow meters. The substrate temperatures ( $T_s$ ) are controlled by adjusting the flow rate of the coolant water and are monitored with an optical pyrometer.

The experimental conditions are as follows: the flow rate ratio of  $O_2$  to  $C_2H_2$  is regulated to 0.7-1.1;  $T_s$  is in the range of 973 K-1373 K; the burner is perpendicular to the substrate surface during growth; the speed of torch is in the range of 0-3 mm/min; the deposition time for a fixed torch is 15 min.

TC4 plate is used as the substrate, of size 15 x 15 mm and 50 x 50 mm. Four different pretreatments for the substrate surface are employed:

- (1) Scratched with 1.5  $\mu$ m diamond paste and then thoroughly cleaned ultrasonically in acetone.
- (2) Coated with a thin film of mechanical pump oil applied by dipping a cotton swab in the oil and smearing it on the substrate surface.
- (3) Etched with metallographic etching acid which is a mixture of hydrofluoric, nitric acid and distilled water, and
- (4) Ground with 1000# waterproof abrasive paper.

The diamond deposits are identified using Raman spectroscopy. The morphology of the diamond is observed by a scanning electron microscope.

## 3.0 Results and Discussion

### 3.1 The Structure of Diamond Films

The result of Raman spectroscopy analysis is shown in Figure 1, which indicates a strong diamond peak at 1333.0  $cm^{-1}$  and a weak graphite peak at 1552.0  $cm^{-1}$ . The full width at half maximum (FWHM) of the peak at 1333.0  $cm^{-1}$ , depicting the crystallinity of the diamond particles, is 4.0  $cm^{-1}$ .

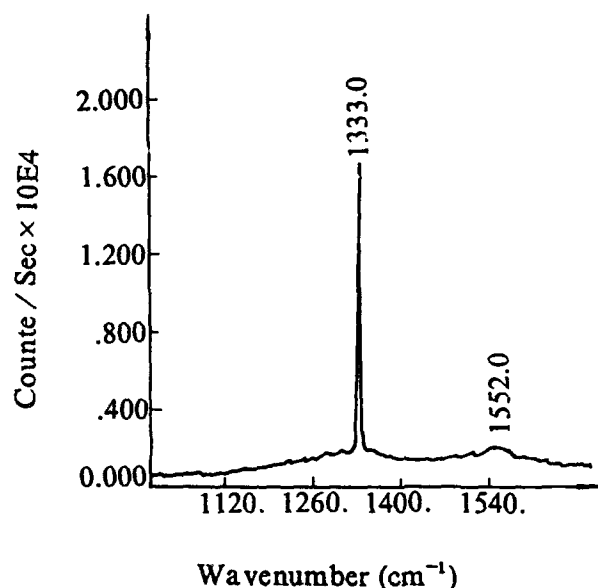


Figure 1: Raman spectrum of the diamond films prepared in this study.

### 3.2 The Morphology of Diamond Films

Two typical morphologies of the deposited films is observed, which is shown in Figure 2. The high quality and well faceted diamond film (as shown in Figure 2(a)) is formed at  $T_s = 1073\text{ K} - 1273\text{ K}$ . When  $T_s > 1373\text{ K}$  or  $< 873\text{ K}$ , diamond particles cannot be obtained. For lower flow ratios ( $< 0.7$ ), only ball-like particles, as seen in Figure 2(b), can be formed. In general, diamond film of high quality can be obtained at higher flow rate ratios of  $\text{O}_2$  to  $\text{C}_2\text{H}_2$ . This is due to the increase in flame temperature. With increasing flow rate ratios and higher flame temperature, more energy is available for  $\text{C}_2\text{H}_2$  molecule to

decompose into the species forming diamond particles. Because the radial and axial distributions of the flame temperature and concentration of the flame species are non-uniform, the relative position of the substrate with respect to the flame has influence on the quality of diamond films. In the present study, high quality diamond film can also be obtained at lower flow ratios by regulating other parameters properly. This indicates that the three factors, as mentioned above, are interrelated.

### 3.3 Effects of Substrate Surface Pretreatments

In order to compare the effects of the substrate pretreatments, all diamond

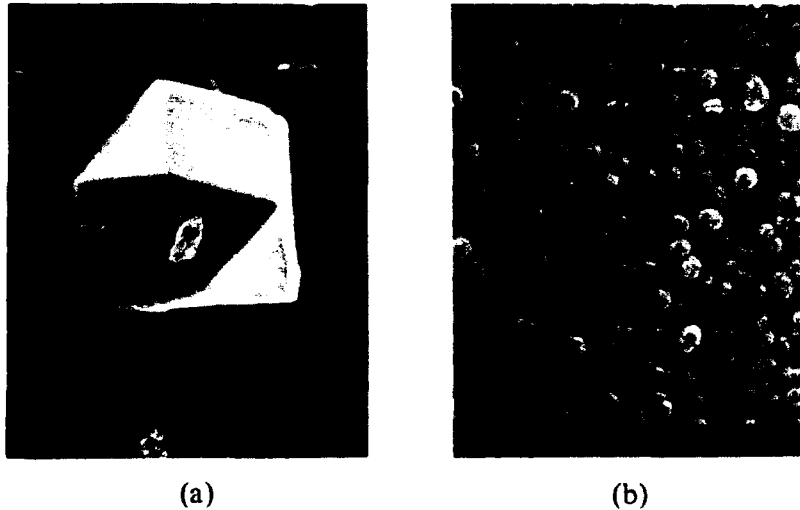


Figure 2: SEM photographs of synthetic diamond films:  
(a) well faceted diamond, and (b) ball like diamonds.

films are prepared with the same technical parameters. Figure 3 shows results of SEM images revealing the nucleation density and surface morphologies of the films deposited on various pretreatment substrates. In addition, Table 1 lists the number of diamond nuclei per square centimeter and maximum particle growth rate. As is shown, the highest nucleation density of diamond crystallites,  $7.5 \times 10^6 \text{ cm}^{-2}$ , is found on the substrate polished with  $1.5 \mu\text{m}$  diamond grit. The nucleation density on the substrate coated with mechanical pump oil is higher, but the nucleation of diamond is very non-uniform with a larger number of secondary grains. The nucleation density on the chemically etched substrate is lower but the

nucleation and growth are very uniform without secondary grain growth. Moreover, the adhesive strength between the film and substrate is enhanced. The higher the nucleation density, the lower the growth rate of the diamond particle (see Table 1).

The most common method of enhancing nucleation is to abrade the substrate with diamond powder. The reasons are as follows (4): abrasion modifies the surface topography by introducing valleys, which are the preferred sites for nucleation; mechanical damage induces dislocation cores, which are the preferred sites for nucleation; and residual diamond powder from the abrasion process can turn into nucleation sites.

*Synthesis of Diamond Thin Films on TC4 by Using a Scanning Linear Flame*

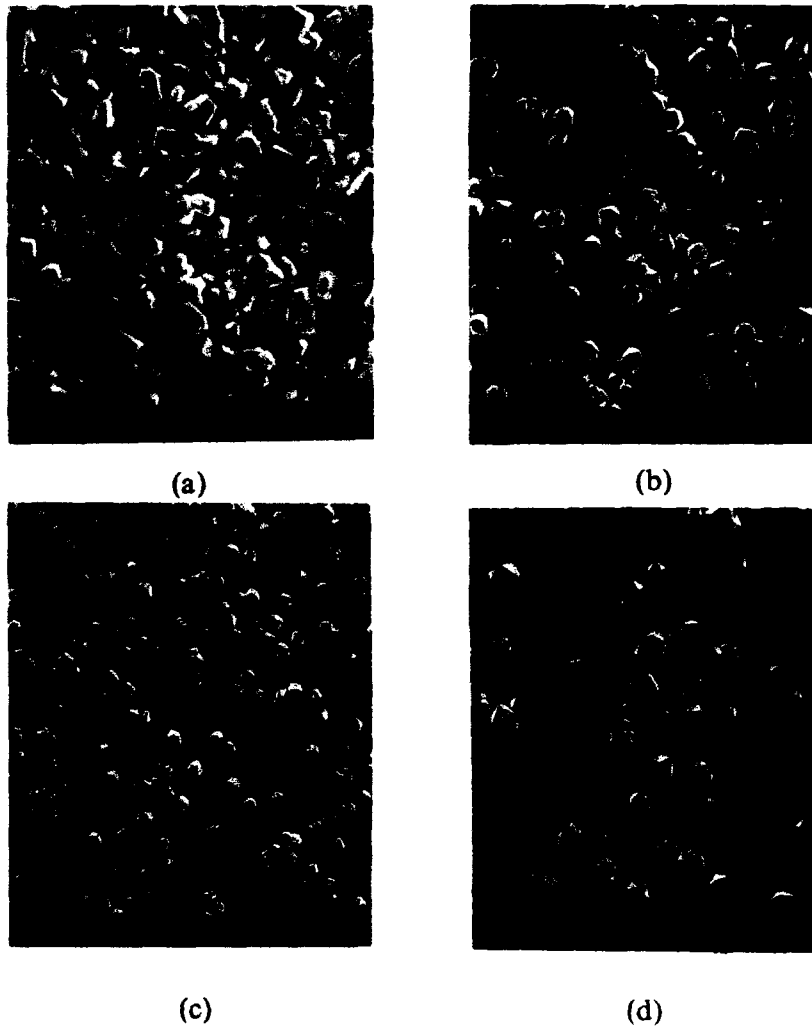


Figure 3: SEM micrographs of diamonds on:  
(a) diamond scratched, (b) oil-coated, (c) chemically etched, and  
(d) water proof abrasive paper ground TC4 substrates.

Our experiments demonstrate that the action of substrate topography on the nucleation of diamond films is important. Nucleation is favored

on prominent features of the substrate, such as edges or sharp valleys caused by polishing with diamond grit and on crystal boundary caused by chemical

Table 1. Nucleation Density and Maximum Growth Rate of Diamond Particles

Methods of Pretreatment	Nucleation Density ( $\text{cm}^{-2}$ )	$V_{\max}$ ( $\mu\text{m/hr}$ )
Abrading with diamond paste	$7.5 \times 10^6$	22
Coating with mechanical oil	$3.8 \times 10^5$	53
Chemically etching	$4.7 \times 10^4$	132
Grinding with waterproof abrasive paper	$4.2 \times 10^4$	150

etching. The nucleation density on the substrate burnished by water proof abrasive paper is less than that with diamond paste. This shows that the effectiveness of the different pretreatments also depends on density, depth of scratch, composition, and size of the polishing compound. These results imply that silicon substrate photoetched to change substrate topography and metal or alloy substrate metallographically etched to alter the grain size, can achieve controlled nucleation. The quantitative relationship between the character of substrate and nucleation of diamond film is being studied further.

### 3.4 Scanning Flame Deposition of Diamond Films

The flame is blowing perpendicularly against the substrate and the moving speed of torch is about 2 mm/min. Figure 4 shows SEM micrographs of the diamond film obtained with a scanning linear flame. From this figure, it can be seen that a uniform well-crystallized diamond film can be obtained by the

moving torch method and the nucleation density is high, when the temperatures of the substrate are kept in the range of 850-950°C. The uniformity, the morphology and the nucleation density of diamond films strongly depend on the substrate temperature. Therefore, it is important to keep the substrate at a constant temperature by employing appropriate cooling methods.

In order to achieve continuous diamond coating over a large area, a flame cover was used to prevent the substrate outside the coated area from oxidation (3). Our experiment indicates that a larger area continuous diamond film can also be deposited by improving the contact condition between the substrate and water-cooling holder and by using an appropriate deposition method without a flame cover.

### 4.0 Conclusions

The quality of diamond thin films depends on the substrate temperature, the flow rate ratio of  $\text{O}_2$  to  $\text{C}_2\text{H}_2$  and the



Figure 4: SEM photograph of diamond film synthesized by moving flame.

relative position of the substrate with respect to the flame. These factors are interrelated. Diamond nucleation is favored on scratch and crystal boundaries. A large, continuous and high quality diamond film can be obtained by a scanning linear flame when employing appropriate cooling methods for the substrate and appropriate deposition methods.

#### 5.0 References

1. Hirose, Y. and Terasawa, Y., Synthesis of Diamond Thin Films by Thermal CVD using Organic Compounds, *Japan Journal of Applied Physics*, Vol.25, No.6, pp.L519-L521, (1986).
2. Lux, B. and Haubner, R., Low Pressure Synthesis of Superhard Coatings, *Journal of Refractories & Hard Metals*, Vol.8, No.3, pp.158-174, (1989).
3. Murakawa, M. et al., An Experiment in Large Area Diamond Coating using A Combustion Flame Torch in its Traversing Mode, *Surface Coating Technology*, Vol.43, No.44, pp.22-29, (1990).
4. Paul A. Dennig and David A. Stevenson, Influence of Substrate Topography on the Nucleation of Diamond Thin Films, *Applied Physics Letters*, Vol.59, No.13, pp.1562-1564, (1991).

## **Comparison of Superplastic Formability Predictions Using 2-D Plane Strain and 3-D Modeling**

**S. Lee and J. Lee**

Department of Mechanical Engineering,  
National Central University, Chung-li, Taiwan, R.O.C.

### **Abstract**

Computational simulations of superplastic forming by 2-D plane strain including simple analytical and finite element and 3-D finite element modeling were compared with each other. The piece being formed was a rectangular pan with a female die. The effect of die entrance radii upon pressurization rate and thickness distribution was examined. Experimental work was conducted on superplastic aluminum-lithium 8090 material for comparison with predictions from simulations.

### **1.0 Introduction**

Superplastic forming (SPF) is a manufacturing process in which bulk or sheet metal components can be formed at relatively low stresses while developing extremely large tensile elongation, at least of the order of several hundred per cent. Superplastic materials unlike conventional ductile metals, are significantly less susceptible to strain localization. In particular, superplastic forming of thin sheet can produce quite complex, light and strong components. The material is typically heated to above half the absolute melting temperature and pressure-formed at a

strain rate between  $10^{-3}$  and  $10^{-5}$   $s^{-1}$  by argon gas.

Mathematical models of the SPF process are used in predicting the pressurization rate for optimum superplastic formability, and also for predicting the distribution of thickness in the formed part so that producibility and structure mechanics analysis can be assessed. Modeling also yields an estimate of forming time, which is required for estimating the cost of a SPF operation. Finite element method (FEM) as well as a simple analytical method has been proposed. Superplastic forming of a rectangular pan has been first

mathematically studied by Ghosh and Hamilton (1) and their method is termed "simple analytical" in this paper. Many numerical models, primarily FEM, have been since then published (2-9). Different models may possibly require rather different computing powers e.g. simple analytical can be executed on a personal computer while 3-D FEM code requires a work station or more powerful computer facility. 2-D plane strain modeling using three computer programs and 3-D modeling using two FEM codes are investigated in this study. In addition to the commonly predicted pressurization rate and thickness distribution, the effect of die entrance radii is studied in this paper.

The material studied here is superplastic Al-Li alloy 8090 which is attractive for possibly enhancing the structural performance of advanced airframe structures. It is relatively new and still being fully evaluated, and intensive research work concerning its behavior are currently being undertaken. A necessary component of any analytical process model is the constitutive equation for the material (relationship between stress, strain, strain-rate, temperature and microstructure). The strain-rate dependency of the flow stress is characterized by the strain-rate sensitivity,  $m$ , which is an important superplastic forming parameter. A number of test techniques have been used for determining  $m$ , including the constant true strain-rate uniaxial tensile test and the biaxial cone test (10). A similar stress versus strain-rate

relationship has been previously published by Chandra and Pilling (10, 11), which is employed in the modeling work of this paper.

## 2.0 Experimental Procedures and Model Descriptions

### 2.1 Materials and Equipment

Al-Li 8090 material was purchased from Superform Metals Ltd., a British company; its composition was, by wt%: 2.33 Li, 1.1 Cu, 0.11 Zr, 0.74 Mg and some minute elements and balance aluminum. Forming work was done on a commercial hot press with 2 mm thick Al-Li sheet, and 120 mm x 40 mm x 20 mm rectangular die made of mild steel. The die was maintained at a uniform temperature of 530°C. For computation, an IBM compatible PC and a RS 6000 work station were employed.

### 2.2 Modeling A Long Rectangular Pan with Simple Analytical Method

The length of the rectangular pan is assumed in this analysis to be substantially greater than the width. This condition is, however, in practical terms thought to be satisfied when the length is three times the width as in our sample pan of size 120 mm x 40 mm. A sketch of relevant geometrical, dimensional symbols during forming process, and picture of a completed work piece, are shown in Figure 1. A condition of plane strain indicates that the longitudinal

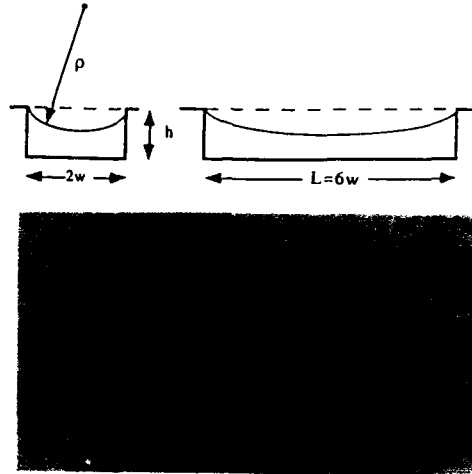


Figure 1: Geometry of the long rectangular pan studied in this paper and the picture of a completed product.

strain,  $\epsilon_2$ , and strain rate,  $\epsilon_{2dot}$ , vanishes, leaving  $\epsilon_{1dot} = \epsilon_{3dot}$ ; then effective strain rate  $\epsilon_{dot} = (2/\sqrt{3}) \epsilon_{3dot}$ . The corner radius is further assumed in this simplified analysis to be zero and frictional effects are negligible. If the design strain rate is  $\epsilon_{dot}$ , the following equations then apply before the sheet metal comes into contact with the bottom or side, depending on whether the box is shallow or deep. For a given radius,  $\rho$  the time of formation is given by

$$t = \{2/(\sqrt{3}\epsilon_{dot})\} \ln\{(\rho/w) \sin^{-1}(w/\rho)\} \quad (1)$$

where  $w$  is the semi-width, and the pressure  $p$  is given by

$$p = (2/3) (s_0/\rho) \exp(-\sqrt{3}\epsilon_{dot}t/2) \sigma \quad (2)$$

where  $s_0$  is the original thickness, and  $\sigma$  can be determined using the constitutive equation mentioned above. P-t relationship can be determined for any  $\rho$  for the above two equations until contact is made at the bottom or side. The thickness at any time is assumed to be constant and is given by

$$s = (s_0/\rho) \exp(-\sqrt{3}\epsilon_{dot}t/2) \quad (3)$$

After contact is made, on the side or the bottom depending on the ratio of  $w/h$  where  $h$  is the depth of the pan, radius  $\rho$  is given by

$$\rho = (y^2 + x^2) / 2y \quad (4)$$

where  $x$  and  $y$  are the unsupported distances along the respective side and bottom die surface.

$$t_{i+1} = t_i + \{2/(\sqrt{3}\dot{\epsilon}_{dot})\} \ln \{[p_i + 1\phi_{i+1} + (\Delta y/2 + \Delta x/2)] / [p_i\phi_i - (\Delta y/2 + \Delta x/2)]\} \quad (5)$$

The time of formation can be determined as shown in equation 5, where  $\phi_i = 2 \tan^{-1}(y/x)$ , and the subscript is the time increment index and  $\Delta x$  and  $\Delta y$  are the respective incremental distances of contact in x and y directions. The thickness formulation remains the same as in the first stage. A complete development of the analysis is given in the work by Ghosh (1), which dealt with Ti-6Al-4V alloy.

### 2.3 Modeling A Long Rectangular Pan With FEM Code (MARC)

MARC, a general purpose and commercially available FEM code, is used. It has an element library containing many elements to choose from. For 2-D case, arbitrary plane-strain and quadrilateral element consisting of 140 elements with 213 nodes are selected. An arbitrary distorted cubic element consisting of 344 elements with 766 nodes is prescribed in 3-D case. The radii of the entrance angle and that between the respective bottom and side walls of the die are 3.5 mm and 2.5 mm. In 3-D case, there are four corners which are laborious to create and are shown in Figure 2. There is a draft angle of  $6^\circ$  on side walls and sticking friction is assumed. Forming pressure control algorithm is based on the philosophy that the maximum strain rate of some element in the work piece stays around a target value. At the beginning of each time increment, all elements are examined and the maximum strain rate

of the previous increment is found. Pressure is adjusted in accordance to the following scheme of:

$$\begin{aligned} p_{i+1} &= 1.3p_i && \text{if } Z < 0.5 \\ p_{i+1} &= p_i && \text{if } 0.5 < Z < 1.1 \\ p_{i+1} &= p_i/1.1 && \text{if } 1.1 < Z < 1.3 \\ p_{i+1} &= p_i/1.2 && \text{if } Z > 1.3 \end{aligned}$$

where  $p_i$  represents the pressure at ith increment, and  $Z$  is the ratio of maximum strain rate ( $\dot{\epsilon}_{dot, max}$ ) to target strain rate ( $\dot{\epsilon}_{dot, target}$ ).

The target strain rate is selected based on the philosophy that high strain rate sensitivity  $m$  is required to be maintained for resisting necking during forming process. By a trial and error method, an initial pressure of 27.584 KPa has been determined, and time increment was chosen to be 5 seconds. Owing to its symmetrical shape, only one half or a quarter of the rectangular pan needs to be considered for 2-D or 3-D cases.

The material's relationship between strain-rate and strain-rate sensitivity  $m$  has been referred to in previous publications. The strain-rate of  $0.001 \text{ s}^{-1}$  and constitutive equation,  $\sigma = 169.64 \dot{\epsilon}_{dot}^{0.478}$  MPa are selected on the basis of Chandra's work for Al-Li 8090 alloy (10).

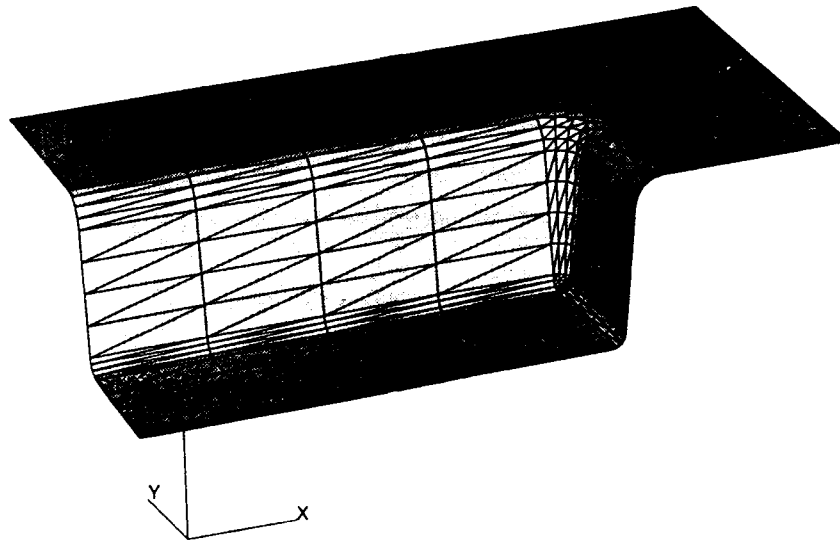


Figure 2: One quarter of the forming die as modeled in computer.

#### 2.4 Modeling with FEM code (SUPFORM)

SUPFORM which is an elastic viscoplastic or rigid viscoplastic finite element code, used solely for superplastic forming, was developed at CEMEF in France. SUPFORM2 is for 2-D computation and can be run on a PC, while SUPFORM3 is for 3-D work and is based on plane stress membrane mechanics for an isotropic Mises material (12). User does not have an element option, time increment is automatically considered and pressurization rate control algorithm is preset internally in contrast to MARC.

#### 3.0 Results and Discussion

##### 3.1 Pressurization Rate Predictions by Different Models

On the basis of  $0.001 \text{ s}^{-1}$  target strain rate, the pressurization rate needed to form a 120 mm x 40 mm x 20 mm rectangular pan as predicted by simple analytical, MARC and SUPFORM are shown in Figure 3. The curve derived on the basis of simple analytical method is observed in this figure to sweep up to a higher pressure level earlier than the others. The simple analytical curve furthermore exhibits a sharp turning point that indicates the moment that forming sheet touches die bottom. The two curves by 2-D and 3-D MARC, are observed to be quite close to each other

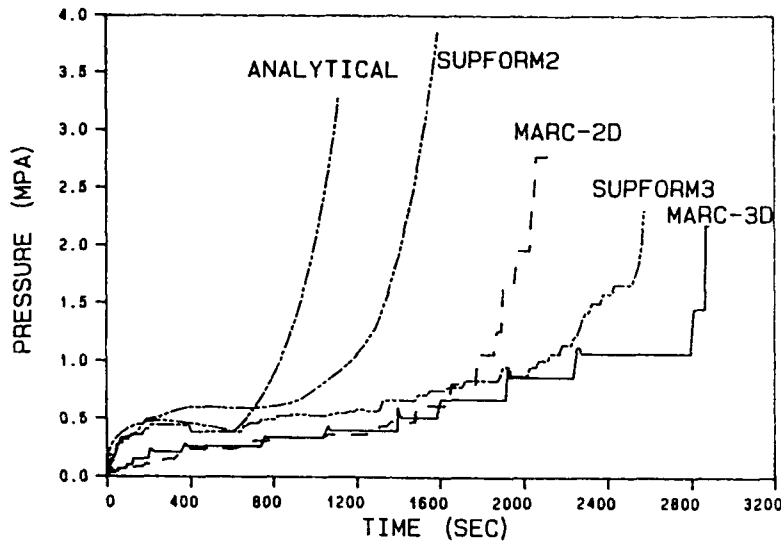


Figure 3: Pressurization rate input to form a 120 mm x 40 mm x 20 mm rectangular pan as predicted by different models.

from the beginning until ~1750 seconds indicating that plane strain assumption is acceptable for approximation regarding pressure profile input when modeling a long rectangular pan.

Three dimensional full scale modeling predicts longer formation time (~330 seconds) required since four corners are formed at the end. This can be accounted for with the assistance of the computer simulated configurations depicted in Figures 4 and 5. The profile of the forming part at  $t=1,810$  seconds, is shown in Figure 4.

The radius of the 2-D corner, which is actually a part of cylindrical surface is observed in this figure to be smaller than

that of the 3-D corner which is approximately a part of the spherical surface. As indicated by the pressure-radius relationship in Equation (2), pressure required increases earlier in 2-D case than in 3-D. FEM modeling has calculated the strain rate of every element. MARC has showed that strain rate in the vicinity of die entrance, shown in Figure 6, is maintained around the target strain rate for a long time.

The computation results of SUPFORM and MARC are compared next. SUPFORM3's prediction has not significantly deviated from MARC 3D's, and is also more realistic. However, SUPFORM3 required much less computer time than MARC-3D, hours

*Comparison of Superplastic Formability Predictions*

---

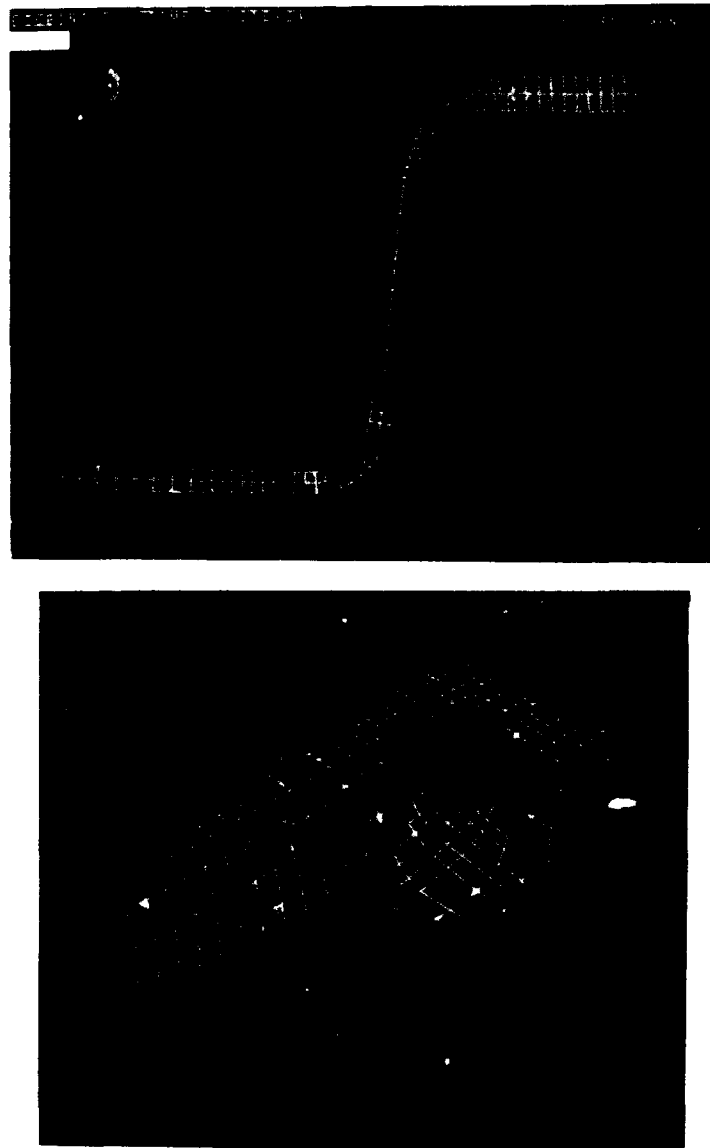


Figure 4: MARC's simulation showing the configuration and strain rate distribution at  $t=1,810$  seconds of the formed pan in 2-D and 3-D.

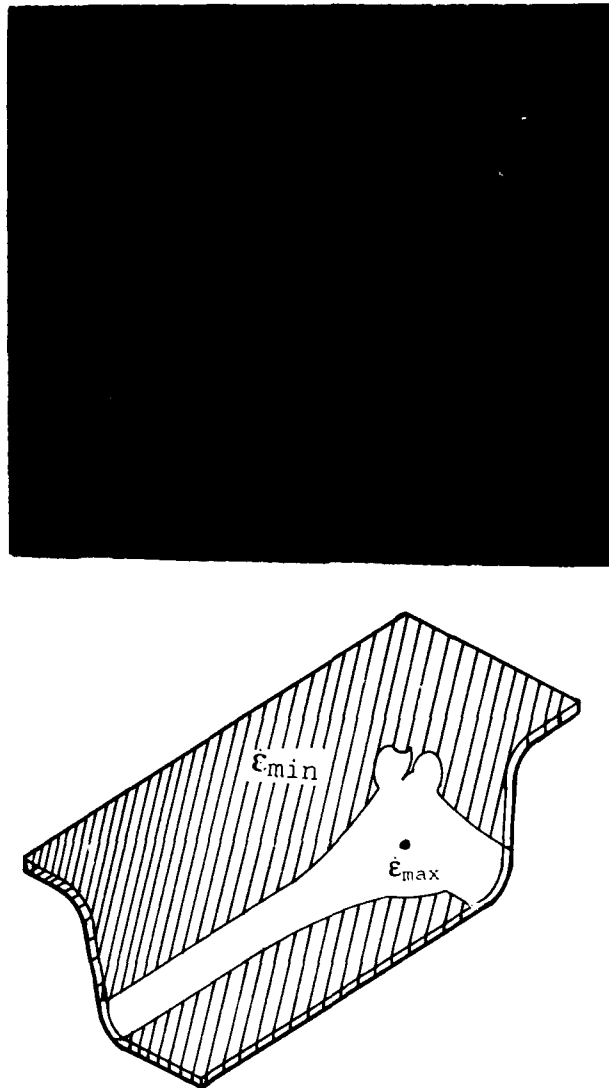


Figure 5: MARC-3D's simulation illustrating the configuration and strain rate distribution at  $t=2,160$  seconds of the formed pan (top), and contour showing the highest and lowest strain rate regions.

*Comparison of Superplastic Formability Predictions*

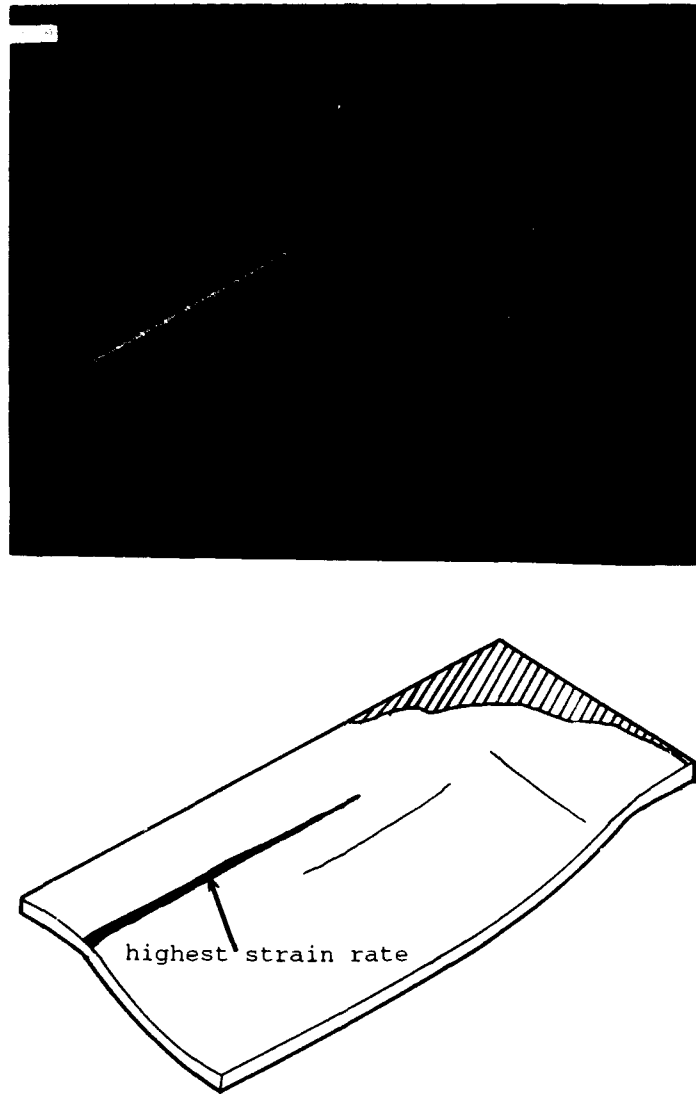


Figure 6: MARC-3D's simulation exhibiting the configuration and strain rate distribution at  $t=300$  seconds of the formed pan (top), and contour showing the region of highest strain rate.

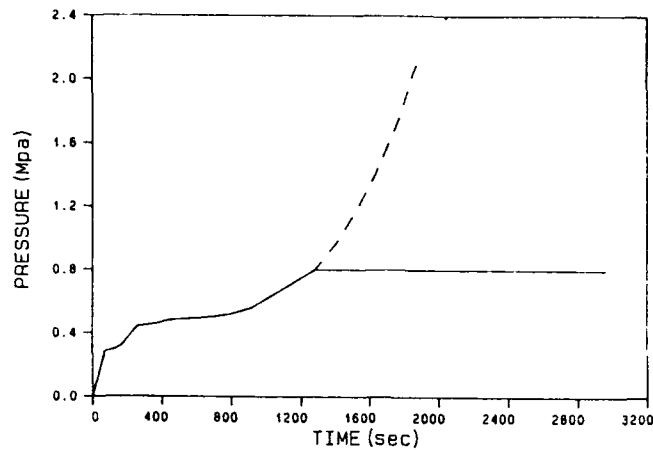


Figure 7: Following the sweeping-up pressurization rate at final stage as prescribed by SUPFORM2 in forming a 120 mm x 40 mm x 20 mm rectangular pan would have led to failure before completion; plateau is determined by trial and error to avoid failure.

versus days on IBM RS 6000/320 work station.

### 3.2 Measured and Predicted Thickness Distribution

Forming experiments were performed at an applied pressurization rate following SUPFORM2's prescription in Figure 3. The rate was flattened during the final stage of this experiments instead of rising all the way (Figure 7), as otherwise rupture would have occurred before completion of the formation of the pan. Thickness distribution computation based on realistic experimental pressurization rate curve and non-modified one are shown in Figures 7 and 8 for comparison. Computed thickness distributions by SUPFORM2 in the above two conditions

are identical except in the region of least thickness. Measured thickness distribution is, however, more uniform than those predicted. This is because sticking friction was assumed, whereas in a real situation, sliding exists even when no lubricant was applied. Another comparison of the thickness distributions by all FEM codes with the measured shows that SUPFORM3 provides the closest prediction (Figure 9).

### 3.3 Effect of Die Entrance Radii

SUPFORM3 was used for simulating the effect of die entrance radii ( $R = 0, 3.5$  and  $7$  mm) upon pressurization rate and thickness distribution. A larger radius is observed to lead to a shorter forming time and a more uniform thickness

**Comparison of Superplastic Formability Predictions**

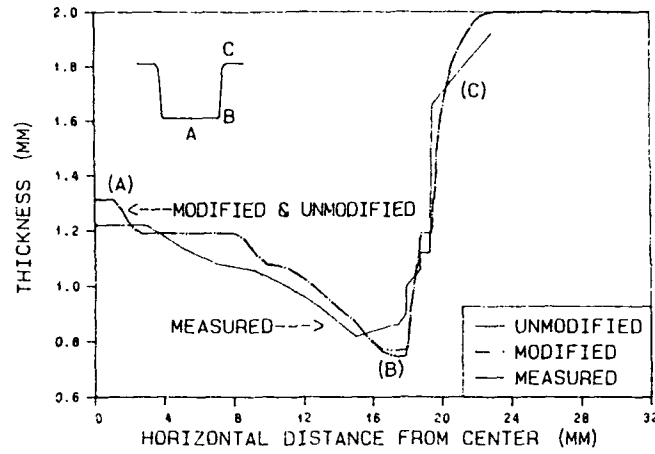


**Figure 8:** Thickness distribution in mid-span section containing half the width, as measured from the formed piece and computed by SUPFORM2 with and without modification in pressurization rate.

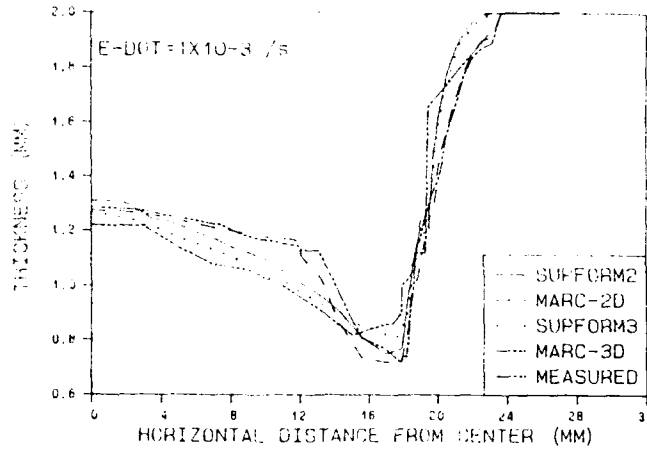


**Figure 9:** Thickness distribution in mid-span section containing half the width, as measured from the formed piece and computed by all FEM models.

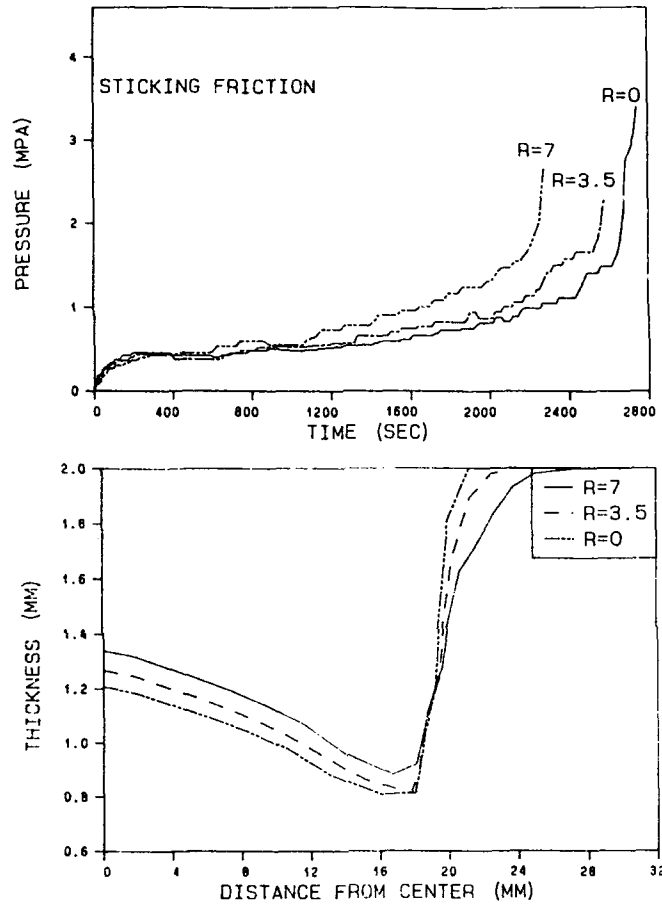


Figure 10: Top - Influence of die entrance radii upon pressurization rate computed by SUPFORM3 with sticking friction assumption. Bottom - Influence on thickness distribution in mid-span section containing half the width.

distribution (Figure 10) in mid-span section containing half the width.

following conclusions can be made:

#### 4.0 Summary

From the above discussions, the

1. Five different modelings yielded non-identical pressurization rate curves and 3-D modeling requires substantially less computer time.

### *Comparison of Superplastic Formability Predictions*

---

2. Thickness distributions predicted by the modeling exhibited a similar trend as those measured from experiment, which confirms the value of simulation.
3. Preliminary study of die entrance radius effect indicated that it is not negligible.

#### **5.0 References**

1. Ghosh, A. K. and C. H. Hamilton, Superplastic Forming of a Long Rectangular Box Section - Analysis and Experiment, Proceedings of American Society for Metals on Process Modeling - Fundamentals and Applications to Metals, pp.303-331, (1979).
2. Rebelo, N. and T. B. Wertheimer, Finite Element Simulation of Superplastic Forming, 16th North American Manufacturing Research Conference, University of Illinois, Urbana, Illinois, pp.107-113, (May 25-27, 1988).
3. Argyris, J. H. and J. St. Doltsinis, A Primer on Superplasticity in Natural Formulation, Computer Methods in Applied Mechanics and Engineering, Vol.46, pp.83-131 (1984).
4. Chandra, N., Analysis of Superplastic Metal Forming by a Finite Element method, International Journal of Numerical Methods in Engineering, Vol.26, pp.1925-1944, (1988).
5. Zang, W. C., R. D. Wood and O. C. Zienkiewicz, Superplastic Forming Analysis using a Finite Element Viscous Flow Formulation, Proceedings of Aluminum Technology '86, London, pp.111.1-111.6, (1986).
6. Bellet, M. and J. L. Chenot, Numerical Simulation of Superplastic Forming, Proceedings of Sixth World Conference on Titanium, France (1988).
7. Bonet, J., R. D. Wood and O. C. Zienkiewicz, Finite Element Analysis of Thin Sheet Superplastic Forming, Mathematical Models for Metals and Materials Applications, Institute of Metals, London, 2.1-2.7, (1988).
8. Bellet, M. and J. L. Chenot, Numerical Modeling of Thin Sheet Superplastic Forming, Proceedings of NUMIFORM '89 Conference, Colorado, pp.401-406, (1989).
9. Zienkiewicz, O.C., The Finite Element Method, Third Edition, McGraw Hill (1977).
10. Goforth, R. E., and N. A. Chandra, Analysis of the Cone Test to evaluate Superplastic Forming Characteristics of Sheet Metal, Superplasticity in Aerospace, The Metallurgical Society, pp.149-166, (1988).

11. Pilling, J. and N. Ridley, Role of Hydrostatic Pressure on Cavitation During Superplastic Flow of Al-Li Alloy, Aluminum-Lithium Alloys III, The Institute of Metals, London, pp.184-190, (1986).
12. Massoni, E., M. Bellet and J.L. Chenot, Thin Sheet Forming Numerical Analysis with a Membrane Approach, Model of Metal Forming Process, Kluwer Academic Publishing, Boston, pp.187-196, (1988).

## **Stretch Formability in HSLA and IF Steels**

**Paolo Matteazzi and Giovanni Farnè**  
Dipartimento di Scienze e Tecnologie Chimiche  
Università di Udine, I-33100 Udine, Italy

**Giuseppe Randi and Marcello Leoni**  
Consiglio Nazionale delle Ricerche  
Istituto di Chimica Fisica Applicata dei Materiali  
Lungobisagno Istria 34, I-16141 Genova, Italy

### **Abstract**

Stretch formability of steel sheets can be evaluated by the strain hardening exponent. Cold rolled High Strength Low Alloy (HSLA) and Interstitial Free (IF) steels having different compositions and processing histories have been studied. Steels were subjected to controlled strains and the values of strain hardening exponents, microstrains and residual stresses were measured. It was found that a linear correlation exists between residual stresses and the strain hardening exponents. A possible mechanism for work hardening in the presence of misoriented grains is proposed taking in account the storage of elastic strain energy and the dislocation movements. A strain interval (10-15%) is proposed for stretch forming operations to minimize residual stresses.

### **1.0 Introduction**

Stretch-forming (a cold forming operation) is employed most extensively in the aircraft industry to produce parts (usually sheets) of large radius of curvature (1). The stress system is biaxial and the stretch-formability is evaluated by the value of  $\epsilon_n$  (true strain at necking) which can be obtained by a

uniaxial tension test (2). The value of  $\epsilon_n$  can be approximated (1) by the strain hardening exponent or index which in turn can be used as a measure of the stretch-formability of the material. The strain hardening exponent "n" is evaluated using equation:

$$\sigma = k \epsilon^n \quad (1)$$

Table 1. Chemical composition of HSLA and IF Steels (wt %).

Steel	C	Si	Mn	Ni	V	Nb	Al	Ti
HSLA 1	0.069	0.011	0.024	0.008	-	0.034	0.061	-
HSLA 2	0.071	0.011	0.024	0.009	-	0.033	0.050	-
HSLA 3	0.043	-	0.190	0.008	-	0.012	0.057	-
HSLA 4*	0.066	-	0.180	0.007	-	0.011	0.006	-
IF 5	0.002	0.006	0.180	0.011	0.014	0.005	0.028	0.180
IF 6	0.002	0.006	0.170	0.011	0.015	0.004	0.030	0.180
IF 7*	0.011	0.006	0.180	0.011	0.015	0.005	0.008	0.120

For all steels, P < 0.009% and Cr < 0.008%.

\* Rimming Steels

where  $k$  is the strength constant from the slope of a log-log plot of true stress ( $\sigma$ ) and true strain ( $\epsilon$ ) (1).

Plastic deformation of steels generates residual stresses and microstrains. Residual stresses arise from elastic response to an inhomogeneous distribution of strains, such as plastic strains (3) whereas microstrains (4) can be correlated with lattice strains generated during the progress of deformation in the plastic interval. X-ray diffraction line positions and shapes are influenced by the presence of residual stresses and microstrains respectively. X-ray diffraction is therefore employed to investigate such effects of plastic deformation (3,4). When the plastic deformation is obtained by the application of a uniaxial stress, then the macroscopic quantity such as the strain hardening index "n" can also be measured.

The purpose of the work is to correlate the microscopic (residual stresses and microstrains) with the macroscopic (strain hardening index "n") data, measured using the progress of plastic deformation, of steel sheets employed in stretch-forming operations. The steels investigated were High Strength Low Alloy (HSLA) and Interstitial Free (IF), which gave rise to different behaviors during stretch-forming, poor and very good respectively.

## 2.0 Experimental Methods

### 2.1 HSLA and IF Steels

Experiments were performed on cold rolled (70% reduction), batch annealed and skin passed HSLA and IF steels (chemical compositions reported in Table 1), produced in experimental batches by Nuova Italsider s.p.a. (Genova, Italy).

Table 2. Experimental Production Data of HSLA and IF Steels

Steel	Hot Rolling Finishing Temp. (°C)	Coiling Temp. (°C)	Sheet Thickness (mm)	Annealing Temp/Time (°C/hr)	ASTM Grain Size
HSLA 1	840	630	1.5	630/10	10.5
HSLA 2	840	630	1.0	650/10	11.9
HSLA 3	840	660	1.5	640/10	9.0
HSLA 4	840	660	1.0	640/10	10.0
IF 5	890	600	1.5	690/6	8.0
IF 6	890	570	1.5	690/6	8.0
IF 7	890	550	1.5	690/6	8.0

Table 2 gives the relevant hot rolling production data, the batch annealing parameters and the ASTM grain sizes after annealing. With the purpose of differentiating the yield stress  $\sigma_y$ , the strain hardening index ( $n$ ) (Table 3) and the microstructural features of these steels, various experimental conditions (Table 2) were adopted to obtain different degrees of coalescence of the secondary phase particles.

The IF 7 steel, for which a low coiling temperature (6) was employed, turned out to have a higher yield strength (Table 3) than the other IF steels and, consequently, a lower strain hardening index " $n$ " (Table 3), which was lower than those of the HSLA steels.

The microstructure of HSLA steels consisted of a matrix of fine ferrite grains (Figure 1a) with a homogeneous dispersion of small carbides (Figure 1b).

The higher coiling temperature for steels 3 and 4 produced increased grain sizes (Table 2). IF steels had (Figure 1c) a ferrite matrix with a larger grain size than the HSLA steels in addition to visible prior austenite grain boundaries and few coarse carbide particles (Figure 1d).

## 2.2 Determination of the Strain Hardening Index

The strain hardening index was measured on flat specimens prepared according to ISO standard N. 2776 by using a universal testing machine at 25°C with a deformation rate of  $10^{-3} \text{ s}^{-1}$ . Measurements were performed in three directions (longitudinal "l", transverse "t", and diagonal "d", at angles with the rolling direction 0°, 90°, 45° respectively) for two deformation intervals (i.e. 9-13% and 12-18%) commonly used for stretching operations.

**Table 3. Yield Strengths and Strain Hardening Indexes**

Steel	$\sigma_y$ (MPa)	$n_l$	$n_t$	$n$	$n_l$	$n_t$	$n$
		(Deformation 9-13%)			(Deformation 12-18%)		
HSLA 1	294	0.156	0.149	0.150	0.161	0.158	0.160
HSLA 2	286	0.160	0.122	0.134	0.173	0.170	0.173
HSLA 3	225	0.203	0.206	0.205	0.211	0.217	0.207
HSLA 4	216	0.193	0.203	0.201	0.211	0.217	0.207
IF 5	169	0.250	0.194	0.219	0.240	0.229	0.237
IF 6	169	0.272	0.264	0.257	0.265	0.247	0.242
IF 7	230	0.190	0.216	0.208	0.191	0.206	0.184

$n_l$  = longitudinal,  $n_t$  = transverse,  $n$  = averaged (equation 2), evaluated with respect to the rolling direction)

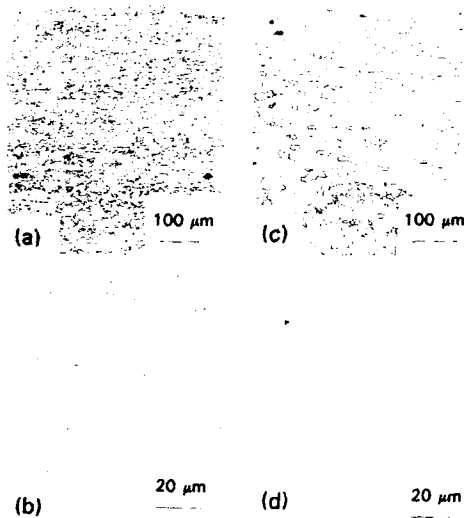


**Figure 1:** Optical micrographs of HSLA (a, b) steel 2 and IF (c, d) steel 5. Etching: (a, c) Nital 4%; (b, d) Picral 4%. Sheet surface at top of (a, c); sheet cross section (b, d).

The average strain hardening index "n" (equation 1), was then calculated by:

$$n = (n_1 + 2n_2 + n_3) / 4 \quad (2)$$

according to the method described in (7). Each "n" value in Table 3 represents the average of triplicate testing.

### 2.3 Microstrains and Residual Stresses

The X-ray diffraction patterns were obtained with a computer controlled diffractometer using Co K $\alpha$  ( $\lambda = 0.1789$  nm) radiation. Data for residual stress analysis were collected using 0.05° steps in 2 $\theta$  angle. The behavior of lattice spacing "d" versus sin<sup>2</sup> $\psi$  (8-11) was evaluated for the (310)  $\alpha$ -Fe line at four  $\psi$  angles ( $\psi = 15^\circ, 30^\circ, 45^\circ, 60^\circ$ ). Peak positions were calculated by parabolic approximation of the top 15% of a peak (12). The (310)  $\alpha$ -Fe line was chosen to minimize the effects of recrystallization texture on d versus sin<sup>2</sup> $\psi$  behaviors (13).

The following values for the constants were employed in the calculation:

$$\begin{aligned} d_0(310) &= 0.09064 \text{ nm,} \\ E &= 1.902 \times 10^5 \text{ MPa, and} \\ N &= 0.328, \end{aligned}$$

where  $d_0(310)$  is the lattice spacing for the unstressed material, E and N are the Young's modulus and Poisson's ratio respectively. Residual stresses were determined in the longitudinal and transverse directions which are also assumed here as correspondent to the direction of the main stresses (14). Each residual stress value given in the following was averaged over 10 samples.

The mean standard deviation on residual stresses was about 12 MPa for HSLA steels and about 8 MPa for IF steels.

Microstrains were evaluated on samples taken along the rolling direction (4,15-19) after controlled plastic deformation in the testing machine. The examined surfaces were obtained by cutting the deformed samples in the center and by an electrolytic polishing 10  $\mu\text{m}$  away. Microstrains were obtained (4) by:

$$\langle \epsilon_L \rangle^2 = G^2_{(220)} / (L) \quad (3)$$

where  $\langle \epsilon_L \rangle^2$  is the mean square strain; L is the columnar length and is equal to "m  $d_{(220)}$ ", where m is an integer and  $d_{(220)}$  is the interplanar spacing;  $G^2_{(220)}$  is an index defining the distribution of microstrains in the direction (L) normal to the (220) planes.

The function  $\langle \epsilon_L \rangle^2$  is obtained by Fourier analysis of (220) line profile and the  $G^2_{(220)}$  value is obtained (equation 3) using  $L=50$  (20). Stokes correction (4, 10, 15, 19) for instrumental broadening was used by taking as a reference the (220) line profile of an undeformed sample.

Measurements of microstrains and residual stresses were then performed on samples deformed with 2% strain steps starting from 5% up to necking. Each measurement was the average of triplicate samples with the same strain.

### 3.0 Results

Since the behavior of  $d$  versus  $\sin^2\psi$  was essentially linear (3) we assumed a biaxial stress state in the analysis. Figures 2 and 3 show the behavior of residual stresses as a function of deformation for HSLA and IF steels respectively. In all cases, a compressive state was found.

The influence of deformation on  $G^2_{(220)}$  values is reported in Figure 4, where a maximum is observed at intermediate strains (9-13%). Since the value of  $G^2_{(220)}$  can be correlated (21) to the dislocation density in the coherent diffraction domain, then Figure 4 can also be assumed to qualitatively show the behavior of the dislocation density versus the plastic deformation.

We should however observe that the possible domain fragmentations over the distance taken to average the strain distribution may lead to a reduction in the  $G^2_{(220)}$  values. This is due to the fact that the resultant misorientation across the new domain boundaries may be such that adjacent domains diffract incoherently and therefore no coherent diffracted intensity can be received (22).

### 4.0 Discussion

#### 4.1 Dislocation Densities and Deformation

After the thermomechanical treatments reported in Table 2 the size of

crystallites, as determined by X-ray diffraction line broadening analysis, were in the range 150-200 nm. We did not investigate the corresponding microstructural evolution although it is probable (22, 23) that the steel sheets evolved from a cold worked cellular substructure characterized by cell walls with high dislocation densities (caused by cold strain) to the formation of subgrains during annealing.

The data reported in Figure 4 reveal that at low strains a limited number of single dislocations are involved as addressed by the low  $G^2_{(220)}$ , so that the walls of the substructure seem to behave like dislocation forest cut by moving dislocations. At higher strains, subgrain boundaries act like grain boundaries, giving rise to a continuous generation of new gliding dislocations (24).

An unusually rapid increase in dislocation density was previously observed during cold plastic deformation of materials containing a fine dispersion of second phase particles (25), where the density becomes particularly high for strains greater than about 5% (26). Even though this refers to face-centered cubic materials, such data are in good agreement with the  $G^2_{(220)}$  behavior observed in the IF and in some HSLA steels. The IF steels 5 and 6, characterized by the presence of finely divided second phase particles, exhibit in fact quite large dislocation density values (Figure 4b); also HSLA steels 1 and 2, having a homogeneous distributions of fine carbides resulting

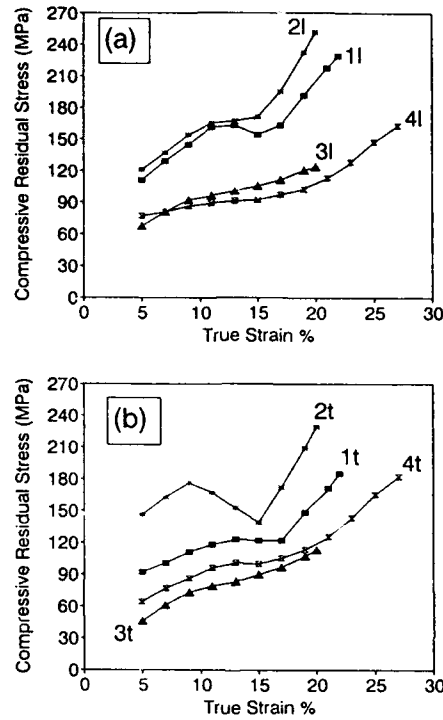


Figure 2: Residual stresses versus true strain for HSLA steels measured in (a) longitudinal "l" and (b) transverse "t" directions with respect to the rolling direction.

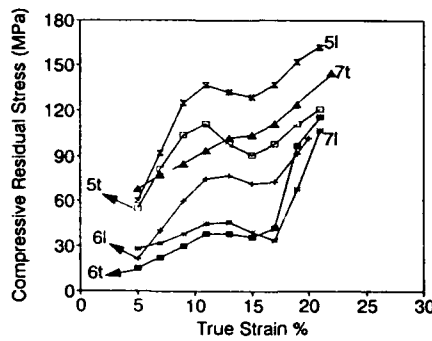


Figure 3: Residual stresses versus true strain for IF steels measured in longitudinal "l" and "t" transverse directions with respect to the rolling direction.

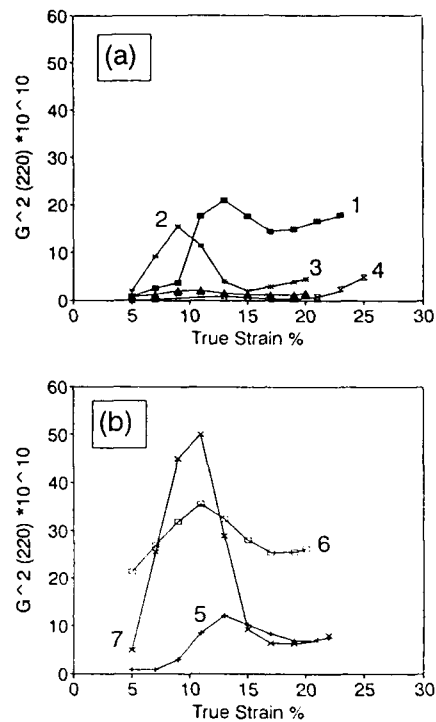


Figure 4. Dislocation density expressed as  $G^2_{(220)}$  versus true strain for: (a) HSLA and (b) IF steels.

from the low coiling temperature, show large dislocation density levels (Figure 4a) in the same strain range. The IF steel 7, which has a lower coiling temperature than steels 5 and 6, show mechanical and microstructural properties (Tables 2, 3) close to the HSLA steels as are the  $G^2_{(220)}$  values.

The decrease of  $G^2_{(220)}$  values at higher strains (12-15%) can be explained by assuming that dislocation tangles form within the subgrains as strain increases; such tangles gradually evolve into new

cellular substructures, with fragmentation of the original subgrains. The misorientation of the new substructures tends in fact to give incoherent X-ray diffraction, leading to reduced  $G^2_{(220)}$  values. This hypothesis is in agreement with data previously reported (27-30) and has been confirmed by TEM observations (24) of decreasing cell size with strain in Fe-C (0.07 wt%) wires and by the observation (31) of cell formation in  $\alpha$ -Fe subjected to a 6% strain. As alloying delays cell formation at high strains (32), this supports the assumption

made for the interpretation of X-ray data (i.e., cell formation may occur in the strain range 9 to 13%). It is in fact in this range that the profile analysis of (220) reflection suggests a progressive decrease in the size of the initial substructures for all the steels under investigation (exception made for steels 4 and 5, for which the variations were small). Experimental data reported in (33) for a steel containing 0.09% C and 0.33% Mn, also support the hypothesis of possible cell formation at 12% strain.

Since it is well known (34-36) that in iron and steel fluctuations of "n" values (the so-called "double n" behavior) occur in the interval 10-13% strain, this seems to suggest a correlation between the grain substructure and the "n" value. As the latter can be attributed to arise from interactions among dislocations, its fluctuations in the 10-13% strain range indicate a correlated variation of the work hardening mechanism as a result of a change in the slip mode (34, 37, 38). The slip mode would change from the movement of single dislocations, within the grains, to the one resulting from the cooperative movement of dislocations in the cell walls. This hypothesis is in agreement with the assumption concerning cell misorientation at increasing strains. In fact, on the basis of a theoretical calculation (24), such misorientation makes the transition of a single dislocation from one cell to another unlikely (24).

The discussion above also allows a coherent interpretation of the behavior of

HSLA steels 3 and 4, which exhibit low  $G^2_{(220)}$  values with negligible peaks, at 9 and 12% strains respectively. The low  $G^2_{(220)}$  values seem to be due to the higher coiling temperatures used for these steels (Table 2) and to the lower Nb content (giving fewer and coarser precipitates). Previously reported results (26) show that a lower content of fine second phase particles leads to a strong decrease of dislocation density (26); the  $G^2_{(220)}$  value is therefore also decreased in comparison with the other steels. It should also be noticed that these steels (3 and 4) are less affected by the "double n" behavior (typical of the other steels, Table 3). This may be ascribed to a greater continuity in the microscopic phenomenon of strain.

#### **4.2 Residual Stresses and Deformation**

The graphs of Figures 2 and 3 show that the residual stresses first increase quite rapidly with strain up to strain levels of 9-13%. With further deformation beyond about 13%, the rate of increase of residual stress diminishes, or even reverses, and then finally with further deformation of 15-16%, the residual stresses begin to increase rapidly again. The behavior observed at intermediate strains, may be interpreted by assuming that the activation of the slip planes in the grains on which the residual stresses are measured may occur later than in the matrix grains (at strains of about 9-13%), as a result of misorientation with respect to the applied load. In this case, an upward trend at the intermediate strains should be ascribed to a

preferential slipping on the slip planes in the matrix grains as compared to the one in grains utilized for the measurements. The effect of such a slipping could be a compression of the (310) planes which is minimized as compared with the one observed at lower strains. A downward trend would imply an opposite behavior due to the easier deformation of the grains utilized for the measurements; by conforming to the matrix grains, they allow a partial pressure relief onto the (310) planes.

This assumption, however, does not allow any connection to be inferred between the dislocation density behavior (i.e.  $G^2_{(220)}$ ) discussed in the previous section and the residual stresses behavior in Figures 2 and 3, although previously reported results showed a possible correlation (39, 40). It has been shown that dislocation tangles occurring after plastic tensile strains, at room temperature, imply small residual stresses in low carbon steel or  $\alpha$ -Fe, while a more uniform dislocation distribution gives rise to higher residual stresses (40). This observation has also been confirmed in other work (12), and the findings are in good agreement with the fact that the maxima in  $G^2_{(220)}$  are observed to occur in the same strain range for which discontinuities are observed in the residual stress behavior.

The differences observed for residual stresses in the longitudinal and transverse directions, in the same sample (Figure 2 and Figure 3), can be interpreted by recalling that, as

demonstrated in (41), in a steel sheet, the work hardening index "n" depends on the direction in which the measurement is performed, as a consequence of texture resulting from rolling. On the other hand, variations of "n" values also imply corresponding variations in the behavior and distribution of the dislocations; consequently we may expect different values of the residual stresses, for the same strain, in the longitudinal and transverse directions (Figures 2 and 3).

#### 4.3 Correlation between Microscopic ( $G^2_{(220)}$ , Residual Stresses) and Macroscopic Parameters

Since the behavior of  $G^2_{(220)}$  values and the meaning of its maxima have been correlated to the dislocation behavior, it appears reasonable to correlate  $G^2_{(220)}$  with "n" values which are (1, 36) strongly dependent on the dislocation behavior. The "n" values reported in Figure 5 are those measured in the longitudinal direction as are the  $G^2_{(220)}$  maximum values. A linear behavior with negative slope is observed for HSLA steels (correlation coefficient 0.99) for  $n_1$  (12-18%). Since the  $G^2_{(220)}$  values depend on dislocation density  $\rho$ , in the coherent diffraction domains, the linear inverse correlation between "n" and  $\rho$  deduced in other work (7, 38) is therefore experimentally verified.

A similar behavior can be observed for the IF steels if we classify steel 7 (Tables 1, 2, 3) as very close to HSLA steels. The above considerations apply

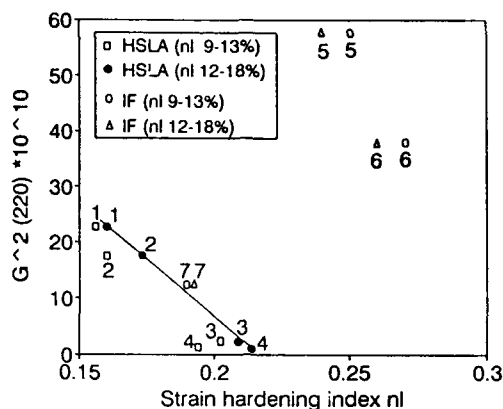


Figure 5:  $G^2_{(220)}$  maximum values versus strain hardening index  $n_l$  (taken in the longitudinal direction respect to the rolling one) for the HSLA and IF steels, in two deformation intervals (9-13% and 12-18%).

also for  $n_l$  (9-13%). This is not surprising as the fluctuations of "n" (the "double n" behavior) occur, in both steel types, close to the  $G^2_{(220)}$  maxima values (section "Dislocation Densities and Deformation"), which turn out to be in an intermediate position between the two strain ranges taken for "n".

Figures 6a and Figure 6b reveal that, although with different slopes, a linear correlation also exists for the behavior of residual stresses versus the strain hardening index; this confirms the validity of the assumption concerning a correlation between residual stresses and dislocations.

### 4.3 Processing Issues

The correlation found between residual stress and strain hardening index allows to assume a possible mechanism for

work hardening in the presence of misoriented grains. Since work hardening may be interpreted as the difficulty for plastic flow to occur, it can be regarded as arising from two main contributions:

- (a) non-plastic behavior of misoriented grains resulting in a storage of elastic strain energy, which can be considered as "tension strain hardening", and
- (b) dislocation movements within the grains, which can be considered as "atomic strain hardening".

Data plotted in Figures 2 and 3 can then be interpreted by assuming that the above two terms can have a different weight depending on the extent of plastic strain. In the materials under

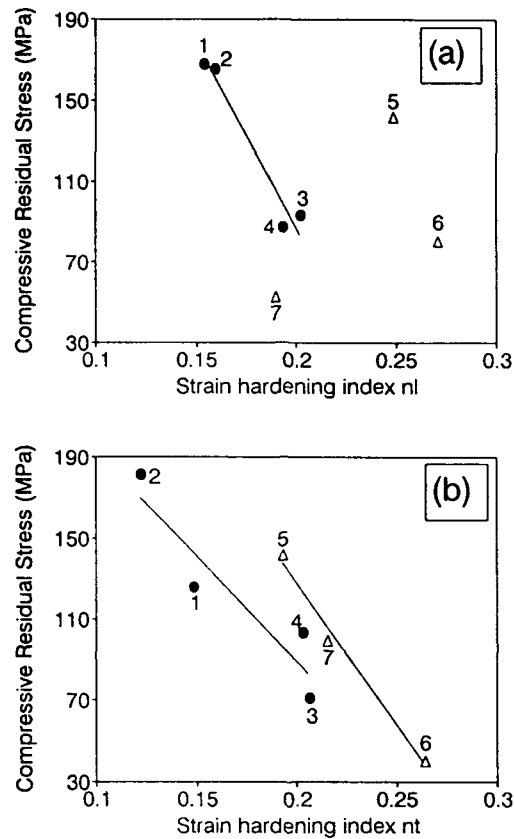


Figure 6: Residual stresses (average) vs. (a)  $n_1$  and (b)  $n_t$  for strain interval 9-13%. Linear best fits for HSLA steels are shown (continuous lines). Symbols are as in Figure 5.

examination, for strain range 10-15%, stretch forming may lead to a structure with a lower "tension strain hardening" contribution. It is therefore advisable to draw the most critical profiles in these strain ranges, due to the greater stability of the resulting structure.

The existence of residual stresses in stretch formed steel sheets may lead to several consequences:

- (a) crack sensitivity due to the residual stress which may add to any applied stress (for example during loading or joining); and

- (b) shape instability for the relaxation of elastic residual strains due to aging (for example as a consequence of low temperature annealing during coating/ processing).

The opportunity to balance the level of deformation for the forming operation with the resulting residual stress is therefore established. In the present work (HSLA and IF steels) a range of deformation (10-15%) is found to give minimized residual stresses (Figures 2 and 3) which, can be evaluated non-destructively. On the other hand, the actual residual stress in the stretch formed sheet should be taken into account in designing the maximum allowable stress due to in-service loading.

## 5.0 Conclusions

The dislocation densities represented by  $G^2_{(220)}$ , calculated from the  $\alpha$ -Fe (220) line profile, show a discontinuous behavior, with maximum values at intermediate strain ranges.

The  $G^2_{(220)}$  maximum values seem to have a macroscopic correspondence in the so-called "double n" behavior revealed in steels for the same strain range and correlated with the dislocation distribution (31, 33, 37, 38).

The significance of  $G^2_{(220)}$  maximum values for the macroscopic behavior in steels is also confirmed by its correlation

with the longitudinal strain hardening index, in good agreement with the physical significance of "n" (37).

The behavior of residual stresses on increasing strains seem to be the consequence of a progressive dislocation redistribution. In particular, the reduction (or even the inversion) in slope shown by residual stresses in the 9-13% strain range has been correlated with the formation of dislocation tangles prior to the reorganization of dislocations into cellular substructures.

The above conclusions lead to the assumption that the residual stresses values correspond to the reduction or inversion in slope (Figures 2 and 3) and that the maximum  $G^2_{(220)}$  values (Figure 4) are related to the same phenomenon of dislocations redistribution. Such values are, therefore, associated with a particular microscopic behavior of the material which brings about a reduction in both  $G^2_{(220)}$  values and residual stresses slope.

A significant evidence of the microscopic similarity of the two quantities was supplied by their parallel behavior when plotted as a function of "n" which is a particularly indicative parameter of the dislocation behavior (35).

Under a technological point of view, the correlation between the residual stresses and the strain hardening index values allows an evaluation of the behavior of cold rolled steel sheets, regarding stretch

formability, in terms of "tension strain hardening" and "atomic strain hardening". A deformation interval 10-15% is found to minimize the residual stresses in HSLA and IF steel sheets.

### 6.0 References

1. Dieter, G.E., *Mechanical Metallurgy*, McGraw-Hill, N.Y., (1986).
2. Keeler, S.P., and W.A. Backofen, *ASM Transactions Quarterly*, Vol.56, p.25, (1963).
3. Noyan, I.C., and J.B. Cohen, *Residual Stress*, Springer Verlag, N.Y., p.122, (1987).
4. Cohen, J.B., and R.L. Rothman, *Advances in X-Ray Analysis*, Vol.12, p.208, (1969).
5. Morrison, W.B., and R.L. Miller, *Ultrafine-Grain Metals*, Syracuse University Press, Syracuse, N.Y., p.348, (1970).
6. Goodman, S.R., P.R. Mould, and J.C. Siple, *Technology of Continuously Annealed Cold Rolled Sheet Steel*, ed. R. Pradhan, TMS, Warrendale, PA, p.167, (1985).
7. Bergström, Y., and B. Aronsson, *Metallurgical Transactions*, Vol.3, p.1951, (1972).
8. Taylor, A., *X-Ray Metallography*, John Wiley & Sons, N.Y., chap.15, (1961).
9. Cullity, B.D., *Elements of X-Ray Diffraction*, Addison-Wesley Publishing Company Inc., Reading, MA, 2nd edition, chap.16, p.454, (1978).
10. Zantopolus, H., and C.F. Jaczak, *Advances in X-Ray Analysis*, Vol.14, p.360, (1971).
11. Cohen, J.B., H. Dölle, and M.R. James, *Accuracy in Powder Diffraction*, NBS Special Publication, No.567, Washington, p.453, (1980).
12. Dölle, H., and J.B. Cohen, *Metallurgical Transactions*, Vol.11A, p.159, (1980).
13. Dölle, H., *Journal of Applied Crystallography*, Vol.12, p.489, (1979).
14. Macherauch, E., and K.H. Kloos, *Residual Stresses in Science and Technology*, eds. E. Macherauch and V. Hauk, DGS Informations-gesellschaft Verlag, Germany, p.22, (1987).
15. Pines, B.Y., and A.F. Sirenko, *Soviet Physics Crystallography*, Vol.7, p.15, (1962).

*Stretch Formability in HSLA and IF Steels*

16. Savitzky, A., and M.J.F. Golay, *Analytical Chemistry*, Vol.13, p.162, (1964).
17. Klug, H.P., and L.E. Alexander, *X-Ray Diffraction Procedure*, John Wiley & Sons, N.Y., 2nd edition, chap.9, (1974).
18. Delhez, D.R., T.H. De Keijser, and E.J. Mittemeijer, *Accuracy in Powder Diffraction*, NBS Special Publication No.567, Washington, p.213, (1980).
19. Gazzara, C.P., J.J. Stiglich, F.P. Meyer, and A.M. Hansen, *Advances in X-Ray Analysis*, Vol.12, p.257, (1969).
20. Morosin, B., *High Pressure Explosive Processing of Ceramics*, eds. R.A. Graham and A.B. Sawaoka, Trans Tech Publications, Switzerland, p.283, (1987).
21. Williamson, G.K., and R. Smallman, *Philosophical Magazine*, Vol.1, p.34, (1956).
22. Kalish, D., and G.B. Le Fevre, *Metallurgical Transactions*, Vol.6A, p.1319, (1975).
23. McQueen, H.J., *Metallurgical Transactions*, Vol.8A, p.807, (1977).
24. Langford, G., and M. Cohen, *Metallurgical Transactions*, Vol.6A, p.901, (1975).
25. Klein, M.J., and R.A. Huggins, *Acta Metallurgica*, Vol.10, p.55, (1962).
26. Brimhall, J.L., and R.A. Huggins, *Transactions TMS AIME*, No.233, p.1076, (1965).
27. Thompson, A.W., *Metallurgical Transactions*, Vol.8A, p.833, (1977).
28. Embury, J.D., A.S. Keh and R.M. Fisher, *Transactions TMS AIME*, No. 236, p.1252, (1966).
29. Boyd, J.D., and J.D. Embury, *Electron Microscopy and Structure of Materials*, ed. G. Thomas, University of California Press, Berkeley (USA), p.48, (1972).
30. Holt, D.L., *Journal of Applied Physics*, Vol.41, p.319, (1970).
31. Keh, A.S., and S. Weissman, *Electron Microscopy and Structure of Materials*, ed. G. Thomas, University of California Press, Berkeley, p.231, (1972).
32. Langford, G., P.K. Nagata, R.J. Sober, and W.C. Leslie, *Metallurgical Transactions*, Vol.3, p.1843, (1972).
33. Morrison, W.B., *Metallurgical Transactions*, Vol.2, p.331, (1971).
34. Morrison, W.B., *Transactions ASM*, Vol.59, p.824, (1966).

35. Bergström, Y., and B. Aronsson, *Metallurgical Transactions*, Vol.1, p.1029, (1970).  
Newkirk and J.H. Wernick, *Interscience-Wiley*, N.Y., p.23, (1962).
36. Bergström, Y., *Proceedings of 8th Biennial Congress IDDRG on Sheet Metal Forming and Formability*, Gothenburg, Sweden, IDDRG Gothenburg, p.43, (September, 1974).  
39. Kolb, K., and E. Macherauch, *Archive Eisenhuettenwesen*, Vol.36, p.9, (1965).
37. Christ, B.W., and G.V. Smith, *Acta Metallurgica*, Vol.15, p.809, (1967).  
40. Bollenrath, F., V. Hauk, and A. Weidman, *Archive Eisenhuettenwesen*, Vol.38, p.793, (1967).
38. Li, J.C.M., *Direct Observation of Imperfections in Crystals*, eds. J.B. Hu, H., *Metallurgical Transactions*, Vol.6A, p.94, (1975).

## **Self-Propagating High Temperature Synthesis (SHS) of Intermetallic Compounds Titanium and Nickel Aluminides**

**H. Y. Sohn and X. Wang**

Department of Metallurgical Engineering  
University of Utah, Salt Lake City, Utah 84112

### **Abstract**

The self-propagating high temperature synthesis (SHS) of titanium and nickel aluminides was investigated. Effect of experimental variables on SHS temperature, burning rate, product composition, and microhardness are discussed. The densities of the products are 70–80% of theoretical values and the microhardness of Ni<sub>3</sub>Al produced is similar to that of low carbon steel. It is also shown that the SHS process is affected by the reactant ratios. Small reactant particle size and moderate preheating result in high SHS rates. A small addition of boron and a small change in the green density do not significantly affect the process.

### **1.0 Introduction**

Self-propagating high temperature synthesis (SHS) utilizes the exothermic heat of a solid-solid or fluid-solid reaction to propagate rapid reaction through the entire body of reactants (1–3) and has been applied to the preparation of a large number of materials such as intermetallic compounds and ceramics (4–6). During SHS processing, very high temperatures can be reached without applying much external energy, once the reactant is ignited. The SHS process has several advantages over conventional processes

such as the simplicity of process, low energy consumption, short reaction time and low processing cost (4). Thus, SHS has recently received considerable attention as an alternative to conventional ceramic or powder metallurgy techniques (7–9). Intermetallic compounds nickel and titanium aluminides have been recognized as potentially useful structural materials (10–20). In this work, the SHS method was used to produce intermetallic compounds nickel and titanium aluminides, with an emphasis on Ni<sub>3</sub>Al and TiAl<sub>3</sub>. The effects of various

experimental variables on SHS results were determined.

## 2.0 Experimental Method

Aluminum, titanium and nickel powders were purchased from Alfa Morton Thiokol, Micron Metals and EM Science, respectively. The nominal size of Al powder was 45  $\mu\text{m}$ . Different particle sizes of Ti and Ni were obtained by screening the powders under argon atmosphere. The initial mixture ratio was selected stoichiometrically according to the intermetallic phases in the Ti-Al and Ni-Al systems (21, 22). They are  $\text{TiAl}_3$ ,  $\text{TiAl}_2$ ,  $\text{TiAl}$  and  $\text{Ti}_3\text{Al}$  for the Ti-Al system and  $\text{NiAl}_3$ ,  $\text{Ni}_2\text{Al}_3$ ,  $\text{NiAl}$  and  $\text{Ni}_3\text{Al}$  for the Ni-Al system. Metal powders of predetermined particle sizes and mass ratios were thoroughly mixed in a roller and pelletized using a double action press. The size of a green pellet was usually 6 cm in length and 1.5 cm square in cross section. These pellets usually had an apparent density of 60% of the full density.

Several small holes were drilled into about one fourth of the width on one side of the sample to accommodate thermocouples which were connected to a PC. A silicon carbide heating element was used as the ignition heat source. Samples were placed 1 to 2 mm below the heating element inside a glove box under an argon atmosphere.

When power was turned on, the top layer of the sample started reacting as

the sample reached the ignition temperature. Electrical power was disconnected as soon as the reaction started. As the sample was ignited and SHS was in progress, time and temperatures of the sample at different positions were recorded. The burning process was recorded by a camcorder. The self-propagating reaction displayed a bright front advancing through the sample from top to bottom.

## 3.0 Results and Discussion

### 3.1 Thermal Behavior of Ti-Al and Ni-Al SHS Reactions

The temperature-time responses for the formation of  $\text{Ni}_3\text{Al}$  and  $\text{TiAl}_3$  are shown in Figures 1a and 1b. Curve 1 in Figure 1a was taken from a position near the ignition heat source and shows a typical ignition curve. The sample temperature increased slowly until there was a sharp increase. The temperature at the point of the sharp increase was taken as the ignition temperature. Curves 2 and 3 in Figure 1a and the curves in Figure 1b were taken from the middle and lower parts of the pellet. There was little heating until the reaction front reached these points. It can be seen that in the middle portion of the pellet, the temperature-time curves remain unchanged with position. These curves were converted to temperature-distance curves with the aid of the burning rate. Most combination of the reactants showed steady planar combustion as characterized by these temperature

*Self-Propagating High Temperature Synthesis (SHS) of Intermetallic Compounds*

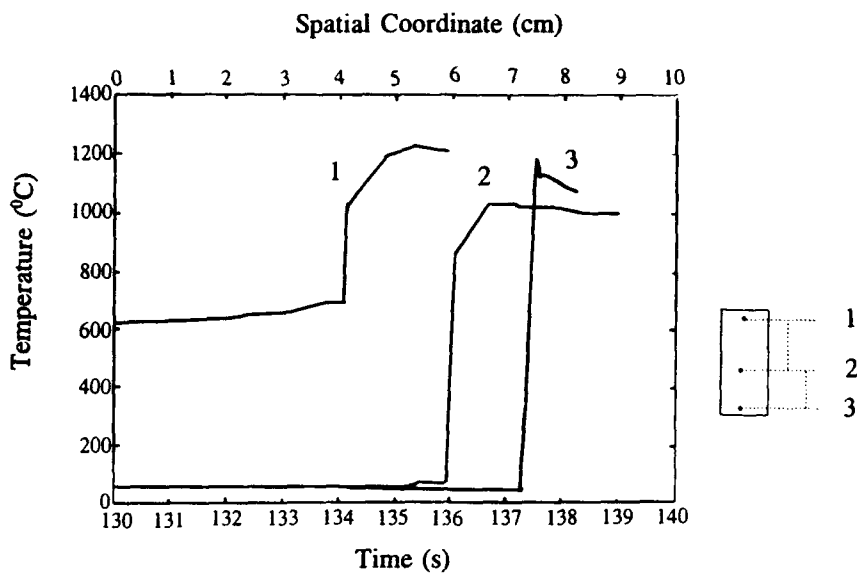


Figure 1a: SHS temperature profile for  $\text{Ni}_3\text{Al}$ .

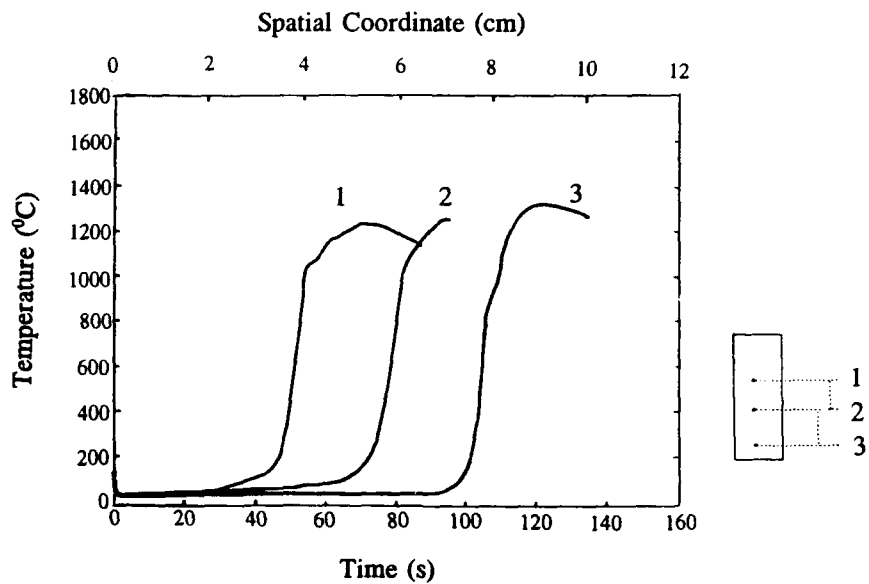


Figure 1b: SHS temperature profile for  $\text{TiAl}_3$ .

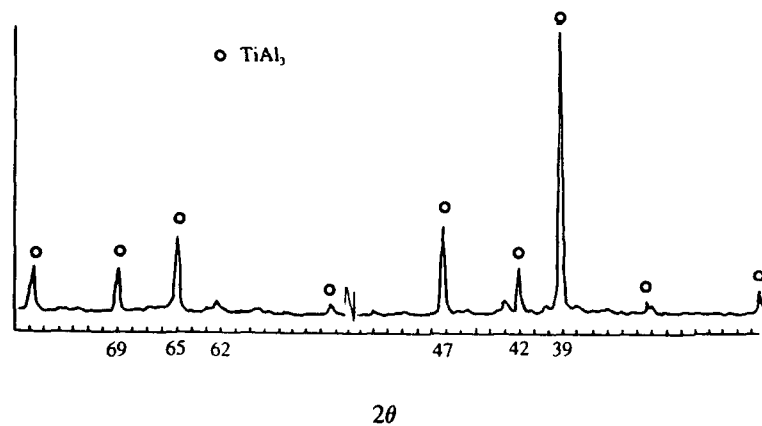


Figure 2a: X-ray diffraction patterns of SHS product  $\text{TiAl}_3$ .

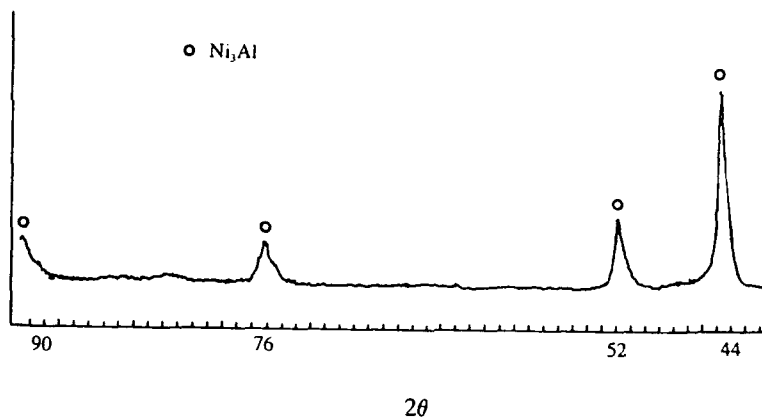


Figure 2b: X-ray diffraction patterns of SHS product  $\text{Ni}_3\text{Al}$ .

curves. Exceptions were the mixtures  $3\text{Ti}+\text{Al}$  and  $\text{Ti}+\text{Al}$ , which underwent spiral combustion.

### 3.2 XRD Analysis

Products of the SHS were analyzed by the X-ray diffraction method (XRD) to

determine the phases. The XRD data for the products from  $\text{Ti} + 3 \text{Al}$  and  $3 \text{Ni} + \text{Al}$  mixtures are shown in Figures 2a and 2b. The diffraction patterns show that the products are basically  $\text{TiAl}_3$  and  $\text{Ni}_3\text{Al}$ , respectively.

**Table 1. The Effect of Initial Mixing Ratio on Composition of SHS Products**

Initial Mixing Ratios	Major Phase in XRD Pattern	Other Compounds in XRD Pattern
3Ni+Al	Ni <sub>3</sub> Al	-
2Ni+3Al	Ni <sub>2</sub> Al <sub>3</sub>	Ni, Al
Ni+Al	NiAl	Ni, Al
Ni+3Al	NiAl <sub>3</sub>	Ni, Al
3Ti+Al	Ti <sub>3</sub> Al	TiAl <sub>3</sub> , TiAl <sub>2</sub> , Al
Ti+Al	TiAl	Ti <sub>3</sub> Al, TiAl <sub>3</sub> , Ti, Al
Ti+2Al	TiAl <sub>2</sub>	Ti, Al, TiAl <sub>3</sub>
Ti+3Al	TiAl <sub>3</sub>	-

The phases observed in other products are listed in Table 1. Major phases correspond to the initial mixing ratios, but samples other than Ni<sub>3</sub>Al and TiAl<sub>3</sub> show various amounts of other phases. These two compositions were selected to further investigate the effects of the initial variables on SHS.

### 3.3 Effect of Particle Size on SHS

Effect of aluminum particle size is not as significant as those of titanium and nickel particle sizes because the ignition temperature exceeds the melting point of aluminum, thus melting it. This liquid aluminum makes good contact with other reactant particles (23). Effect of particle size on the SHS reaction was studied for the formation of TiAl<sub>3</sub>. Several sizes of the titanium particles were selected by sieving, while the aluminum size was kept at the nominal size of 45 μm.

Figure 3 shows effect of particle size on the ignition temperature and maximum reaction temperature. Larger particles required higher ignition temperatures and resulted in lower maximum reaction temperatures, because of somewhat increased heat loss due to a lower burning rate and in some cases due to incomplete reaction.

Figure 4 shows that burning rate decreased significantly with increasing particle size. This is because larger particles react more slowly which in turn increases heat loss and lowers the reaction temperature.

Particle size also affected the volume change between the reactant pellet and the product. Figure 5 shows that titanium particle size between 76 to 106 μm mixed with aluminum particles of ~45 μm size gave the maximum volume shrinkage. This is likely caused by a better infiltration of liquid aluminum in

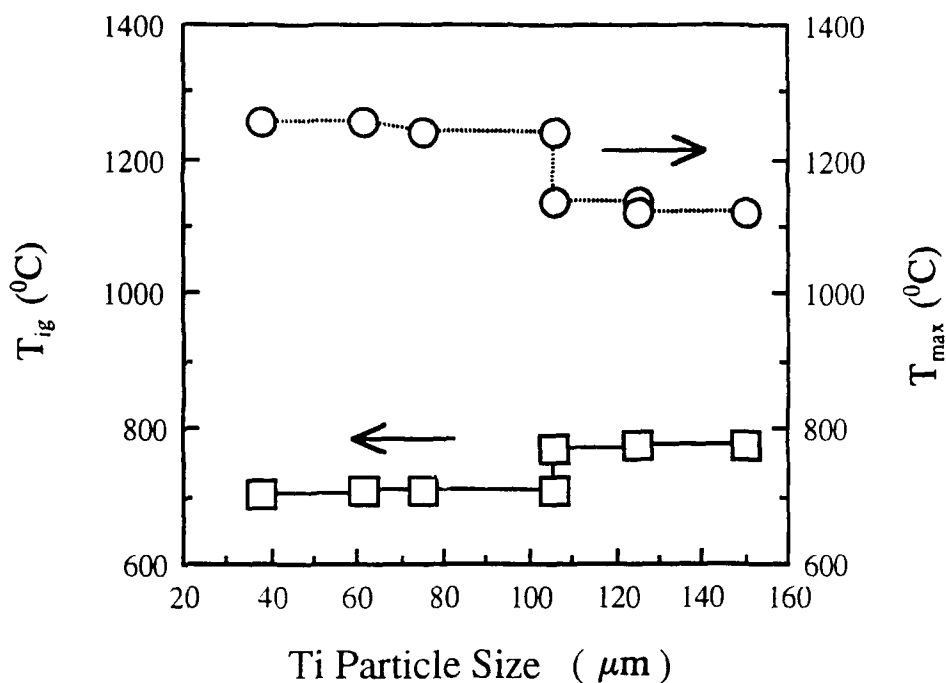


Figure 3: Effect of particle size on  $T_{ig}$  and  $T_{max}$  for SHS of  $TiAl_3$ .

this size range. In this figure, % densification is defined as

$$\% \text{ densification} = \frac{P_g - P_p}{P_g} \times 100,$$

where  $P_g$  is green porosity and  $P_p$  is product porosity.

#### 3.4 Effect of Preheating on SHS

Effect of preheating was investigated by preheating the sample uniformly to a predetermined temperature and holding it for five minutes before ignition. The systems of  $Ti + 3Al$  and  $3Ni + Al$  were selected with nominal particle sizes of

aluminum, titanium and nickel of 45 μm, 45 μm and 10 μm, respectively.

Preheating contributed to an increase in the shrinkage of the pellet during the reaction as shown in Figure 6. Higher the preheating temperature, greater was the shrinkage. Preheating increases the temperature that the sample experiences throughout the reaction, which promotes uniform melting and spreading of molten aluminum, thus reducing the voidage. Such a product with a lower voidage has a greater hardness as shown in Figure 7.

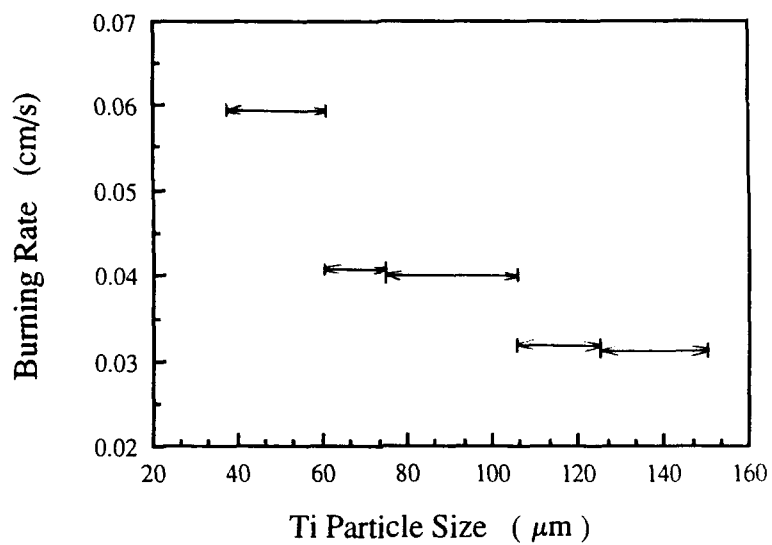


Figure 4: Effect of particle size on burning rate for SHS of  $TiAl_3$ .

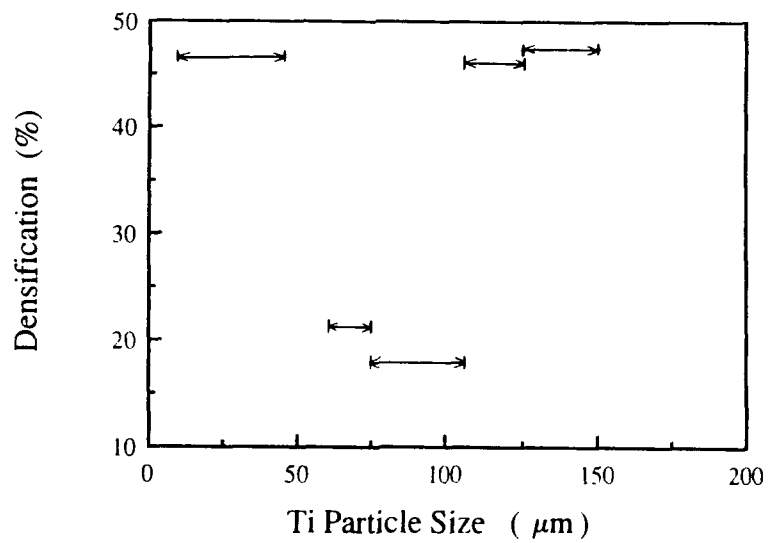


Figure 5: Effect of particle size on densification in SHS of  $TiAl_3$ .

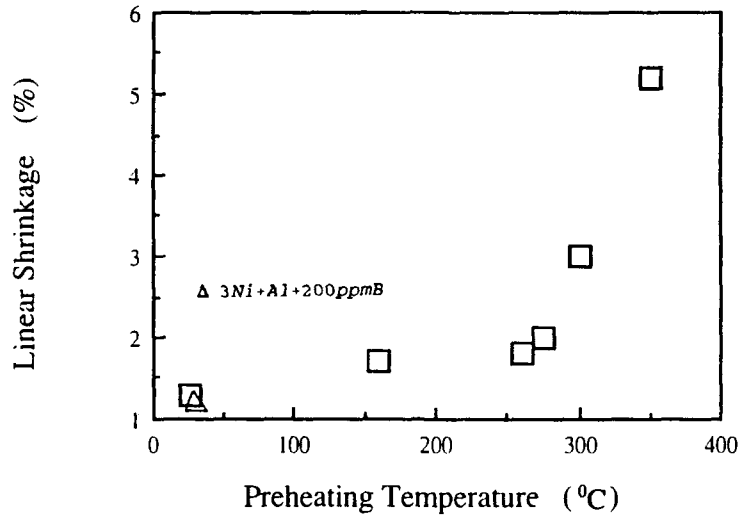


Figure 6: Effect of preheating on linear shrinkage in SHS of Ni<sub>3</sub>Al.

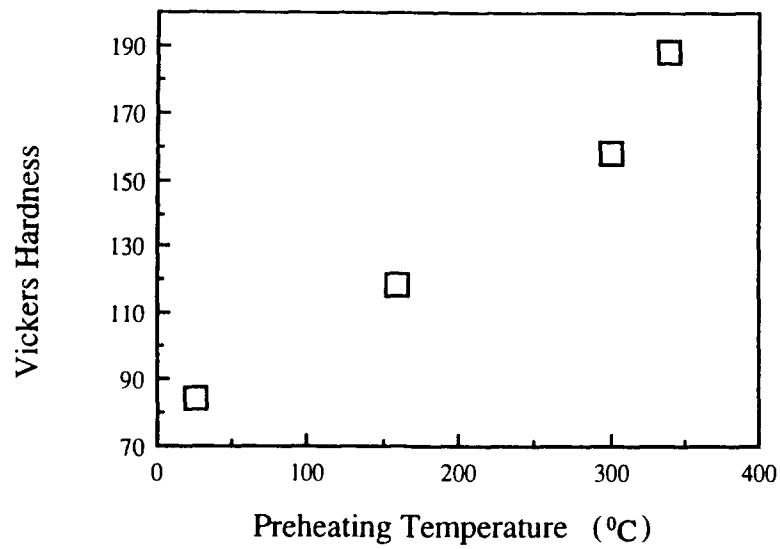


Figure 7: Effect of preheating on microhardness of SHS product Ni<sub>3</sub>Al.

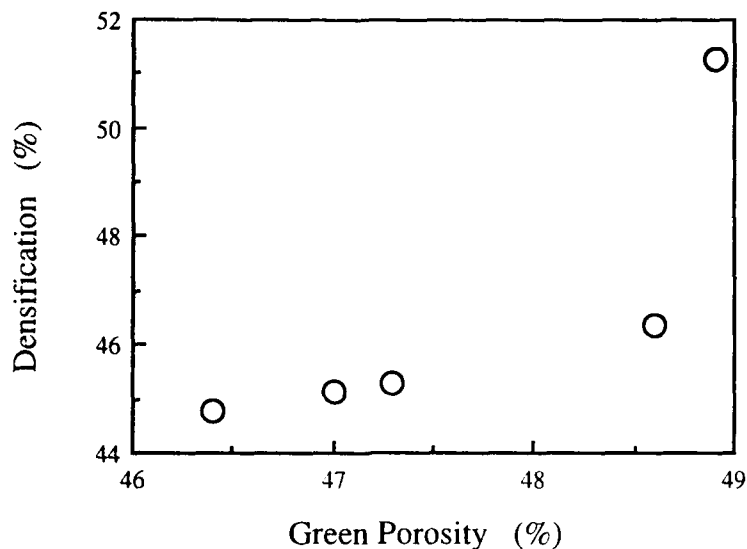


Figure 8: Effect of porosity on densification in SHS of  $TiAl_3$ .

In Figure 7, each value represents an average of thirty points with a load of 25 gms.

### 3.5 Effect of Green Density on the SHS

Pellet porosity was calculated based on apparent pellet density and true densities of the reactant metals (24). Densification of the pellet increased with increasing green porosity, as shown in Figure 8 for the case of  $TiAl_3$ . A loose compact of powders of 3 Ni + Al, obtained by simple pouring, did not sustain reaction and in the case of a similarly obtained mixture of Ti + 3Al, the burning rate was half the value for a sample with 50% theoretical density. This was caused by poor contact between reactant

particles. Variation in the density between 50 and 55% did not significantly affect the burning rate and the maximum temperature.

### 3.6 Effects of Atomic Ratio on the SHS

Each of the Ti-Al and the Ni-Al systems has four basic intermetallic phases. As discussed earlier, the composition of the products was determined by the initial mixture ratio of the reactant metals.

The maximum temperature was also affected by the initial mixture ratio, as shown in Figure 9. Effect of aluminum content is consistent with the variation of the enthalpy of intermetallics formation with aluminum content.

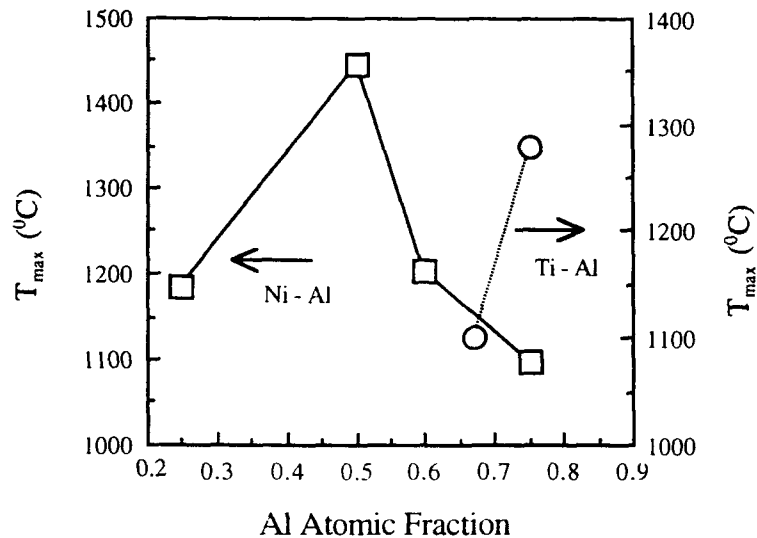


Figure 9: Effect of initial mixing ratio on reaction temperatures.

For the Ni-Al system, the heat of reaction has a maximum at Al atomic fraction of 0.5 (22). For the Ti-Al system, enthalpy data are available only in the Al atomic fraction range of 0.2 to 0.6 in which the heat of reaction increases monotonically with Al content. A mixture with a large exothermic heat of reaction was easily ignited and more completely reacted.

Microhardness of the nickel aluminides produced from pellets of 60% theoretical density was between that of cutting tool steel and low carbon steel, as shown in Figure 10. Boron dopant, which improves ductility did not affect microhardness (25, 26).

#### 4.0 Conclusions

SHS process can be used to produce titanium and nickel aluminides. Intermetallic phases with 70 to 80% of theoretical density were obtained without external pressure. Initial mixture ratios, particles sizes, and preheating temperatures are the major factors affecting the synthesis process. Mixtures of 3 Ni + Al and Ti + 3 Al yielded single intermetallic phases of Ni<sub>3</sub>Al and TiAl<sub>3</sub>, respectively. Other mixtures, 2 Ni + 3 Al, Ni + Al, Ni + 3 Al, 3 Ti + Al, Ti + Al, Ti + 2 Al, Ti + 3 Al, formed major phases corresponding to the initial mixing ratios, but they also contained small amounts of other phases. There exists an optimum particle size range of the higher melting reactant, which gives

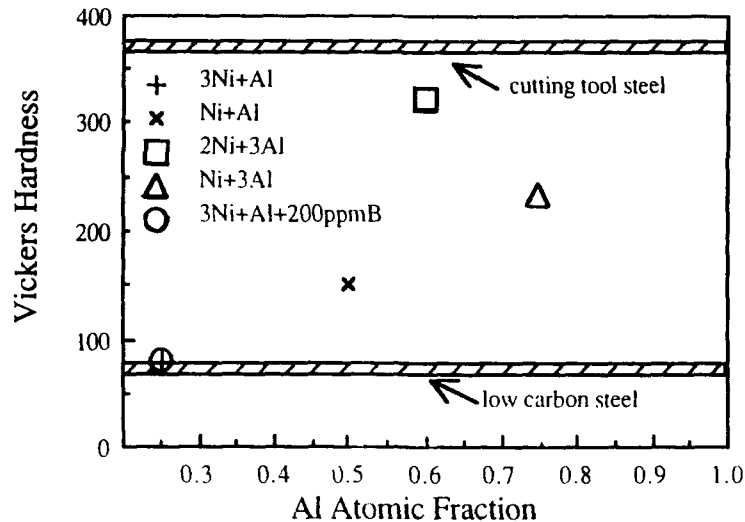


Figure 10: Effect of initial mixing ratio on microhardness of product nickel aluminides.

a maximum product density when reacted with fine aluminum powder (45  $\mu\text{m}$ ). For titanium, this range was determined to be 76 to 106  $\mu\text{m}$ . Preheating of the green pellet prior to ignition also improved the product density.

### 5.0 Acknowledgments

This work was supported in part by the state of Utah Mineral Leasing Fund, the University of Utah Research Committee Grant and the Department of the Interior's Mineral Institutes program under allotment grant numbers G1184149, G1194149, and G1104149.

### 6.0 References

1. Munir, Z., Synthesis of High Temperature Materials by Self-Propagating Combustion Methods, *Ceramic Bulletin*, Vol.67, No.2, pp.342-349 (1988).
2. Merzhanov, A. G. and I. P. Borovinskaya, A New Class of Combustion Process, *Combustion Science and Technology*, Vol.10, No.5/6, pp. 195-201 (1975).
3. Hlavacek, V., Combustion Synthesis: A Historical Perspective, *Ceramic Bulletin*, Vol.70, No.2, pp.240-243 (1991).
4. Frankhouser, W. I., K. W. Brendley, M. C. Kieszek, and S. T. Sullivan,

- Gasless Combustion Synthesis of Refractory Compounds, Noyes Publications, Park Ridge, New Jersey, pp.5-60, 106-117 (1985).
5. Merzhanov, A. G., and I. P. Borovinskaya, Self-Propagating High Temperature Synthesis of Refractory Inorganic Compounds, Doklady of the Academy of Sciences of the U.S.S.R., Earth Sciences Sections, Vol.204, No.2, pp.366-338 (1972).
  6. Fleischer, R. L. and A. I. Taub, Selecting High Temperature Structural Intermetallic Compound: The Materials Science Approach, Journal of Metals, Vol.41, No.9, pp.8-11 (1989).
  7. Philpot, K. A., Z. A. Munir, and J. B. Holt, An Investigation of the Synthesis of Nickel Aluminides through Gasless Combustion, Journal of Materials Science, Vol.22, pp.159-169 (1987).
  8. Wang, L. L., Z. A. Munir, and J. B. Holt, The Combustion Synthesis of Copper Aluminides, Metallurgical Transaction B, Vol.21B, pp.567-577 (1990).
  9. Merzhanov, A. G., Self-propagating High Temperature Synthesis: Twenty Years of Search and Findings, Paper presented at 41st Pacific Coast Regional Meeting of American Ceramic Society, San Francisco, California (October 23-26, 1988).
  10. Alman, D. E. and N. S. Stoloff, Processing and Properties of Intermetallic Matrix Composites, Symposium Proceedings of High Temperature Ordered Intermetallic Alloys IV, held Nov. 27-30, 1990, Boston, Massachusetts, ed. L. A. Johnson, D. P. Pope, and J. O. Stiegler, Materials Research Society, Vol.213, pp.989-1000 (1991).
  11. German, R. M., A. Bose, and N. S. Stoloff, Powder Processing of High Temperature Aluminides, Symposium Proceedings of High Temperature Ordered Intermetallic Alloys III, held Nov.29 - Dec.1, 1988, ed. C. T. Liu, A. I. Taub, N. S. Stoloff, and C. C. Koch, Materials Research Society, Vol.133, pp.403-414 (1989).
  12. Destefani, J. D., Advances in Intermetallics, Advanced Materials and Processes, Vol.135, No.2, pp.37-40 (1989).
  13. Bose, A., B. Moore, R. M. German, and N. S. Stoloff, Elemental Powder Approach to  $Ni_3Al$  Matrix Composites, Journal of Metals, Vol.40, No.9, pp.14-17 (1988).
  14. Fleischer, R. H., Review, High-Strength, High temperature Intermetallic Compounds, Journal of Materials Science, Vol.22, No.7, pp. 2281-2288 (1987).
  15. Taub, A. I. and R. L. Fleischer, Intermetallic Compounds for High

*Self-Propagating High Temperature Synthesis (SHS) of Intermetallic Compounds*

- Temperature Structural Use, Science, Vol.243, No.4891, pp.616-621 (1989).
16. Froes, F. H., Structural Intermetallics, Journal of Metals, Vol.41, No.9, pp.6-7 (1989).
  17. Upadhy, K., Ceramic and Composites for Rocket Engines and Space Structure Materials, Journal of Metals, Vol.44, No.5, pp.15-17 (1992).
  18. Sikka, V. K., Commercialization of Nickel Aluminides, Symposium Proceedings, High Temperature Aluminides and Intermetallics, held October 1-5, 1989, Indianapolis, Indiana, ed. S. H. Whang, C. T. Liu, D. P. Pope, and J. D. Stiegler, The Minerals, Metals and Materials Society, Warrendale, Pennsylvania, pp.505-519 (1990).
  19. Larsen, J. M., K. A. William, S. J. Balsone, and M. A. Stuck, Titanium Aluminides for Aerospace Applications, Symposium Proceedings of High Temperature Aluminides and Intermetallics, held October 1-5, 1989, Indianapolis, Indiana, ed. S. H. Whang, C. T. Liu, D. P. Pope, and J. D. Stiegler, The Minerals, Metals and Materials Society, Warrendale, Pennsylvania, pp.521-530 (1990).
  20. Schulson, E. M., Structure, Properties and Potential Applications of Intermetallic Compounds Produced from Powders, The International Journal of Powder Metallurgy, Vol.23, No.1, pp.25-32 (1987).
  21. Murray, J. L., Phase Diagrams of Binary Titanium Alloys, ASM International, Metals Park, Ohio, pp.10-14 (1987).
  22. Hultgren, R., Selected Values of Thermodynamics Properties of Binary Alloys, American Society for Metals, p.193 (1973).
  23. German, R. M., Supersolidus Liquid Phase Sintering, Part I: Process Review, The International Journal of Powder Metallurgy, Vol.26, No.1, pp.23-26 (1990).
  24. German, R. M., Liquid Phase Sintering, pp.10-22, Plenum, New York (1985).
  25. Liu, C. T. and J. A. Stiegler, Ductile Ordered Intermetallic Alloy, Science, Vol.226, No.4675, pp.636-642 (1984).
  26. Nieh, T. G., C. M. McNally, and J. Wadsworth, Superplasticity in Intermetallic Alloys and Ceramics, Journal of Metals, Vol.41, No.9, pp.31-35 (1989).

## **Processing, Microstructures, and Properties of Cr-Cr<sub>3</sub>Si, Nb-Nb<sub>3</sub>Si, and V-V<sub>3</sub>Si Eutectics**

**B.P. Bewlay, J.A. Sutliff, M.R. Jackson, and K.M. Chang**

General Electric Company  
Corporate Research and Development Center  
P.O. Box 8, Schenectady, New York 12301

### **Abstract**

The present paper examines the potential of refractory metal-A15 silicide composites as structural materials for high temperature applications. Three eutectic systems are considered, Cr-Cr<sub>3</sub>Si, Nb-Nb<sub>3</sub>Si, and V-V<sub>3</sub>Si, since they all have melting points above 1700°C and densities lower than Ni-based superalloys. Eutectic compositions were selected because directional solidification of eutectics can be used to generate aligned composite microstructures. The present paper describes processing, microstructures and properties of directionally solidified Cr-Cr<sub>3</sub>Si, Nb-Nb<sub>3</sub>Si, and V-V<sub>3</sub>Si. Based on microstructural and chemical analyses, some phase diagram modifications are suggested. The orientation relationships between the refractory metal and A15-silicide phases were characterized using transmission electron microscopy. In the Cr-Cr<sub>3</sub>Si eutectic a strong orientation relationship was observed; there was excellent lattice matching of the (110) in Cr and (210) in Cr<sub>3</sub>Si. Room temperature and elevated temperature microhardness and fracture toughness are also reported; these indicate good strength retention in Nb-Nb<sub>3</sub>Si at elevated temperatures.

### **1.0 Introduction**

Intermetallics such as Cr<sub>3</sub>Si, Nb<sub>3</sub>Si, Nb<sub>5</sub>Si<sub>3</sub> and V<sub>3</sub>Si, have recently been investigated as potential structural materials for high temperature applications, because of their high melting points (> 1700°C) and high

temperature strengths (1-12). Unfortunately, limited low temperature toughness has hindered the development of these intermetallics. A common approach which has been proposed to increase the toughness of intermetallics is to generate a two phase microstructure of the intermetallic phase toughened

with a ductile phase. In pursuit of this goal, it was recognized that eutectics can play an important role (13). The present paper discusses the potential of directionally solidified two phase alloys in the Cr-Si, Nb-Si and V-Si systems, as high temperature structural materials. Three eutectics, Cr-Cr<sub>3</sub>Si, Nb-Nb<sub>3</sub>Si, and V-V<sub>3</sub>Si were selected because of their high melting points (> 1700°C) and low densities (< 7.5 Mg/m<sup>3</sup>).

In the present study, a strong emphasis was placed on the preparation of aligned composite structures based on high temperature eutectics. For this purpose a Czochralski crystal growth technique with cold crucible melting was developed for directional solidification of intermetallic composites (7). Crystal growth of intermetallics, such as Cr<sub>3</sub>Si, has also been performed previously by zone melting (14). However, cold crucible Czochralski crystal growth offers certain advantages over zone melting, such as alloy preparation, and compositional control. Other processes which have been used for preparation of two phase refractory metal-silicon alloys include arc melting, mechanical alloying and hot pressing of elemental powders, but alignment of the individual phases in the composite is not possible using these techniques.

Phase equilibria are very important in the context of eutectic solidification, because they control the volume fractions of the respective phases and therefore the mechanical properties. Unfortunately, there are inaccuracies in

the phase diagrams with regard to these compositions. In the Cr-Si system, the eutectic between b.c.c. Cr and A15 Cr<sub>3</sub>Si is at 15% Si (15, 16). All compositions in the present paper are in atomic %. The recommended phase diagram compositions of Cr and Cr<sub>3</sub>Si at the eutectic temperature are 9.5% Si and 22.5% respectively. However, there is a lack of agreement in previous literature regarding these compositions (17-20). Si concentrations in Cr at the eutectic temperature as low as 2.3% (13), and as high as 10.7% (18) have been reported. In addition, Cr<sub>3</sub>Si compositions between 15 and 24% Si have been published. The volume fraction of Cr<sub>3</sub>Si in the eutectic, as predicted using the phase diagram compositions at the eutectic temperature is 0.42 (15).

The Nb-Si system possesses a eutectic between Nb and Nb<sub>3</sub>Si at 18.7% Si and 1882°C. The preferred phase diagram solid solubility of Si in the terminal Nb at the eutectic temperature is ~4.8% Si, but recent data suggest it is less than this, since a Si solubility limit of 1.3% at 1700°C was measured (2). Nb<sub>3</sub>Si is a line compound and decomposes into Nb and Nb<sub>5</sub>Si<sub>3</sub> at 1720°C (16). The calculated volume fraction of Nb<sub>3</sub>Si at the eutectic temperature is 0.68.

Smith (21) has reviewed the V-Si phase diagram data reported previously (22-24). In the preferred phase diagram, the eutectic between V and V<sub>3</sub>Si is at 13% Si and 1870°C (21). The Si concentrations of V and V<sub>3</sub>Si at the eutectic temperature are 7% and 19%

respectively. The volume fraction of V<sub>3</sub>Si predicted by the recommended phase diagram is 0.50 at the eutectic temperature (16).

Although, there is some mechanical property data available on Cr-Si alloys (3, 9, 11), there is almost no data available on aligned Cr-Cr<sub>3</sub>Si eutectics, principally due to difficulties associated with preparing the same. Newkirk and Sago reported tensile and yield strengths of a range of arc-melted binary Cr-Si alloys, including a maximum yield strength of 360 MPa at 1200°C in an 18.6% Si alloy (9). The temperature dependence of the microhardness of Cr-Si alloys close to the Cr<sub>3</sub>Si composition has been reported by Fleischer for temperatures up to 1200°C (11).

Single phase and two phase Nb-Si alloys have been studied recently by Mendiratta et al. for high temperature applications, because they have good strength retention at temperatures above 1000°C (1, 2). In addition, the use of hot extrusion in increasing the room temperature fracture toughness of Nb-Si alloys has been a major advance (1). However, the poor oxidation resistance remains a challenging problem in these alloys. In the case of Cr-Si alloys, Aitken (25) and Mazdiyasi and Miracle (13) have reported promising oxidation resistance of Cr-Cr<sub>3</sub>Si eutectic at 800°C and 1200°C. Anton and Shah (1) and McKee and Fleischer (26) also reported that stoichiometric Cr<sub>3</sub>Si has similar oxidation resistance to MoSi<sub>2</sub> below 1200°C.

The present paper describes directional solidification of Cr-Cr<sub>3</sub>Si, Nb-Nb<sub>3</sub>Si and V-V<sub>3</sub>Si eutectic alloys using cold crucible Czochralski crystal growth. Phase morphologies, chemistries and volume fractions of the directionally solidified eutectics are described together with fracture toughness and microhardness measurements for temperatures up to 1250°C. The orientation relationships between the refractory metal and A15-silicide phases, as determined using transmission electron microscopy, are also discussed.

## 2.0 Experimental

Eutectic alloys were directionally solidified using Czochralski cold crucible crystal growth, as shown schematically in Figure 1, in order to generate aligned two-phase microstructures (7). Samples were prepared from 99.99% pure Cr, Nb, or V together with 99.999% pure Si using induction melting in a segmented, water-cooled copper crucible, of the form shown in Figure 2 (27). A 50 kW, 345 kHz induction generator was used to melt the alloy and levitate it from the hearth of the water-cooled copper crucible during directional solidification. The alloys were triple melted in order to improve their homogeneity. Cold crucible induction melting had two major benefits for the high temperature alloys used in the present study. First, the levitation reduced physical contact between the melt and the crucible, and thereby minimized contamination of the

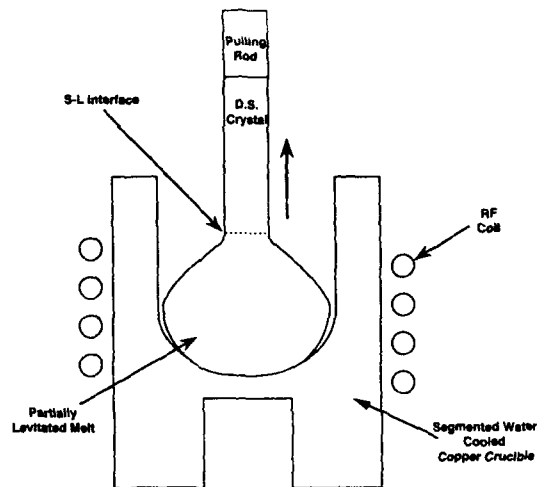


Figure 1: Schematic diagram showing Czochevski crystal growth from a melt which is levitated within a segmented water-cooled copper crucible.

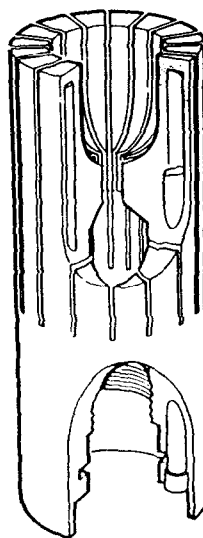


Figure 2: Schematic diagram showing the water-cooled copper crucible and its internal cooling channels (27).

melt by the crucible. Second, the stirring induced by the electromagnetic field homogenized the melt.

Directional solidification of eutectic alloys was initiated by lowering into the melt a previously prepared seed crystal of the same alloy, and then withdrawing the seed at a controlled rate. The seed was rotated at 20 rpm to improve the thermal symmetry during directional solidification. Alloy melting and directional solidification were performed under an atmosphere of ultra high purity argon. A constant growth rate was employed during each experiment, and the furnace power was adjusted to maintain as stable a melt temperature distribution as possible. Particular attention was given to control of the withdrawal rate, temperature gradient in the crystal and the temperature distribution in the melt. In order to improve control of these last two parameters, an infra-red imaging camera was used to generate a thermal map of both the melt pool and the sample during directional solidification. The thermal mapping system was based on a General Electric charge-injection device TN 2500 series television camera. Samples up to ~10 mm diameter and ~100 mm long were grown.

Longitudinal and transverse sections of the directionally solidified eutectics were prepared for optical microscopy and scanning electron microscopy (SEM) using standard techniques. Electron microprobe analysis was also employed to determine the composition of

individual phases. Samples were prepared for transmission electron microscopy (TEM) by mechanically grinding both transverse and longitudinal slices to foils of a thickness of ~100  $\mu\text{m}$ . The foils were then thinned to electron transparency and examined using a Philips EM430 transmission electron microscope (TEM) operated at 300 kV.

Microhardness testing was performed in order to determine the variation of strength with temperature, and to estimate the brittle to ductile transition temperature by the presence or absence of cracks at the indentation. Measurements were performed under vacuum as a function of temperature at 200°C increments for temperatures from 25°C up to 1250°C. Microhardness indentations were generated using a Vickers diamond indenter with a 500 gms load, on a longitudinal section in a direction perpendicular to the growth direction. Typically an indentation covered at least, and usually more than, 8 rods/lamellae.

Since the directionally solidified samples did not have a large enough diameter to provide full size bend bars, as recommended by ASTM E399, fracture toughness measurements were performed on sub-size bend bars with a rectangular cross section of 3.8 x 5.1 mm. Bend bars were machined so that the growth direction of the samples was parallel to the longitudinal axis of the bend bar. The bars were tested by four point bending using a strain rate of  $8.5 \times 10^{-3}$   $\text{mms}^{-1}$ .

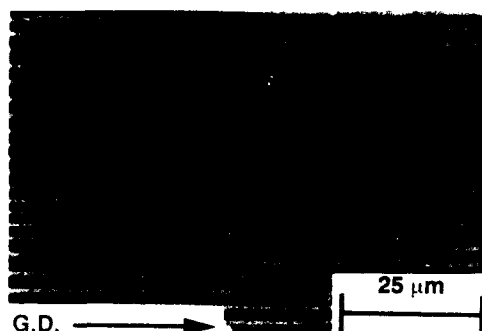


Figure 3a: Scanning electron micrographs (positive BSE) of longitudinal sections of Cr-15% Si directionally solidified at rates of  $8.3 \times 10^{-2} \text{ mms}^{-1}$

### 3.0 Results and Discussion

#### 3.1 Cr-Cr<sub>3</sub>Si

Figure 3a shows a scanning electron micrograph taken using a back scattered electron detector (BSE), of the longitudinal section of a lamellar Cr-15% Si eutectic sample directionally solidified at  $8.3 \times 10^{-2} \text{ mms}^{-1}$ . The eutectic had an interlamellar spacing of  $2.2 \pm 0.3 \text{ mm}$ . The structure contained several eutectic grains with their longitudinal grain boundaries parallel to the growth direction. There was occasional alteration of the lamellar spacing along the length of sample, as indicated by the occurrence of lamellar terminations. A volume fraction of Cr<sub>3</sub>Si of  $0.62 \pm 0.1$  was measured using image analysis, as shown in Table 1. No primary Cr-rich or Cr<sub>3</sub>Si dendrites were observed.

Figure 3b shows a micrograph of the longitudinal section of a Cr-15% Si

sample grown at a faster rate of  $1.6 \times 10^{-1} \text{ mms}^{-1}$ . The microstructure was less regular than that in Figure 3a, and there is a tendency towards the formation of cells. Some of the lamellae were bent away from the longitudinal axis of the sample at the cell boundaries. This is a relatively common feature of eutectics which have grown with a cellular solid-liquid interface.

A bright field transmission electron micrograph of the longitudinal section of a directionally solidified Cr-Cr<sub>3</sub>Si is shown in Figure 4. A high density of dislocations was observed in the Cr-rich phase and very few dislocations were observed in the Cr<sub>3</sub>Si. Two crystallographic orientation relationships were measured between the Cr-rich and Cr<sub>3</sub>Si phases by electron diffraction. The habit plane was always  $(110)_{\text{Cr}}$  and the growth direction of the eutectic was always parallel to  $(001)_{\text{Cr}_3\text{Si}}$ . These two orientation relationships are described by:

**Table 1. Measured Eutectic Compositions, Phase Volume Fractions, and Morphologies**

Refractory Metal	Silicide	Eutectic Point		Eutectic Density (Mg/m <sup>3</sup> )	Second Phase morphology	A15 Volume Fraction
		Temp. (°C)	Composition (at.%Si)			
V	V <sub>3</sub> Si	1870	12.6 ± 0.2	5.9	Rod	0.48 ± 0.02
Nb	Nb <sub>3</sub> Si	1883	18.2 ± 0.2	7.4	Rod/Plate	0.64 ± 0.02
Cr	Cr <sub>3</sub> Si	1705	15.0 ± 0.2	6.7	Lamellar	0.62 ± 0.02

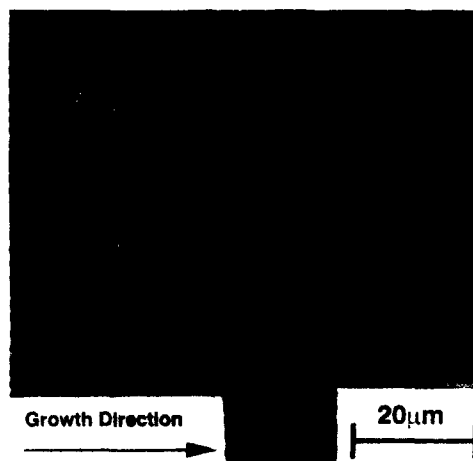


Figure 3b: Scanning electron micrographs (positive BSE) of longitudinal sections of Cr-15% Si directionally solidified at rates of  $1.6 \times 10^{-1} \text{ mms}^{-1}$ .

(111)<sub>Cr</sub> || (001)<sub>Cr<sub>3</sub>Si</sub> and  
 (110)<sub>Cr</sub> || (210)<sub>Cr<sub>3</sub>Si</sub>  
 (001)<sub>Cr</sub> || (001)<sub>Cr<sub>3</sub>Si</sub> and  
 (110)<sub>Cr</sub> || (210)<sub>Cr<sub>3</sub>Si</sub>

Both of these orientation relationships were observed in many eutectic grains examined in several TEM foils. The second of the above orientation

relationships was observed more frequently than the first.

The measured volume fraction of Cr<sub>3</sub>Si in the eutectic was  $0.62 \pm 0.1$ , and was larger than the predicted volume fraction of 0.42. The volume fraction of Cr<sub>3</sub>Si in the 15% Si eutectic was calculated from the phase diagram by taking the compositions of the Cr-rich and Cr<sub>3</sub>Si

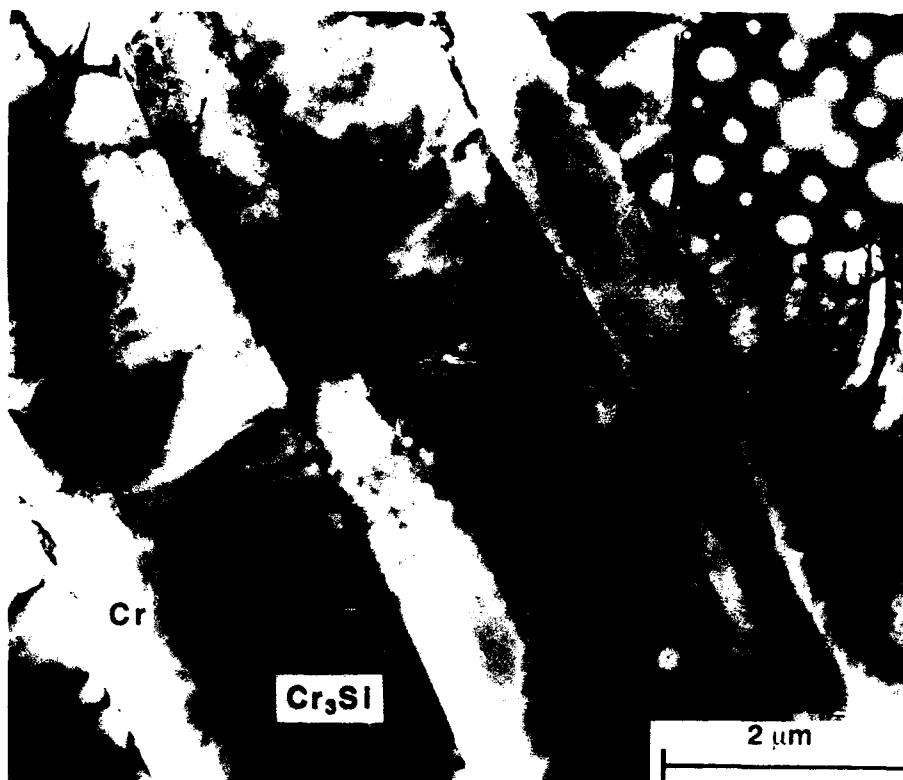


Figure 4: Bright field transmission electron micrograph of the transverse section of a Cr-Cr<sub>3</sub>Si eutectic directionally solidified at  $8.3 \times 10^{-2} \text{ mms}^{-1}$ , together with an electron diffraction pattern showing the first of the orientation relationships that were observed.

phases at the eutectic temperature as 9.5 and 22.5% Si respectively, and assuming there was no further modification of the composition of the phases during post-solidification cooling. Densities of  $6.91 \text{ Mg/m}^3$  and  $6.47 \text{ Mg/m}^3$  for the Cr-rich and Cr<sub>3</sub>Si phases were calculated using lattice parameters of 0.2880 nm for the Cr-rich phase (19, 28), and 0.4560 nm for Cr<sub>3</sub>Si (19). There are three possible

reasons for the difference in the measured and predicted volume fractions. First, there may be inaccuracies in the preferred phase diagram (15) of the eutectic composition, the composition of the Cr-rich phase, the composition of Cr<sub>3</sub>Si, or any combination of the above. Second, the actual densities of the two phases at the eutectic temperature may be different

from the calculated densities. Third, the Cr-rich and Cr<sub>3</sub>Si phase compositions may change from the compositions at the eutectic temperature during post solidification cooling. No dendrites were observed in the Cr-15% Si composition, which supports the previous data that this composition is on, or close to, the eutectic composition, and eliminates this as a possible cause for the volume fraction difference. Non-equilibrium effects associated with directional solidification are unlikely to account for the size of the volume fraction difference that was observed.

In order to examine the phase composition issues in more detail, Cr-15%Si samples were heat treated at 1200, 1400, and 1600°C. Microprobe data indicated that both the Cr-rich and Cr<sub>3</sub>Si phases contained less Si than suggested by the phase diagram (29). This is the most likely explanation for there being a larger volume fraction of Cr<sub>3</sub>Si than Cr. For example, in the sample heat treated at 1600°C the measured composition of the Cr-rich phase was 7.8% Si and that of Cr<sub>3</sub>Si was 20.8% Si. The phase diagram compositions of Cr and Cr<sub>3</sub>Si at the same temperature are 8.8% Si and 22.5% Si respectively. A volume fraction of Cr<sub>3</sub>Si of 0.56 was calculated for the measured compositions at 1600°C. This value is nearer the measured value of 0.62. The volume fraction of Cr<sub>3</sub>Si at 1600°C, based on the preferred phase diagram (15), is 0.45.

Interplanar distances in the Cr-rich and Cr<sub>3</sub>Si phases are shown in Table 2 for

low index planes. These were calculated using lattice parameters of 0.2880 nm for the Cr-rich phase (19, 28) and 0.4560 nm for Cr<sub>3</sub>Si (19). These data show that the (110) plane in Cr has almost exactly the same interplanar spacing as the (210) plane in Cr<sub>3</sub>Si; there is ~0.1% difference between the two. The interplanar spacings and diffraction data suggest that the orientation relationship between Cr and Cr<sub>3</sub>Si is controlled by lattice matching in the two eutectic phases. Since the total interfacial area of the lamellar eutectic is very large, lowering of the interfacial area by selection of a preferred orientation relationship makes a significant contribution to the thermodynamic stability of the lamellar eutectic. Table 2 also shows a close match between the inter-planar spacings of the (200) plane in Cr and the (310) plane in Cr<sub>3</sub>Si. However, these planes were not observed as the lamellar interface plane.

### 3.2 Nb-Nb<sub>3</sub>Si

A scanning electron micrograph (BSE) of the transverse section of a Nb-18.7% Si sample directionally solidified at  $8.3 \times 10^{-2} \text{ mms}^{-1}$  is shown in Figure 5. Faceted dendrites were observed within eutectic cells. EDAX indicated that the dendrites were Nb<sub>3</sub>Si. These primary Nb<sub>3</sub>Si dendrites had a width of  $20 \pm 4 \mu\text{m}$ , and the eutectic cell size was  $75 \pm 10 \mu\text{m}$ . This microstructure has been discussed in detail elsewhere (7). Although the preferred phase diagram composition of the Nb-Nb<sub>3</sub>Si eutectic is 18.7% Si (16), the microstructure

Table 2. Interplanar Distances(Å) in Cr, Cr<sub>3</sub>Si, V and V<sub>3</sub>Si

hkl	Cr	Cr <sub>3</sub> Si	V	V <sub>3</sub> Si
100	-	4.56	-	4.725
110	2.036	3.224	2.141	3.341
111	-	2.633	-	2.728
200	1.440	2.280	1.514	2.363
210	-	2.039	-	2.113
211	1.176	1.862	1.236	1.929
220	1.018	1.612	1.071	1.671
221	0.960	1.520	1.009	1.575
300	0.960	1.520	1.009	1.575
310	0.911	1.442	0.958	1.494
311	0.868	1.375	0.913	1.425
321	0.770	1.219	0.809	1.263
322	0.699	1.106	0.735	1.146

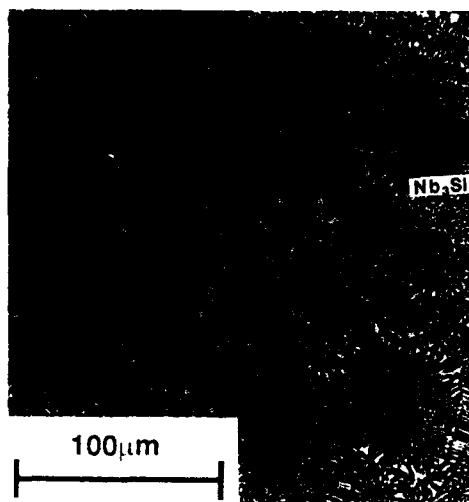


Figure 5: Scanning electron micrograph (positive BSE) of the transverse section of Nb-18.7% Si directionally solidified at  $8.3 \times 10^{-2} \text{ mms}^{-1}$ , showing faceted Nb<sub>3</sub>Si dendrites.

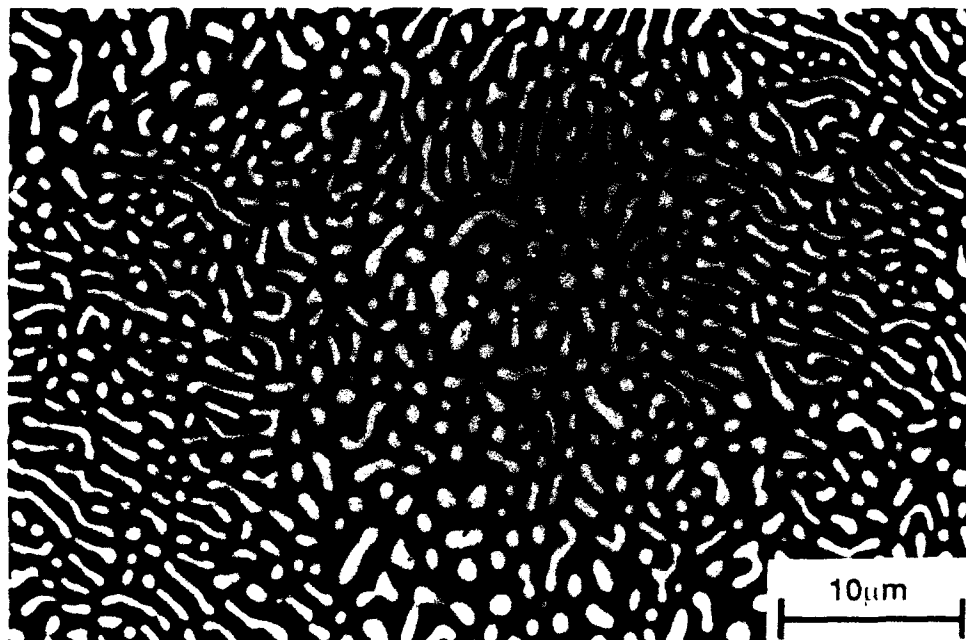
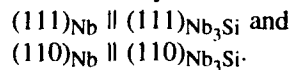


Figure 6: Scanning electron micrograph (positive BSE) of the transverse section of Nb-18.2% Si directionally solidified at  $8.3 \times 10^{-2} \text{ mms}^{-1}$ .

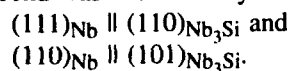
observed in these samples indicated that the 18.7% Si composition was hyper-eutectic. Therefore samples with reduced Si concentrations were prepared to determine the eutectic composition.

The microstructure of a transverse section of an Nb-18.2% Si sample directionally solidified at  $8.3 \times 10^{-2} \text{ mms}^{-1}$  is shown in Figure 6. The microstructure contained Nb rods and plates in a Nb<sub>3</sub>Si matrix. These rods and plates were aligned with the growth direction to within 10°. There were no Nb-rich or Nb<sub>3</sub>Si dendrites in this composition, which indicated that the

eutectic point was 18.2% Si, assuming limited compositional range for two phase solidification. The total volume fraction of Nb rods and plates was measured using image analysis as  $0.36 \pm 0.02$ , as shown in Table 1. The rods and plates had a width of  $1.2 \pm 0.2 \mu\text{m}$ . There was no evidence of eutectoid decomposition of the Nb<sub>3</sub>Si phase in the as-solidified samples. Cockeram et al. observed two orientation relationships between the Nb and Nb<sub>3</sub>Si in these directionally solidified samples (5). The first was described by



The second was described by



The microstructure of Nb-Nb<sub>3</sub>Si was very sensitive to eutectic growth conditions and alloy composition. The correct eutectic composition and growth rate were required for formation of an aligned Nb-Nb<sub>3</sub>Si eutectic microstructure. If a fast growth rate, such as 0.25 mms<sup>-1</sup> was used, eutectic cells were formed and there was also a tendency towards banding along the length of the sample. If a slow growth rate, such as 8 x 10<sup>-3</sup> mms<sup>-1</sup> was used, some break up of the Nb rods occurred, as shown in Figure 7.

The volume fraction of Nb in the Nb-Nb<sub>3</sub>Si eutectic for the 18.2% Si composition was calculated as 0.32 and the measured volume fraction of Nb was 0.36 ± 0.02. The volume fraction was calculated from the recommended phase diagram assuming that the composition of the Nb-rich and Nb<sub>3</sub>Si phases were 4.8 and 25.1% Si respectively. Densities were calculated from lattice parameter measurements assuming that Nb<sub>3</sub>Si has an A15 structure (16); there is some uncertainty regarding the crystal structure of Nb<sub>3</sub>Si at the eutectic temperature. There is only a small difference between the predicted and observed volume fractions of Nb; this may be due to a smaller Si concentration in Nb at the eutectic temperature than indicated by the phase diagram. Preliminary analysis of the phase compositions by electron microprobe

analysis indicated that the Si concentration of the Nb in the directionally solidified Nb-Nb<sub>3</sub>Si eutectic was 2%.

### 3.3 V-V<sub>3</sub>Si

Figure 8 shows a scanning electron micrograph of the transverse section of a V-V<sub>3</sub>Si sample, with a composition of V-12.6%Si, directionally solidified at 8.3 x 10<sup>-2</sup> mms<sup>-1</sup>. Negative polarity BSE showed the V<sub>3</sub>Si as the light phase, consisting of rods and plates, in a V-rich matrix. The rod diameter/plate width was 1.8 ± 0.2 μm. There was a suggestion in some areas of the microstructure that the V<sub>3</sub>Si rods had a hexagonal cross-section, but this was not a dominant feature. Micrographs of longitudinal sections showed that the aspect ratio of the rods was generally greater than 20 and sometimes as high as several hundred. The volume fraction of the V-rich phase was measured using image analysis as 0.52 ± 0.02, as shown in Table 1.

Samples of V-13% Si which were directionally solidified over a range of growth rates between 3.3 x 10<sup>-2</sup> and 8.3 x 10<sup>-2</sup> mms<sup>-1</sup> all contained a small volume fraction of V<sub>3</sub>Si dendrites, as identified using EDAX. Unlike the faceted Nb<sub>3</sub>Si dendrites, V<sub>3</sub>Si dendrites had a regular dendrite morphology. In order to determine the eutectic composition, several V-Si samples with compositions between 11.0 and 13.3 Si were prepared. The eutectic point of V-V<sub>3</sub>Si was measured as 12.6 ± 0.1% Si, using metallography, EDAX and wet

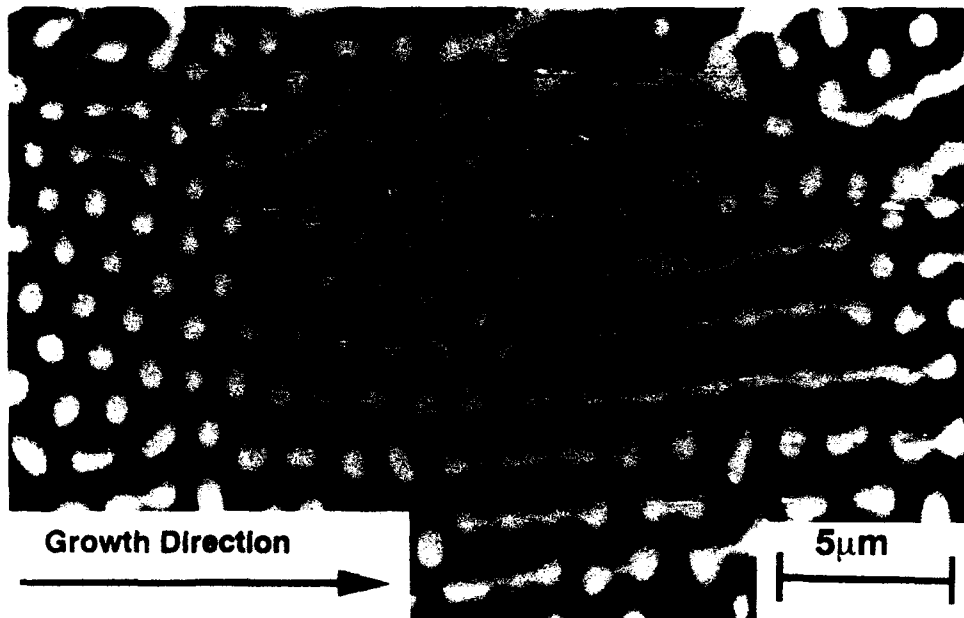


Figure 7: Scanning electron micrograph (positive BSE) of a longitudinal section of Nb-18.2% Si directionally solidified at a slower growth rate of  $8.3 \times 10^{-3} \text{ mms}^{-1}$ , showing break up of the Nb rods.

chemical analysis (inductively coupled plasma emission spectroscopy).

A transmission electron micrograph of the transverse section of the V-V<sub>3</sub>Si eutectic is shown in Figure 9. This micrograph was from a region where there was a slightly higher density of plates rather than rods. The plate-shaped phases were V<sub>3</sub>Si and the matrix was V. There was a high density of dislocations, or possibly twins, in the V-rich matrix. An interesting feature of this microstructure was that cracks which originated in V<sub>3</sub>Si were blunted in the V-rich phase. The crystallographic

orientation relationship observed by electron diffraction using TEM was that the (111)<sub>V</sub> was parallel to the (001)<sub>V<sub>3</sub>Si</sub> which was parallel to the growth direction of the sample. The (210)<sub>V<sub>3</sub>Si</sub> was close to (110)<sub>V</sub> but there was  $\sim 4^\circ$  difference between the two. Table 2 shows interplanar distances in the V-rich and V<sub>3</sub>Si phases for low index planes, calculated using lattice parameters of 0.3028 nm and 0.4725 nm respectively (21). Unlike the case of the Cr-Cr<sub>3</sub>Si eutectic, there is not so good matching of the interplanar spacings between V and V<sub>3</sub>Si. The planes with closest matching are the (110)<sub>V</sub> and (210)<sub>V<sub>3</sub>Si</sub>

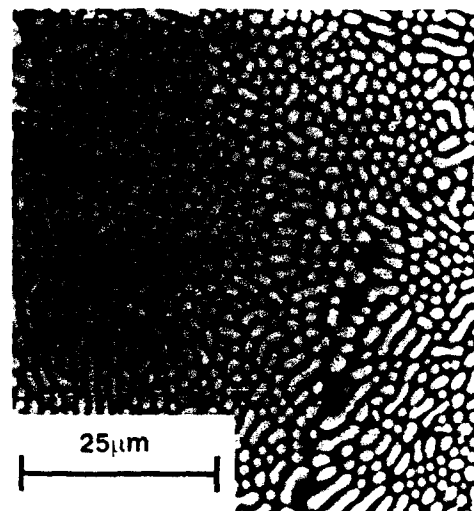


Figure 8: Scanning electron micrograph (negative BSE) of the transverse of V-V<sub>3</sub>Si directionally solidified at  $8.3 \times 10^{-2} \text{ mms}^{-1}$ .

planes, which have interplanar spacings of 0.2141 and 0.2113 nm respectively.

In the directionally solidified sample, the V-rich phase was the matrix with a volume fraction of 0.48 of V<sub>3</sub>Si rods. This was very close to the volume fraction of 0.5 calculated from the phase diagram. The small difference could be due to the fact that the eutectic concentration was slightly lower in Si than indicated by the recommended phase diagram. Microprobe data indicated that the Si concentrations of the V-rich and V<sub>3</sub>Si phases in the eutectic were  $4.5 \pm 0.2$  and  $20.1 \pm 0.2$  respectively. It is interesting that the V<sub>3</sub>Si existed as rods rather than lamellae, particularly as the volume fraction of rods of 0.48 was substantially greater than the theoretical limit of 0.32 (30) for

equal interfacial free energies per unit area in the lamellar and rod structures. There are two possible reasons for the V-V<sub>3</sub>Si eutectic having a rod/plate structure rather than a lamellar structure. First, the growth rates investigated ( $3.3$  to  $8.3 \times 10^{-2} \text{ mms}^{-1}$ ) may not have been favorable for growth of lamellae. Second, the average interfacial free energy per unit area may be unfavorable for a lamellar structure. Poor lattice matching at the interface, as discussed above, would be a cause of the same.

### 3.3 Microhardness and Fracture Toughness Measurements

Figure 10 shows the variation of microhardness with temperature for the three eutectics. The room temperature hardnesses of Cr-Cr<sub>3</sub>Si and Nb-Nb<sub>3</sub>Si



Figure 9: Bright field transmission electron micrograph of the transverse section of V-V<sub>3</sub>Si directionally solidified at 8.3 x 10<sup>-2</sup> mms<sup>-1</sup>.

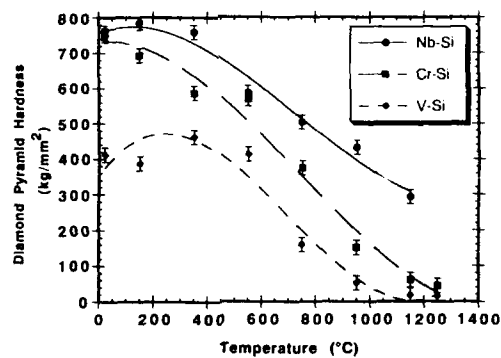


Figure 10: The variation of microhardness of Cr-Cr<sub>3</sub>Si, Nb<sub>3</sub>Si, V-V<sub>3</sub>Si, with temperature.

**Table 3. Fracture Toughness and Microhardness Crack Measurements for Cr-Cr<sub>3</sub>Si, Nb-Nb<sub>3</sub>Si, and V-V<sub>3</sub>Si Eutectics**

Eutectic	Temperature (°C)	K <sub>Q</sub> (MPa√m)	Temperature at which no cracks were detected (°C)
Nb-Nb <sub>3</sub> Si	20	6.0	-
V-V <sub>3</sub> Si	20	6.8	-
Cr-Cr <sub>3</sub> Si	20	7.3	550
Nb-Nb <sub>3</sub> Si	400	5.8	750
V-V <sub>3</sub> Si	400	16.5	550

were nearly twice that of V-V<sub>3</sub>Si. There was a continuous reduction in microhardness of Cr-Cr<sub>3</sub>Si with increasing temperature, until the microhardness approached that of V-V<sub>3</sub>Si at 1250°C. Fleischer (11) also reported a substantial reduction in microhardness of arc-melted Cr-Cr<sub>3</sub>Si two phase alloys of compositions close to Cr<sub>3</sub>Si above 750°C. Nb-Nb<sub>3</sub>Si has the best strength retention at elevated temperatures of the three eutectics investigated, probably because it has a greater volume fraction of the stoichiometric A15 phase than either Cr-Cr<sub>3</sub>Si or V-V<sub>3</sub>Si. The lower melting temperatures and off-stoichiometric compositions of Cr<sub>3</sub>Si and V<sub>3</sub>Si may also be factors.

After the microhardness measurements had been performed, the indentations in the samples were examined for cracks. Table 3 shows the temperatures at which cracks were no longer detected. Table 3 also shows fracture toughness

measurements of the three silicide eutectics at 20°C, and of Nb-Nb<sub>3</sub>Si and V-V<sub>3</sub>Si alone at 400°C. At 400°C the fracture toughness of V-V<sub>3</sub>Si was significantly higher than that of Nb-Nb<sub>3</sub>Si. The greater fracture toughness may be due to the fact that in the V-V<sub>3</sub>Si eutectic there is a larger volume fraction of the V-rich phase which has a lower ductile-brittle transition temperature (DBTT) than the Nb rods in the Nb-Nb<sub>3</sub>Si eutectics. In addition, the continuous phase in the V-V<sub>3</sub>Si is the V, whereas the continuous phase in Nb-Nb<sub>3</sub>Si is the intermetallic. At 20°C the fracture toughness of all the directionally solidified eutectics was less than 10 MPa√m. Newkirk and Sago (9) measured the fracture toughness of arc-melted Cr-15.5% Si as 7 MPa√m, which is similar to the fracture toughness of Cr-15% Si measured in the present study.

Dislocations were observed in the Cr-rich phase but not the Cr<sub>3</sub>Si. The cause

of these dislocations is differential thermal contraction between the Cr-rich and Cr<sub>3</sub>Si phases during post-solidification cooling to room temperature. The coefficient of thermal expansion of Cr is larger than that of Cr<sub>3</sub>Si (31, 32), and as a result the Cr phase contracts more than the Cr<sub>3</sub>Si on post-solidification cooling. This introduces compressive stress in the Cr<sub>3</sub>Si and a tensile stress in Cr. The high dislocation density in Cr suggests that the induced tensile stress was sufficient to cause significant plastic deformation in the same. The same was also observed in the case of V-V<sub>3</sub>Si, but to a larger degree because there is a greater difference in the coefficients of thermal expansion of the individual phases (31, 32). In the case of the V-V<sub>3</sub>Si eutectic, the total expansion of V is 11% greater than that of V<sub>3</sub>Si between room temperature and 1100°C. Hence, in the directionally solidified sample, dislocations were observed in V, but not in V<sub>3</sub>Si. The presence of these mobile dislocations in Cr and V, and the compressive stress in the brittle Al<sub>5</sub>'s, may be exploited to improve the room temperature toughness of these composites.

The thermal expansion argument does require some further explanation in the case of the Cr-Cr<sub>3</sub>Si eutectic, because the coefficients of thermal expansion of Cr and Cr<sub>3</sub>Si are similar up to ~1030°C and are almost independent of temperature. However, above 1030°C the coefficient of thermal expansion of Cr increases with temperature, but that of Cr<sub>3</sub>Si

remains almost independent of temperature. Between room temperature and 1030°C there is only ~4% difference between the total expansions of Cr and Cr<sub>3</sub>Si; Cr<sub>3</sub>Si in fact expands slightly more than Cr. However, above 1030°C, the total thermal expansion of Cr increases faster than that of Cr<sub>3</sub>Si and this generates dislocations in Cr on post-solidification cooling.

#### 4.0 Conclusions

Directionally solidified Cr-Cr<sub>3</sub>Si had a regular lamellar structure with volume fraction of Cr<sub>3</sub>Si of  $0.62 \pm 0.02$ . The lamellar structure generated at a growth rate of  $8.3 \times 10^{-2}$  mms<sup>-1</sup> had an interlamellar spacing of  $2.2 \pm 0.3$  μm. At faster growth rates lamellae were still observed but some band formation occurred and the microstructures were generally less regular. Dendrites of Cr or Cr<sub>3</sub>Si were not observed in any of the Cr-Cr<sub>3</sub>Si samples. The measured volume fraction of Cr<sub>3</sub>Si was much greater than that predicted from the previously recommended phase diagram.

Microprobe analysis of heat treated samples suggested that this was because both the Cr and Cr<sub>3</sub>Si contained less Si than indicated by the phase diagram. The growth direction of the eutectic was parallel to the (001) in Cr<sub>3</sub>Si. The preferred lamellar interface plane was observed to be (110)<sub>Cr</sub> and (210)<sub>Cr<sub>3</sub>Si</sub>. Two crystallographic orientation relationships between the Cr and Cr<sub>3</sub>Si were observed, the predominant one

being that where the (001) in Cr was parallel to (001) Cr<sub>3</sub>Si. The preferred orientation relationship is stable because of close matching of two different sets of lattice planes.

The Nb-Nb<sub>3</sub>Si eutectic consisted of rods and plates of Nb in a Nb<sub>3</sub>Si matrix. Faceted Nb<sub>3</sub>Si dendrites were observed in the Nb-18.7% Si sample. Microstructural and chemical analyses indicated that the Nb-Nb<sub>3</sub>Si eutectic composition was Nb-18.2% Si. In directionally solidified samples of Nb-18.2% Si which were grown at  $8.3 \times 10^2$  mms<sup>-1</sup>, rods and plates of Nb aligned with the growth direction were observed, with a total Nb volume fraction of  $0.36 \pm 0.02$ . Microprobe data indicated that the Nb contained ~2% Si. The Nb-Nb<sub>3</sub>Si eutectic microstructure is very sensitive to growth conditions. At slow growth rates break up of the Nb rods was observed.

Directionally solidified V-V<sub>3</sub>Si eutectic consisted of V<sub>3</sub>Si rods and plates in a V matrix. The rod diameter/plate width was  $1.8 \pm 0.2$  μm when directionally solidified at  $8.3 \times 10^2$  mms<sup>-1</sup>. The measured volume fraction of V<sub>3</sub>Si was  $0.48 \pm 0.02$ , which was close to that predicted by the phase diagram. Faster growth rates than  $8 \times 10^2$  mms<sup>-1</sup> generated bands in the microstructure, and at very slow growth rates, such as  $8 \times 10^{-3}$  mms<sup>-1</sup>, almost complete spheroidization of the V<sub>3</sub>Si occurred. The (111)<sub>V</sub> was parallel to the (001)<sub>V<sub>3</sub>Si</sub> which was parallel to the growth direction of the sample. The (210)<sub>V<sub>3</sub>Si</sub>

was close to (110)<sub>V</sub> but there was ~4° difference between the two; there was not as good matching of the interplanar spacings between V and V<sub>3</sub>Si as there was between Cr and Cr<sub>3</sub>Si.

Of the three systems investigated, Nb-Nb<sub>3</sub>Si has the best strength retention at elevated temperatures, but it has very low room temperature toughness. V-V<sub>3</sub>Si is the toughest eutectic but it has inadequate strength at elevated temperature for it to be considered seriously as a high temperature structural material.

## 5.0 Acknowledgments

The authors would like to thank D.J. Dalpe for the directional solidification experiments, R. Casey for the SEM, and Lou Pelouso for the microprobe. We are also very grateful to Prof. H. A. Lipsitt, Wright State University, for his suggestions and comments. The authors are also grateful to Dr. T. B. Cox and Dr. A. I. Taub for their support during this study.

## 6.0 References

1. Mendiratta, M. G., J. J. Lewandowski and D. M. Dimiduk, Metallurgical Transactions, Vol.22A, pp.1573-1581, (1991).
2. Mendiratta, M. G., and D. M. Dimiduk, Scripta Metallurgica and

*Processing, Microstructures, and Properties of Cr-Cr<sub>3</sub>Si, Nb-Nb<sub>3</sub>Si, and V-V<sub>3</sub>Si Eutectics*

- Materiala, Vol.25, pp. 237-242, (1991).
3. Anton, D. L., and D. M. Shah, Development of Potential Intermetallic Compounds, US Air Force Report WRDC TR-90-4122, (1990).
  4. Cockeram, B., M. Saqib, R. Omlor, R. Srinivasan, L. E. Matson, and I. Weiss, Scripta Metallurgica and Materiala, Vol.25, pp.393-398, (1991).
  5. Cockeram, B., H. A. Lipsitt, R. Srinivasan and I. Weiss, Scripta Metallurgica and Materiala, Vol.25, pp. 2109-2114, (1991).
  6. Rigney, J. D., P. M. Singh and J. J. Lewandowski, Journal of Metals, Vol.44, No.8, pp.36-41, (1992).
  7. Chang, K. M., B. P. Bewlay, J. A. Sutliff and M. R. Jackson, Journal of Metals, Vol. 44 (6), p. 59-63, (1992).
  8. Bewlay, B. P., J. A. Sutliff, K. M. Chang and M. R. Jackson, in Processing and Fabrication of Advanced Materials for High Temperature Applications, ed. V. A. Ravi and T. S. Srivatsan, TMS, Warrendale, PA, pp.213-224, (1992).
  9. Newkirk, J. W., and J. A. Sago, Intermetallic Matrix Composites, Vol.194, ed. D. L. Anton, P. L. Martin, D. B. Miracle, and R. McMeeking, Materials Research Society, Pittsburgh, PA, pp.183-189, (1990).
  10. Nekkanti, R.M., and D.M. Dimiduk, Intermetallic Matrix Composites, Vol.194, ed. D. L. Anton, P. L. Martin, D.B. Miracle and R. McMeeking, Materials Research Society, Pittsburgh, PA, pp. 175-182, (1990).
  11. Fleischer, R. L., Intermetallic Matrix Composites, Vol.194, ed. D. L. Anton, P. L. Martin, D. B. Miracle and R. McMeeking, Materials Research Society, Pittsburgh, PA, pp. 249-256, (1990).
  12. Shah, D. M., D. L. Anton and C. W. Musson, in Intermetallic Matrix Composites, Vol.194, ed. D. L. Anton, P. L. Martin, D. B. Miracle and R. McMeeking, Materials Research Society, Pittsburgh, PA, pp. 333-340, (1990).
  13. Mazdiyasn, S., and D. B. Miracle, in Intermetallic Matrix Composites, Vol.194, ed. D. L. Anton, P. L. Martin, D. B. Miracle and R. McMeeking, Materials Research Society, Pittsburgh, PA, pp. 155-162, (1990).
  14. Chang, C.S., and D. P. Pope, High Temperature Ordered Intermetallic Alloys IV, Vol.213, ed. D. L. Anton, P. L. Martin, D. B. Miracle, and R. McMeeking, Materials

- Research Society, Pittsburgh, PA, pp.745-750, (1990).
15. Gokhale, A. B., and G. J. Abbaschian, *Bulletin of Alloy Phase Diagrams*, Vol.8, pp.474-484, (1987).
  16. Massalski, T.B., *Binary Alloy Phase Diagrams*, ASM Metals Park, Ohio (1991).
  17. Kieffer, R., F. Benesovsky, and H. Schroth, *Zeitschrift für Metallkunde*, Vol.44, pp. 437-442, (1953).
  18. Nowotny, H., H. Schroth, R. Kieffer, and F. Benesovsky, *Monatsh. Chem.*, Vol.84, pp.579-584, (1953).
  19. Chang, Y.A., *Transactions of AIME*, Vol.242, pp.1509-1515, (1968).
  20. Kocherzhinsky, Yu.A., *Thermal Analysis*, Proceedings of 3rd ICTA, Davos, 1, pp.549-559, (1971).
  21. Smith, J. F., *Bulletin of Alloy Phase Diagrams*, Vol.6, pp.266-271, (1985).
  22. Jorda, J. L., and J. Muller, *Journal of Less Common Metals*, Vol.84, pp.39-48, (1982).
  23. Kieffer, R., R. Benesovsky, and H. Schmid, *Zeitschrift für Metallkunde*, Vol.47, pp.247-253, (1956).
  24. Greiner, E. S., and H. Mason, *Journal of Applied Physics*, Vol.35, pp. 3058-3059, (1964).
  25. Aitken, E. A., *Intermetallic Compounds*, ed. by J. H. Westbrook, Krieger Publishing Co., Huntington, N.Y., 1977, p. 513.
  26. McKee, D. W., and R. L. Fleischer, in *High Temperature Ordered Intermetallic Alloys IV*, Vol.213, ed. L. A. Johnson, D. P. Pope and J. O. Stiegler, Materials Research Society, Pittsburgh, 1991, 969-974.
  27. Hukin, D. A., US Patent 3702368 (1972).
  28. Pyatovka, T. M., V. I. Suikov, A. K. Shtolts, V. L. Zagrayazhsky, and P. V. Geld, *Izv. Akad. Nauk SSSR Neorg. Materials*, Vol.7, No.10, pp.1755-1758, (1971).
  29. Sutliff, J. A., B. P. Bewlay and H.A. Lipsitt, submitted for publication in *Scripta Metallurgica and Materiala*, Feb. 1993.
  30. Hunt, J. D., and J. P. Chilton, *Journal of Institute of Metals*, Vol.91, pp.338-342, (1962).
  31. Touloukian, Y. S., R. K. Kirby, R. E. Taylor and P. D. Desai, *Thermal and Physical Properties of Matter*, Vol.12: *Thermal Expansion-Metallic Elements and Alloys*, Plenum Press, New York, 1969.
  32. Touloukian, Y. S., R. K. Kirby, R. E. Taylor, and T. Y. R. Lee,

*Processing, Microstructures, and Properties of Cr-Cr<sub>3</sub>Si, Nb-Nb<sub>3</sub>Si, and V-V<sub>3</sub>Si Eutectics*

---

Thermal and Physical Properties of Matter, Vol.13: Thermal Expansion - Nonmetallic Solids, Plenum Press, New York, 1969.

## **Magnesium Filtration with Ceramic Foam Filters and Subsequent Quantitative Microscopy of the Filters**

**P. Bakke**

Sintef Metallurgy, N-7034 Trondheim, Norway

**T.A. Engh**

The Norwegian Institute of Technology  
Division of Metallurgy, N-7034 Trondheim, Norway

**E. Bathen**

Microscan, Tonstadgrenda 23, N-7075 Tiller, Norway

**D. Øymo and**

Norsk Hydro A.S., Research Center, N-3901 Porsgrunn, Norway

**A. Nordmark**

Sintef Production Technology, N-7034 Trondheim, Norway

### **Abstract**

Magnesium alloy AZ91 melts have been filtered through ceramic foam filters in laboratory scale experiments. Inclusion contents in the melts were adjusted by adding fractions of return die cast metal. During the experiments metal flow and metal temperatures were logged. The results show that the transition from depth to cake filtration is quite pronounced. This indicates that depth filtration and cake filtration act in sequence. Some of the filters have been sliced in the flow direction and analyzed for oxide inclusions employing automatic image analysis. The results from the metallographic examinations indicated that the filtration efficiency of the ceramic foam filters was very good. However, the filter life might be considered unacceptable.

### **1.0 Introduction**

Most of the world's magnesium production is consumed in non-structural applications such as alloying in aluminum and desulphurizing of steels.

Over the years, however, magnesium based alloys have proven to be highly competitive materials for construction purposes and automotive applications, especially when weight is the critical parameter. In order to achieve high

corrosion resistance and improved mechanical properties, impurities which enter the metal during manufacturing and metal handling must be controlled. Recycling of magnesium scrap has hitherto been troublesome due to the high levels of inclusions and other contaminants.

According to investigations by Simensen and Oberländer the inclusions that we can expect to find in magnesium and magnesium alloys are (1):

- Iron-rich intermetallic particles,
- Magnesium oxides/nitrides as films, lumps and loosely connected agglomerates,
- Carbides, ( $Al_4C_3$ ,  $CaC_2$ ) and
- Chlorides.

In certain cases sulfide inclusions have also been discovered. In the molten metal, chlorides are present as liquid inclusions; the others as solids. No detailed specification on inclusion levels in magnesium exists. This is probably due to difficulties in measuring the inclusion content both with respect to sampling and metallographic analysis. There is no doubt, however, that inclusions may adversely affect the final metal products (2).

Inclusions and dissolved elements enter the magnesium melt in a number of ways and at various steps in the production route. This includes the smelting process, holding, alloying, metal transfer and casting. In scrap remelting surface oxides, lacquers, paints

and lubricants may generate extra contamination.

Besides settling in holding furnaces, the refining of inclusions in magnesium can broadly be classified into flux and fluxless methods. Flux is used as a protection against surface oxidation and burning as well as for refining. Flux refining, developed in pre-war Germany, has been a common method for removal of inclusions from magnesium alloy melts (3,4).

Fluxes normally consist of chlorides of the alkaline and alkaline-earth metals. As the flux melts, chlorine and hydrochloric acid fumes are liberated. Also, the flux containing sludges causes a disposal problem (5). All this has motivated the search for flux-free alternatives for protection as well as for refining. Today,  $SF_6$ -blends are used extensively as protective atmospheres for magnesium melts in cast houses (6).

Fluxless refining incorporating filtration has sporadically been tested in magnesium (5,7,8,9). A flux-free two-furnace refining system for magnesium has also been tried out successfully (10). Our conviction is that melt refining methods used extensively in other metals, such as aluminum, may be applicable to magnesium as well. The reason is that the physical properties of the melts and the inclusions are very much the same. The principles for inclusion removal are also very often independent of the metal to be refined (2). As a result, transfer of a well

established process from one metal to another may only involve material problems. In the case of filtration this means that we have to find a filter material that does not react with or dissolve in the molten magnesium.

Molten metal filtration very often puts two incompatible requirements on the industrial filter:

- i. Large volumes of metal should be filtered before the pressure drop over the filter becomes too large, and
- ii. The filter should remove virtually all inclusions. Therefore, filtration is often a matter of compromise between filter life and metal cleanliness.

In order to lower the content of detrimental particles prior to casting, filtration with ceramic foam filters is common in casting of aluminum (11, 12, 13). It is also being applied to steels (14, 15, 16). The aim of this work has been to study the performance of ceramic foam filters in magnesium with respect to capacity and flow rates. Some of the results have been presented in a previous paper (9). An equally important part of the investigations has been to study particle deposition inside the ceramic foam filters using quantitative microscopy.

## 2.0 Filtration Theory

Generally, we distinguish between two modes of filtration, depth filtration and cake filtration. In depth filtration the

inclusions are captured inside the filter, while in cake filtration the inclusions get stuck on other inclusions in front of the filter. We expect this classification of filtration modes to be valid regardless of filter media, provided that the filter material does not dissolve in the melt, react with the melt or react with the inclusions.

The filtration theory is thoroughly described elsewhere, for instance by Frisvold (17) and Engh (18) (depth filtration) and by Apelian and coworkers (19) (cake filtration). Here, only the main results are reviewed.

### 2.1 Depth Filtration

The most important parameter in a filtration process is the filtration efficiency  $E$ , which for a filter of length  $L$  can be expressed as shown in equation 1, where  $c_0$  is the concentration of inclusions in the unfiltered metal and  $c_{out}$  the concentration of inclusions in the filtered metal.  $\eta$  is the collision efficiency, which for the different collision mechanisms is thoroughly examined in the literature (17, 18, 20).  $a_s$  is the surface area per unit volume length (18) and  $\beta$  is the ratio of the collector surface projected in the flow direction to the total collector surface area.

$$E = \frac{c_0 - c_{out}}{c_0} = 1 - \exp(-\eta a_s \beta L) \quad (1)$$

An important example is a filter consisting of spherical collectors of diameter  $2R$ . The void fraction in the filter is denoted  $\epsilon$ . Then  $\beta=1/4$  and

$$E = 1 - \exp\left(-\frac{3\eta L(1-\epsilon)}{4R\epsilon}\right) \quad (2)$$

For the direct interception mechanism it is found that the collision efficiency  $\eta=3d/2R$ , where  $d$  is the inclusion diameter (17). The filtration efficiency (equation 1) is generally an increasing function of inclusion size. For ceramic foam filters, experiments referred to by Netter and Conti have confirmed that filtration efficiency increases as inclusion size increases and filter pore size decreases (21).

Let  $c_{dep}$  denote the concentration of particles deposited per unit filter length. The inclusion deposition function inside a deep bed filter can then be written as shown in equation (3) (22), where  $z$  is a position inside the filter,  $0 < z < L$ .

$$c_{dep}(z) = c_0 \eta \alpha_s \beta \cdot \exp(-\eta \alpha_s \beta z) \quad (3)$$

Equation (3) predicts that when inclusions are assumed to be completely mixed in the transverse direction of the flow, the particle deposition decreases exponentially as a function of distance into the filter  $z$ . Remember that the collision efficiency generally is an

increasing function of inclusion size (17,20). Then, according to equation (3), the particle deposition function decreases more rapidly for larger inclusions than for smaller ones. As a result, the size distributions of inclusions at different depths inside the filter should generally be different.

## 2.2 Cake Filtration

The inverse average mass flow ( $t/m$ ) as a function of accumulated filtered mass  $m$  during cake filtration can be expressed as (18,19)

$$\frac{t}{m} = \frac{\mu}{\rho A \Delta p} \left( r_f L + \frac{r_c c}{2c_c \rho A} m \right) \quad (4)$$

where  $\mu$  is melt viscosity,  $\rho$  is melt density,  $A$  is the filter cross section and  $\Delta p$  is the available pressure.  $r_f$  and  $r_c$  are resistances in the filter and cake, respectively, in units of  $m^2$ .  $c$  and  $c_c$  denote volume fractions of inclusions in the melt and filter cake. Generally  $c \ll c_c$ . Plotting  $t/m$  as a function of filtered mass  $m$  should then result in a straight line.

$$\frac{t}{m} = a + bm \quad (5)$$

where:

$$a = \frac{\mu L r_f}{\rho^2 A g h}$$

and

$$b = \frac{\mu c r_c}{2c_c \rho^3 A^2 g h}$$

Here we have introduced  $\Delta p = \rho g h$  where  $h$  is the metallostatic head and  $g$  is the acceleration due to gravity.  $a$  and  $b$  may also be regarded as resistances for filter and cake, respectively, since they are proportional to the resistances  $r_f$  and  $r_c$ .

Initially, in the depth filtration mode, we should expect a constant  $t/m$  ratio, since  $r_c=0$ . After a time  $t_d$ , which corresponds to a filtered mass  $m_d$ , the cake filtration starts and  $r_c$  attains a non-zero value.  $t_d$  and  $m_d$  depend on the inclusion content in the incoming metal.

### 2.3 Depth and Cake Filtration in Sequence

In aluminum melts, experiments by Eckert and coworkers (23) clearly show the straight line predicted by equation (5) (see Figure 1). At the start of filtration in Figure 1, an almost constant flow rate is perceptible. Another example from aluminum is illustrated in Figure 2 (24). In this diagram a constant flow rate filtration is followed by a decrease in metal flow. The decreasing flow rate near the end represents the cake filtration mode. The constant flow rate corresponds to depth filtration which means that the cake resistance  $r_c$  is negligible.

To describe the performance of a filter throughout the filtration process, we have to look closely at the various operation periods and the transition between them. The theory, briefly presented here, is developed to describe experiments concerning filtration of magnesium using ceramic foam filters (see also a previous paper (9)). The theory should also be applicable to filtration of other metals employing various inert depth filter media.

We assume that ceramic foam filters have a certain depth filtration capacity which is exceeded after a time. Then, cake filtration becomes predominant.

During operation, a ceramic foam filter is expected to undergo three different stages:

- The priming period.
- The depth filtration period.
- The cake filtration period.

During the priming period, which is expected to be short in comparison with the others, the metal enters some or all of the filter pores and heats the filter if it is not already preheated. The fraction of the filter pores infiltrated depends on filter pore size, surface tension of the melt and pressure head. During the priming period, the metal flow through the filter increases from zero up to a stationary value. In Figure 2 the priming period is represented by the initial increasing flow rate (24). In the experiments shown in Figure 3, the sampling time of one second was too long to describe the priming period.

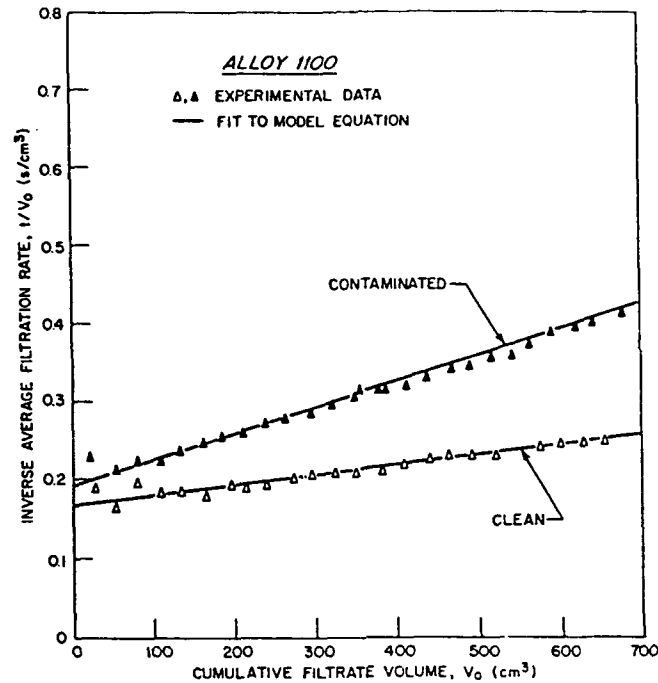


Figure 1: Time per volume vs. filtered volume for aluminum alloy melts. Near the beginning, flow rate is almost constant ( $t/V = \text{constant}$ ) before  $t/V$  starts to increase linearly as a function of filtered volume. In this case, transition from depth to cake filtration occurs very early (23).

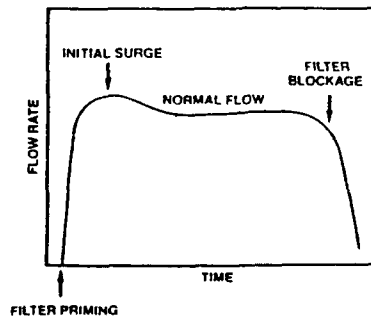


Figure 2: Flow rate as a function of time for filtration by ceramic foam filters. We see that after an initial period (priming period) the flow is almost constant (depth filtration mode) before it starts to decrease (cake filtration mode) (from Kendrick and Hack (24)).

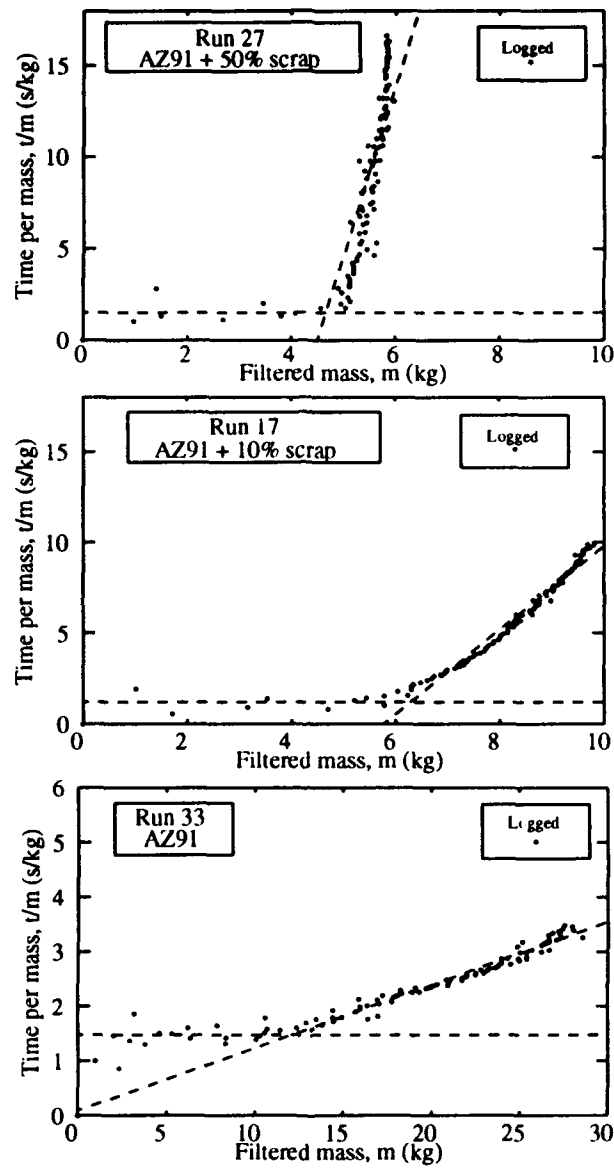


Figure 3: Inverse average flow ( $t/m$ ) as a function of filtered mass for experiments a) 27, b) 17 and c) 33 containing different fractions of return die cast metal.

During the depth filtration stage, the metal flow through the filter is found to be approximately constant. Build-up of inclusions does not seem to affect the overall resistance in the filter, and an almost constant flow rate is maintained. This situation corresponds to negligible cake resistance,  $r_c = 0$  in equation (4), which in turn leads to  $t/m = a$ .

During the cake filtration period, inclusions deposit in front of the filter. The metal flow decreases and finally terminates due to the resistance from the increasing build-up of inclusions at the filter inlet.

In Figure 3, the two latter periods are illustrated quite well in  $(m, t/m)$  diagrams recorded from filtration experiments using magnesium alloy AZ91 (9% Al, less than 1% Zn and approximately 0.2% Mn). We see that in Figure 3a, which shows an experiment using an AZ91 melt with 50% scrap metal added, the flow was nearly constant until about 4.5 kg metal was filtered. This corresponds to approximately 6 seconds. Then, cake filtration took over and the metal flow decreased rapidly. Figure 3b shows an AZ91 melt with 10% scrap metal added. In this case 6-7 kg was filtered in the depth filtration mode. In an experiment using pure AZ91, Figure 3c, 11-12 kg was filtered at an almost constant flow rate.

In order to describe the experimental results, the following hypotheses

concerning filter capacity and inclusion size distribution are put forward:

- i. No cake filtration during the depth filtration period can be detected. There is no depth filtration during the cake filtration period; that is, when cake filtration has started only the cake acts as a filter. Its filtration efficiency is  $E = 1$ .
- ii. A certain number of inclusions of a given size distribution must pass the filter inlet before cake filtration becomes dominant. Thus, during the depth filtration period, the filter may capture a certain number of particles of the given size distribution. This mass of inclusions,  $m_d$ , is proportional to the mass of melt filtered before cake filtration starts,  $m_d$ .

These assumptions are in accordance with the results from Eckert and coworkers (23) and Kendrick and Hack (24) shown in Figures 1 and 2, respectively.

The introduction of a depth filtration period  $t_d$  and a depth filtered mass  $m_d$  modifies equation (5) to

$$\frac{t}{m} = a \quad (6a)$$

where  $t < t_d$  and  $m < m_d$ . With  $t \geq t_d$  and  $m \geq m_d$ , equation (6a) becomes

$$\frac{t}{m} = a + b(m - m_d) \quad (6b)$$

The mass filtered during the depth filtration period  $m_d$  can be determined by studying the changes of  $t/m$  as a function of accumulated filtered mass  $m$ . In Figure 3 the depth filtered masses are defined as the point where the dashed lines intercept.

### **3.0 Experimental Methods and Results**

The experimental set-up is described in detail in another paper (9). The main features of the experimental arrangement are also shown in Figure 4.

Inclusion levels in the melts were adjusted by adding fractions of return die cast scrap metal. The additional inclusion content was proportional to the fraction of scrap metal added (9). The AZ91 ingots were melted prior to addition of the scrap. During melting and pouring the melt was protected with a  $SF_6 - CO_2$  - air blend. No fluxes were added. Thermocouples were positioned inside the filter as well as in the crucible (see Figure 4). These were connected to a computer in order to record the temperatures every second. The filtered metal was collected in a ladle placed on a balance. The filtered metal was weighed automatically at one second intervals throughout the experiments. Neither the sand mould nor the filter were heated prior to the filtration runs. The temperature of 740°C in the ladle was sufficient to allow the metal to flow through the inlet (gating) system and filter.

The ceramic foam filters used in these experiments consisted of 68.2%  $Al_2O_3$ , 14.6%  $SiO_2$ , 15.2%  $ZrO_2$ , 1.3%  $TiO_2$  and 0.7% others ( $K_2O$ ,  $CaO$ ,  $HfO_2$ ,  $Fe_2O_3$  and  $MgO$ ). The filter material was tested with respect to reactivity with the magnesium melt. The elements in the filter did not dissolve noticeably in the melt.

Filter manufacturers commonly characterize the pore size of the filters by the number of pores per linear inch, ppi. Filters with pore sizes 10 and 20 ppi were used. Approximate pore sizes were thus 2.5 and 1.25 mm, respectively.

Before the experiments, samples were taken from the melt with a filter sampler. The samples were analyzed quantitatively with respect to inclusions (9).

#### **3.1 Filter Resistance**

According to Dawson and Shortall (25), ceramic foam filters generally consist of rounded polyhedra with diameter  $d_r$ . The polyhedra are connected to each other through openings or windows with diameter  $\phi$ . Generally  $\phi < d_r$ . Gauckler and coworkers state that the mean window and pore sizes determine the filter resistance and volume flow (26).

The filter parameter  $a$  which as seen from equation (5) is proportional to the filter resistance  $r_f$ , has been determined for all 18 filtration experiments. " $a$ " is the average of  $t/m$  during the depth filtration period. Thus,  $1/a$  is an

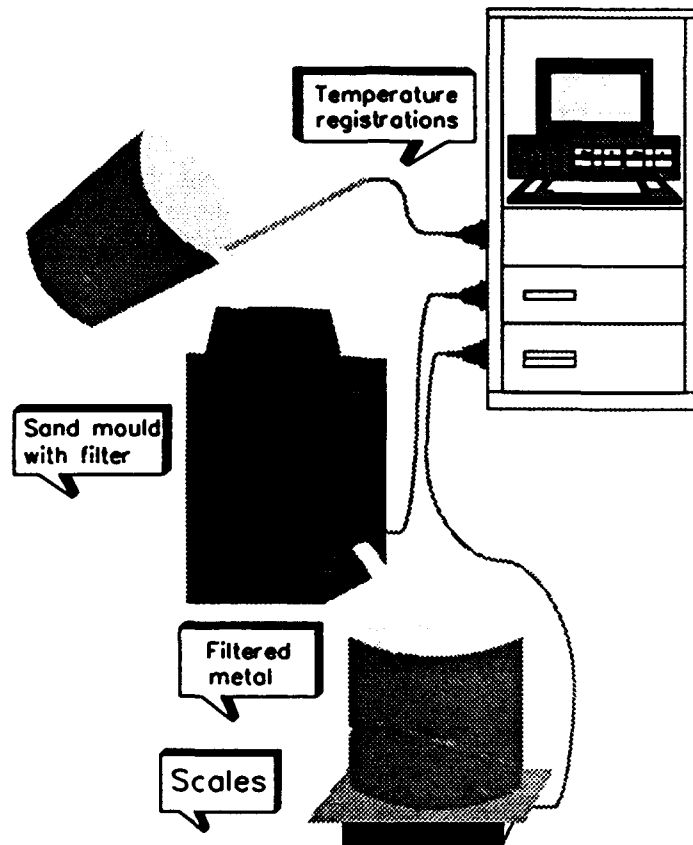


Figure 4: Experimental arrangement. The temperatures in the ladle and inside the filter as well as the accumulated mass of filtered metal were logged at one second intervals throughout the experiments.

averaged mass flow of metal through the filter in the depth filtration mode. In all runs the priming period is negligible, thus the calculated "a" values are based on mass data from  $t=0$ . Based on "a", the filter resistance  $r_f$  can be determined from equation (5). In the calculation of the filter resistance the viscosity is

considered as constant,  $\mu=1.25 \cdot 10^{-3} \text{ kgm}^{-1}\text{s}^{-1}$  (27).

Figure 5 shows the filter parameter  $a$  as a function of scrap content fraction  $\alpha$  (9). We see, as could be expected from the theory, that the filter parameter "a" does not depend significantly on inclusion content. However, it is also

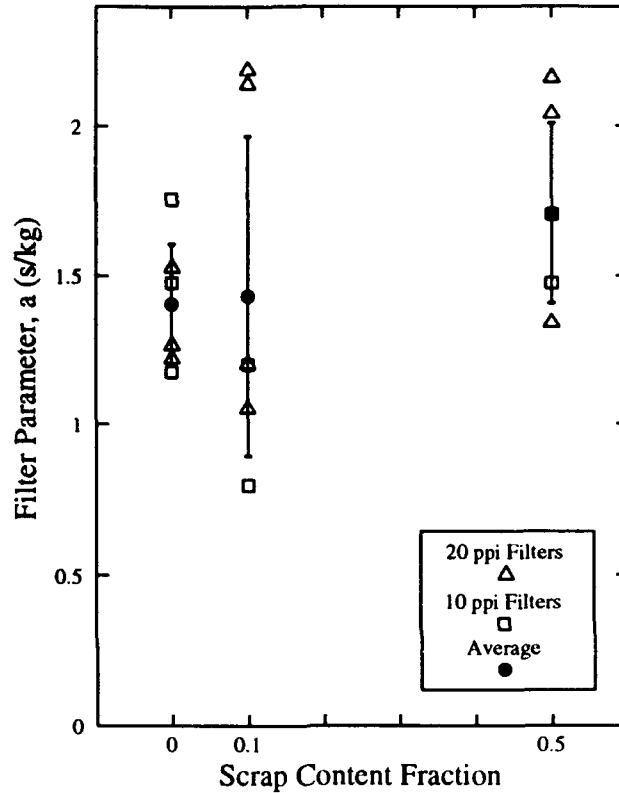


Figure 5: The filter parameter  $a$  as a function of scrap content fraction  $\alpha$ . The average value of  $a$  and the standard deviation at each scrap content ( $\alpha = 0, 0.1$  and  $0.5$ ) is indicated. At a given scrap content the average of "a" is calculated over all experiments, regardless of filter pore size (from Bakke and coworkers (9)).

seen that the scatter in the results is great, especially for the melts with 10% scrap addition.

In advance of the metal filtration experiments a filter resistance for every filter was determined by pressure drop measurements at a constant water flow. The filter resistances measured for water

were, however, 10 to 20 times lower than those calculated from the magnesium filtration experiments by equation (5). This is at least in part due to the fact that the interfacial tension of liquid magnesium vs. the ceramic material  $\sigma$  is much greater than that for water vs. filter material. We have no data for how magnesium or water "wets"

this specific ceramic material. However, the surface tension of magnesium vs. argon is approximately eight times that of water vs. air (28). An estimate of the pressure needed to penetrate a pore opening with diameter  $\phi$  is shown in equation (7) (29).

$$\Delta p = \frac{4\sigma}{\phi} \quad (7)$$

The pressure required for magnesium to penetrate a pore opening should be about eight times that for water. As a result, the smaller pores were not penetrated when filtering magnesium, and only parts of the filters were filled.

When measuring pressure loss over the filter in water, the filter was the only resistance between the two measuring points. In the melt experiments, however, the filter was mounted in an inlet (gating) system inside a sand mould. Therefore, an additional resistance was due to the wall roughness, bends, contractions and expansions in the gating system. Measurements to determine the pressure drop only over the filter proved to be difficult and were not undertaken. However, calculations of metal head loss caused by wall roughness and changes in geometry (bends, contractions etc.), based on loss factors from Olson and Wright (30), indicate that the metal head loss  $h_L$  was at most 5% of the original metal head. As a result, the filter was clearly the main source of pressure loss in the system. Nevertheless, when solving equation (5) with respect to  $r$ , we use  $h-h_L$  instead of  $h$ .

As already pointed out, when measuring filter resistances for water we should bear in mind the large difference in surface tensions of water and metal. Smaller filter pore sizes will probably lead to even larger discrepancies. To some extent, however, the difference in the measured filter resistances for the water and metal can be compensated by applying larger pressures during metal filtration. In other words, we should be sure that the available metal head is sufficient to force the metal into all parts of the filter.

### 3.2 Resistance in Filter Cake

Measurement of the cake parameter "b" can give an indication of melt cleanliness. From equation (5) we see that the cake parameter "b" is proportional to the inclusion content in the melt "c". If only small amount of metal is filtered in cake filtration mode, this indicates that the metal has a high content of inclusions. This is seen from Figure 3, where the steepest slope (Figure 3a) indicates the most impure melt.

Figure 6 shows the cake parameter "b" as a function of scrap content fraction  $\alpha$  (9). It is seen that the numerical value of "b" increases strongly with increasing scrap content (increasing inclusion content). For the metal with 10% scrap added, the values are five times higher than that for the ingot metal. Please note that the plots of "b" in Figure 6 are exponential.

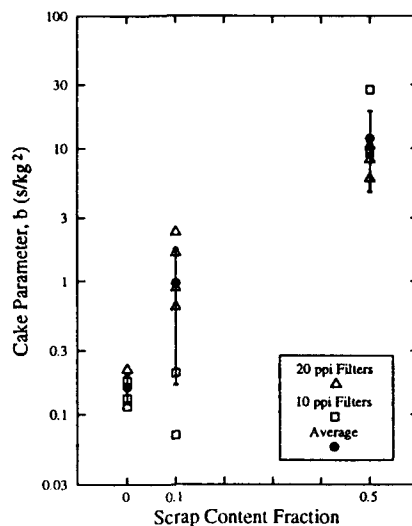


Figure 6: The cake parameter "b" as a function of scrap content fraction  $\alpha$ . Note that the ordinate axis is exponential. The average of "b" and the standard deviation at each scrap content ( $\alpha = 0, 0.1$  and  $0.5$ ) is indicated. At a given scrap content, the average of "b" is calculated over all experiments, regardless of filter pore size (9).

### 3.3 Filtered Mass of Metal in Depth Filtration Mode vs Inclusion Content

The masses  $m_d$  were determined for the filtration runs based on the changes in  $t/m$  as a function of "m". From Figure 3, it is seen that this change from depth to cake filtration is fairly pronounced so that in most cases it is easy to determine ( $t_d, m_d$ ). Previously (9), it has been shown that there exists a linear relation between the inverse mass of metal filtered in depth filtration mode, the inclusion content in the ingot metal and the extra inclusion content in the scrap metal. In Figure 7,  $1/m_d$  is plotted as a

function of  $\alpha$  (scrap content fraction). The regression line is also drawn.

### 3.4 Quantitative Microscopy

Metallographic examination of ceramic foam filters based on light microscopy and image analysis has previously been applied successfully on aluminum sampling filters (22, 31, 32, 33) and on magnesium sampling filters (9, 34). Here, the same equipment and procedures have been adapted to investigate oxide inclusions in ceramic foam filters in order to determine the number and size distributions and depth distributions of oxides.

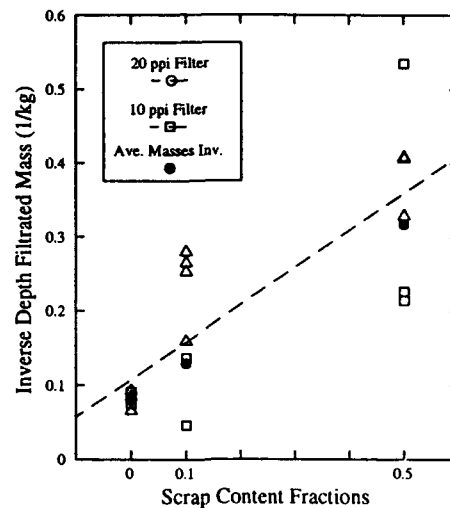


Figure 7: The inverse depth filtered masses  $1/m_d$  as a function of scrap content fraction  $\alpha$ . The solid triangles indicate the inverse of the averaged masses. At a given scrap content the average of  $m_d$  is calculated over all experiments, regardless of filter pore size. The regression line is also indicated.

In the image analysis algorithm, measuring fields of size approximately  $360 \times 320 \mu\text{m}$  are examined. These are placed in a rectangular array so that rows of fields are positioned at various depths in the filter. In these coarse ceramic foam filters the measuring fields may occasionally contain only melt or only filter material. However, the distance between the fields at each depth is predetermined as constant and thereby independent of the local geometry of the filter. As a result, 10 fields or more at each depth should represent the filter quite well. The number of depths to be investigated and the distance between them can be chosen by the user.

In each measuring field, a primary image of melt and filter material (collector) is initially generated. Based on predetermined intensity ranges, the program distinguishes between melt, collector and inclusions. Succeeding images of inclusions are acquired, and these interact with the primary image ensuring that no detail outside the melt areas contribute to the inclusion images (31).

Distribution by area and number per square mm are measured. The latter are based on registration of convexities in agglomerates or clusters of particles rather than separate details (31). Also, the number of separate particles is

recorded. The counted inclusions are grouped in 13 particle classes according to the size of the individual particle. The particle class "i" is defined by the size of the largest hexagon that can be inscribed in the image of the sectioned particle. The width of each particle class is approximately 2.75  $\mu\text{m}$ . The largest particle class is thus 33  $\mu\text{m}$  and above. The particle diameter in particle class "i",  $d_i$ , is defined as the midpoint of particle class "i". For example, the diameter of particles in class 1,  $d_1$ , is 1.4  $\mu\text{m}$  and  $d_2$  equals 4.1  $\mu\text{m}$ . The output of the program gives the discrete size distribution at each depth, thus the depth distribution of particles inside the filter is assessed.

Very often the agglomerate oxides appear to consist of numerous small particles. The image analysis algorithm may count these as small individual particles and not as one particle. This may lead to a large contribution to the smallest particle classes in the size distribution, while the total volume fraction of inclusions becomes smaller.

The image analysis algorithm determines oxide lumps very well, but the program probably does not treat oxide films in the best manner. If oxide films contain convexities, they will be counted as several smaller particles according to the number of convexities. However, films can be taken into account by user interaction during program execution.

### **3.5 Preparation of Filters for Metallographic Analysis**

At the end of each filtration experiment the metal inside the mould and gating system was allowed to solidify. Thereafter, the sand mould was broken and the filter removed. In order to preserve the filter cake, the gating system was cut off more than one cm above the filter inlet. Three ceramic foam filters, from experiments 27, 30 and 31 from melts containing 50%, 10% and 0% return metal respectively, have been cut in two in the flow direction and subsequently polished. Later, they have been examined metallographically employing the automatic image processing algorithm briefly discussed above.

### **3.6 Depth Distributions**

Depth distributions of captured inclusions obtained from the three ceramic foam filters investigated are shown in Figure 8. Note that the ordinate axis in Figure 8 is exponential. The depth distribution is given as area fraction of inclusions (%) relative to the melt. We observe that the depth distribution of inclusions rapidly approaches zero for the highly contaminated melt (run 27). In other words, inclusions deposit near the filter inlet, and we scarcely have depth filtration at all. For the ingot melt (run 31) we obviously have depth filtration since inclusions are found nearly all the way through the filter.

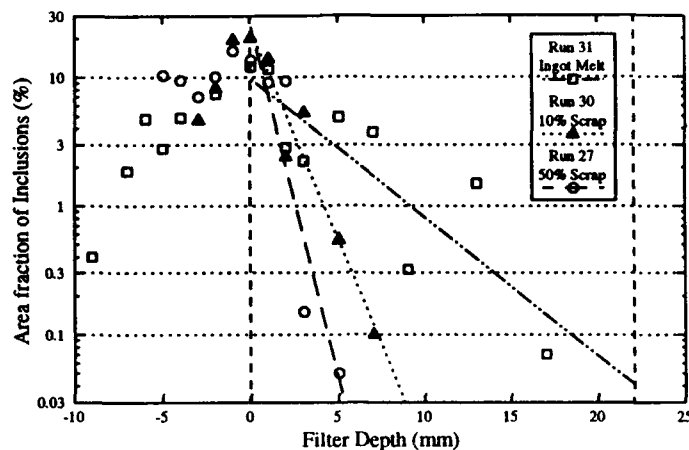


Figure 8: Area fractions of inclusions deposited at various levels in front of and inside the three ceramic foam filters investigated (depth distributions). The regression lines assuming exponential depth distribution are indicated. For runs 27 and 30 only the cakes closer than 5 mm were investigated. Please note that the plots are exponential.

Furthermore, we notice from Figure 8 that the amount of inclusions deposited at the filter inlet in the three filters investigated is fairly similar. The deposited area fraction varies from 12% in the ingot melt case (run 31) to 20% in the 10% scrap case (run 30). The 50% scrap case (run 27) falls in between (13%). These variations do not seem to be systematic from any point of view. The discrepancies, which are within a factor of two, may be due to different size distributions in the three melts. Figure 9 illustrates clearly that the size distributions in the three cases are different. The inconsistencies may also be due to problems associated with an exact determination of the filter inlet. As mentioned earlier, the measuring fields which are approximately  $320 \times 360 \mu\text{m}$ ,

are very small compared to the filter geometry. Therefore, it is difficult to decide the exact position of the inlet. Also, variations among the filters as well as local variations at the filter inlets may have influenced the results. However, based on the data in Figure 8, we may deduce that the area fraction of inclusions deposited at the filter inlet determines the transition from depth to cake filtration. A certain number of inclusions of a given size distribution passes the filter inlet in the depth filtration mode. Some of these particles are necessarily retained at the filter inlet, thus building up a "critical" fraction of inclusions there. When this critical fraction of inclusions is exceeded, cake filtration takes over. The detailed mechanisms for the transition is not very

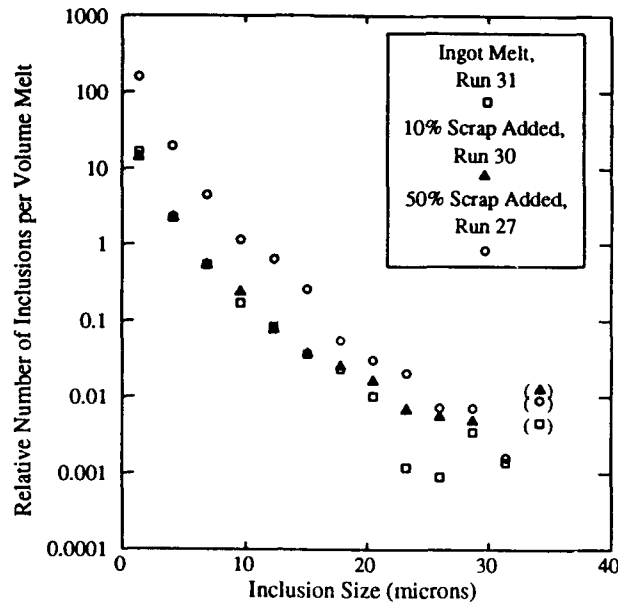


Figure 9: Size distributions of deposited oxide inclusions averaged over all depths from melts with three different scrap content fractions (0%, 10% and 50%) obtained from image analysis on ceramic foam filters. Symbols in parentheses indicate values accumulated for sizes greater than 34  $\mu\text{m}$ .

well understood. It has been suggested (35) that the transition is governed by particle deposition taking place on already deposited particles protruding into the melt. It seems plausible that the complicated mechanisms that determine the transition from depth to cake filtration depend on area fraction of inclusions at filter inlet, size distribution of the inclusions, void fraction of the filter, pore openings, flow conditions and probably also the wetting properties of the metal, inclusions and filter material.

In Figure 8, regression lines for exponential depth distributions are also

indicated. A relative estimate of the volumes of deposit are obtained by integrating the exponential deposition curves. The results show that the deposited volumes of inclusions varies within only a factor two; the 50% scrap case (run 27) has the smallest deposit, while the ingot melt case has the largest (run 31). The 10% scrap case falls in between.

The fact that apparently no particles are found near the filter outlet indicates that all inclusions are captured inside and in front of the ceramic foam filter, and as a result, the filtration efficiency is very

close to one for the inclusion size classes investigated, that is particles above  $\sim 2.7 \mu\text{m}$ .

### 3.7 Number and Size Distributions

Size distributions per filter area at various depths inside the ceramic foam filters are shown in Figures 10, 11 and 12. Figure 10 is from an AZ91 ingot melt (run 31), Figure 11 is from an AZ91 melt with 10% scrap metal added (run 30) and Figure 12 is from an AZ91 melt with 50% scrap added (run 27). We see clearly that the larger inclusions are captured at an earlier stage than the small ones. This is in agreement with the predictions in equation (3).

Although we know that inclusions may have any shape, in the following we assume that they are spherical. The number and size distribution per unit volume melt can then be obtained (34, 36, 37). The number and size distribution per unit volume, averaged over all depths, from the three filters investigated, are shown in Figure 9. We see that the size distribution for run 31 (AZ91 ingot melt) is similar to run 30 (10% scrap added) up to particle size  $20 \mu\text{m}$ . Above  $20 \mu\text{m}$ , the number of inclusions in run 30 is greater. Generally, the size distribution for run 27 (50% scrap added) is much higher than in the other two melts.

### 3.8 Calculation of Inclusion Levels

Still assuming spherical inclusions, the number and size distribution from the

inclusion counts in the filter and in the cake can be integrated to give the total inclusion content in the melt on, for instance, a ppm basis (33, 34). In the integration we assume a uniform distribution of inclusions over the entire filter cross section "A" at each depth. Since several of the pores were not infiltrated, this assumption is only an approximation. As pointed out previously, the effective filter cross section is less than the apparent,  $A_f < A$ . The average % of melt at each depth which is an output from the automatic image analysis, is generally smaller than the measured void fraction of the filters. This indicates that a substantial amount of pores were empty, and thereby regarded as collectors (filter material) by the computer program. This confirms that the effective filter cross section is less than expected,  $A_f < A$ . Therefore the calculation of total inclusion contents from analysis of the ceramic foam filters clearly overestimates the total inclusion levels. Visual observations of the filters also indicate that parts of the filters were not filled with metal.

The size distribution inside the ceramic foam filter has been determined, after excluding information pertaining to cake. From this, the volume of inclusions deposited inside the filter  $V_f$  can be calculated (34). We have found that for ingot metal (run 31)  $V_f$  is largest ( $V_f = 0.66 \text{ cm}^3$ ) while in the 50% scrap case (run 27)  $V_f = 0.30 \text{ cm}^3$ . The 10% scrap melt (run 30) falls in between ( $V_f = 0.47 \text{ cm}^3$ ). These results compare quite well with the integrals over the exponential

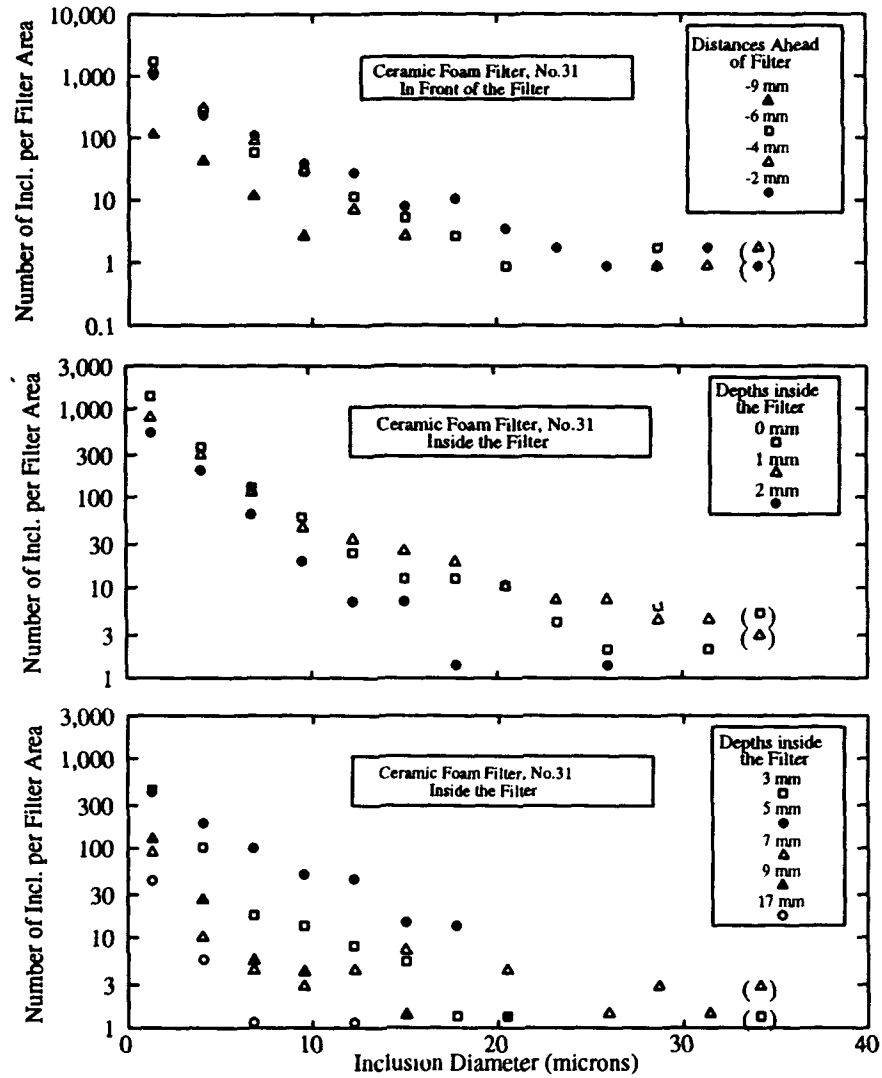


Figure 10: Size distributions at various depths in a ceramic foam filter through which AZ91 ingot melt was filtered (run 31). The top figure shows size distributions at four levels in front of the filter. The two other figures are from levels inside the filter. Symbols in parentheses indicate values accumulated for sizes greater than 34  $\mu\text{m}$ . The filter depth is approximately 22 mm.

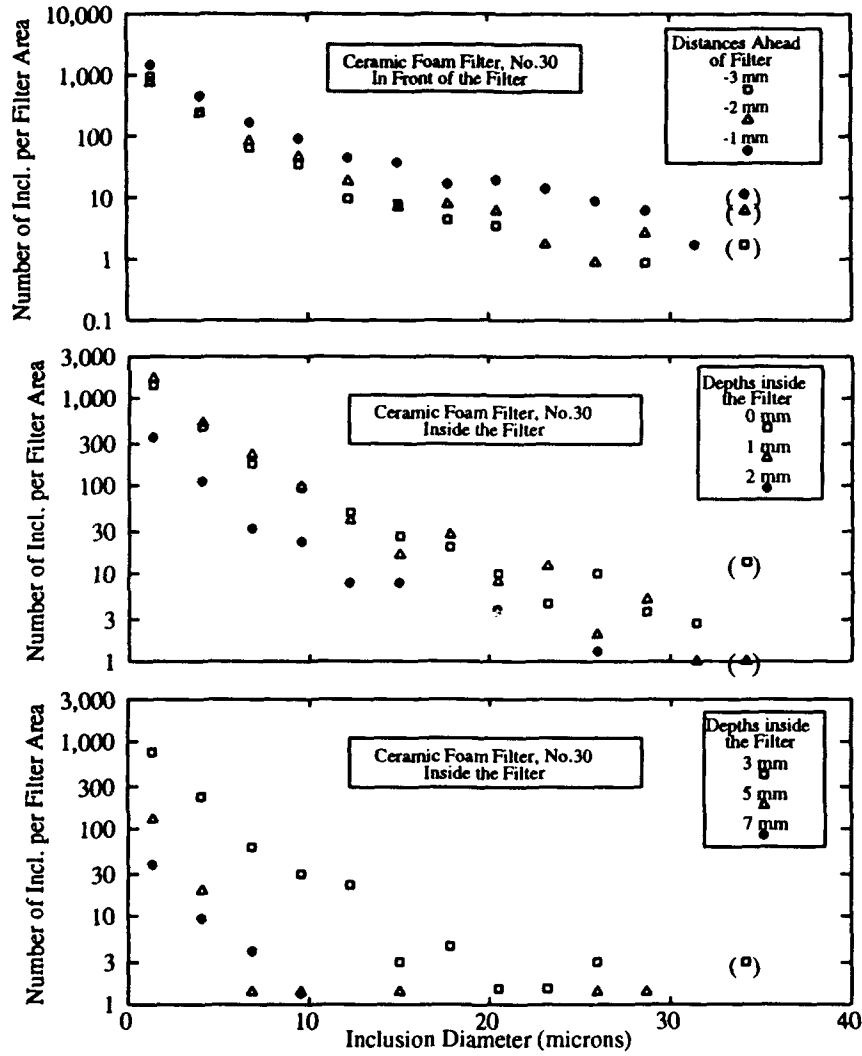


Figure 11: Size distributions at various depths in a ceramic foam filter through which AZ91 ingot melt with 10% scrap added was filtered (run 30). The top figure shows size distributions at three levels in front of the filter. The two other figures are from inside the filter. Symbols in parentheses indicate values accumulated for sizes greater than 34  $\mu\text{m}$ . The filter depth is approximately 22 mm.

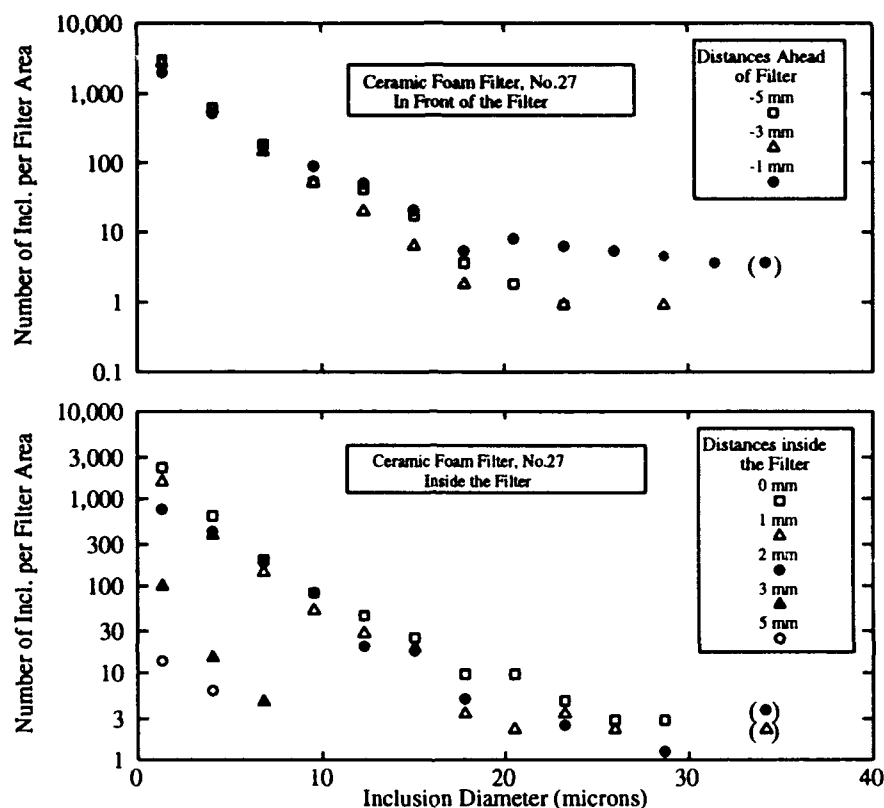


Figure 12: Size distributions at various depths in a ceramic foam filter through which AZ91 ingot melt with 50% return die cast metal added was filtered (run 27). The top figure shows size distributions at three levels in front of the filter. The bottom figure are from inside the filter. Symbols in parentheses indicate values accumulated for sizes greater than 34  $\mu\text{m}$ . The filter depth is approximately 22 mm.

deposition curves in Figure 8. The discrepancies in  $V_f$  which are within a factor of two, can partly be due to the different size distribution of inclusions in the various melts. Furthermore, the start of cake filtration may also depend upon the occurrence of particles or films larger than the pore openings. Although

the size distributions in Figure 9 indicate that the number of large particles in the most impure melt is about same as in the ingot melt, this may not be the case.

The occurrence of small particles (the first three or four classes) are about 10 times more than that in the 50% scrap

melt. As discussed previously, several of these particles may in fact be connected and thus constitute a larger particle or film where the size is large enough to block pore openings.

## 4.0 Discussion

### 4.1 Temperature Effects

It is recommended (12) that the filter should be preheated prior to filtration in order to ease priming, eliminate moisture and minimize thermal shock damage to the filter. It may therefore be argued that more pores could have been filled and the total throughput of the filters could have been greater if the filters and the molds were preheated. However, it is doubtful that the increase would have been significant. If the melt temperature is high enough, the metal contains enough heat to bring the filter temperature up to a level high above the melting point of the metal. In most of the experiments, a metal temperature of 740°C provided a temperature of about 720°C inside the filter as soon as the first metal is registered on the balance. The superheat thus compensated for the lack of preheat as far as priming was concerned.

From Figure 13, we see that a small metal flow amplifies the temperature drop inside the filter. The large metal flow in Figure 13c (run 33) provides enough heat to keep the filter temperature at a high level throughout the filtration process. The temperature

drop is, however, large for the most contaminated melts. For experiment "a", (run 27) the temperature has decreased to about 600°C at the end of the experiment. In Figure 13 b (run 17) the temperature has fallen to approximately 620°C while for the ingot melt in "c", (run 33) the temperature was still above 700°C after 100 seconds of filtration.

### 4.2 Pore Sizes

Figures 5 and 7 show that there is little difference in the performance of 20 and 10 ppi filters. This is probably due to the fact that the two filter types contains a wide range of pore and window sizes. However, since the flow during depth filtration in both 20 and 10 ppi filters is essentially the same (the parameter "a" in Figure 5), we may deduce that both filter types contain approximately the same number of small windows that have not been penetrated by melt during operation. The void fraction was determined to be 0.82 for both filter types. This underlines the similarity of the 10 and 20 ppi filters.

### 4.3 Comparing the Size Distributions Measured on Sampling Filters and Ceramic Foam Filters

As mentioned earlier, samples were taken from the melt prior to filtration (9). It was expected that these samples should give a true representation of the melt to be filtered. However, the inclusion content in the melt is apparently higher when determined from the ceramic foam filters than that

Magnesium Filtration with Ceramic Foam Filters

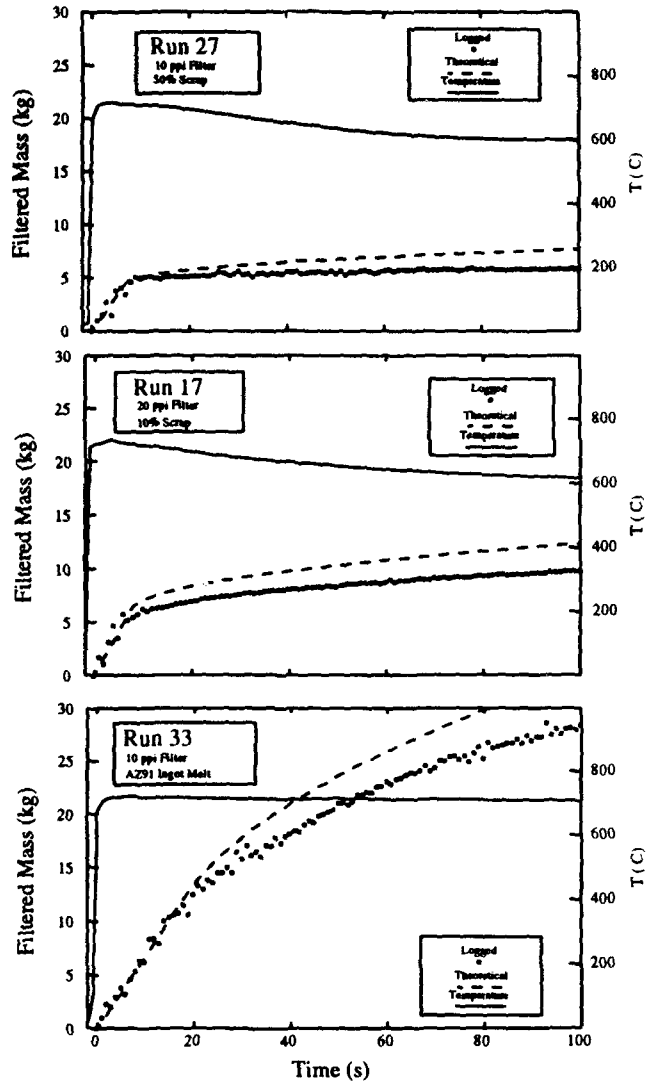


Figure 13: Accumulated filtered mass vs. time for experiments a) 27, b) 17 and c) 33. The temperatures inside the filters are also given.

obtained from the sampling filters. An explanation is that additional inclusions have been introduced during transport of melt from the crucible to the ceramic foam filter. This transport involved pouring of liquid metal followed by a turbulent metal flow upstream of the filter in the gating system inside the sand mould. Besides this potential generation of oxide inclusions, sand grains from the walls of the mould may also have been entrapped in the melt.

A second explanation of the discrepancy among the measured size distributions is that the ceramic foam filters were studied at a magnification half of that employed when investigating the magnesium sampling filters (9). At a low magnification it is not possible to separate details as clearly as at the high magnification. As a result, clusters or agglomerates of particles may appear as one large inclusion and not as a collection of smaller inclusions. Clearly, the size distribution acquired from image analysis of samples is sensitive with respect to the magnification.

The discrepancy between the size distributions may also be due to different filtration efficiencies in the two filter types (ceramic foam filter and sampling filter). As explained previously the filtration efficiency in the ceramic foam filters seem to be very close to one while in the sampling filter it is probably lower, especially for the smaller inclusions (9).

#### **4.4 The Importance of Clean Input Metal**

The filter life can be defined as the amount of metal that can be filtered before the filter is blocked. These experiments have demonstrated that the mass of metal filtered in the depth filtration mode gives an indication of melt cleanliness; the more metal filtered the cleaner was the metal that entered. The filter life increases with increasing cleanliness of this metal. We must also remember that according to equation (1), a mechanical filter only removes a part of the inclusions in the melt. This summarizes to a conclusion that may seem obvious, but nevertheless has to be emphasized repeatedly: the cleaner the metal that goes in, the longer is the filter life and the cleaner is the output metal. As a result, if we want to use ceramic foam filters industrially, the metal to be filtered should be as clean as possible. Scrap metal, in particular, should be refined to the extent possible before filtration, for instance by settling and flotation. Settling and flotation remove mainly the large inclusions. These tend to give an early transition to cake filtration.

#### **5.0 Conclusions**

Depth distributions of inclusions inside the ceramic foam filters show that no particles are deposited near the filter outlet. This indicates that the filtration efficiency equals unity, at least for the particle classes investigated. As a result,

the ceramic foam filters seem to be effective from a melt refining point of view. However, metal throughputs are probably on the lower side of what is required industrially.

Image analysis of inclusions in a filter used for sampling gives a very good measure of melt cleanliness and filtration efficiency. Roughly speaking, depth and cake filtration act in sequence. During depth filtration a certain number of inclusions of a given size distribution passes the filter inlet. Some of these particles are necessarily retained at the filter inlet, thus building up a "critical" fraction of inclusions there. When this critical fraction is exceeded, cake filtration finally takes over.

In the cake filtration mode the cake parameter "b" which is proportional to the inclusion content in the melt, can give a measure of the melt cleanliness.

The surface tension of the melt controls the infiltration of the filter (priming period). Since surface tension of liquid magnesium is much greater than that of water, it is difficult to translate the resistance measurements of ceramic foam filters from water to molten magnesium.

The melt to be filtered through a ceramic foam filter, or a mechanical filter in general, should be as clean as possible in order to delay the onset of cake filtration. When cake filtration starts, for all practical purposes the filter life must be considered as expired.

## **6.0 Acknowledgments**

The authors gratefully acknowledge the financial support of this work by Norsk Hydro and the Royal Norwegian Council for Scientific and Industrial Research (NTNF) under the Expomat program.

## **7.0 References**

1. Simensen, C. J. and B. Oberländer, A Survey of Inclusions in Magnesium, *Praktische Metallographie*, Vol.17, p.125, (1980).
2. Engh, T. A., Principles of Metal Refining, Oxford University Press, Oxford, Ch.1, (1992).
3. Emley, E. F., Principles of Magnesium Technology, Pergamon Press, Oxford, p.71, (1966).
4. Høy-Petersen, N., T. Aune, T. Vrålstad, K. Andreassen, D. Øymo, T. Haugerød, and O. Skåne, Magnesium, *Ullmann's Encyclopedia of Industrial Chemistry*, 5th Ed., Vol.A15, VCH Verlagsgesellschaft, Weinheim, Germany, p.559, (1990).
5. Petrovich, V. W. and J. S. Waltrip, Flux-free Refining of Magnesium Die Cast Scrap, *Light Metals 1989*, ed. P.G. Campbell, TMS-AIME, p.749, (1989).

6. Fruehling, J. W. and J. D. Hanawalt, Protective Atmospheres for Molten Magnesium, Transactions of American Foundry Society, p.159, (1969).
7. Unsworth, W., Control of Intermetallic Particles in Magnesium Alloys by Filtration, Metallurgia, p.15, (July, 1960).
8. Okumura, A., H. Suwa, R. Kanzawa, K. Fukizawa and T. Suzuki, Manufacture of Magnesium Alloy Wheels, International Magnesium Association, 46th Annual World Magnesium Conference, (May 16-19, 1989).
9. Bakke, P., A. Nordmark, E. Bathen, T. A. Engh and D. Øymo, Filtration of Magnesium by Ceramic Foam Filters, Light Metals 1992, ed. E.R. Cutshall, TMS-AIME, p.923, (1992).
10. Øymo, D., O. Holta, O. M. Hustoft, and J. Henriksson, Magnesium Recycling in the Die Casting Shop, Proceedings of the 1992 Conference on the Recycling of Metals, Düsseldorf/Neuss, Germany, p.143, (13-15 May, 1992).
11. Mollard, F. R. and N. Davidson, Experience with Ceramic Foam Filtration of Aluminum Castings, American Foundry Society, 84th Annual Meeting; St.Louis, Missouri, p.595, (April 21-25, 1980).
12. Dore, J. E., A Practical Guide on How to Optimize Ceramic Foam Filter Performance, Light Metals 1990, ed. C. M. Bickert, TMS-AIME, p.791, (1990).
13. Neff, D. V., Scrap Melting and Metallurgical Processes Employed in Aluminum Recycling, Extraction, Refining and Fabrication of Light Metals, Proceedings of the International Symposium, Ottawa, Ontario, p.393, (August 18-21, 1991).
14. Apelian, D., S. Luk, T. Piccone and R. Mutharasan, Removal of Liquid and Solid Inclusions from Steel Melts, Proceedings of Steel Making Conference, 69, Book 1, p.957, (1986).
15. Wieser, P. F., Fundamental Considerations in Filtration of Liquid Steel, Steel Making Proceedings, Vol.69, Washington D.C., p.969, (April 6-9, 1986).
16. Bates, P. and R. A. P. Kent, The Use of Ceramic Foam Filters in the Production of High Integrity Steels and Ni-base Alloys, ISIJ (Iron and Steel Institute of Japan) International, Vol.32, No.5, p.682, (1992).
17. Frisvold, F., Filtration of Aluminum. Theory, Mechanisms and Experiments, Dr.Ing. Thesis, Norwegian Institute of Technology, Trondheim, Ch.2, (1990).

18. Engh, T.A., Principles of Metal Refining, Oxford University Press, Oxford, Ch.5, (1992).
19. Apelian, D., C. E. Eckert, R. Mutharasan and R. E. Miller, Refining of Molten Aluminum by Filtration Technology, International Seminar on Refining and Alloying of Liquid Aluminum and Ferro-Alloys, Trondheim, p.121, (August 26-28, 1985).
20. Rasch, B., Removal of Inclusions from Molten Aluminum using Gas Purging and Filtration, Dr.Ing. Thesis, Norwegian Institute of Technology, Trondheim (in Norwegian), Ch.5, (1987).
21. Netter, P. and C. Conti, Efficiency of Industrial Filters for Molten Metal Treatment: Evaluation of a Filtration Process Model, Light Metals 1986, ed. R. E. Miller, TMS-AIME, p.847, (1986).
22. Frisvold, F., T. A. Engh, and E. Bathen, Measurement of Filtration Efficiency of an ALCOA 528 Filter, Light Metals 1990, ed. C. M. Bickert, TMS-AIME, p.805, (1990).
23. Eckert, C. E., R. Mutharasan, D. Apelian and R. E. Miller, An Experimental Technique for Determining Specific Cake Resistance Values in the Cake Mode Filtration of Aluminum Alloys, Light Metals 1985, TMS-AIME, p.1225, (1985).
24. Kendrick, R. and J. A. Hack, The Practical Application of Ceramic Foam Filters to Nonferrous Metals, The Foundryman, p.228, (May, 1988).
25. Dawson, J.R. and J. B. Shortall, The Microstructure of Rigid Polyurethane Foams, Journal of Materials Science, Vol.17, p.220, (1982).
26. Gauckler, L. J., M. M. Waeber, C. Conti and M. Jacob-Duliere, Ceramic Foam for Molten Metal Filtration, Journal of Metals, p.47, (September, 1985).
27. Brandes, E. A., ed. Smithells Metals Reference Book, 6th edition, Butterworth & Co., London, p.14-7, (1983).
28. Weast, R. C., ed. CRC Handbook of Chemistry and Physics, 58th edition, CRC Press, Palm Beach, FL, p.F32 and F45, (1978).
29. Defaye, R., and I. Prigogine, Surface Tension and Adsorption, Longmans, Green & Co. Ltd, London, p.7, (1966).
30. Olson, R. M. and S. J. Wright, Essentials of Engineering Fluid Mechanics, 5th edition, Harper & Row Publishers, New York, Ch.9, (1990).
31. Bathen, E., Investigations of Inclusions in Aluminum Melts by

- Image Analysis, International Seminar on Refining and Alloying of Liquid Aluminum and Ferro-Alloys, Trondheim, p.174, (August 26-28, 1985).
32. Engh, T. A, B. Rasch and E. Bathen, Deep Bed Filtration Theory Compared with Experiments, Light Metals 1986, ed. R. E. Miller, TMS-AIME, p.829, (1986).
33. Frisvold, F., Filtration of Aluminum. Theory, Mechanisms and Experiments, Dr.Ing. Thesis, Norwegian Institute of Technology, Trondheim, p.91, (1990).
34. Bakke, P., Measurement and Removal of Inclusions and Hydrogen in Magnesium, Dr.Ing. Thesis, Norwegian Institute of Technology, Trondheim, p.119, (1992).
35. Johansen, S. T. and N. M. Anderson, A Mathematical Model for Large Scale Filtration of Aluminum, EPD Congress 90, ed. D. R. Gaskell, TMS-AIME, p.441, (1990).
36. DeHoff, R. T. and F. N. Rhines, Quantitative Microscopy, McGraw Hill, New York, p.151, (1968).
37. Simensen, C. J. and U. Hartvedt, Analysis of Oxides in Aluminum by Melt Filtration, Zeitschrift für Metallkunde, Band 76, Heft 6, p.409, (1985).

## **Transformation and Sintering of $\gamma$ -AlOOH and TiN Composites**

**A. Kuzjukēvičs**

Nagaoka University of Technology, Nagaoka, 940-21 Japan

**M. Dehler**

Fachhochschule Rheinland-Pfalz, 5410 Höhr-Grenzhausen, Germany

**K. Ishizaki**

Nagaoka University of Technology, Nagaoka, 940-21 Japan

**J. Grabis, and**

Institute of Inorganic Chemistry, Latvian Academy of Sciences, Salaspils  
Latvia, LV-2169

**J. Kriegesmann**

Fachhochschule Rheinland-Pfalz, 5410 Höhr-Grenzhausen, Germany

### **Abstract**

The transformation and sintering of  $\gamma$ -AlOOH (pseudoboehmite) and TiN composites obtained by the hydrolysis of ultra fine AlN-TiN powders was studied at temperatures between 450 and 1600°C. The formation of  $\alpha$ -Al<sub>2</sub>O<sub>3</sub> occurs at temperatures as low as 950°C and transformation is completed at 1000°C in composites with TiN concentration greater than 8.4 wt%. Pure  $\gamma$ -AlOOH obtained by the hydrolysis of ultra fine AlN transforms to  $\alpha$ -form at 1150°C. The composites of  $\gamma$ -AlOOH and TiN can be pressureless sintered to a density as high as 0.95 of the theoretical density. Segregation of TiN particles on grain boundaries decreases their mobility and, as a result, grains become finer with increasing concentration of TiN.

### **1.0 Introduction**

The high hardness, high temperature strength and chemical resistance of ceramic tools, especially those based on Al<sub>2</sub>O<sub>3</sub>-TiC, make them particularly useful for high speed finishing

operations of superalloys, hard chill cast irons, and high strength steels (1). TiN, compared to TiC, has higher E-modulus (2) and therefore a higher E-modulus is expected for the Al<sub>2</sub>O<sub>3</sub>-TiN composites compared with Al<sub>2</sub>O<sub>3</sub>-TiC.

Table 1. Characteristics of Ti-Al-O-N Composites

Composite	Ti fraction, (Ti)/((Al)+(Ti))	Concentration, wt%		Relative density of green bodies*
		TiN	Al <sub>2</sub> O <sub>3</sub>	
C-1	0.070	8.4	91.6	0.314
C-2	0.110	13.0	87.0	0.310
C-3	0.135	15.9	84.1	0.310
C-4	0.208	24.1	75.9	0.322
C-5	0.327	37.1	62.9	0.356

\* Calculated as a fraction of the  $\alpha$ -Al<sub>2</sub>O<sub>3</sub> and TiN composite theoretical density.

Manufacturing of the Ti-Al-O-N composites has been a subject of extensive investigations (3-11). The composites were prepared by an in-situ reaction between TiO<sub>2</sub> and AlN with or without addition of Al<sub>2</sub>O<sub>3</sub> during sintering or hot pressing (3-6, 9, 12), by the sol-gel method (7), or by sintering or hot pressing of Al<sub>2</sub>O<sub>3</sub> and TiN mixtures (8). Additionally the preparation of Al<sub>2</sub>O<sub>3</sub>-TiN composites by floating-type fluidized-bed chemical vapor deposition has been discussed (11). Among the above mentioned preparation methods, an application of a component with nanosize particles is reported in the case of Al<sub>2</sub>O<sub>3</sub> mixture with ultra fine TiN powder (8,11) and composite fabrication by a sol-gel method (7). In the present study, the sintering and transformation of  $\gamma$ -AlOOH (pseudoboehmite) and TiN composites are investigated, when both component particles are nanosize.

## 2.0 Experimental

An ultra fine AlN-TiN composite made by RF plasma chemical synthesis (13) was a precursor for the preparation of  $\gamma$ -AlOOH and TiN composites. (The composite was supplied by the Institute of Inorganic Chemistry of the Latvian Academy of Sciences). Characteristic features of the AlN-TiN powder composites are particles, in which the TiN nucleus is surrounded by an AlN shell with resultant average particle size of 0.04-0.08  $\mu$ m, and homogeneous distribution of TiN and AlN (14). The titanium fraction, i.e., (Ti)/((Ti)+(Al)) ratio and calculated corresponding concentrations of TiN and  $\alpha$ -Al<sub>2</sub>O<sub>3</sub> in the Ti-Al-O-N composites are shown in Table 1.

To obtain  $\gamma$ -AlOOH and TiN composite the AlN-TiN powder was hydrolyzed in

boiling water. The water/AlN weight ratio was  $> 50$ . According to the X-ray pattern (Figure 1a) the hydrolysis of ultra fine AlN leads to formation of the pseudoboehmite. In contrast with boehmite the pseudoboehmite is poorly crystallized with broadened diffraction peaks and has enlarged lattice parameter "b" (15). After drying, the slurries were preheated in vacuum at  $450^{\circ}\text{C}$  for 3 hours to complete the  $\gamma\text{-AlOOH} \rightarrow \gamma\text{-Al}_2\text{O}_3$  transformation.  $\gamma\text{-Al}_2\text{O}_3$  and TiN were the only phases observed after preheating (Figures 1b and 1c).

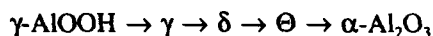
Pellets with diameter of  $\sim 18$  mm and 3 mm height were made by uniaxial pressing (20 MPa), followed by cold isostatic pressing (200 MPa) after crushing of the preheated ( $450^{\circ}\text{C}$ ) powder and screening through 250 mesh. The relative density of green bodies is shown in Table 1. Samples were sintered in alumina crucibles under nitrogen (0.1 MPa) at temperatures from  $900^{\circ}\text{C}$  to  $1600^{\circ}\text{C}$  for 1 hr. A heating rate of 400 K/h was used for all experiments. To evaluate the influence of the TiN on the  $\gamma\text{-AlOOH} \rightarrow \alpha\text{-Al}_2\text{O}_3$  transformation, heat treatments of pure boehmite made by hydrolysis of ultra fine AlN were also carried out under the same conditions.

### 3.0 Results and Discussion

#### 3.1 Transformation to $\alpha\text{-Al}_2\text{O}_3$

Previous studies of the dehydration of boehmite have shown that a series of

transitional phase aluminas are produced before final conversion to  $\alpha\text{-Al}_2\text{O}_3$  (16):



Transformation temperatures are somewhat variable, apparently dependent on the crystallinity and previous history of the boehmite and on the conditions of heat treatment. The dehydration of boehmite is topotactic (i.e., the crystal structure transforms without destruction of the original crystal morphology) and occurs at  $\sim 450^{\circ}\text{C}$  to form  $\gamma\text{-Al}_2\text{O}_3$ . With further heating, transformations to the other transitional-phase aluminas such as  $\delta$  and  $\Theta\text{-Al}_2\text{O}_3$  also occur topotactically. In the final transformation step  $\Theta$ -phase transforms to  $\alpha$ -alumina by a nucleation and growth process at  $\sim 1200^{\circ}\text{C}$  (17).

Similar transformation sequence is observed in the case of pseudoboehmite derived by hydrolysis of the ultra fine AlN (Figure 2). According to the X-ray diffraction pattern  $\gamma\text{-Al}_2\text{O}_3$  transforms to  $\delta\text{-Al}_2\text{O}_3$  which is stable up to  $\sim 950^{\circ}\text{C}$  (Figure 2a). It transforms to the  $\Theta$ -phase at  $1000^{\circ}\text{C}$  (Figure 2b) which is stable to about  $1100^{\circ}\text{C}$  (Figure 2c). The formation of  $\alpha\text{-Al}_2\text{O}_3$  occurs at  $1150^{\circ}\text{C}$  (Figure 2d). Lattice parameters of the  $\alpha$ -phase were  $a = 0.47629$  and  $c = 1.2996$  nm. They decreased after heating at  $1200^{\circ}\text{C}$  to  $a = 0.47585$  and  $c = 1.2989$  nm, approaching the tabular values of corundum,  $a = 0.4758$  and  $c = 1.2991$  nm (18), which indicates the completion of the transformation.

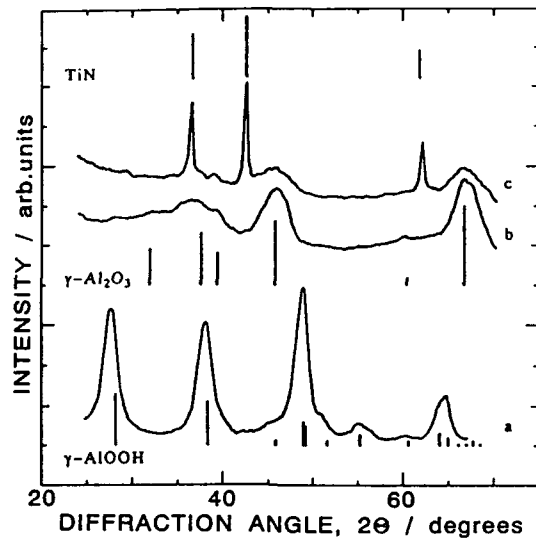


Figure 1: X-ray diffraction patterns of (a) as-hydrolyzed ultra fine AlN and (b) after preheating of the as-hydrolyzed sample for 3 hours at 450°C; (c) hydrolyzed and preheated powder composite C-2.  $\gamma$ -Al<sub>2</sub>O<sub>3</sub> and TiN are the only phases observed after preheating at 450°C.

The presence of ultra fine TiN in  $\gamma$ -AlOOH notably changes the temperature stability range of transitional-phase aluminas (Figure 3). The formation of  $\alpha$ -Al<sub>2</sub>O<sub>3</sub> was observed at temperatures as low as 950°C (Figure 3a). It is also remarkable that the  $\alpha$ -Al<sub>2</sub>O<sub>3</sub> coexists with  $\delta$ -Al<sub>2</sub>O<sub>3</sub> and no presence of  $\Theta$ -phase is seen on the X-ray pattern (Figure 3a).  $\alpha$ -Al<sub>2</sub>O<sub>3</sub> is the only oxide phase observed after heating of composite C-2 at 1000°C (Figure 3b). However, traces of non-transformed alumina are still detectable at this temperature with a smaller amount of TiN (Figure 3c).

As mentioned above,  $\Theta$  to  $\alpha$ -alumina transformation occurs by a nucleation and growth process. Introduction of  $\alpha$ -Al<sub>2</sub>O<sub>3</sub> seed particles increased the rate of heterogeneous nucleation by providing low energy nucleation sites (19). This results in an increase in transformation kinetics and lowering of the  $\Theta$  to  $\alpha$ -alumina transformation temperature by as much as 150°C (from 1220 to 1070°C) with an optimum seeding concentration of  $\sim 5 \cdot 10^{10}$  seeds/mm<sup>3</sup> of 0.1  $\mu$ m sized  $\alpha$ -alumina particles (20). However, further increasing the amount of seeded grains does not influence significantly the final step of transformation and can result in a decrease of density due to less control of

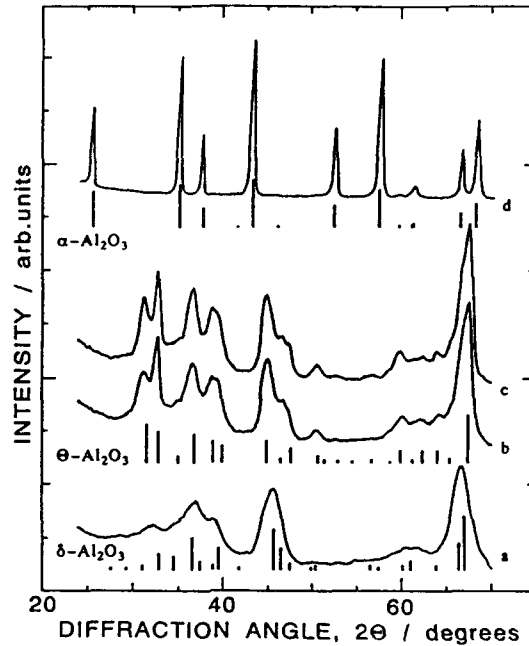


Figure 2: X-ray diffraction patterns of  $\gamma$ -AlOOH heated at (a) 950°C, (b) 1000°C, (c) 1100°C, and (d) 1150°C. The formation of  $\alpha$ - $\text{Al}_2\text{O}_3$  occurs at  $\sim$ 1150°C.

seed dispersion and the formation of agglomerates. Compared to this optimum value, the concentration of TiN ultra fine particles in composite C-2 is  $\sim$ 10 times larger, while particles are smaller and are homogeneously distributed. These seem to be the main conditions needed to promote efficient transformation to  $\alpha$ -alumina.

Although nucleation is essential to initiate transformation, the majority of transformation occurs during the growth step. This means, once nucleated, the transformation is limited only by the energy barrier for material transport

across the interphase boundary (19). An increase of the diffusion distance from the parent phase to the  $\alpha$ - $\text{Al}_2\text{O}_3$  nuclei leads to uncompleted transformation in composite C-1 with  $\sim$ 1.5 times lower TiN particle concentration and, consequently, much larger alumina volume compared with the C-2 composite. The untransformed alumina observed in C-1 composite at 1000°C (Figure 3c) is believed to be the  $\Theta$ -phase since it coincides with the appearance of the  $\Theta$ - $\text{Al}_2\text{O}_3$  in pure boehmite (Figure 2b).

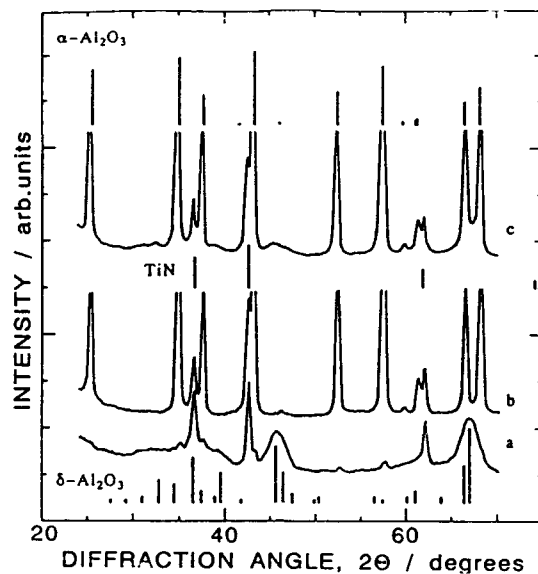


Figure 3: X-ray diffraction patterns of composites C-1 and C-2 heated at (a) 950°C, (b) 1000°C and (c) 1000°C; (a) and (b) refer to C-2; (c) refers to C-1.  $\alpha$ - $\text{Al}_2\text{O}_3$  coexists with  $\delta$ - $\text{Al}_2\text{O}_3$  at 950°C.

### 3.2 Phase Composition

X-ray diffraction patterns of the sintered C-5 composite and starting TiN-AlN composite powder are shown in Figure 4. Besides TiN and  $\alpha$ - $\text{Al}_2\text{O}_3$  as the major phases additional diffraction maxima appear on the X-ray pattern of the sample sintered at 1200°C. Two of them at  $2\theta=46.5$  and  $48.5^\circ$  could be attributed to the pseudobrookite (Figure 4b).

The maximum at  $2\theta\approx 39.8^\circ$  (Figure 4b) most likely belongs to  $\text{Ti}_2\text{AlN}$  which forms during nitridation of  $\text{Ti}_3\text{Al}$  (21). Traces of  $\text{Ti}_3\text{Al}$  are seen in the starting TiN-AlN powder (Figure 4a). Traces of the  $\text{Ti}_2\text{AlN}$  and pseudobrookite remain after sintering at 1600°C (Figure 4c).

Changes of the lattice parameters of TiN and  $\alpha$ - $\text{Al}_2\text{O}_3$  (composite C-5) with sintering temperature are shown in Figure 5. Compared to the starting value, the lattice parameter of TiN decreased after preheating due to the oxidation of TiN. An increase of the parameter at temperatures  $> 1000^\circ\text{C}$  is caused by the grain growth of TiN and transition from the ultra fine to coarse grain state (14). Similar to pure alumina derived from pseudoboehmite its lattice parameters decreased in the temperature range of 1000-1200°C indicating the completion of the  $\Theta$  to  $\alpha$ -alumina transformation. An increase of the lattice parameters at higher temperatures is due to interaction

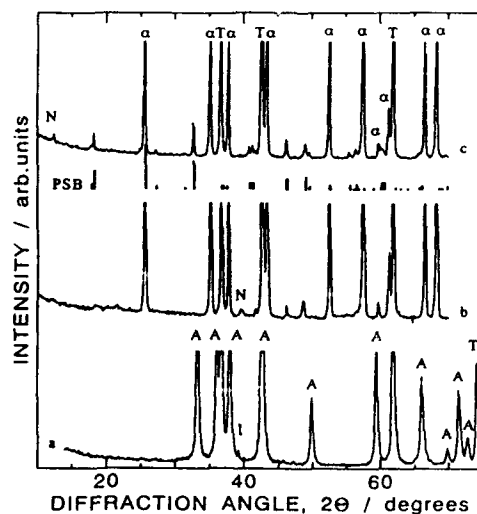


Figure 4: X-ray diffraction patterns of (a) starting TiN-AlN ultra fine powder C-5, (b) composites C-5 sintered at 1200°C for 1 hr and (c) composites C-5 sintered at 1600°C for 3 hrs. Line identification: (T) TiN, (A) AlN, ( $\alpha$ ) Al<sub>2</sub>O<sub>3</sub>, (PSB) pseudobrookite, (N) Ti<sub>2</sub>AlN, (I) Ti<sub>3</sub>Al.

between TiN and matrix and dissolution of Ti<sup>3+</sup> in the  $\alpha$ -Al<sub>2</sub>O<sub>3</sub> lattice (8).

### 3.3 Sintering Behavior

It has been reported that the sinterability of Ti-Al-O-N composites is low and a value of an apparent porosity of 49% was obtained at 1800°C for pressureless sintered Ti<sub>0.6</sub>Al<sub>3.2</sub>O<sub>3.0</sub>N<sub>2.0</sub> (12). Using the ultra fine precursor material provides a significant improvement in the relative density (Figure 6). The highest relative density of 0.95 is achieved with composition C-1 sintered at 1600°C. A decrease in relative density is observed with an increase in the amount of TiN at 1300°C and higher temperatures. As mentioned before, the relative density

was calculated as a fraction of the  $\alpha$ -Al<sub>2</sub>O<sub>3</sub> and TiN composite theoretical density without taking into account the presence of other phases. The appearance of the pseudobrookite and Ti<sub>2</sub>AlN (Figure 4), both with smaller density compared with TiN, results in lower density of the sintered composites. However, partial decomposition of TiN causing the formation of additional porosity might be also considered as a reason for a decrease in relative density. A decrease of the (N)/(Ti) ratio and weight loss of ultra fine TiN is observed in vacuum at temperatures higher than 1000°C (14). The other reason might be a decrease in mobility of grain boundaries.

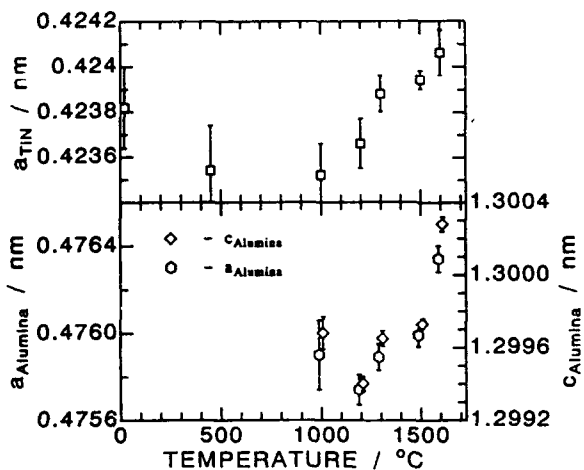


Figure 5: Changes of the lattice parameters of TiN and  $\alpha$ -Al<sub>2</sub>O<sub>3</sub> with sintering temperature.

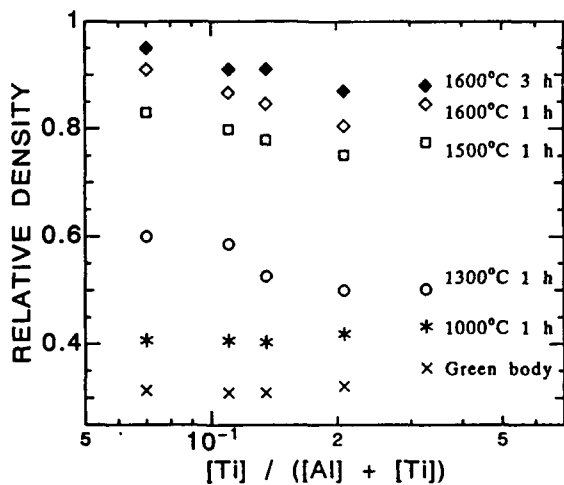


Figure 6: Relationships between relative density of sintered composites and titanium ratio.



Figure 7: Fracture surfaces of composites sintered for 1 hr at 1600°C.

The average  $\text{Al}_2\text{O}_3$  grain size also changes with an increase in the amount of TiN as revealed by SEM fractography of composites fractured by bending at room temperature (Figure 7). Small grains seen in C-1, C-2, and C-3 are TiN. For C-4 and C-5 the difference in the grain size of TiN and  $\text{Al}_2\text{O}_3$  becomes smaller, but the TiN grains are still recognizable.

For composites sintered at  $1600^\circ\text{C}$  grain size decreases from 3-5  $\mu\text{m}$  (composite C-1) to less than 1  $\mu\text{m}$  (composite C-5). A reason for the correlation between the  $\text{Al}_2\text{O}_3$  grain size and TiN concentration is, at first, the amount of the  $\alpha$ -alumina nuclei formed during the  $\Theta$  to  $\alpha$  transformation which increases with the TiN concentration. The presence of the TiN particles on grain boundaries must also inhibit the grain growth due to a requirement for additional energy to move the boundary from the TiN inclusions (22). This effect is proportional to the size of the inclusion and inversely proportional to the volume fraction of inclusions. This, together with the influence of the amount of nuclei, leads to a smaller grain size.

#### 4.0 Conclusions

The transformation and sintering of  $\gamma$ -AlOOH (pseudoboehmite) and TiN composites has been studied at temperatures between  $450$  and  $1600^\circ\text{C}$ . Composites were prepared by the hydrolysis of ultra fine AlN-TiN

powders obtained by RF plasma chemical synthesis.

The formation of  $\alpha$ - $\text{Al}_2\text{O}_3$  occurs at temperatures as low as  $950^\circ\text{C}$  and is completed at  $1000^\circ\text{C}$  in composites with TiN concentration greater than 8.4 wt%. Pure  $\gamma$ -AlOOH obtained by the hydrolysis of ultra fine AlN transforms to  $\alpha$ -form at  $1150^\circ\text{C}$ .

$\gamma$ -AlOOH and TiN composites can be pressureless sintered to a density as high as 0.95 of the theoretical density. Segregation of TiN particles on the grain boundaries decreases their mobility and, as a result, grains become finer with increasing concentration of TiN.

#### 5.0 Acknowledgments

The authors gratefully acknowledge Prof. T. Millers (Institute of Inorganic Chemistry, Latvian Academy of Sciences) and Dr. D. Perera (Australian Nuclear Science and Technology Organization) for their valuable suggestions.

#### 6.0 References

1. Tool Materials, Encyclopedia of Chemical Technology, 3rd edition, Vol.23, pp.273-309, (1978).
2. Wernisch, J., W. Wruss, Ch. Nissel, and B. Lux, Diffusions untersuchung an Phasengrenzen von  $\text{Al}_2\text{O}_3/\text{TiC}$ ,

- Sprechsaal, Vol.118, No.10, p.921, (1985).
3. Mukerji, J. and S. K. Biswas, Synthesis, properties and oxidation of alumina-titanium nitride composites, *Journal of the American Ceramic Society*, Vol.73, No.1, p.142, (1990)
  4. Sperisen, T. and A. Mocellin, Investigation of the displacement reaction in mixed AlN-TiO<sub>2</sub> powders, Part I. Microstructural changes at 1 atmosphere of nitrogen, *Journal of Materials Science*, Vol.27, No.5, p.1121, (1992).
  5. Sperisen, T. and A. Mocellin, Investigation of the displacement reaction in mixed AlN-TiO<sub>2</sub> powders. Part II. Atmosphere effects, *Journal of Materials Science*, Vol.27, No.5, p.1129, (1992).
  6. Mocellin, A. and G. Bayer, Chemical and microstructural investigations of high-temperature interactions between AlN and TiO<sub>2</sub>, *Journal of Materials Science*, Vol.20, No.10, p.3697, (1985).
  7. Han, K., Composites of titanium nitride/alumina/titanium aluminum oxynitride, U.S. Patent Application US 502,709 (1990).
  8. Mnatsakanyan, J. D., Yu. N. Vil'k, Yu. N. Paputskii, L. V. Kozlovskii, and S. S. Ordan'yan, Phase interaction and mass transfer in the Al<sub>2</sub>O<sub>3</sub>-TiN system during sintering, *Powder Metallurgy, USSR*, No.11, p.32, (1985).
  9. Perera, D. S., Phase relationships in the Ti-Al-O-N system, *British Ceramic Transactions Journal*, Vol.89, No.1, p.57, (1990).
  10. Kanamaru, M. and H. Okada, Alpha-alumina ceramics with high strength, *Japan Kokai Tokyo Koho JP Vol.02*, No.141, p.467 (1990).
  11. Isao, K., H. Noriyasu, I. Kenji, and S. Natsukaze, Synthesis of titanium nitride-alumina composite powder by floating-type fluidized-bed chemical vapor deposition (CVD), *Nippon Seramikkusu Kyokai Gakujutsu Ronbunshi*, Vol.97, No.12, p.1525, (1989).
  12. Perera, D. S., S. Moricca, and S. Leing, Study of different sintering techniques for a Ti-Al-O-N composite, *Hot Isostatic Pressing - Theory and Application*, ed. M. Kozumi, Elsevier Science Publishing, p.439, (1992).
  13. Grabis, J., I. Ubele, and A. Kuzjukevics, Physical and chemical properties of the titanium and aluminum highly dispersed powders, *Latvian Journal of Chemistry*, No.3, p.279, (1982).
  14. Millers, T. and A. Kuzjukevics, Micromonocrystals of refractory compounds: composition, structure

- and properties, *Progress in Crystal Growth and Characterizations*, Vol.16, p.367, (1988).
15. Baker, B. R., and R. M. Pearson, Water content of pseudoboehmite: A new model for its structure, *Journal of Catalysis*, Vol.33, No.1, p.265, (1974).
16. Wefers, K. and C. Misra, Oxides and hydroxides of aluminum, Alcoa Technical Paper No. 19, Revised. Alcoa, (1987).
17. Dynys, F. W., and J. W. Halloran, Alpha alumina formation in alum derived gamma alumina, *Journal of the American Ceramic Society*, Vol.65, No.9, p.442, (1982).
18. JCPDS card No 10-0173.
19. Shelleman, R. A. and G. L. Messing, Liquid-phase-assisted transformation of seeded  $\gamma$ -alumina, *Journal of the American Ceramic Society*, Vol.71, No.5, p.317, (1988).
20. Kumagi M., and G. L. Messing, Controlled transformation and sintering of a boehmite sol-gel by  $\alpha$ -alumina seeding, *Journal of the American Ceramic Society*, Vol.68, No.9, p.500, (1985).
21. Yoshimura, M., M. Nishioka, and N. Ishizawa, Synthesis of AlN and TiN from Al and Ti-Al alloy by arc image heating, *Journal of Materials Science Letters*, Vol.9, No.1, p.322, (1990).
22. Kingery, W. D., H. K. Bowen, and D. R. Uhlmann, *Introduction to Ceramics*, 2nd edition, John Wiley & Sons, New York, (1976).

## **Book Reviews**

### ***Fundamentals of Shaped Charges***

W.P. Walters and J.A. Zukas

This book is a very good introduction to the concept of the shaped charge and the use of metal liners in shaped charges. The most common, and best known, use of shaped charges is in ordnance devices for the defeat of armor. This application is extensively discussed by the authors, likely due to their background and connection to the U.S. Army Ballistic Research Laboratory (now the U.S. Army Research Laboratory, Weapons Technology Directorate). They do not ignore other applications and discuss them as well. These include demolition work, eg. buildings and bridges; construction (rock breaking), tunneling, well drilling, breaking log jams, ice dams and timber cutting. A unique application is in tapping steel mill furnaces. The shaped charge is used as a means to open-up plugged tap holes; this is sometimes called salamander blasting.

The first three chapters of this book give a basic understanding of shaped charges without resorting to equations, a phenomenological description. Included is a history of their development and an attempt is made to dispel any of the

reader's misconceptions about these devices and the way they operate. The third chapter is devoted to a description of shaped charge applications.

The two chapters that follow begin with mathematical depiction of the effect of explosive loading on metal liners and descriptions of shape charge jet formation. These chapters are invaluable to anyone desiring a detailed understanding and the extensive references allow the reader who seeks more a means to obtain further information. Chapter 7 of this book gives a unique insight in that there exists a relationship between explosive welding, bonding and forming and the formation of the shaped charge jet. It is pointed out that the similarities between these processes mean that many of the geometry related requirements are also the same.

Chapter 8 includes a discussion of the break-up of the shaped charge jet and the consequence of particulation of the jet. The typical jet has a very high tip velocity while the tail is at a somewhat

### ***Book Reviews***

---

relatively lower velocity. This causes the jet to stretch to extreme lengths and the length is directly related to the penetration performance. The jet length is limited by its eventual axial break-up, this leads to great reductions in effectiveness. The chapter examines various theories of jet particulation and break-up and offers solutions to early break-up times. Chapter 9 is related in that it looks at models that predict penetration and as a result incorporate the discussion of the previous chapter quite extensively.

Chapters 10 and 13 are somewhat related in that the former discusses aspects of fabricating the metallic liners including the geometry and metallurgical requirements. The latter chapter considers generalities related to design and fabrication. It is more a compilation of "rules of thumb" and simple equations that can lead to successful design of shaped charge liner devices.

The last chapter, 14, is loaded with figures, photographs and micrographs that describe the shaped charge liners, jet formation, target interaction, microstructural effects and results of computer simulations. The visual information in this chapter is almost worth all the previous discussion, equations and descriptions.

This book is well written with numerous references and would provide the interested reader a sufficient background to pursue greater depth in the field of shaped charge liners and liner materials.

---

*To obtain contact:*  
John Wiley & Sons, New York, NY  
398 pages, hardcover, 1989, 2nd Printing

*Reviewed by:*  
Robert J. Dowding  
U.S. Army Research Laboratory  
Materials Directorate, Watertown, MA 02172

***Handbook of Structural Ceramics***  
M. Schwartz

Although there has been and continues to be a considerable interest in using ceramic materials in structural applications, there is no concise handbook available for the designer to get the data needed for accomplishing design tasks. In addition, most of the design engineers are unaware of the recent developments in the materials arena especially in relation to the ceramic materials that this book is timely and fills a very important need. The book is well organized and is easy to read and understand.

The book starts with a general introduction to the exciting field of ceramics in the first chapter. It details all the current uses and describes the general technology behind traditional and advanced ceramics. It also gives the novice an overview of the important characteristics about ceramics in general and thus lays the ground work for the need to learn about ceramic materials and their processing. The section on market potential brings a real world perspective for the practicing engineer/businessman who has to always wonder where the market is and if it is possible to penetrate the market and under what conditions. The section on education has clearly brought out the difficulties with the current educational system resulting in the problems with the use of advanced ceramic materials.

Chapter 2 is on the mechanical properties of ceramics and begins with a comparison with metals, showing the brittle nature and low strain tolerance of ceramic materials. Strength testing methods are dealt with in detail with mention about the Weibull Modulus and its importance. The section of fracture deals with the nature of fracture in ceramic materials and the methods of fracture toughness determination. The design section deals with the problems faced with designing with ceramics and how probabilistic design is better suited than deterministic design. The problems with surface effects are detailed in the next section which shows the need to pay special attention to the surfaces and surface effects in these materials both in design and manufacture. Special considerations on designing with composites are outlined in the next section. The section on non destructive evaluation, although short, describes the methods used and also mentions the need for proof testing.

Chapter 3 on commercial structural ceramics deals with the problems of standardization and the current approaches to achieve some type of standardization of these materials. It is well known that this is a major problem and hinders progress in terms of designing with ceramic materials. The excellent descriptions and the table of properties that follow touch on all the important commercial ceramic materials

## **Book Reviews**

---

and the modified ceramic materials that are available in the market place. Alumina, silicon carbide, silicon nitride, SIALONs and zirconia ceramics are discussed in detail. The compilation of the property data is very useful.

Chapter 4 deals with ceramic powder production and densification processes. The difficulties with the starting materials (powders) are detailed after which the powder production methods are described. The description of processes for powder production enable the reader understand the processes and the tables/charts show the relative advantage and disadvantage of each of the processes. The polymer pyrolysis is described at length which is very useful for the ceramist unfamiliar with the process. An introduction to special processes such as chemical vapor deposition, functionally gradient processing etc. introduces the reader to such novel processing methods. The next section describes the method of production of the commonly used ceramic powders such as silicon carbide, silicon nitride, aluminum nitride, boron nitride, titanium diboride, alumina and zirconia. The reason for reinforcements for ceramics and the method of production of reinforcing materials is dealt with in the next section.

Chapter 5 on greenware fabrication, initiates with a short description of composite production methods which is followed by a concise but informative section on additives. Forming processes such as pressing methods, extrusion,

injection molding, casting methods, dynamic compaction, cryogenic processing and drying methods are discussed in the next sections. Special processes such as squeeze casting and a few other newer techniques are discussed in the closing section of the chapter.

Chapter 6 discusses high temperature consolidation processes. After a briefing on sintering mechanisms and sintering aids, the author details hot pressing, pressureless sintering, reaction sintering, overpressure sintering, hot isostatic pressing and sinter/hip processing. The methods are in considerable detail. Novel methods such as pressure-assisted and plasma sintering, microwave sintering etc. are described in the later section of the chapter. Microwave processing which is becoming a very important method has been dealt with in fair detail.

Chapter 7 on fabrication and manufacturing methods discusses the various methods that are generally in use for the fabrication of products from ceramic materials. Mechanical, chemical, electrical and radiation techniques are detailed. The descriptions present an excellent overview of the production methods. Advantages and disadvantages of each of the manufacturing methods are also mentioned. Examples given for each of the cutting methods and the tables and charts showing the differences in the methods and the applicability of the methods are very useful in understanding the manufacturing

methods. The section on cutting tool materials is informative, although it does not seem to fit into the overall scheme of the chapter. This could have been a separate chapter by itself. Ceramic joining methods are dealt with in the next section of the chapter, in good detail. The joining methods such as bonding with adhesives, brazing, welding, diffusion bonding and some special methods are discussed. A discussion on coating methods such as chemical vapor deposition, physical vapor deposition and a short section on testing coatings conclude the chapter.

Chapter 8 entitled applications for ceramic materials and processes, begins with electronic, electromechanical, magnetic and optical functional property statement and table and a section on mechanical and tribological properties. The markets for structural ceramics is dealt with in fair detail in the next section touching on all the important areas for tribological applications, cutting tools, bearings, biological applications and heat exchangers. There is a separate section dealing with military and space applications such as turbines, armor, radomes and laser mirrors. A fairly detailed section on heat engine applications is followed by the electronic ceramics area. In each of these sections, the author has gone into considerable details and it is easy enough even for the novice to understand the application areas. The chapter closes with a short section on non-destructive evaluation.

Some of latest processing developments in the areas of sol-gel processing, gel casting, microwave processing, injection molding, chemical vapor infiltration and chemical vapor deposition is at the beginning of Chapter 9. The need for improvement in the traditional and nontraditional fabrication processes and a brief description on superplasticity of ceramics follow. Improvements and new approaches in the areas of nondestructive and destructive testing are outlined in the next section. The developments in the application areas are mentioned in the next section. Some of the newer techniques such as the Lanxide process, Ion implantation, self propagating high temperature synthesis, composites using whiskers and continuous fibers and some combination methods are mentioned as the fabrication methods under further development. A short section on reliability and design with and a section on future trends conclude the chapter.

The book is well researched and written. The author has considerable knowledge and expertise in ceramics material development and applications which comes across nicely throughout the book. Extensive application overviews, examples, comparison tables and property data make this a very useful reference book. I am sure that the book will be very useful to application engineers to learn about the new ceramic materials and enable them to use the new materials that are available. The book will also serve as an excellent resource for those in the materials development/research arena to explore at

***Book Reviews***

---

alternate processes for the development of new materials and the problems associated with the processes and what they need to be watchful. It is obvious that the author has put in substantial effort to review and research each of the areas covered. The references and the bibliography are extensive, which bear evidence to this fact. In conclusion, the Handbook of Structural Ceramics is an excellent reference book and should be part of every ceramics reference library.

*To obtain contact:*  
McGraw-Hill Inc.  
11 West 19th Street, New York, NY 10011  
550 pages, hard cover, 1992.

*Reviewed by:*  
P.N. Vaidyanathan  
Assistant Director, MicroFabritech  
Department of Materials Science &  
Engineering, University of Florida  
Gainesville, FL 32611

***Ferroelectric Films, Volume 25: Ceramic Transactions***

edited by A.S. Bhalla and K.M. Nair

This book is a collection of papers presented at the Symposium on Ferroelectricity Thin Films for the 93rd Annual Meeting of the American Ceramic Society in Cincinnati, Ohio, April 28 - May 3, 1991. The 35 articles are devoted to preparation, characterization and applications of ferroelectric films. It attempts to provide an in depth overview of ferroelectric films.

The first two articles give generalities which are of great interest for those who envisage to work in the field of ferroelectric films. A background on ferroelectricity is followed by an history of ferroelectric films. The various film deposition techniques are described. Details are given in particular about the sol-gel process. Tables present the film materials, the phenomenon involved and the corresponding applications.

Most of the studied materials are lead perovskites: PZT (75%), PLZT and PMN (5%). The other materials (20%) are other perovskites ( $\text{BaTiO}_3$ ,  $\text{KNbO}_3$ ),  $\text{Bi}_4\text{Ti}_3\text{O}_{12}$ ,  $\text{LiNbO}_3$ ,  $\text{LiTaO}_3$ ,  $\text{ZnSnO}_3$  and tetragonal tungsten bronzes.

The film deposition techniques described are for about half, vapor phase (R.F. magnetron sputtering, C.V.D., M.O.C.V.D., ion beam assisted sputtering,...) and for half, liquid phase (sol-gel, M.O.D.,...). The experimental

process is given in details depending on the material prepared (nature of the substrate, elaboration of the target, sputtering conditions,...).

Many characterizations of the films are undertaken:

- thickness, chemical composition, morphology, domain structure, defects,...
- crystallinity, symmetry, orientation,...
- dielectric, ferroelectric, piezoelectric, electrooptic and photocurrent response properties,...
- reliability,...

The various properties are correlated to the elaboration parameters. Some examples are given here for PZT ( $\text{PbZr}_x\text{Ti}_{1-x}\text{O}_3$ ). The largest values of the remanent polarization and the lowest values of the coercive field are obtained for a composition corresponding to about  $x = 0.90$ . A brief annealing at  $650^\circ\text{C}$  for only 20 seconds imparts the perovskite phase. The stoichiometry can be controlled using an automated ion beam sputter-deposition system. The films prepared by ion-assisted deposition show better morphology and unique grain distribution. The use of alkoxide based polymeric precursor solutions allows to reduce the number of deposition steps, process highly desirable for commercial scale integration.

***Book Reviews***

---

Interface layers between the film and the electrodes can be largely removed by annealing... Such kinds of relations have been also determined for the other materials.

This book contains a great number of data and references. Tables and figures are of good quality. This book is not only a must for the shelf of any serious student of ferroelectric films but also a very useful service for the scientific community.

***To obtain contact:***

The American Ceramic Society, Westerville  
Ohio, 469 pages, hard cover, 1992

***Reviewed by:***

Jean Ravez  
Laboratoire de Chimie du Solide du CNRS  
351 cours de la Liberation  
33405 TALENCE cedex

*Forming Science and Technology for Ceramics*  
*Volume 26: Ceramic Transactions*  
edited by Michael J. Cima

This book is one of a series in which the most recent project findings in ceramic forming science are detailed by several investigators. This book is devoted to issues in ceramic 'green' forming before firing - such as formulations for achieving optimum dispersions of raw materials that are required for the process, forming to shape such as slip casting, (pressure) slip casting, gel-casting, tape casting, (low-pressure) injection molding, and 'dry' pressing, and some relevant binder removal considerations. A limited number of articles are also included regarding the machining of ceramics in the green state and hole drilling in the fired state for alumina sheet. The articles are brief and assume that the reader is already aware of the scientific principles and fundamentals which are involved in the different forming steps in making and shaping ceramic green ware.

Before we write in detail about the contents of the book, here is an overall impression of this book. Contrary to the title and what is covered in the preface, this book is not meant for knowing what is the current state-of-the-art technology related to the forming of ceramic bodies. Although the science involved is covered in isolated fashion, it is not coherent by any means. The articles have not been segmented in a sequence of how a ceramic green ware is formed by various

process steps in a step wise fashion. This makes it difficult to go directly to the specific area of forming and processing and learn what current technology may offer a practical solution. Such lack of coherence makes the book difficult to read and to form an overall view of how the book is supposed to convey the status of current technology in the ceramic industry. Also, the articles describe the findings and offer explanations for observations of very limited experiments related to specific systems and as such do not contribute to the technology that one might practice on an industrial scale in order to improve the process yield.

Although the editor states in the preface that the information contained in the book is a step towards increasing the reliability of ceramics as well as reducing their cost, information has not been presented in explicit fashion that addresses, either directly or indirectly, the stated objective. The reviewer found a serious flaw to be the lack of addressing the scale up issues involved in laboratory practice to either pilot scale or production scale. This issue is by far the most important in the forming technology for ceramics for speedier commercialization. We already have enough science - but we have not even attempted to define, describe, and propose methods to investigate or find

### **Book Reviews**

---

solutions to these issues in the manufacturing plant. If one is looking towards finding the answers to real problems in industry, as the reviewer was - especially after reading the first sentence of the preface - one will be disappointed. The reviewer wishes that the editors considered the seriousness of the lack of reliability in making ceramics as well as the inability to form ceramics with very high yield; the people involved in industrial manufacture have said time and again that they need more help in scale up issues. This has been largely ignored in this book. This is a serious flaw especially if the book is purported to contain information regarding the technology for forming fine ceramics.

The reviewer has artificially segmented the contents of the book into these topics:

- a. Fine powder synthesis using sol-gel techniques,
- b. Characterization of surface characteristics of the powders,
- c. Characterization of powder agglomerates,
- d. Drying of powders,
- e. Characterization of ceramic slips,
- f. Drying of cast objects,
- g. Binder removal technologies,
- h. Ceramic green-shaping processes, and
- i. Machining.

We will review the general contents of each of these topics.

The first four papers are devoted to the fine powder synthesis, the science of which is adequately addressed. The colloidal stability of the precipitating material has been deemed to be more important than the nucleation processes by studying the titanium alkoxide in the first paper. The second paper, conversely, addresses the nucleation issue with the objective to obtain mono-dispersed, sub micron particles of barium titanates and yttrium barium cuprates. Because of the nature of the limited experimentation and explanation of observed results, no information can be discerned that can be said to contain technological value.

The discussion on characterization techniques is quite informative and perhaps useful in directly applying the findings to current industry practice. The characterization of alumina coating by using surface-sensitive x-ray photoelectron spectroscopy technique, as demonstrated by Malghan et. al. has good potential as a quality control tool in the important mixing step. The mapping of acoustophoretic mobility through the measurement of electrokinetic sonic amplitude has been demonstrated to be a viable tool by these authors in a later paper. The characterization of slurries by determining the zeta potential has been used by several authors - but there is nothing novel here and this is a technique that is already practiced in manufacturing.

The subject of agglomerates and their characterization is considered in two papers by using both light scattering technique and rheological property determinations. Both are good papers confirming the usefulness of the application of these techniques in detecting agglomeration for the very fine powders. The subject of agglomeration is visited again in a later paper that deals with the making of solid fuel cell ceramics through colloidal processing. There is one paper that describes a laboratory spray drier behavior on the formation of non-spherical spray dried powder. The results are fundamental in nature and provide no clues to scale up issues in spray drying. The drying of green-formed shapes without cracking is a subject that has a large interest since it directly affects the process yield and therefore the cost. There is a single paper advocating a theory that considers the sol-gel drying process and several papers that illustrate the effect of atmospheric moisture content as well as the effect of inclusions that dry along with the matrix. A paper (by Tang and Cima) deals with the deformation of multi-layer ceramic green ware during the binder removal which is attributed to delamination. The possible causes are convincingly explained; however, no results are reported with further experiments that would overcome this problem. The subject of the binder is revisited after several papers that deal with novel ceramic processing techniques. Some alcohol-based binders were explored but with limited success.

The technology of green forming and shaping of ceramics needs advances that will introduce the least stresses during forming, be amenable to large and complex shape fabrication, and finally advances in instrumented processing that can offer monitoring and feed back control during such shaping procedures. Unfortunately no papers deal with these subjects in a meaningful and helpful fashion to be of use to the industrial manufacturer. One article is devoted to foamed ceramics which concerns with the explanation of observed foam-body characteristics to the processing variables including processing additives. The article regarding the Quickset injection molding, as a review, offers the reader the advantages of low pressure molding. Although no details have been given, the article claims that instrumented processing can be handled well by this process. The requirement of well-dispersed powders, as contrasted to the powders with agglomerates that give rise to ring-porosity structure around the grains, in obtaining a fine-grained homogeneous microstructure has been confirmed by Salomoni et. al. with respect to alumina and zirconia. The importance of sheet forming technology via tape casting in the forming of electronic ceramics is well recognized in the book with the inclusion of five articles devoted to this subject. All of them have good scientific concepts and proof-of-concept type experimental investigations and data. Once again, the feature that is missing in the articles is how to translate the findings into useful industry practice where one needs to

## **Book Reviews**

---

demonstrate the repeatability of these findings. However good may be the intentions of near net-shape green forming that may be practiced, green machining to net shape before firing is a requirement for many components. Additionally, the technology involved in the machining after firing without introducing damage and at low cost is of interest in the manufacturing of ceramics. The reviewer was glad to see at least four articles devoted to this subject. The via hole drilling using an electron-beam perforation system at high speeds for sintered  $Al_2O_3$  plates has been demonstrated by Sakurai et. al. although not enough detail can be discerned.

Overall, this book contains a good compilation of the various recent scientific approaches to establish a better understanding of the processing variables. The results presented here may be useful in the future to manufacture flaw-free and reliable ceramics. The documentation of the proceedings of the Symposium on "Forming Science and Technology for Ceramics" as published in this book format will undoubtedly stimulate more basic research, as written by the Editor in the preface. However, the reviewer takes exception to the misleading statements in the first paragraph of the preface. The book contains no explicitly useful information that is technology-oriented that will

- a. reduce the cost of the existing processes, and
- b. reduce the time involved in various processing steps, as was alluded to in the preface.

We have a long way to go from these limited number of scientific concepts to real applications of these results in an industrial environment. The reviewer wishes that, as a start, at least some papers were devoted to scale-up issues and repeatability issues that plague the ceramic industry for rapid successful commercialization. Unless these issues are addressed by the engineers and scientists involved in ceramic processing, the goals identified in the first paragraph of the preface of the book will be difficult to reach.

The articles in the book could have been organized better to have a smoother flow in terms of the steps involved in ceramic processing. The articles are very short and not detailed enough to be of help in particular situations where low yields are encountered in ceramic processing. Several articles can be used in ceramic processing courses in colleges for the purpose of stimulating the students to help offer solutions using the science of ceramic processing addressed. This book should be considered to be of the general interest-type.

---

*To obtain contact:*  
The American Ceramic Society  
Westerville, Ohio  
250 pages, 1991

*Reviewed by:*  
Dr. M. Srinivasan  
Vice President, Materials Solutions  
P.O. Box 663, Grand Island, NY 14072

***Surface Modification Technologies V***  
edited by T. S. Sudarshan and J. F. Braza

This book is a compilation of eighty four papers and posters that were presented at the Fifth International Conference on Surface Modification Technologies. The conference was held in Birmingham, UK, from 2-4 September 1991. Technical reports by scientists from about twenty-three countries are included in this book. It covers an impressive range of topics:

1. Orthopedic implants,
2. Diamond and related coatings, 3. Vapor deposition,
4. Ceramic coatings,
5. Optical coatings,
6. Laser processing and characterization,
7. Characterization of surfaces, and 8. Tribological evaluations.

First paper in this book is a review of materials used for orthopedic implants. Ultrahigh molecular weight polyethylene (UHMWPE) applications with various surface modifications was discussed along with limitations of existing total joint systems. Hard coatings on UHMWPE include TiN, amorphous diamond like coatings and in-situ oxidation of zirconium. Next twelve papers presented clinical studies for performance of orthopedic bearing surfaces. Wear of the articulating surfaces of total joint implants is considered to be a major problem that puts severe limitations on performance

of the implant. The causes and effects of wear debris are studied in connection with the stresses on implant components, clinical rates of wear, amount of wear debris, biological responses to particulate debris etc.

Several interesting approaches taken to examine the usefulness of a particular fabrication method include:

1. Use of human bone cell cultures in an in-vitro study to investigate biocompatibility of wear particles. Temperature and particle concentrations were the variables for this case.
2. Studying wear behavior of alumina ceramic and UHMWPE implant bearing surfaces by experimentally characterizing several implant surfaces up to nine years after surgery.
3. Usefulness of Titanium and its alloys as biomaterials is investigated. Various deposition techniques including plasma nitriding are described.
4. Titanium based materials are used to attach, retain and release antibiotics, by forming a porous surface coating by anodizing.
5. An alumina head with an UHMWPE socket irradiated with gamma radiation was found to be a good hip prosthesis by a Japanese team.

## Book Reviews

---

6. Wear resistance of alumina and diamond like coatings was investigated by Auger, X-Ray and SIM spectroscopy and wear resistance data.
7. Ion implantation of metallic components has also been discussed in some papers for altering wear properties.

Other papers in this book deal with modifications of materials properties by growth of various films: barium titanate, titanium nitriding, metallic hard layer coatings (CrN, TiN, Ti-Al-V-N) and ceramic coatings ( $Al_2O_3$ , SiN, SiC), diamond and diamond like carbon, metallic (Al, Cu, Ag), TiC. Diamond and diamond like carbon (DLC) are topics of interest for over ten papers.

Various aspects about thin films were considered:

1. Hydrogen content of CVD diamond,
2. Practical application of semiconducting diamond films for electronic devices,
3. Review of n and p type doping of diamond,
4. Deposition of diamond and DLC film by ion beam, RF plasma ion source, laser ablation and flame combustion,
5. Characterization of thin films by analytical techniques (HRTEM, SEM, electron diffraction, electron energy loss spectrometry, Auger electron spectroscopy, X-Ray photoelectron and secondary ion

mass spectroscopy, Raman spectra etc.),

6. Tribological behavior,
7. Mechanical strength and wear resistance,
8. Corrosion resistance, and
9. Adhesion strength.

Plenty of characterization and physical property data are available in these papers through the above analytical techniques. Influence of deposition techniques on adhesion and wear resistance of diamond and DLC films was summarized by the editors of this book. It is their observation that this area is full of diverse opinions and conclusions. I agree that there is a need for systematic data compilation in this field.

Other techniques for coatings included in this book are:

1. Laser cladding,
2. Laser alloying of predeposited powders,
3. Laser melting with shot peening,
4. Chemical deposition for solar energy applications,
5. Caustic flame machining etc.

The possible applications for these modified surfaces or materials are diverse in nature. Some of them are:

1. Bio materials for surgical implants,
2. Micro-electronic devices,
3. Solar applications,
4. Auto industry, and
5. Aircraft and space industry.

A book like this is a good start to appreciate the diversity and complexity of the topic. The papers are well written and are easy to read. The book itself is crisply typeset and printed with good reproductions of figures.

This book contains a vast amount of information which may make it cumbersome for many readers. Certain papers that are of interest to a particular group of people, may be totally unsuitable for other group. The connection between scientific data and production specifics is also not clearly defined in any of the papers. The book provides a good overview of surface modification techniques but its' possible integration into manufacturing in various types of industries is not very clear.

Thin film and other surface modification technologies have been utilizing a very fascinating technique of computer simulations to aid the process.

Simulations are used to understand and predict the effects of processes on thin film growth, defect formations and microscopic properties. This important aspect is completely missing from this book. Entire emphasis is on experimental characterizations and follow up studies. The reader can make his or her reading complete by referring to some simulation studies. Apart from these draw backs, this book appropriately covers current status of surface modification technologies.

---

*To obtain contact:*

The Institute of Materials  
1 Carlton House Terrace, London SW1Y 5DB  
Hardcover, 902 pages

*Reviewed by:*

A. S. Nandedkar  
President, CASA Services, 15 Dartantra Drive  
Hopewell Junction, NY 12533  
Tel. and Fax (914) 226-1925

***Pressure Effects on Materials, Processing and Design***  
Materials Research Society Symposium Proceedings, Volume 251,  
edited by K. Ishizaki, E. Hodge, and M. Concannon

This volume represents the collected papers from a symposium Pressure Effects on Materials Processing and Design held in Boston, Massachusetts, on December 3-5, 1991, as part of the annual Materials Research Society (MRS) meeting.

As such, it is not a coherent textbook, covering all of the items one would normally expect in a text such as theory, equipment, techniques, etc. Rather, it is a collection of papers mainly representing applications of gas pressure in materials processing, although a few papers do contain some theoretical background. Most deal with some aspect of hot-isostatic-pressing (HIP). Many, in fact more than half, of the papers are written by foreign authors (mostly Japanese) and several of these papers should have been more strongly edited for grammar. The sentence construction and word use often leaves the reader unclear as to what is actually meant. The 43 papers are probably organized in parallel with the symposium, into sections entitled General Papers, New Applications, Porous Materials, Densification, Electronic Materials and Glass, and Superconductors. This organization is somewhat unfortunate, as it occasionally lumps together papers with no common thread. The first named editor, Ishizaki, is listed as an author of 14 of the papers, and his apparent strong

bent for applied research sets the tone for the book.

The first section is led off by one of Ishizaki's papers, a good one describing the effects of total pressure on reactions which may occur between gases and solids. He points out that one cannot ignore the effect of total system pressure on thermodynamics of such reactions when working at elevated pressures. Ishizaki devises so-called "HIP phase diagrams" to display free energies as a function of temperature, partial pressure, and total pressure.

The next three papers bear no relationship to the first, covering a new family of high temperature alloys based on zirconium silicide, HIPing of powder mixtures, and pore elimination from alumina under HIP conditions. The last two papers in this section (General Papers) deal with hot isostatic forging and the development of a volumetric dilatometer for use at elevated temperatures and pressures. While these papers represent good ideas and some nice work, they do not relate to each other at all and are symptomatic of the general lack of organization in the book. The reader has to scan the entire table of contents, studying the titles individually, in an attempt to locate papers relevant to his interests.

The second paper, on zirconium - silicon alloys, in fact does not strictly relate to high pressure technology at all. The authors describe the properties of these new powder metal materials, which are difficult to sinter and had to be densified by HIP. The third paper, on HIPing of powder mixtures, provides a good study of the effects on densification of mixing two sizes of monosized powders at various volume fractions. The fourth paper describes the elimination of pores during HIP of alumina, using direct microscopic evidence. They show that the overpressure of the HIP cycle will in fact remove even the large, interglomerate pores which grow into stable configurations during normal sintering. Unfortunately, it appears that some of the figures and captions have been reversed. Again, better proofing should have been performed by the editors.

The paper on hot isostatic forging (HIF) shows some rather remarkable results with powder metal alloy steels, Ti alloys, and nickel aluminide composites being shaped and forged at high pressures in minutes, as compared to several hours for normal sintering. Often, very much lower temperatures are utilized during HIF and, in combination with the shorter times, novel microstructures and properties can be attained. The high temperature dilatometer description includes a detailed sketch, should the reader desire to fabricate one. No real examples of its use are provided, however.

The second section, New Applications, contains some elegant scientific studies mixed in with some general overview papers. Again, this reviewer would quibble with the organization of the book. A paper on materials processing through levitation in high gas pressure describes formation of a perfect polyethylene sphere from a rectangular chunk without contamination from a crucible or furnace. The high pressure HIP gas is of such a density that the polyethylene remains levitated. This is an interesting idea, but of little practical use since gas density decreases with temperature increase, and even the densest HIP gases, such as krypton or xenon, do not exceed densities of about three grams per cubic centimeter. Thus, few materials could be levitation processed, and the expense would be very high. On the other hand, this section contains a well written overview of surface engineering by HIP. The author defines surface engineering as the use of HIP processes to improve the properties of conventional coatings, or produce new types of coatings that would be difficult or impossible to attain by other techniques. Papers on oxidation of silicon - germanium alloys, and attaining high nitrogen concentration in Fe-Ni-Cr alloys, represent excellent scientific work, but are very specifically applied to the materials under discussion. A paper on bimetallic coatings for twin-screw extruder barrels, and one on gas-pressure sintered silicon nitride, are short on descriptions of the HIP cycle and its effects. Rather, these papers deal with description of the

## **Book Reviews**

---

properties of materials made by pressure densification. A final paper from this section is a good overview article on equipment for atmosphere-controlled HIPing and its applications.

The third section deals exclusively with porous materials and has papers describing preparation of porous metals, structural ceramics, and electronic ceramics. The metal, subject of two papers, is copper, while the ceramics include alumina, silicon nitride, lead zirconate titanate, and composites of alumina-BN and alumina-alumina. All of these materials are generally made through cyclic application of pressure in a HIP, such that the pores which are formed are long and rather more straight, like tubes, than one could obtain through normal techniques for fabricating porous materials. Applications for such materials include use as gas or liquid metal filters, bearings, catalyst supports, electrodes, and piezoelectric devices.

The fourth section deals with densification, a topic which has been repeatedly dealt with in other papers already, as mentioned. Six papers deal with ceramics, two with carbon-carbon, and one with metals. The papers discuss specific ceramics such as alumina, titanium diboride, Si/TiC composite mixtures, and silicon nitride, while there is also an excellent invited paper on densification of ceramics by gas pressure sintering, and one describing the (proposed) combination of rate-controlled sintering plus HIP. The

carbon-carbon papers deal with effects of high gas pressures on phase and microstructure development of C/C composites, while the lone metallurgical paper describes the application of HIP to Co-based alloys and nickel aluminides.

The fifth section, Electronic Materials and Glass, contains seven papers; three on glass and four on electronic ceramics. The ceramics include BaTiO<sub>3</sub>, Mn-Zn ferrites, MgAl<sub>2</sub>O<sub>4</sub> spinel, and lead-lanthanum-zirconate-titanate. These mostly relate to control of the atmosphere during HIP, since the stoichiometry of these materials plays such an important role in defining their properties. One of the glass papers more strictly relates to ceramics as they are affected by the diffusion of the glass HIP capsule material into the ceramic. Another paper is an excellent review of pressure effects during densification on the properties of glasses. The last paper deals with optical absorption of silica glasses produced by HIPing.

The final section of the book contains seven papers on high temperature ceramic superconductors. These materials are in a rapid state of development, and these papers reveal new data on phase assemblages, microstructures, and thermodynamics in these systems. Oxygen pressure HIPing is the dominant technique described.

In summary, this book contains several perhaps very useful papers, depending on the reader's viewpoint, but it is not the type of book the individual

*Book Reviews*

---

researcher would buy to put on his shelf. It is better to let the local library purchase it and then borrow it to refer to the one or two or three papers of relevance to your work. The book is not a textbook, lacking much of the fundamental information one would expect from a text. Further, its organization leaves much to be desired. However, many of the papers contained within are worthy of note.

*To obtain contact:*  
Materials Research Society, Pittsburgh, PA  
344 pages, 1992

*Reviewed by:*  
Arvid Pasto, Ph. D.  
Leader, Ceramic Processing Group, Oak  
Ridge National Laboratory, Metals and  
Ceramics Division, Oak Ridge, TN 37831

## Conference Review

### *The First International Conference on Tungsten and Tungsten Alloys*

This conference was held in late 1992. The attendance was approximately 150 scientists and engineers from government, industry and academia representing 14 countries. The conference discussed processing, applications, quasistatic and dynamic mechanical behavior, micro-structure, and ballistic properties of tungsten-based materials. Additionally, a poster display of several papers on these topics was held. The focus of the meeting was very strongly towards defense applications of tungsten heavy alloys, specifically for kinetic energy (KE) penetrators.

From the general session, held the first day, the attendees gained a common knowledge base for interpreting subsequent presentations. The paper describing "Critical Developments in Tungsten Heavy Alloys" was presented by R.M. German (Pennsylvania State University, University Park, PA) and highlighted the importance of using the powder metallurgy approach to producing state of the art tungsten heavy alloys. Proper process control was shown to result in alloys of superior quality.

L.S. Magness of the Army Research Laboratory's (ARL) Weapons Technology Directorate (WTD), Aberdeen, MD, discussed the "Properties and Performance of KE Penetrator Materials". Critical factors that limit the use of tungsten alloys in an important potential defense application were discussed in this paper. Magness also illustrated the differences in the deformation behavior of various penetrator materials. Specifically, the deformation behavior of tungsten heavy alloy versus the current KE penetrator material, depleted uranium (DU), is meaningful to the overall ballistic performance of each of these materials. The tungsten alloys tend to deform plastically which results in a stable mushroom cap at the nose of the penetrator whereas the DU alloy sloughs off this build-up through a shear localization mechanism that keeps the nose sharp.

G.L. Krasko of ARL's Materials Directorate (MD), Watertown, MA, examined the cohesion of the grain boundaries of commercially pure tungsten and described their

embrittlement by impurities through electronic calculations. The principles of modeling of the energetics and the electronic structure of various impurities on an idealized  $\Sigma 3$  (111) grain boundary were also discussed. The calculations confirmed that excess quantities of nitrogen, oxygen, phosphorus, sulfur and silicon could lead to intergranular decohesion. On the other hand, the calculations also revealed that boron and carbon are cohesion enhancers. Microalloying with boron was theoretically shown to be the most likely method of developing ductility in "pure" polycrystalline tungsten due to a site competition effect where boron has the lowest energy at the grain boundary.

As mentioned previously, much of the work presented had application in defense, namely kinetic energy (KE) penetrators. It was demonstrated in Magness's paper that a shear localization failure during penetration was beneficial to the overall performance of the KE penetrator in that a minimum nose diameter was maintained. This effect maximizes the depth of penetration for a given energy. The alloy work that has been ongoing for the last few years has tried to induce that type of failure in a tungsten-based material (alloy or composite) and much of that work was summarized at this meeting. The general thrust of the alloy development work has been to find a substitute for the traditional nickel-iron heavy alloy matrix. It is believed that by replacing the matrix with a material more prone to shear failure, a DU-like performance

could be attained in a tungsten-based material. To put significant resources behind this type of concept one must have a reasonable belief that it has an excellent possibility for success.

B.D. Baker and P.S. Dunn of Los Alamos National Laboratory, Los Alamos, NM provided the proof of principle for this alloy development approach. In two companion papers, "Matrix Substitution: Fabrication and Properties" and "Target Penetrator Interaction: 70 Vol.% Tungsten/30 Vol.% Uranium", they showed that a tungsten composite with a DU matrix behaved in a manner similar to the monolithic DU alloy that is now used in Army anti-armor projectiles. The volume relationship between tungsten and uranium was chosen to mirror the percentages between tungsten and matrix phases in the heavy alloy. This work paves the way for future matrix substitution work with identification of the alternate matrix as the first hurdle to be addressed in the near term.

There were several papers presented that examined high strain rate mechanical behavior and ballistic performance of tungsten heavy alloys. Two companion papers, "Influence of Microstructure on Shear Localization in Tungsten Heavy Alloys" and "The Role of Swaging on Dynamic Deformation of Tungsten Alloys" revealed the compressive high strain rate behavior of commercially available tungsten heavy alloys. They observed a strong dependence of shear localization on the amount of prior cold

work, grain size and tungsten volume fraction. It was shown that greater amounts of swaging result in more intense shear bands and that this effect was enhanced by finer grain sizes and lower volume fractions of tungsten.

The ballistic properties of tungsten heavy alloys are of great interest to those applying them to kinetic energy penetrators. Previously, Magness showed that these alloys are inferior to depleted uranium alloys and stated that the mechanical properties of the tungsten alloys should have no effect on the depth of penetration (DOP) ballistic performance. This was verified by other authors who examined a wide range of tungsten alloys of varying strengths and densities and found that strength and tensile elongation, over a wide range, had no influence on the performance. The only apparent driver of DOP performance was density where high density gave a small increment of improvement.

A unique cyclic heat treatment was presented that was shown to improve the toughness of the heavy alloy. The authors demonstrated a three-fold

increase in the Charpy toughness by repetitively annealing at 1150°C and water quenching. This improvement was shown to be the result of the near elimination of tungsten grain contiguity. Over the course of 20 thermal cycles, contiguity was reduced from 0.34 to less than 0.05. Interestingly, no change was noticed in the tensile properties.

Based on the breadth of subjects covered at this meeting and the enormous interest generated by interaction and cooperation it is intended that a Second International Conference on Tungsten and Tungsten Alloys be held in November, 1994.

---

*To obtain Proceedings contact:*

The Metal Powder Industries Federation  
105 College Road East, Princeton,  
NJ 08540-6692, Tel. (609) 452-7700.

*Reviewed by:*

Robert J. Dowding  
U.S. Army Research Laboratory  
Arsenal Street, AMSRL-MA-MB, Watertown  
MA 02172-0001, Tel: (617) 923-5340, and

Animesh Bose  
Paramtech Corporation  
2221 Pineview Way, Petaluma, CA 94952  
Tel: (707) 778-2262

## Forthcoming Meetings

### February, 1994

- 27-3 **6th International Symposium on Experimental Methods for Microgravity Materials Science, 123rd TMS Annual Meeting:** San Francisco, CA, Dr. Robert Schiffman, R.S. Researcher Inc., 1960 Saunders Rd., Riverwoods, IL 60015, Tel/Fax: (708) 940-7417
- 27-3 **International Symposium on Actinides: Processing and Materials:** San Francisco, CA, Obtain abstract forms from: Marlene Karl, Technical Program Coordinator, TMS-Meetings Dept., 420 Commonwealth Dr., Warrendale, PA 15086, Phone: (412) 776-9050, Fax: (412) 776-3770. Send abstracts to: Brajendra Mishra, Metallurgical & Materials Engineering, Colorado Scholl of Mines, Golden, CO 80401, Fax (303) 273-3795.
- 21-25 **APS March Meeting:** Pittsburgh, PA, American Physical Society, 335 E. 45 St., New York, NY 10017-3483, Tel: (212) 682-7341.
- 17-19 **JFCC International Workshop on Fine Ceramics '94:** Mikawa Heights, Koda-Cho, Nukata-Gun, Aichi Pref., Japan. Secretariat: Noriyuki Kosuge, Japan Fine Ceramics Center, 2-4-1 Mutsuno, Atsuta, Nagoya, 456 Japan, Tel: +(81) 52-871-3500, Fax: +(81) 52-871-3599.
- 27-31 **6th International Conference on Indium Phosphide and Related Materials:** Santa Barbara, CA, IEEE/LEOS, 445 Hoes Lane, P.O. Box 1331, Adelaide, Australia. Send Abstracts to: Prof. Ken Strafford, Chairman of the Organizing Committee, Surface Engineering Conference, C/Techsearch Inc., G.P.O. Box yy2471, Adelaide, South Australia 5001, Tel: +(61) 8-267-5466, Fax +(61) 8-267-4031.

### March, 1994

- 7-10 **Second Australian International Conference on Surface Engineering: Coatings and**

*Forthcoming Meetings*

---

Piscataway, N.J. 08855, Tel: (908) 562-3893, Fax: (908) 563-1571.

- 29-31 **Fiber Reinforced Composites:** Newcastle, U.K., The Institute of Materials, 1 Carlton House Terrace, London SW1Y 5DB, Tel: +(44) 71-839-4071, Fax: +(44) 71-839-2078.

**April, 1994**

- 4-8 **MRS Spring Meeting:** San Francisco, CA, M. Geil, Materials Research Society, 9800 McKnight Blvd., Pittsburgh, PA 15237, Tel: (412) 367-3003, Fax: (412) 367-4373.

- 18-20 **First International Symposium on Semiconductor Processing and Characterization with Lasers, Applications in Photovoltaics:** Stuttgart, Germany, Dr. M. Breiger, Institut für Technische Physik, DLR Stuttgart, Pfaffenwaldring 38-40, D-7000 Stuttgart 80, Germany, Tel: +(49) 711-6862-770, Fax: +(49) 711-6862-788.

- 19-21 **The Best in Melting and Metal Treatments:** University of Warwick, U.K. Hywel Morgan, Conference Coordinator, BCIRA Membership Services, Alvechurch, Birmingham B48 7QB, U.K.

- 25-29 **ICMCTF:** San Diego, CA, USA Greg Exarhos, Pacific NW Lab, PO Box 999, MS K2-44, Richland, WA 99352, Tel: (509) 375-2440, Fax: (509) 375-2186.

**May, 1994**

- 8-11 **International Conference on Powder Metallurgy and Particulate Materials:** Toronto, Ontario, Canada, MPIF, 105 College Road East, Princeton, N.J. 08540-6692, Fax 609-987-8523.

- 24-26 **International Conference on Superplasticity in Advanced Materials (ICSAM 94):** Moscow, A. Alaykin, Moscow Steel and Alloy Institute, Moscow, Russia, Tel: +(7) 95-236-1210, Fax: +(7) 95-237-8756.

- 29-1 **5th International Symposium on Ceramic Materials & Components for Engines:** Shanghai, China, Prof. Xiren Fu, Shanghai Institute of Ceramics, Chinese Academy of Sciences, 1295 Dingxi Road, Shanghai 200050, China.

- 30-1 **Euromat 94:** Balatonszeplak, Hungary, Hungarian Mining and Metallurgical Society, Tel: +(36) 1-201-7337, Fax: +(36) 1-156-1215.

*Forthcoming Meetings*

---

**June, 1994**

- 1-4 **Forum on New Materials: Advances in Inorganic Films & Coatings:** Florence, Italy, 8th CIMTEC, Forum on New Materials, Topical Symposium I, P.O. Box 174, 48018 Faenza, Italy, Tel: +(546) 22-461, Fax: +(546) 664-138
- 6-10 **PM 94:** Paris, France, Societ  Francaise de Metallurgie et de Materiaux, Tel: + 1-47-67-88-71, Fax: +1-47-67-85-77.
- 6-10 **International Symposium on Optical Interference Coatings:** Grenoble, France, SPIE, P.O. Box 10. Bellingham, WA 98227-0010, Tel: (206) 676-3290, Fax: (206) 647-1445.
- 17-22 **International Conference on PTM, Solid to Solid Phase Transformations In Inorganic Materials '94:** Nemacon Woodlands, Pittsburgh, PA, TMS, Meeting Services, 420 Commonwealth Drive, Warrendale, PA 15086-9987.
- 27-29 **International Symposium on Superalloys and Derivatives:** Pittsburgh Airport Marriott, Pittsburgh, PA, TMS, Meeting Services, 420 Commonwealth Drive, Warrendale, PA 15086-9987, Tel: (412) 776-9050, Fax: (412) 776-3770.

**July, 1994**

- 17-22 **International Conference On New Diamond Science and Technology:** Japan New Diamond Forum, Sumitomo Seimei Midousuji Bldg., 13F, 14-3, Nishitenma 4 -chome, Kita-Ku, Osaka 530, Japan, Fax: +(81) 6-311-2130.

**September, 1994**

- 21-23 **TMS Extraction and Process Metallurgy Meeting, Second International Symposium on Metallurgical Processes for The Year 2000 and Beyond:** San Diego, CA at the Rancho Bernardo Inn; General Meeting Chairman: H.Y. Sohn; Dept. of Metallurgical Engineering, 412 WBB, University of Utah, Salt Lake City, UT 84112-1183, Tel: (801) 581-6386, Fax: (801) 581-5560.

**October, 1994**

- 3-7 **ICNM-2: Second International Conference on Nanostructured Materials,** Greece, Contact: H. Gleiter, Universitat des Saarlandes, Fax: +(49) 681-302-5222.
- 24-28 **AVS 41st National Symposium:** Denver, CO, USA. AVS, 335 E. 45th St., New York, NY 10017, Tel: (212) 661-9404.

***Forthcoming Meetings***

---

**November, 1994**

15-17 **3rd International Conference on Behavior of Materials during Machining:** Warwick, U.K., The Institute of Materials, 1 Carlton House Terrace, London SW1Y 5DB, Tel: +(44) 71-839-4071, Fax: +(44) 71-839-2078.

28-2 **MRS Fall Meeting:** Boston, MA, M. Geil, Materials Research Society, 9800 McKnight Rd., Pittsburgh, PA 15237, Tel: (412) 367-3003, Fax: (412) 367-4373.

**May, 1995**

22-24 **Zinc & Lead '95:** Sendai, Japan. M. Hino, Department of Metallurgy, Faculty of Engineering, Tohoku University, Aoba, Aramaki, Sendai, Japan 980, Fax: +(81) 22-268-2949, or J.E. Dutrizac, CANMET, 555 Booth Street, Ottawa, Ontario, Canada K1A 0G1, Tel: (613) 995-4823, Fax: (613) 995-9041.

**October, 1995**

16-20 **AVS 42nd National Symposium:** Minneapolis, MN, USA. AVS, 335 E. 45th St., New York NY 10017, Tel: (212) 661-9404.

**October, 1996**

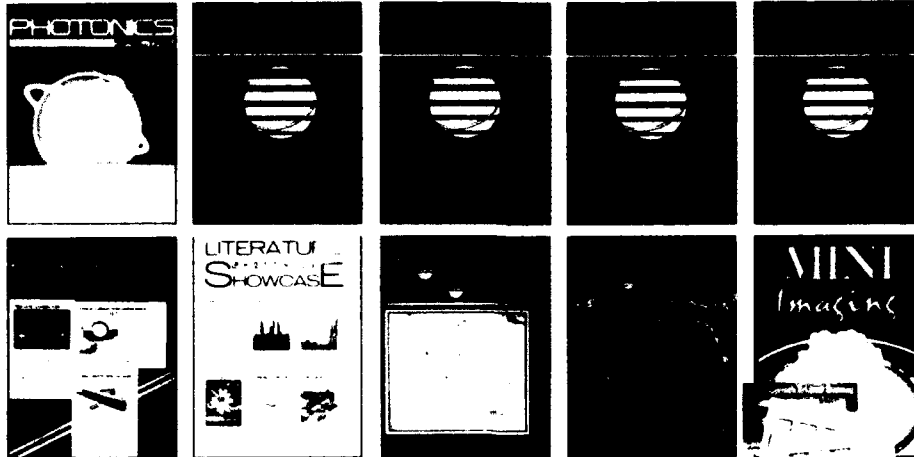
14-18 **AVS 43rd National Symposium:** Philadelphia, PA. AVS, 335 E. 45th St., New York NY 10017, Tel: (212) 661-9404.

***Please send announcement of meetings to:***

Dr. T.S. Sudarshan  
Editor  
Materials Modification, Inc.  
2929-P1, Eskridge Center  
Fairfax, VA 22031

## The Complete Photonics Library

These eleven leading publications serve every major segment of the photonics technology.



### PHOTONICS SPECTRA

**Photonics Spectra** is today's news, information and technology solutions source for photonics (optics, lasers, fiber optics, electro-optics, imaging and optical computing). It is the magazine referred to worldwide by the largest purchasing audience of engineers, scientists, designers and specifiers, a BPA-qualified circulation of 81,492 as of May 1992, and a total distribution of over 90,000. Each month, **Photonics Spectra** provides global news reports, technology and applications updates, in-depth staff reports, articles by industry experts, and 27 departments.

### THE PHOTONICS CORPORATE GUIDE® TO PROFILES & ADDRESSES

The four-volume **Photonics Directory**, published for 39 years, is considered to be the most trusted reference in the photonics industry. It is also the only directory with a paid circulation. **The Photonics Corporate Guide**, Book 1 of the set, provides complete profiles on 3500 international manufacturers — addresses, phone and FAX numbers, sizes, personnel and products — plus a special catalog section.

### THE PHOTONICS BUYERS' GUIDE® TO PRODUCTS & MANUFACTURERS

Book 2, **The Photonics Buyers' Guide**, has more than 1680 product categories that list products by manufacturers or distributors and identifies them as custom or stock items.

### THE PHOTONICS DESIGN & APPLICATIONS HANDBOOK®

Book 3, **The Handbook**, has more than 400 pages of practical information, with new developments and technology know-how for today's design and applications engineers. It is completely revised and updated each year to ensure that the latest technology is covered.

### THE PHOTONICS DICTIONARY™

Updated and expanded each year, Book 4 is the only **Dictionary** in the industry. It has more than 5500 technical terms and definitions, with illustrations, abbreviations and symbols.

### LITERATURE SHOWCASE

The **Photonics Literature Showcase** is exclusively devoted to high-quality promotion of brochures, catalogs and other literature, and features full-color photographs, concise copy and reader service numbers for immediate response. The 78,000 circulation is a combination of the US circulations of **Photonics Spectra** and **The Photonics Directory**.

### PHOTONICS PRODUCT PORTFOLIO

The **Photonics Product Portfolio** is the industry's only product publication, featuring full-color photos, descriptions and reader service numbers. It is distributed to 78,000 decision-makers three times a year.

### THE PHOTONICS EUROPEAN DIRECTORY™

The **Photonics European Directory** contains addresses, telecommunications numbers and products for photonics manufacturers, distributors and suppliers in Europe and Israel. This important publication is distributed to the European and Israeli circulations of **Photonics Spectra** and to attendees of major European trade shows.

### THE PHOTONICS PACIFIC RIM / ASIAN DIRECTORY™

The **Photonics Asian/Pacific Rim Directory** reaches more than 10,000 important buyers in Asia and the Pacific Rim countries, a combination of **Photonics Spectra** readers and members of societies in these countries.

### MINI-MAGAZINE

Special segments of photonics technology are highlighted monthly. These include detectors, fiber optics, optics, lasers, imaging, spectroscopy and positioning. These special sections are overprinted and distributed at trade shows for maximum impact.

### PHOTONICS POSTCARDS

**Photonics Spectra Postcards** are published three times a year and reach 70,000 domestic subscribers. A unique advertising package with established impact, the **Postcards** go to engineers, designers, managers, specifiers and researchers.

Stay ahead of the latest developments in fiber-reinforced composite materials, including thermoplastic, metal, and ceramic matrix composites with the new edition of...

# Fiber-Reinforced Composites

Materials, Manufacturing, and Design

Second Edition,  
Revised and Expanded

(Mechanical Engineering Series/83)

**P. K. MALLICK**

*The University of Michigan—Dearborn*

May, 1993

576 pages, illustrated

\$150.00

\$ 65.00 *on orders of five or more copies,  
for classroom use only*

## Praise for the previous edition...

"P. K. Mallick has done an excellent job in writing a very readable and comprehensive textbook which should greatly assist both those studying composites and those lecturing on the subject. The presentation is good, the diagrams are clear, and the book is well worth having as a reference text by anyone working in the field."

—*Advanced Composites Bulletin*

"...provides valuable background information on composites."

—*Ceramic Bulletin*

"...the author has covered a vast expanse of knowledge in a reasonable number of words."

—*Applied Mechanics Reviews*

## Marcel Dekker, Inc.

270 Madison Avenue, New York, NY 10016  
(212) 606 9000

Hetgasse 4, Postfach 812, CH-4001 Basel, Switzerland  
Tel 061 261 8482

Maintaining the broad, interdisciplinary perspective that made the first edition so popular, this **Second Edition** of an invaluable **reference/text** provides comprehensive discussions of **all** aspects of fiber-reinforced composites, including materials, mechanics, properties, test methods, manufacturing, and design.

Written from a conceptual point-of-view and emphasizing fundamentals, **Fiber-Reinforced Composites, Second Edition** offers fully up-to-date, thoroughly expanded sections on

- fibers and matrix, including thermoplastic matrices
- discontinuous fibers and laminated structures
- static mechanical properties, fatigue properties, and damage tolerance
- resin flow, bag molding, filament winding, and resin transfer molding
- environmental effects
- and much more!

Enhancing those didactic features that sent the first edition into multiple printings and led to its adoption at a host of colleges and universities, including the *United States Air Force Academy*, *Stevens Institute of Technology*, and *Pennsylvania State University*, the **Second Edition** offers many **more** application examples and worked-out problems in each chapter and provides entirely **new** coverage of current topics such as

- thermoplastic composite manufacturing
- delamination initiation
- metal and ceramic matrix composites
- woven fabrics
- residual stresses
- alternative micromechanical equations
- and more!

With over **1000** literature citations, figures, tables, and display equations, **Fiber-Reinforced Composites, Second Edition** is an incomparable **reference** for mechanical, manufacturing, materials, aerospace, automotive design, and structural engineers, and the **text** of choice for upper-level undergraduate and graduate students in these disciplines.

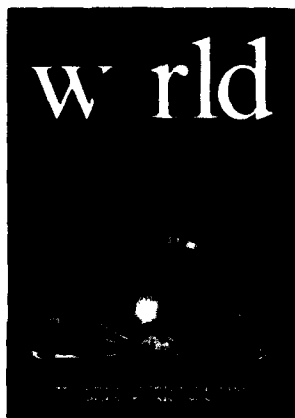
## Contents

Introduction
Materials
Mechanics
Performance
Manufacturing
Design
Metal and Metal Ceramic Composites
Appendixes
Woven Fabric Terminology
Residual Stresses in Fibers and Matrix in a Lamina due to Cooling
Alternative Equations for the Elastic and Thermal Properties of a Lamina
Halpin-Tsai Equations
Typical Mechanical Properties of Unidirectional Continuous Fiber Composites
Properties of Various SMC Composites
Typical Mechanical Properties of Metal Matrix Composites
Determination of Design Allowables
Useful References
Selected Computer Programs

ISBN: 0-8247-9031-0

*This book is printed on acid-free paper.*

**in** two leading publications from  
The Institute of Materials . . .



#### Materials World (monthly)

As the monthly members' journal of The Institute of Materials, *Materials World* embraces the whole spectrum of materials - metals, ceramics, plastics, rubber, glasses and composite materials, with particular emphasis on advanced technologies, latest developments and new applications.

The journal gives regular coverage to topics of fundamental importance to those in industry, including: analytical techniques, joining technology, materials development, materials processing, microscopy, powder technology, quality assurance, testing (destructive and NDT) and thermal processing.

The journal contains regular sections on international news, conferences, courses and exhibitions, new books and publications, Institute news, products and equipment.

*Materials World* is a leading advertising medium for products and services for the materials industries.

#### 1994 Subscription Rates

EC Non-EC  
£136.00 US\$283.00

#### MATERIALS SCIENCE AND TECHNOLOGY



#### Materials Science and Technology (monthly)

*Materials Science and Technology* carries refereed papers on a variety of topics relevant to those concerned with the production, processing, structure and properties, and application of structural and engineering materials and their future development.

Types of contribution include . . .

- \* refereed papers on research and practice
- \* critical assessments
- \* overviews on topics of current importance
- \* book reviews
- \* diary of forthcoming events

#### 1994 Subscription Rates

EC Non-EC  
£438.00 US\$837.00

Free sample copies on  
request!

For further information about books or journals published by The Institute of Materials or to place your order, please contact:

Credit card holders  
fax your order now on  
011 44 71 839 2078 !!



The Institute of Materials  
Sales & Marketing Department  
1 Carlton House Terrace  
London SW1Y 5DB, UK  
Tel. (071) 976 1338 Fax. (071) 839 2078  
(Registered with Charity No. 269275)

# SILICATES INDUSTRIELS

## Ceramic Science and Technology

Journal of the Belgian Ceramic Society

*WILL ORGANIZE IN 1994*

### The CCCIII conference

#### Advisory Board of the Journal

J.F. BAUMARD	(F)
R.J. BROOK	(GB)
F. CAMBIER	(B)
S. DE AZA	(E)
G. FANTOZZI	(F)
S. HAMPSHIRE	(IRL)
J.M. HAUSSONNE	(F)
H.W. HENNICKE	(D)
W. HOLAND	(D)
C. PALMONARI	(I)
M. PATEL	(IND)
J.P. SKALNY	(USA)
S. SOMIYA	(J)
N. TENOUTASSE	(B)
F. THEVENOT	(F)
H. YANAGIDA	(J)

#### Editorial Board

J. TIRLOCC	(CRIBC, B)
P.H. DUVIGNEAUD	(ULB, B)

#### Editor

R. RICHEZ  
4, Avenue Gouverneur CORNEZ  
B-7000 MONS (Belgium)

### CERAMIC-CERAMIC COMPOSITES III

Ceramic-Ceramic Composite materials comprised of a ceramic matrix reinforced with particles, allotropic phases, short and long fibres, whiskers or platelets, have been developed by the academic and industrial sectors over recent years.

Two very successful international conferences on this topic have already been organised by the Belgian Ceramic Society and its journal "Silicates Industriels (Ceramic Science and Technology)" in April 1987 and October 1989.

Since then, many developments in the processing, the characterization and the applications of this family of materials have occurred and the Organizing Committee of CCC I and CCC II considered it timely to plan the third event in this series. It will take place in **October 18-20, 1994** in MONS (Belgium).

The conference will include both scientific and industrial communications, with selected invited papers to review the state of the art. Proceedings will be published in special issues of the journal.

If you are interested in attending this meeting, please contact :

Dr F. Cambier  
Belgian Ceramic Society  
Av. Gouverneur Cornez, 4 - B-7000 Mons  
Tel +32/65/348000 - Fax +32/65/348005

Annual subscription rate for foreign countries : 5,200 Belgian francs  
Address : SILICATES INDUSTRIELS - Avenue Gouverneur Cornez, 4, B-7000 MONS (Belgium)  
phone : 32/65/348000 - fax : 32/65/348005  
Bank : Crédit Communal de Belgique - account n°068-0528690-67

Learn the latest methods and the most time-saving, cost-efficient procedures with the new edition of

# Project and Cost Engineers' Handbook

**aace**

Sponsored by AACE International  
(The Association for Total Cost Management)

THIRD EDITION, REVISED AND EXPANDED

(Cost Engineering Series 19)

edited by  
**KENNETH K. HUMPHREYS**  
**LLOYD M. ENGLISH**

AACE International, Morgantown, West Virginia

November, 1992  
512 pages, illustrated  
\$65.00

An incomparable  
on-the-job reference and the perfect  
self-study guide for cost engineering  
certification candidates!

#### Praise for the second edition!

"This is not only a basic reference book but has been planned as a guide to individuals to study for recognition as a Certified Cost Engineer. It is a worthy addition to the cost engineering series and every member of the cost engineering profession should have their own personal copy."

—*The Cost Engineer*

Maintaining and enhancing the authoritative coverage of all aspects of cost engineering that made this the standard reference in the field, *Project and Cost Engineers' Handbook, Third Edition* continues to provide detailed discussions of such topics as project evaluation, cost projection and control, project management, planning and scheduling, operations research, and cost reporting.

Designed as a day-to-day resource for practitioners and as a self-study guide for the AACE International cost engineers' certification examination, *Project and Cost Engineers' Handbook, Third Edition*

- aids conceptual estimating with worked examples, formulas, figures, charts, and definitions
- explains key methods and basic principles
- supplies sample working documents and checklists for estimates, coding accounts, and monitoring and interpreting project data
- and much more!

Offering state-of-the-art information on actual industry practices furnished by recognized leaders in the field, *Project and Cost Engineers' Handbook, Third Edition* presents such new features as

- up-to-the-minute approaches to scheduling and the use of scheduling software
- an examination of the burgeoning potential of personal computer systems and programs
- elucidations of the current tax law plus examples of Modified Accelerated Cost Recovery System tax calculations
- an explanation of tax evaluation methods outside the U.S.
- an exhaustive appendix of suggested readings for in-

This one-of-a-kind volume is indispensable for cost, project, and design engineers, project managers, cost estimators and controllers, planners and schedulers, and upper-level undergraduate and graduate students in engineering, economy, construction estimation, planning and scheduling, and network analysis courses.

#### CONTENTS

Cost Engineering Basics  
Cost Accounting  
Cost Estimating  
Economic Equivalence and Profitability  
Cost Control and Reporting  
Project Management and Schedule Control  
Cost Indexes, Escalation, and Location Factors  
Operations Research Techniques  
Computer Applications for Project Control  
Appendix A: Certification Examination Study Guide  
Appendix B: Standard Cost Engineering Terminology  
ISBN 0-8217-8746-3

**Marcel Dekker, Inc.**

270 Madison Avenue, New York, NY 10016

■ (212) 696-9000

Hutgasse 4, Postfach 812, CH-4001 Basel, Switzerland

■ Tel. 061-261-8482

Learn to design passive polymer components and systems that fully integrate optics and electronics with...

With contributions by leading international experts from the United States, Europe, and Japan!

# POLYMERS FOR LIGHTWAVE AND INTEGRATED OPTICS

## Technology and Applications

(Optical Engineering Series/32)\*

### CONTENTS

edited by

**LAWRENCE A. HORNAK**

West Virginia University, Morgantown, and  
AT&T Bell Laboratories, Holmdel, New Jersey

July, 1992

768 pages, illustrated  
\$150.00

This unique, single-source reference offers up-to-the-minute coverage of the **entire** field of polymer integrated optics, including passive polymer materials and their applications, and second- and third-order nonlinear materials.

Providing detailed reviews of traditional topics and explicating the latest research, **Polymers for Lightwave and Integrated Optics**

- delineates fundamental areas such as theoretical modeling, design, and the synthesis and characterization of optical polymer materials
- treats passive polymers for optical fibers, integrated waveguides, holograms, and microelements
- discusses passive polymer integrated optics, polymer optical interconnections, and all-optical and electro-optic switching
- examines system application issues such as processibility, materials and functional compatibility, and optical/electronic interfaces
- emphasizes the interdependencies of systems and materials
- furnishes perspectives on future directions
- and much more!

With over **1800** literature citations and figures, **Polymers for Lightwave and Integrated Optics** is an invaluable resource and practical guide for optical systems, electrical and electronics, and laser engineers and designers, materials research scientists, optical physicists, and graduate-level students in these disciplines.

#### Passive Optical Polymers and Applications

Polymeric Optical Fibers

*Toshikuni Kato*

Polymer Optical Fibers in Data Communications and Sensor Applications

*J. Theis, A. Brockmeyer, W. Grob, and T. F. Steblin*

Graded Index Materials and Components

*Yasuhiko Koike*

Patterning Poly(methyl methacrylate)

*Hilmar Franke*

Photopolymers for Holography and Waveguide Applications

*Bruce M. Monroe and William K. Smothers*

Microoptical Grating Elements

*Nobuhiko Kawatsuki and Masao Uetsuki*

Synthesis and Application of Polysilyne Thin Film Optical Waveguide Media

*Timothy W. Weidman, Elizabeth W. Kuczek,*

*Patricia A. Bianconi, and Lawrence A. Hornak*

Polyimide Lightguides

*Hilmar Franke*

Polyimide Materials for Waveguide Applications

*B. L. Booth*

Polymer Optics in the Information Age

*Dau is H. Hartman*

#### Nonlinear Optical Polymers and Applications

Optical Polymers and Multifunctional Materials

*R. A. Norwood, T. Finkelsky, H. A. Goldberg, G.*

*Khanarian, J. B. Stamatoff, and H. N. Yoon*

Molecular Polymeric Materials for Nonlinear Optics

*Kenneth D. Singer*

Guest-Host Polymer Systems for Second-Order Optical Nonlinearities

*Philip Pantelis and Julian R. Hill*

Nonlinear Optical Side-Chain Polymers and Electro-Optic Test Devices

*C. P. J. M. van der Vorst, W. H. G. Horsbuis, and*

*G. R. Mohlmann*

Fabrication and Characterization of Polymeric Lightwave Devices

*William R. Holland*

Large-Scale Integration of Electro-Optic Polymer Waveguides

*R. Lytel, G. F. Lipscomb, J. T. Kenney, and E. S. Binkley*

Polymer Etalons and Free Space Interconnects

*Stephen T. Nowel and Charles A. Eldering*

Third-Order Optical Processes in Linear Chains: Electron Correlation Theory and Experimental Dispersion Measurements

*J. R. Heflin and A. F. Garito*

Third-Order Nonlinear Optical Processes and Ultrafast Dynamics in Polymers

*Takayoshi Kobayashi*

Third-Order Materials: Processes and Characterization

*F. Kajzar, J. Messier, J. M. Nizet, and P. Ramond*

Third-Order Nonlinear Optical Properties of Polymeric Materials

*Toshikuni Kato and Takashi Kuribara*

All-Optical Phase Modulation in Polydiacetylene Waveguides

*M. Takur*

Holographic Memories Using Organic Storage Materials

*W. Driemeter and M. D. Lechner*

Material Structures of Organic Molecules and Matrices for Persistent Spectral Hole Burning

*Uichi Itoh and Toshiro Tam*

ISBN: 0-8247-8697-1

*The book is printed on acid-free paper.*

**Optical Engineering** is a series of individual volumes under the general editorial direction of Brian J. Thompson, Provost and Professor of Optics, University of Rochester, Rochester, New York.

**Marcel Dekker, Inc.**

270 Madison Avenue  
New York, NY 10016  
(212) 696-9000

Hutgasse 4, Postfach 812  
CH-4001 Basel, Switzerland  
Tel. 061-261-8482

Get easy access to techniques that offer controlled, reproducible, and well-defined properties when working with the...

# Preparation of Thin Films

**JOY GEORGE**  
*Cochin University of Science and Technology,  
Cochin, Kerala, India (retired)*

February, 1992  
384 pages, illustrated  
\$125.00 (U.S. and Canada)  
\$143.75 (All other countries)

  
Marcel  
Dekker,  
Inc.

270 Madison Avenue  
New York, NY 10016  
(212) 696-9000

Hutgasse 4, Postfach 812  
CH-4001 Basel, Switzerland  
Tel. 061-261-8482

This book provides, in a single source, an up-to-date and comprehensive account of various deposition techniques for the preparation of thin films of elements, compounds, alloys, ceramics, and semiconductors—emphasizing inorganic compound thin films.

*Discusses high vacuum and chemical deposition methods used for preparing high temperature superconducting oxide thin films—an area of unprecedented research activity!*

#### *Preparation of Thin Films*

- describes thin film preparation by vacuum evaporation—offering classification according to the mode of heating
- details thin film preparation by the sputtering technique and its variants—including triode, getter, radio frequency, magnetron, and ion beam sputtering
- examines ion beam and ion-assisted techniques—discussing the ion-plating and hot hollow cathode approaches
- explores reactive deposition techniques—presenting the reactive evaporation, reactive sputtering, reactive ion beam sputtering, and reactive ion plating methods
- covers epitaxial methods such as metal organic chemical vapor deposition and molecular beam epitaxy—considering techniques for producing high quality semiconductor thin films for device applications
- and much more!

Illustrated with over 200 drawings and tables and containing more than 1000 bibliographic references, *Preparation of Thin Films* is important reading for plastics, materials, and process engineers; industrial physicists; physical, surface, colloid, and polymer chemists; and graduate and postgraduate students in these disciplines.

## Contents

Vacuum Evaporation  
Sputtering  
Ion Beam and Ion-Assisted Deposition  
Reactive Deposition Techniques  
Ionized Cluster Beam Methods  
Chemical Methods of Film Deposition  
Epitaxial Film Deposition Techniques  
Other Methods of Film Deposition  
Summary

ISBN: 0-8247-8196-1

*This book is printed on acid-free paper.*

Increase your understanding of ceramic technology and its practical applications with the new edition of...

# MODERN CERAMIC ENGINEERING

Properties, Processing, and Use in Design

Second Edition,  
Revised and Expanded

(Improved Materials Series 11)

**DAVID W. RICHERSON**

Consultant, and University of Utah, Salt Lake City

January, 1992 872 pages, illustrated

\$125.00 (U.S. and Canada)

\$143.75 (All other countries)

\$ 55.00 on orders of five or more copies,  
for classroom use only

## International praise for the first edition...

"...a welcome book, since it fills the gap between introductory materials science and engineering courses and the classic ceramic text of Kingery [Bowen and Uhlmann]...."

"...recommended for classroom use."

—*American Ceramic Society*

"...though written as a textbook—complete with chapter problems—the book is quite a useful reference."

"...recommended for anyone who by choice or necessity will be dealing with the manufacture, finishing or assembly of ceramic parts."

—*The Carbide and Tool Journal*

"...contains much information that would be hard to find elsewhere in a single source...."

"The book is well produced with a high standard of illustration and lay-out."

—*The British Ceramic Society Journal*

"...Students of ceramics will be immensely benefited in gathering a comprehensive understanding and the practitioners of ceramics will find this publication a practical guide."

—*The Indian Ceramic Society Journal*

Maintaining the non-mathematical approach that made the first edition so popular, this reference/text describes the source of physical, thermal, mechanical, electrical, magnetic, and optical properties in ceramics; reviews the fabrication processes used for manufacturing ceramic components; and discusses the selection and design of ceramic components for advanced engineering applications.

Updated and revised throughout, here are some of the changes in the *Second Edition of Modern Ceramic Engineering*

- a new chapter on toughening and ceramic matrix composites
- a new chapter on phase equilibrium
- expanded material on crystal structure and crystal chemistry
- expanded discussions on electrical, dielectric, optical, and mechanical properties
- expanded chapters on all aspects of processing of ceramics
- and more!

continued on the back ➡

## Marcel Dekker, Inc.

270 Madison Avenue, New York, NY 10016  
(212) 696-9000

Hutgasse 4, Postfach 812, CH-4001 Basel, Switzerland  
Tel. 061-261-8482

# MODERN CERAMIC ENGINEERING

Second Edition

Additionally, this practical volume offers several self-study and teaching features, including

- introductions for each section of the book summarizing the objectives of the section and its content chapter by chapter
- end-of-chapter problems that clarify and reinforce important concepts
- a new glossary with easy-to-understand definitions
- over 500 drawings, photographs and micrographs, and tables to help readers grasp information easily and quickly
- a Solutions Manual (for instructors only)\*\*

*Presents unique coverage on the design of brittle materials and the use of composite fabrication to decrease brittle behavior!*

*Modern Ceramic Engineering, Second Edition* serves as an invaluable desk-top reference for mechanical, ceramic, materials, chemical, design, and manufacturing engineers and as an excellent text for upper-level undergraduate and graduate students in these disciplines.

\*\*Requests for the Solutions Manual must be made on official school stationery.

## Contents

### Structures and Properties

Atomic Bonding and Crystal Structure  
Crystal Chemistry and Specific Crystal Structures  
Phase Equilibria and Phase Equilibrium Diagrams  
Physical and Thermal Behavior  
Mechanical Behavior and Measurement  
Electrical Behavior  
Dielectric, Magnetic, and Optical Behavior  
Time, Temperature, and Environmental Effects on Properties

### Processing of Ceramics

Power Processing  
Shape-Forming Process  
Densification  
Final Machining  
Quality Assurance

### Design with Ceramics

Design Considerations  
Design Approaches  
Failure Analysis  
Toughening of Ceramics  
Applications: Material Selection

### Glossary

ISBN: 0-8847-8634-3

*This book is printed on acid-free paper.*

\* *Engineered Materials* is a series of individual volumes under the general editorial direction of Dr. Peter Hilton, Arthur D. Little, Inc., Cambridge, Massachusetts

Mail today!

Mail to: Promotion Dept., MARCEL DEKKER, INC.  
270 Madison Avenue, New York, N. Y. 10016

Please send me \_\_\_\_\_ copy(ies) of *Modern Ceramic Engineering, Second Edition* by David W. Richerson at \$125.00 plus \$1.50 for postage and handling per volume. On prepaid orders, please add \$ .50 per volume.

I enclose payment in the amount of \$ \_\_\_\_\_ by:  check  money order  
 Visa  MasterCard (4-digit interbank no. \_\_\_\_\_)  Am. Exp.

Card No. \_\_\_\_\_ Exp. Date \_\_\_\_\_

Please bill my company: P.O. No. \_\_\_\_\_

Signature \_\_\_\_\_  
(must be signed for credit card payment)

Name \_\_\_\_\_

Address \_\_\_\_\_

City/State/Zip \_\_\_\_\_

N. Y. residents must add appropriate sales tax. Prices are 15% higher outside the U.S. and Canada, and subject to change without notice.

Marcel Dekker, AG, Basel, bills in U.S. dollars at the United States export price. Payments are accepted in U.S. dollars or in Swiss francs at current day payment conversion rates. Domestic billings in Switzerland are in Swiss francs.

Form No. 119186

Printed in U.S.A.

  
For Credit Card and  
Purchase Orders, and Customer Service  
CALL TOLL-FREE 1-800-228-1160  
Mon.-Fri. 8:30 a.m. to 5:45 p.m. (EST)  
or FAX your order to 914-796-1772

Analyze all major metal manufacturing processes—  
*more efficiently and effectively—with ...*

# Estimating and Costing for the Metal Manufacturing Industries

(Cost Engineering Series/18)

**ROBERT C. CREESE**

*West Virginia University, Morgantown*

**M. ADITHAN** and **B. S. PABLA**

*Technical Teachers Training Institute, Chandigarh, India*

August, 1992

288 pages, illustrated

\$99.75

\$49.75 \* on orders of five or more copies,  
for classroom use only

## Contents

This practical **reference/text** provides a thorough overview of cost estimating as applied to various manufacturing industries—with special emphasis on metal manufacturing concerns

**Presents examples and study problems illustrating potential applications and the techniques involved in estimating costs!**

Containing both U.S. and metric units for easy conversion of world-wide manufacturing data. **Estimating and Costing for the Metal Manufacturing Industries**

- outlines professional societies and publications dealing with cost estimating and cost analysis
- details the **four basic metalworking processes**: machining, casting, forming, and joining
- reveals **five techniques** for capital cost estimating, including the **new AACE International's Recommended Practice 16R-90** and the **new** knowledge and experience method
- discusses the effect of scrap rates and operation costs upon unit costs
- offers **four formula methods** for conceptual cost estimating and examines material-design-cost relationships
- describes cost indexes, cost capacity factors, multiple-improvement curves, and facility cost estimation techniques
- offers a generalized metal cutting economics model for comparison with traditional economic models
- and more!

**Estimating and Costing for the Metal Manufacturing Industries** serves as an on-the-job, single-source **reference** for cost, manufacturing, and industrial engineers and as an important **text** for upper-level undergraduate, graduate, and postgraduate students in cost estimating, engineering economics, and production operations courses.

Introduction  
Cost Estimation  
Costing  
Analysis of Overhead Expenses  
Break-Even Analysis  
Depreciation, Taxes, Cash Flow, and Time Value of Money Considerations  
Costing for Materials with Design Considerations  
Conceptual Cost Estimating Techniques  
Basic Costing for Machining Processes  
Basic Costing for Welding Processes  
Basic Costing for Casting Processes  
Basic Costing for Forging Processes  
Cost Indexes, Cost Capacity Factors, and Improvement Curves  
Facility Capital Cost Estimation and the Estimation of Operating Costs  
Appendix: A Generalized Metal Cutting Economics Model for Single-Pass Cutting in Turning, Drilling, Shaping, and Milling Operations

ISBN: 0-8247-8712-9

*This book is printed on acid-free paper*

**A Solutions Manual to the end-of-chapter problems is available FREE OF CHARGE to instructors only. Requests for the manual must be made on official school stationery.**

**marcel  
dekker,  
inc.**

270 Madison Avenue, New York, NY 10016  
(212) 696-9000

Hutgasse 4, Postfach 812, CH-4001 Basel, Switzerland  
Tel: 061-261-8482

## Preparation of Manuscripts

A paper submitted for publication must be an original work that is **not** being considered for publication elsewhere.

### 1.0 Directions for Submission:

One original manuscript carefully inserted in a folder, and three (3) copies of the manuscript must be submitted to one of the Editors:

T.S. Sudarshan  
Materials Modification Inc.  
2029-P1 Eskridge Center  
Fairfax VA 22031

T.S. Srivatsan  
Dept. of Mechanical Engineering  
The University of Akron  
Akron, OH 44325

### 2.0 Format of Manuscript:

Page size is 17.8 x 25.4 cms (7" x 10"). General format of the manuscript should be as follows: Title of article, names and full addresses of authors, abstract (maximum 150 words) and text discussion. All headings including title, should be Initial caps only.

The text discussion should be divided into such major sections as:

- 1.0 Introduction
- 2.0 Methods
- 3.0 Results
- 4.0 Discussions
- 5.0 Conclusion
- 6.0 Acknowledgments, and
- 7.0 References.

Center title and abstract headings. All other headings should be flush with the left margin. Secondary headings, throughout the paper, should be numbered such as 2.1, 2.2 etc. . No foot notes should be included.

### 3.0 Guidelines for Style:

- No underlining any where; use only bold or italics. Also no All-Caps.
- Single line spacing only throughout.
- No tabs or indents anywhere in the paper, except for the indents in References.
- Use Times Roman 11 point throughout and do not change the font anywhere in the text.
- The superscript and subscript codes must not cover any blanks or tab character.
- There should not be any hard returns inside a paragraph. The text should wrap automatically.
- Use only superscripted "o" for degree symbol.
- Number each page of the manuscript (not the word processing file) lightly at the bottom of the sheet with a light blue pencil.
- Use only SI units throughout. Use negative indices rather than an oblique, thus:  $g\ m^{-2}$  **not**  $g/m^2$ . Do not use Imperial units.

### 4.0 References:

References should be listed at the end of the paper in the order in which they occur in the text. They should be indicated within the text by sequential numerals in parentheses, at the end of the sentence. The references consecutively numbered in numerical order, should be separated from one another by an extra line of space. References to journal articles should include (1) surname, first and middle initials, (2) journal, (3) volume number, (4) first page, and (5) year, in that order. References to books should include (1) author, surname, first and middle initials, (2) title of book, (3) editor of book (if applicable), (4) edition

of book (if any), (5) publisher, (6) city of publication, (7) page reference, and (8) year of publication.

Use Indent key in word processor after entering reference number. Expand all abbreviations such as "Proc.", "Inst.", "J.", etc. For the first author, enter last name first. For journal articles, the issue **must be** specified in the format: "Vol.37, No.2, p.81, (1990)."

#### **5.0 Tables:**

Tables should be typed as part of the text, and must be separated from the text by a two-line space above and below the table. If using WordPerfect software, please use Table option to create tables. Use Arabic numerals for the table number. Tables should be inserted in the text close to the point of reference, and authors must make sure that a table does not run over to the next page. Titles should be typed single-spaced preceded by the word Table. Please remember that the available width in the printed page is only 17.8 cms (5.25").

#### **6.0 Illustrations:**

Graphs, and other numbered figures should be drawn using graphics software and printed on laser printer. They must be placed on separate sheets of white paper and placed at the end of the text. Two graphs or figures should be placed per page. Allowing for figure captions, each figure must fit within the size 12.7 wide x 7.6 cms high (5" x 3"). Figures should not be placed in the body of the text. Photographs must be glossy black and white prints and must have µm markers. Illustrations larger than 12.7 x 7.6 cms will be rejected. Figure numbers, name of first author, and arrow indicating "top" should be written

in light blue pencil on the back or typed on a gummed label, which should be attached to the back of the illustration. For graphs, legend for symbols used (eg. ⊕, ⊖, Δ) must be placed within each graph, and **not** in the caption. Captions for the figures should be typed single spaced on a separate sheet, along the full width of the page, and preceded by the word Figure and a number in Arabic numerals.

#### **7.0 Printing of Manuscript:**

The manuscript must be printed on good quality white bond paper measuring approximately 21.6 x 27.9 cms (8.5" x 11"), with 4 cms (1.63") margin on left and right and 3.81 cms (1.5") on top and bottom.

#### **8.0 Word Processing File:**

We require 3.5", 1.44 MB M.S.DOS format (IBM compatible) diskettes for all papers. Use only Word Perfect, Word, or Wordstar. Use only brand name diskettes. Please label the diskette with the first author's full name, title of paper, and Word Processor used. Make sure that the hard copy matches exactly with the computer file.

#### **9.0 Key Words:**

All papers must have a list of 15 **key words** listed on a separate sheet of paper, one per line and first letter capitalized. The list must also be included in the diskette submitted.

#### **10.0 Computer Virus:**

All authors must ensure virus-free diskettes. A contaminated diskette will entail a substantial clean up charge, as we would then have to disinfect our entire computer system.

# MATERIALS AND MANUFACTURING PROCESSES

Volume 9, Number 1, 1994

## CONTENTS

<b>Diamond Materials for Electromagnetic Railguns</b> .....	1
<i>N. B. Dahotre, M. H. McCay, and T. D. McCay</i>	
<b>Synthesis of Diamond Thin Films on TC4 by Using a Scanning Linear Flame</b> .....	37
<i>G. F. Zhang and X. Zheng</i>	
<b>Comparison of Superplastic Formability Predictions Using 2-D Plane Strain and 3-D Modeling</b> .....	45
<i>S. Lee and J. Lee</i>	
<b>Stretch Formability in HSLA and IF Steels</b> .....	59
<i>P. Matteazzi, G. Farnè, G. Randi, and M. Leoni</i>	
<b>Self-Propagating High Temperature Synthesis (SHS) of Intermetallic Compounds Titanium and Nickel Aluminides</b> .....	75
<i>H. Y. Sohn and X. Wang</i>	
<b>Processing, Microstructures, and Properties of Cr-Cr<sub>3</sub>Si, Nb-Nb<sub>3</sub>Si, and V-V<sub>3</sub>Si Eutectics</b> .....	89
<i>B. P. Bewlay, J. A. Sutliff, M. R. Jackson, and K. M. Chang</i>	
<b>Magnesium Filtration with Ceramic Foam Filters and Subsequent Quantitative Microscopy of the Filters</b> .....	111
<i>P. Bakke, T. A. Engh, E. Bathen, D. Øymo, and A. Nordmark</i>	
<b>Transformation and Sintering of <math>\gamma</math>-AlOOH and TiN Composites</b> .....	139
<i>A. Kuzjukėvičs, M. Dehler, K. Ishizaki, J. Grabis, and J. Kriegesmann</i>	
<b>Book Reviews</b> .....	151
<b>Conference Review</b> .....	171
<b>Forthcoming Meetings</b> .....	175

**MARCEL DEKKER, INC.** New York, Basel, Hong Kong  
Contributions to this journal are published free of charge